Piezoelectric Energy Harvesting From Fluid Flow

by

Hüseyin Doğuş Akaydın

A dissertation submitted to the Graduate Faculty in Mechanical Engineering
in partial fulfillment of the requirements for the degree of

Doctor of Philosophy

The City University of New York

2012

This manuscript has been read and accepted for the
Graduate Faculty in Engineering in satisfaction of the
dissertation requirement for the degree of Doctor of Philosophy.

Yiannis Andreopoulos, Principal Adviser

Date

Chair of Examining Committee

Ardie Walser

Date

Executive Officer

Examining Committee:

Niell Elvin, Co-adviser
Department of Mechanical Engineering, The City College of The City University of New York

Taehun Lee
Department of Mechanical Engineering, The City College of The City University of New York

Latif Jiji
Department of Mechanical Engineering, The City College of The City University of New York

Sheldon Weinbaum
Department of Biomedical Engineering, The City College of The City University of New York

THE CITY UNIVERSITY OF NEW YORK

Abstract

Piezoelectric Energy Harvesting From Fluid Flow

Hüseyin Doğuş Akaydın

Advisers: Yiannis Andreopoulos and Niell Elvin

The conversion of the kinetic energy of a fluid into electrical energy through flow-induced vibrations on piezoelectric structures is investigated. "Aeroelectromechanics" of flow-powered piezoelectric harvesters is introduced, the efficiency components are delineated, and the figures of merit are defined. Wind tunnel tests were performed on two kinds of harvesters: i) A cantilevered piezoelectric beam in the wake of a circular cylinder, ii) A cantilevered piezoelectric beam carrying a tip mass on its free end. The comparison of the two revealed the prime effect of aeroelastic efficiency in total efficiency. A semi-analytical model to account for strain transfer from a passive substrate to a piezoelectric patch through an elastic bonding layer was developed. It was shown that, under certain conditions, the electric output of the piezoelectric harvesters can be predicted based on strain measurements on test models built without using piezoelectric materials. The potential of turbulent boundary layers for energy harvesting was also investigated. Two flexible piezoelectric beams of different lengths were tested at various distances off the wall of wind tunnel at different flow speeds. It was found out that the power output is maximal when the beam is within a certain wall-distance region inside the boundary layer, and that the size of this region is larger for the shorter beam. The interaction of a flexible piezoelectric beam with vortex rings was another topic investigated. Time-resolved PIV images were taken synchronously with strain, base-force and piezoelectric voltage data as a vortex ring

travels over a piezoelectric beam. The dynamic tip deflection of the beam estimated using the PIV data in a potential flow solution was found comparable to the measured tip deflection. In addition to the experimental work, a computational framework for modeling aeroelectromechanical interactions was developed by integrating an electrical circuit analysis code to a flow simulation program through external scripting. The framework was applied for the case of a flexible piezoelectric beam in the wake of a cylinder. A reasonable agreement was obtained between the computer simulations and the experimental results.

Acknowledgements

I first thank my principal advisor Professor Yiannis Andreopoulos for giving me the opportunity to work with him and for supporting me in many ways during my stay at The City College of New York. Professor Andreopoulos' extensive experience in diverse subjects in fluid mechanics and willingness to explore still more of them have made working for him an exciting learning experience. Under his guidance, I enjoyed a freedom in scientific exploration which contributed immensely to my skills and confidence in conducting scholarly research.

Since his visit to our laboratory in July 2008, Dr. Niell Elvin has been driving our research with his technical expertise, hands-on experience, all-time availability, and let's-do-it attitude. Not only is he our walking library of structural dynamics, energy harvesting and electric circuits, but also he is our prime connection to the rest of the energy harvesting community. I am fortunate meeting him and engaging in this fruitful research topic for my doctoral research under his co-advisement.

I would like to thank Alexis Pierides, Savvas Xanthos, Amir Elzawawy and Oleg Goushcha for being great friends and labmates to work with. I extend my thanks professors Sheldon Weinbaum, Latif Jiji and Taehun Lee for serving in my examining committee despite a short notice.

I acknowledge the scholarship from Michael Pope Fund and CBET Grant #1033117 from National Science Foundation which financially supported this research.

Finally, I dedicate this dissertation to my parents, who have longingly supported my endeavors abroad, and to my dear wife who patiently made all the hardships more bearable.

Piezoelectric Energy Harvesting From Fluid Flow

Table of Contents

Bibliography

List of Figures

Chapter 1

Introduction

Chapter 2

Energy Harvesting From Highly Unsteady Fluid Flows Using Piezoelectric Materials

Chapter 3
Wake of a cylinder: A paradigm for energy harvesting with piezoelectric materials

Chapter 4
Experimental Study of a Self-Excited Piezoelectric Energy Harvester

Chapter 5
Performance of a Self-Excited Fluidic Energy Harvester

Chapter 6

Further Work

List of Tables

Chapter 1

Introduction

Chapter 3

Wake of a cylinder: A paradigm for energy harvesting with piezoelectric materials

Chapter 4

Experimental Study of a Self-Excited Piezoelectric Energy Harvester

Chapter 1

Introduction

1. Energy Harvesting Paradigm

During the past two decades, there has been a tremendous increase in speed and availability of wireless computing accompanied with a significant decrease in power consumption and size of wireless devices. However, a complimentary increase in power density of batteries has not been observed. The battery capacity therefore continues to limit off-grid operation time of an electrical device. This limit could be tolerable for many portable electronic devices that can be readily recharged or when battery replacement is possible. However, the feasibility of WSN (wireless sensor network) implementation is decided primarily upon the battery capacity of its sensors nodes. These sensor nodes have no wired connection for data or electrical power transmission and are typically embedded in or deployed to inaccessible or remote locations. Examples include sensors embedded in concrete blocks of bridges for structural health monitoring, deployed to ocean floor for tsunami warning systems, or placed throughout the HVAC (heat, ventilation and air conditioning) ducts of a large building for pervasive monitoring and control of energy flow (Figure 1). While the absence of wires lowers installation cost and complications of WSNs, battery replacement or recharging, if possible, remain as a costly maintenance operation.

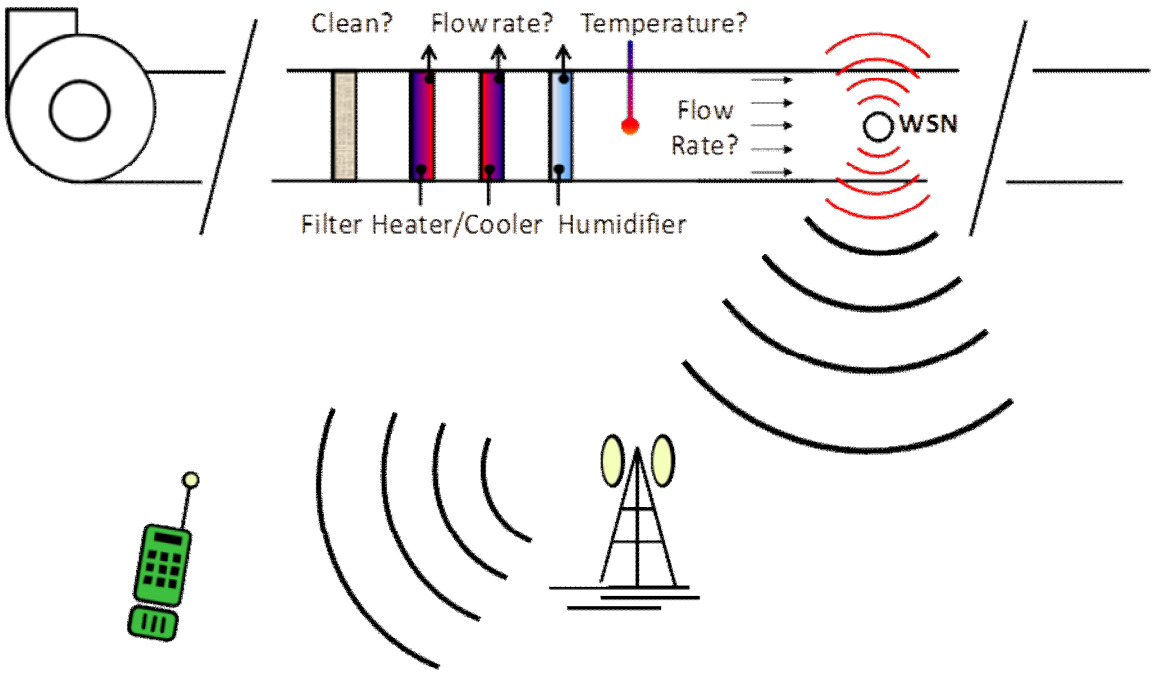

Figure 1: Conceptual application of a wireless sensor node to an HVAC system.

As power technology improvement stalled, before the anticipated prospects of WSN technologies spurred the search for alternative ways of powering wireless sensor nodes and resulted in emergence of a multidisciplinary research area called "energy harvesting" over the past decade. "Energy harvesting" can be defined as generation of *small* amounts of electrical energy from ambient sources such as light, mechanical vibrations, fluid flow, electromagnetic radiation, temperature gradient, chemicals…etc readily present within an ambient environment. Some classical examples are solar-powered calculators, self-winding wristwatches, and piezoelectric lighters. "Small" in this definition refers to amounts enough to run a low-power electronic device continuously or in a duty cycle. Considering most wireless sensors in the market, this amount is currently around a few mW or less. The amount of harvested energy is usually orders of magnitude smaller than the energy involved in the operation of the system

hosting the energy harvester. Therefore, the impact of energy drawn by the energy harvester(s) on the operation of the host system is usually neglected.

By converting the available energy around the sensors to the electrical energy they need, energy harvesting methods liberate the wireless sensors from batteries and result in substantial savings in the maintenance costs of a wireless sensor network. The ease of installation of energy harvesting sensor nodes can increase the number of measurement locations, which would have been less in a battery-operated or wired solution. Even if the energy harvested by each of these sensors is small, they could facilitate the control of much larger amounts of energy in the host system, and potentially increase its overall energy efficiency. Energy harvesting paradigm can therefore serve for "sustainability" or "green energy" causes by reducing energy waste. Additionally, energy harvesting technologies enable deployment of sensors for disaster alert or fault alert systems and has a potential to save lives. Reduction of chemical waste due to battery disposal is an added environmental benefit of energy harvesting technology. Furthermore, it may be possible in the future to improve the efficiency of current energy harvesting methods to a level that makes their large-scale implementations feasible as alternative sources of energy. Because of its immediate applications and future prospects in energy management and generation the research in energy harvesting has a positive impact on the wellbeing of society.

2. Piezoelectric Materials

Piezoelectric materials create an electric potential when under an applied mechanical strain. This is known as the "direct piezoelectric effect". Conversely,

piezoelectric materials become mechanically strained when under an applied electric potential. This is known as the "converse piezoelectric effect". The piezoelectric effect is naturally observed in some materials such as Rochelle salt, cane sugar, bone and quartz. Most modern piezoelectric devices use specially synthesized materials exhibiting high piezoelectric effect. Two piezoelectric materials in common use are PZT (Lead Zirconate Titanate), which is manufactured in form of ceramics or single crystals, and PVDF (Polyvinylidene fluoride), which is a polymer manufactured in form of thin films. PZT ceramics are brittle but they exhibit a strong piezoelectric effect whereas PVDF films are very flexible but their piezoelectricity is much weaker.

The piezoelectric effect arises from a special asymmetry in the arrangement of the atoms constituting the material. Due to this asymmetry, the atoms displace in preferred directions (dipole directions) when under an applied mechanical stress. Within an "unpoled" piece of piezoelectric material, these asymmetries are distributed randomly and the overall effect of the dipoles vanishes (Figure 2). However, the randomly distributed dipole directions can approximately be aligned along a prescribed direction by a process called "poling". Poling typically involves application of a strong electric field along a certain direction called the "poling direction" while keeping the piezoelectric material heated near a critical temperature T_C known as the "Curie point" for allowing the dipoles easily align themselves along the applied electric field. Once the poling process is completed and the temperature is decreased below the Curie point, the directions of the dipoles remain locked even after the electric field is removed.

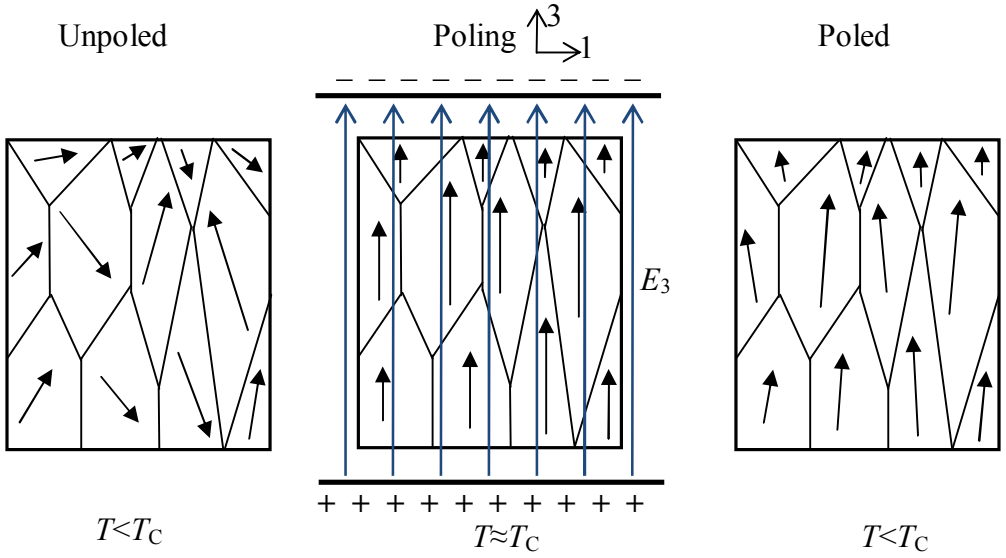

Figure 2: Poling process of a piezoelectric material.

When mechanical stress is applied to a poled piezoelectric material in a certain direction, all the dipoles tend to change length along the same direction due to their locked alignments (Figure 3). The aligned change of the length of the dipoles results in a net change in the separation of electric charges throughout the material. The electrons then displace along the poling direction and accumulate at a surface, which they render negatively charged, while leaving the opposite surface positively charged. This causes an electric field to form between two opposing faces of the material. The electric field E_3 observed (or applied) along a poling direction 3 is proportional to the strain S_3 applied (or observed) in the same direction with a piezoelectric constant d_{33}. Similarly, E_3 observed (or applied) along a direction 3 is proportional to the strain S_1 applied (or observed) in a perpendicular direction 1 through a piezoelectric constant d_{31}. Typical values of these constants are $d_{33}=390\times10^{-12}$ m/V and $d_{31}=-190\times10^{-12}$ m/V for PZT-5A [1] and $d_{33}=-33\times10^{-12}$ m/V and $d_{31}=23\times10^{-12}$ m/V [2].

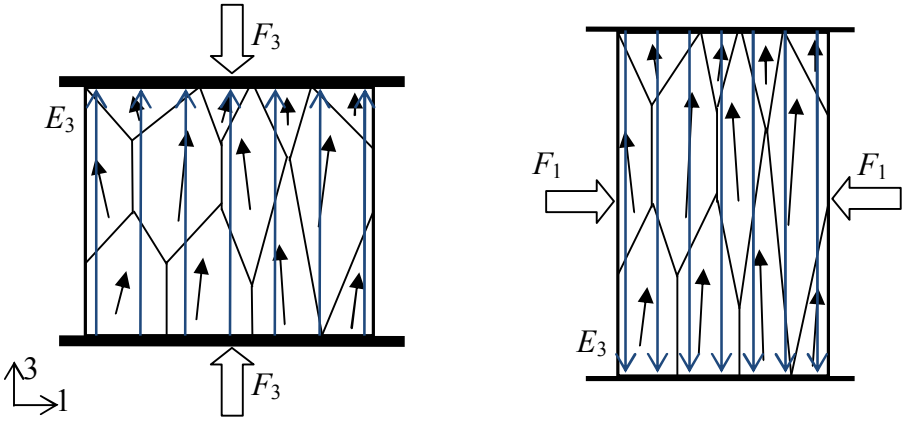

Figure 3: Qualitative relationship between mechanical stress and electric field in a piezoelectric material.

If electrodes are connected to these surfaces, the charges flow through an attached circuit from one surface to the other until the charges are balanced between the two surfaces. Reversing the direction of the applied stress creates an electric field and charge flow in the opposite sense; and as expected, a periodic change in the applied stress produces an alternating current (AC) through the attached circuit. Figure 4 depicts the operation principle of a common harvester configuration called "bimorph bender" which consists of a non-piezoelectric center layer sandwiched between two piezoelectric layers. Bending of a bimorph piezoelectric beam by a periodic excitation force creates a periodic strain field along the length of the beam (1-direction) and induces an alternating electric field along the poling direction. The strength of this electric field and the resulting current through the circuit are proportional to piezoelectric coefficient (d_{31}), Young's modulus of the piezoelectric material (Y_p) and the time rate of change of strain in the 1-direction. The piezoelectric layers of a bimorph bender can be positioned with opposite poling directions (3 and -3 directions) and connected in series for amplifying the voltage output.

If the layers point in the same poling direction, then they can be connected in parallel for obtaining a higher current.

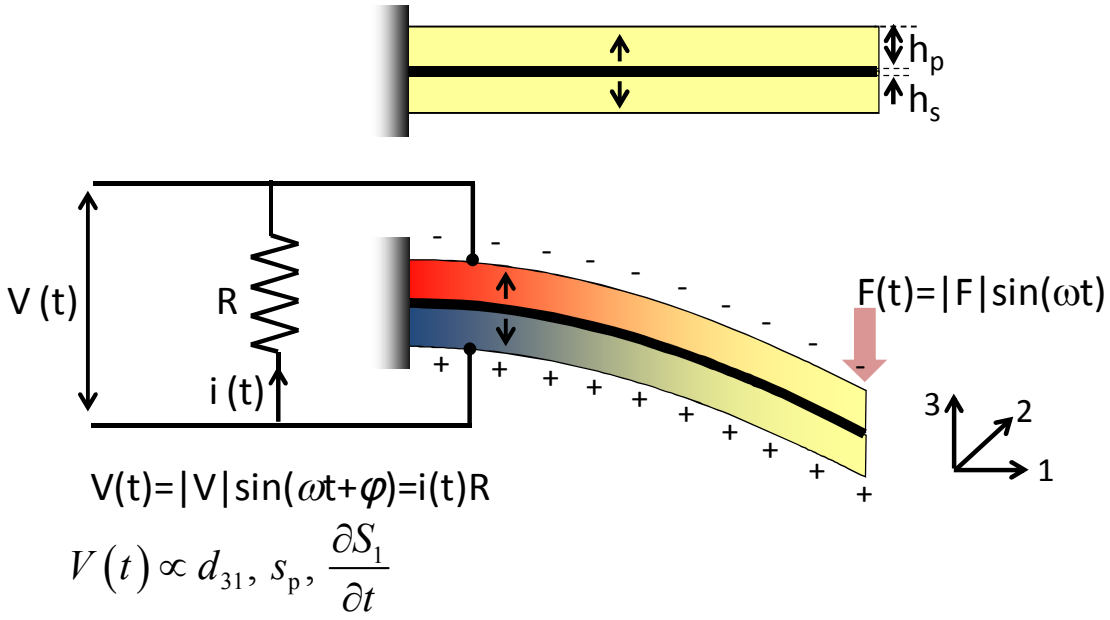

Figure 4: Operation principle of a piezoelectric bimorph bender for energy harvesting.

3. Potential of Fluid Flow for Energy Harvesting

While the ambient energy could be present in various forms around a sensor node, none of these energy sources are continuously available, nor does a given conversion method have general applicability. For example, solar collectors do not work at night or during long winters in Polar Regions; or work efficiently in the absence of direct sunlight (inside buildings, in dusty environments, or in deep undersea locations). Thermal sources (hot pipes, furnaces…etc) may not be present everywhere inside a setting or have enough potential for energy harvesting. Ambient vibrations in an environment are usually not desired, and are deliberately suppressed for system efficiency and comfort reasons. This limitation poses a challenge for energy harvesting based on the vibrations on the host structure. The potentials of magnetic, radio frequency and chemical sources of energy in

the surrounding environment are often limited due to similar reasons. There are cases; however, where a significant amount of kinetic energy is available in the form of fluid flow such as in wind, in ocean currents, or in ventilation ducts or water pipes. Exploitation of fluid flow for energy harvesting therefore extends the application of wireless sensing technologies to the situations when/where other sources of ambient energy are practically not available.

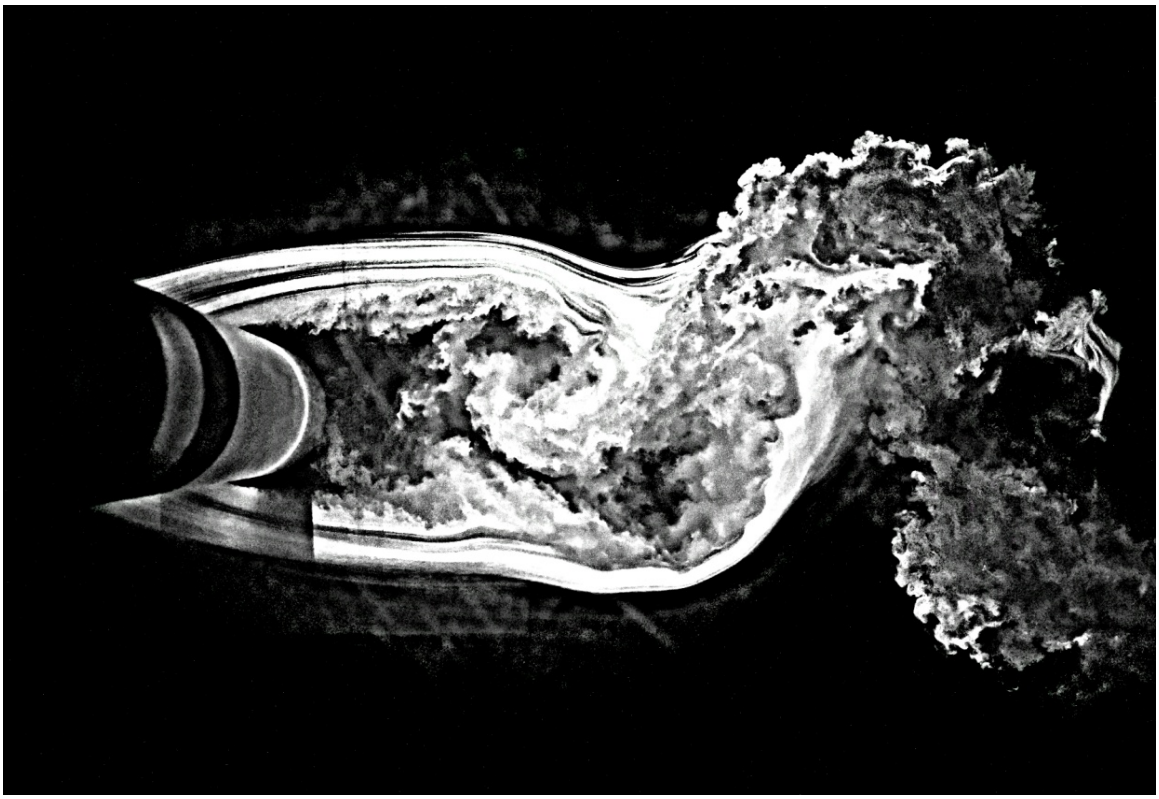

Figure 5: Flow behind a long circular cylinder. Re≈70,000. Visualization is done in the CCNY Aerolab wind tunnel by injecting theatrical smoke into the flow far upstream and photographing the wake with a digital camera.

The focus of this dissertation is conversion of the kinetic energy of fluid flow to electrical energy by means of the piezoelectric effect. Fluid flows contain large amounts of mechanical energy in many different scales as seen in Figure 5. The mechanical power carried by a cross section of a flow is proportional to the third power of flow speed. For

example, in air flowing at 1 m/s (typical for an HVAC system), the available mechanical power is about 600 mW per square meter of duct cross section. Flow of air at a speed of 10 m/s (typical for wind power generation), however, carries about 600 W per square meter of cross section. While a wind turbine based on electromagnetic conversion is an efficient generator at large scales, reducing its size to the micro-scale disproportionally degrades the turbine's aerodynamic performance, increases its stall speed, lowers its voltage output, and complicates its design and manufacturing [3]. Piezoelectric conversion, on the other hand, leads to mechanically simpler and arguably more durable harvesters in small scales while generating higher voltages needed for AC (alternating circuit) to DC (direct circuit) rectification. However, the bulk kinetic energy in a uniform fluid flow is useful only when it creates oscillatory deformations on the piezoelectric structure. The efficiency of this "aeroelastic conversion" is the key for a successful piezoelectric energy harvester operating in uniform fluid flow and investigated in detail in this dissertation.

4. Aeroelectromechanics

Insertion of a piezoelectric structure in a fluid flow results in a series of mutual interactions between the flow of the fluid, structural mechanics of the harvester and the electric field generated by the piezoelectric material. A visual description of this three-way interaction known as "aeroelectromechanics" is given in Figure 6. The kinetic energy of a uniform and steady fluid flow is converted to time-dependent strain energy within the harvester through flow-induced vibrations. The efficiency of this conversion is called the "aeroelastic efficiency", η_{ae}. Once the time-dependent strain energy is

generated in the piezoelectric structure by the fluid flow, it is converted to AC electrical energy through the direct piezoelectric effect with an associated "electromechanical efficiency" η_{em}. Finally, the AC electrical energy is rectified and conditioned to DC (direct current) through a series of electrical circuits, and the resulting charge is typically stored in devices such as rechargeable batteries, capacitors etc. before being supplied to the electronic device (e.g., a wireless sensor node). The efficiency of this conditioning process is termed as "electrical conditioning efficiency", η_{ec}. The total efficiency of the harvester then can be expressed as follows:

$$\eta_t = \eta_{ae}\eta_{em}\eta_{ec} \tag{1}$$

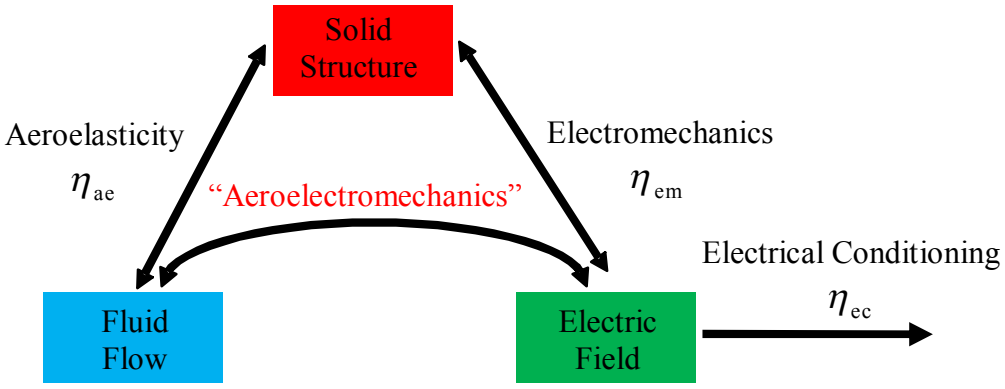

Figure 6: The aeroelectromechanical interactions and the conversion efficiencies in a fluidic energy harvester.

The mutual interaction between incompressible flow of a Newtonian fluid, linear elastic deformation of a piezoelectric structure and resulting electric field through the structure is given by the incompressible Navier-Stokes equations, Equation (2) [4], coupled with linear piezoelectric constitutive equations, Equations (3) [5]:

$$\frac{\partial u_{\mathrm{i}}}{\partial t}+u_{\mathrm{j}}\frac{\partial u_{\mathrm{i}}}{\partial x_{\mathrm{j}}}=-\frac{1}{\rho}\frac{\partial p}{\partial x_{\mathrm{i}}}+\nu\frac{\partial^2 u_{\mathrm{i}}}{\partial x_{\mathrm{j}}\partial x_{\mathrm{j}}} \tag{2}$$

$$S_{ij}=s^{\mathrm{E}}_{ijkl}T_{kl}+d_{kij}E_k \tag{3a}$$

$$D_i=d_{ikl}T_{kl}+\varepsilon^{\mathrm{T}}_{ik}E_k \tag{3b}$$

where u is velocity, p is pressure, ρ is density and ν is kinematic viscosity of the fluid whereas S is strain, T is stress, E is electric field and D is electric displacement in the piezoelectric structure, and s^{E} is elastic compliance constant under constant electric field, ε^{T} is permittivity constant under constant stress and d is the piezoelectric constant of the piezoelectric material. In the absence of the piezoelectric term $d_{kij}E_k$, Equations (2) and (3a) pose the notoriously challenging problem of aeroelasticity. The flow-induced pressure distribution over the boundaries of a solid structure results in a stress field (T) and deformation on the solid structure while the deformation of the structure alters the flow field and pressure distribution. Depending on the level of aeroelastic coupling, the dynamics of one domain (i.e. fluid or solid) can dominate that of the other; however, there are many cases where the influence of theses domains on each other is equally significant and mutual (e.g. flutter of wings, galloping of wires, vibration of reed valves…etc). With the presence of the piezoelectric term $d_{kij}E_k$, the problem becomes even more complicated; the flow-induced pressure variations over the boundaries of the piezoelectric structure create mechanical stresses which result in an electric field and charge displacement through the structure. This sequence of interactions due to the direct piezoelectric effect is termed the "sensing mode" of operation. Conversely, displacement of charges induces an electric field that creates mechanical strain on the piezoelectric structure, and the resulting deformation of the structure alters the pressure distribution

and therefore the flow field. In this case, the sequence of the interactions is due to the converse piezoelectric effect and named as "actuation mode" of operation. Although in most cases one mode of operation is more significant and dominates the other one, in principle the sensing and actuation modes (i.e. direct and converse piezoelectric effects) are present at the same time, resulting in a mutual interaction between the flow field and electric field through the stress field in the piezoelectric material. For the case of harvesters investigated in this study, the converse piezoelectric effect is insignificant, i.e. the effect of the changes in the electric field on the flow field are too small to be observed experimentally. Nevertheless, the computational framework present in this dissertation considers the mutual interaction between the all three domains. For the purposes of theoretical design and experimental validation, the aeroelastic side of the problem alone presents some major challenges that have been addressed in this work. For example, the frequency and magnitude of aerodynamic forces change significantly due to deformation and motion of the flow-powered harvester. Therefore, the force coefficients based on stationary and rigid approximations cannot be used for designing these harvesters. Furthermore, three dimensionality of the flow becomes important in the determination of the geometric proportions of the harvester. In this study a good combination of geometric dimensions and shapes for building a practically useful flow-powered harvester was found through an experimental design exploration. The comparison of two distinct harvester concepts revealed the crucial importance of aeroelastic effects in total performance of a flow-powered harvester. In addition, it was shown that it is possible to predict the performance of these harvesters reliably based on measurements taken on dummy models containing no piezoelectric components, thus allowing for decreasing the

cost and burden of design explorations, which could require the testing of many different test models.

5. Organization of the Dissertation

This dissertation presents some of the work done for flow-powered piezoelectric energy harvesting project at CCNY's (The City College New York) Aerodynamics Laboratory. The major tasks of this doctoral research can be listed as follows

(i) Experimentally investigate the behavior of flexible piezoelectric structures subject to various flow conditions

(ii) Develop and verify a computational framework to predict the electrical output of a piezoelectric structure subject to a specific flow condition.

Since the first tests performed in late July 2008, five original research articles were published based on this doctoral research. Three of these articles were peer-reviewed, and their manuscripts are presented in chapters 2, 3 and 5. In Chapter 4, the manuscript of an article published in a conference proceeding was presented to explain the transition between chapters 3 and 5. The order of the manuscripts is chronological and reflects the continual progress of the work for this dissertation.

In Chapter 2, the behavior of a flexible piezoelectric beam in the wake of a circular cylinder and in a turbulent boundary layer is experimentally investigated. The concept of "aeroelectromechanics" which involves the consideration of the coupled interactions of fluid dynamics, structural dynamics, and electric field is introduced. A computational framework developed for aeroelectromechanical simulations is demonstrated for the case of a piezoelectric beam in the wake of a circular cylinder.

Chapter 3 further investigates the characteristics of the wake of a circular cylinder for piezoelectric energy harvesting. The variation of the extracted power with respect to the position of the harvester in the wake of the cylinder, namely the "power landscape" of

the wake, is studied in detail. Some statistical characteristics of the time-dependent behavior of the beam in near and far wake regions are determined. The two mechanisms by which a travelling vortex creates force on the flexible beam are explained with support of flow-visualization. Finally, some potential flow calculations for a vortex near an infinitely long rigid wall are present to demonstrate the effect of distance and strength of a vortex on the pressure distribution on the wall.

The configurations studied in the first two chapters relied on fluctuations present upstream of the piezoelectric beam. If the incoming flow is steady and uniform (i.e. turbulence, bluff-body wakes or gusts are not present), then a plain piezoelectric beam will create little or no vibration to produce electric power. It is possible however, to modify the shape of the beam so that it can generate and sustain large-amplitude vibrations induced by a uniform and steady flow. In Chapter 4, a new configuration having such a "self-excited" feature is introduced. In this configuration, a small circular cylinder is attached on the free end of a cantilever piezoelectric beam, thus allowing the aerodynamic forces acting on the cylinder to deform the beam periodically. Despite its prospects, however, the electrical power output of the initial design was not too impressive. Several factors lowering the performance of the configuration were identified: (i) end-effects due to the low aspect ratio of cylinder, (ii) splitter-plate effect due to the relatively large width of the beam and (iii) due to high stiffness of the beam precluding the aeroelastic effects.

In Chapter 5, the issues on the design presented in the previous chapter are addressed. In this study, a longer piezoelectric structure carrying a cylinder of higher aspect ratio was studied. The increased aspect ratio of the cylinder decreased the end

effects and the splitter-plate effect mentioned earlier. The increased length of the beam decreased its stiffness and resonant frequency, allowing the structure to create and lock-in flow-induced vibrations at much lower speeds than before. An analysis of efficiency components revealed that the aeroelastic efficiency of the design presented in Chapter 5 was much larger than that of the design presented in Chapter 1. It was found that the increase in aeroelastic efficiency was due to the contribution of the aerodynamic forces on the cylinder to bending of the beam as was hypothesized previously. It was further found out that the cross-flow motion of the cylinder dramatically increases the dynamic lift forces acting on the cylinder as compared to those acting on a stationary cylinder. Coupled with the structural resonance, this aeroelastic effect results in largely amplified tip deflections and increases the electric power output of the harvester.

Some of the work done for this dissertation has not yet been published elsewhere. Chapter 6 is devoted to present these work. In the first section of this chapter, the effect of changing the tip mass shapes of a self-excited energy harvester is investigated. In the second section, the response of a shorter piezoelectric beam in a turbulent boundary layer is compared with that of a longer one studied in Chapter 1. In the third section, first an experiment for taking measurements and PIV images while a vortex ring travels above a flexible beam is introduced, then comparison of the measurements with estimations using potential flow theory is presented.

Finally in Chapter 7, an overall summary of the work done for the tasks of the dissertation is given.

References

1. Piezo Systems, Inc. www.piezo.com

2. Measurement Specialties, Inc. www.meas-spec.com

3. Mitcheson P D Yeatman E M Rao G K Holmes A S Green T C 2008 Energy Harvesting from Human and Machine Motion for Wireless Electronic Devices *Proceedings of the IEEE* 96(9): 1457-86

4. Panton R 1996 *Incompressible Flow* John Wiley & Sons, Inc. 2nd Ed.

5. Erturk A, Inman D J 2011 *Piezoelectric Energy Harvesting* John Wiley & Sons, Inc.

Chapter 2

Energy Harvesting From Highly Unsteady Fluid Flows Using Piezoelectric Materials

Hüseyin Doğuş Akaydın, Niell Elvin, Yiannis Andreopoulos

Published on 29 March 2010 in

Journal of Intelligent Material Systems and Structures, 21(13):1263-1278 (2010)

Abstract

In the present work we explore some aspects of energy harvesting from unsteady, turbulent fluid flow using piezoelectric generators. Turbulent flows exhibit a large degree of coherence in their spatial and temporal scales which provides a unique opportunity for energy harvesting. The voltage generated by short, flexible piezoelectric cantilever beams placed inside turbulent boundary layers and wakes of circular cylinders at high Reynolds numbers is investigated. Matching the fluid flow's predominant frequency with the natural frequency of the piezoelectric generator appears to maximize the piezoelectric output voltage. This voltage is also dependent on the generator's location inside the flow field. A three-way coupled interaction simulation that takes into account the aerodynamics, structural vibration and electrical response of the piezoelectric generator has been developed. The simulation results agree reasonably well with the experimental

data paving the way of using such a tool to estimate the performance of different energy harvesting devices within unsteady flow fields.

Keywords: piezoelectric, energy harvesting, unsteady flow, turbulence, cylinder wake, vortex street, boundary layer, flow-structure interaction, aeroelasticity, electromechanics, aeroelectromechanics

1. Introduction

Recent advances in microelectronics have led to a substantial increase in processor speeds (approximately a thousand times) over the last two decades. However, battery energy densities have only increased by a factor of two over the same time period (Paradiso and Starner, 2005). Supplying adequate electrical power is one of the major bottlenecks preventing the further miniaturization of wireless devices such as sensor nodes. A continuous source of electrical energy to replace (or supplement) existing powering methods without periodic battery recharging (or replacement) would be highly desirable. One method of supplying the required power for small electronic devices is by harvesting the energy available in its operational environment. A typical sensor, say a strain gage used for structural health monitoring, generally has a power consumption requirement of approximately 1 mW. The emerging field of energy harvesting focuses on finding and improving methods of generating sufficient energy for such small electronic devices. Since energy harvesting is a multidisciplinary topic, the research in this area is conducted in many fields such as structural mechanics, material science, chemistry, electronics, computer science and more recently, fluid mechanics. Detailed surveys of the

current state of the technology are presented by Mitcheson et al. (2008), Paradiso and Starner (2005) and Gilbert and Balouchi (2008).

Environmental power sources for energy harvesting include: mechanical vibrations, light, heat and electromagnetic radiation. In this paper we focus on mechanical vibration scavenging which is typically done using an electrostatic, electromagnetic or piezoelectric approach. Materials having piezoelectric properties generate electricity when exposed to a mechanical strain, and conversely change shape when exposed to an electric field. By storing the electrical charge generated during the mechanical straining of a piezoelectric material, it is possible to power an electronic device such as a wireless sensor. Piezoelectric energy harvesters are solid-state devices which do not require many moving components that thus not likely to need long term maintenance. Piezoelectric materials also readily lend themselves to MEMS (micro electromechanical systems) fabrication techniques which can greatly decrease the overall size of the device. Furthermore their energy output typically produces relatively high voltages and low currents (as compared to traditional electromagnetic generators) which make them suitable for many sensing and low power electronic applications. To date piezoelectric, self-powered electronic devices are either: small, imbedded sensors emitting wireless signals used to assess the mechanical performance of a structure (Ha and Chang, 2005; Lajnef, Chakrabartty and Elvin, 2006; Discenzo, Chung and Loparo, 2006;) or wireless transmitters such as active RFID (radio frequency identification) tags (Kymissis, et al, 1998; Kimura, 1998).

In addition to those small-scale applications, there are conceptual designs for using piezoelectric materials for large-scale energy harvesting such as the ocean-wave

driven piezoelectric harvester of Taylor et al. (2001). Due to increased environmental awareness, the possibility of using piezoelectricity as a "green energy" source have given rise to ideas such as piezoelectric subway platforms, conveyor bands, turnstiles, stairs, pavements, highways, railroads, bridges, disco dance floors etc.; and some of these large-scale concepts are being currently implemented. Further advances in piezoelectric materials research would enable a greater conversion rate of ambient mechanical energy to electrical energy. Such developments now position these materials as viable alternative energy sources, to obviate the need for or augment the use of batteries and wired power.

2. Piezoelectric Energy Harvesting from Fluid Flow

Recent surveys on the use of piezoelectric energy harvesting from structural deformations and vibrations (Sodano, Park and Inman, 2004; Anton and Sodano, 2007) show that the research in energy harvesting by piezoelectric materials focuses primarily on harvesting energy from the mechanical vibration of the structure to which the harvester is attached. Studies on the conversion of the kinetic energy of fluid flow in this field remain fairly limited.

Most of the research in piezoelectric energy conversion from fluid flow has concentrated on various windmill designs (Schmidt 1992, Priya et al. 2005, Myers et al. 2007). Advances in modern micro-manufacturing techniques may make it possible to shrink the sizes of these turbines to the centimeter scale. However the performance of turbine based generators greatly degrades as the surface-related phenomena (such as viscous losses on the blade channels and frictional losses on bearings) start to dominate their dynamics. In fact, even the perfect, no-loss turbine is limited to convert 59.3% of

the flow energy which is known as "Betz limit" (Douglas et al., 2005) and losses reduce this fraction down to 10% or far less as shown by Mitcheson et al. (2008). Moreover, the added mechanical complexities and susceptibility to clogging, increases the cost and maintenance requirements of such harvesters.

An alternative to the micro-turbine design is to place a simple bending piezoelectric structure directly into the fluid flow. Although Schmidt (1992) introduced such a concept via his "oscillating blade" design, the idea was largely neglected until the work of Allen and Smits (2001). Allen and Smits (2001) studied the behavior of long and very flexible piezoelectric strips (so-called "eels") in the wake of a flat plate normal to a flow. They presented results on structural response of the eel based on modal analysis and provide PIV (particle image velocimetry) images to support and interpret their predictions. They concluded that for the maximum coupling between the eel and the vortex street, the eel should have a small enough stiffness as not to dampen the oscillations, and its natural frequency should match to the shedding frequency of the upstream vortices. The eel concept has been applied to harvest energy from ocean waves by Taylor et al. (2001). An attempt to analytically model the vortex street in the wake of bluff body was done by Pobering and Schwesinger (2004) to show the feasibility of the energy harvesting eel concept. Recently, Robbins et al. (2006) have investigated the performance of piezoelectric sheets in airflow using a synchronized-switching circuit for improved electrical energy conversion.

In the present work we consider the case of flow kinetic energy harvesting in the wake of a circular cylinder at high Reynolds numbers and inside a turbulent boundary layer. Our research approach involves a combination of experimental and computational

work. The experiments have been simulated experimentally by modeling the three-way interactions of the turbulent flow, piezoelectric structure and the harvester electronic circuit *at the same time*. This is in contrast to previous work in this field which has largely concentrated on studying one or more aspects of the electrical, structural and fluid problems. Thus the present approach has the potential of revealing physical aspect of this three-way interaction which have not been observed before. In addition to our novel computational approach, this paper presents, for the first time, experimental data obtained in turbulent boundary layers.

3. The Present Approach

A performance analysis for inertial harvesters (Mitcheson et al., 2008) shows that the harvested power (P) is proportional to vibration amplitude and the cube of the operation frequency[*]:

$$P \propto y_t \times f^3 \tag{1}$$

where y_t corresponds to the tip displacement of a cantilevered piezo-beam, f is the frequency of vibration of the harvester. Thus for the same tip displacement, an increased operational frequency increases the output power. Ceramic based piezoelectric materials such as PZT (Lead Zirconate Titanate) typically operate at frequencies in the kHz range. However, their brittleness and high stiffness make them unfavorable for fluid energy harvesting structures which generally operate in conditions of high displacements and

[*] In case of a piezoelectric generator, an accurate modeling of coupling of electrical and mechanical domains is required to calculate the correct values of power output as suggested by Erturk and Inman (2008a). For the purpose of the simplified scale-analysis, this coupling is ignored.

strain levels. Plastic based piezoelectric materials such as PVDF (Polyvinylidene Fluoride) on the other hand, can be flexed with very little force to relatively high mechanical strain levels without damage. However their electromechanical coupling coefficients are typically much lower than for PZT.

Turbulent flows are characterized by a large number of temporal and spatial scales with significant kinetic energy distributed over these scales. The available power in the fluid flow is proportional to U_f^3, where U_f is a characteristic velocity which is proportional to a typical length scale L_f, and a frequency scale f_f. The available power in such a fluctuating flow is therefore proportional to L_f^3 and f_f^3. In this paper we investigate the energy conversion performance of a PVDF cantilever structure with a relatively large tip displacement and high operational frequency in highly-unsteady turbulent flows. This generated energy can be used for continuously powering a small electronic device, or the generated energy can be stored for intermittent use at a later stage. The electronic device could be a sensor that is used to measure the unsteady characteristics of the flow (such as turbulence levels, flow speed, vortex shedding frequency etc.) and then to send wireless information to a remote receiver.

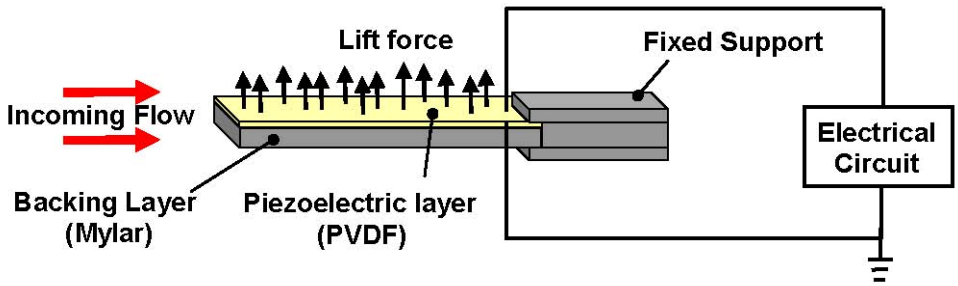

Figure 1: A schematic diagram of the piezoelectric generator in a flow field.

Chapter 2: Energy Harvesting From Highly Unsteady Fluid Flows Using Piezoelectric Materials

The basic design of the proposed harvesting device consists of a cantilever PVDF beam and the associated electronics, as schematically shown in Figure 1, placed within an unsteady fluid flow. One such unsteady fluid flow is the wake behind a cylinder (the so called "Karman Vortex Street") which consists of a staggered array of vortices (Figure 2). These vortices are periodically shed from the top and bottom of the cylinder and rotate in alternating directions. If a flexible beam is placed in the vortex street, the consecutive vortices passing along the top and bottom surfaces of the beam will dynamically change the static pressure on the surface of the beam and thus cause it to oscillate.

Vortex shedding from a circular cylinder is chosen in the present study since it has been extensively studied (Roshko, 1953; Roshko, 1961; Lienhard, 1966; Unal and Rockwell, 1988a) for a wide range of Reynolds number, and the downstream conditions at the location of the piezoelectric beam are well characterized. A fully turbulent vortex street (as studied in the present paper) is expected to form at Reynolds numbers near 10,000. The flow structure in the wake of a cylinder at a similar Reynolds number has been investigated numerically and experimentally by Dong et al. (2006). It should be noted that based on the previous studies on rigid or hinged splitter plates in a vortex street (Unal and Rockwell, 1988b; Shukla, Govardhan and Arakeri, 2009) the presence of the piezoelectric generator is expected to alter the flow field in the wake of the cylinder.

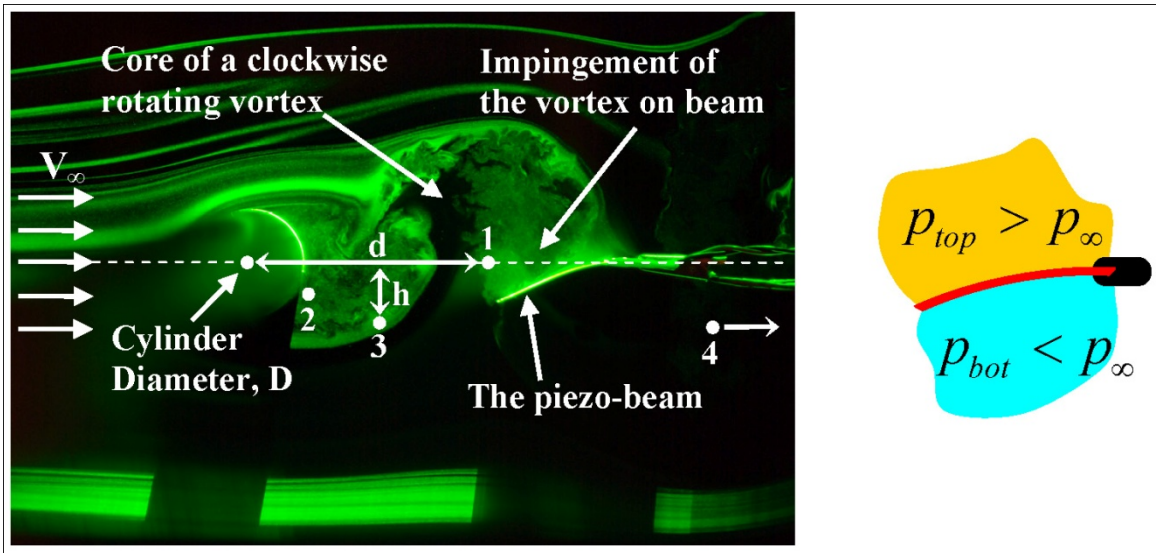

Figure 2: The concept of placing an elastic beam into the vortex street to induce vibration (smoke is used for flow visualization behind the circular cylinder). Designated points (1, 2, 3 and 4) represent approximate measurement locations. Background is a flow visualization picture obtained by the illumination of smoke particles released upstream with a laser sheet coming from the top of the figure. The black shadows on the bottom are cast by the cylinder and the beam.

3.1. Computational Methods and Modeling

Energy harvesting from a flexible piezoelectric structure within a fluid flow involves the mutual interactions of (i) the fluid flow, (ii) the electromechanical structure and (iii) the attached electrical circuit. The fluid flow pressure exerts a force on the generator causing it to deform and thus inducing mechanical strains within the piezoelectric layers. The mechanical strain generates a charge in the piezoelectric layers which is then used by the harvester circuit. The response of the circuit feeds back into the piezoelectric structure, changing its shape and thus modifying the fluid flow field. These mutual interactions can be described by the governing equations of each subsystem with the addition of the appropriate coupling terms. In flow speeds less than 0.3 of speed of the sound, the flow can be considered incompressible, which is valid for the cases presented herein. The incompressible flow of a Newtonian fluid such as air can be

described by the continuity (equation 2a) and N-S (Navier-Stokes) equations (equation 2b) in index notation as

$$\frac{D\rho}{Dt} + \rho S_{kk} = 0 \tag{2a}$$

$$\rho \frac{DV_i}{Dt} = -\frac{\partial p}{\partial x_i} + \frac{\partial \tau_{ij}}{\partial x_j} \tag{2b}$$

where $\frac{D}{Dt} = \frac{\partial}{\partial t} + V_k \frac{\partial}{\partial x_k}$ is the total derivative operator, p is the pressure in the fluid, ρ is the fluid density, V_i is the fluid velocity vector, τ_{ij} is the stress tensor and S_{kk} is the strain rate tensor. Equations (2) and (3) are subject to the no slip boundary conditions on the surface of the moving structure:

$$V(x,y,z) = V_\Omega(x,y,z) \text{ where } x,y,z \in \Omega \tag{3}$$

where Ω is the wet surface of the deforming structure, V_Ω is velocity of Ω, p is the pressure in the flow; ρ and μ are the density and dynamic viscosity of the fluid respectively. The shape of the structure modifies the flow field through the boundary conditions; while p_Ω, the pressure acting on Ω, generates the forcing term F in the structural equation as shown below. Note that the contribution of the shear stresses over the surface of the structure is relatively small and is thus neglected.

Under linear Euler-Bernoulli beam assumptions with the piezoelectric poled through the thickness, the constitutive equations for electromechanical coupling are one dimensional and given by:

$$T_1 = S_1 c_{11}^E - E_3 e_{31} \tag{4}$$

$$D_3 = S_1 e_{31} + E_3 \varepsilon_{33}^S \tag{5}$$

where the subscripts $_1$ and $_3$ respectively show the directions of the length and thickness of the beam, T_1 is the stress and S_1 is the strain along the length of beam; D_3 is the electric displacement and E_3 is the electric field through the thickness of the piezoelectric layer. c_{11}^E is the elastic stiffness (Young's modulus) at constant electric field, ε_{33}^S the electric permittivity at constant strain and e_{31} is the piezoelectric constant. The three equations (2), (4) and (5) form a coupled system of equations governing the *aero-electro-mechanical* behavior of the generator and must be solved for the common unknowns (V_Ω, p_Ω, T_1, and D_3). This concept is also depicted in Figure 3.

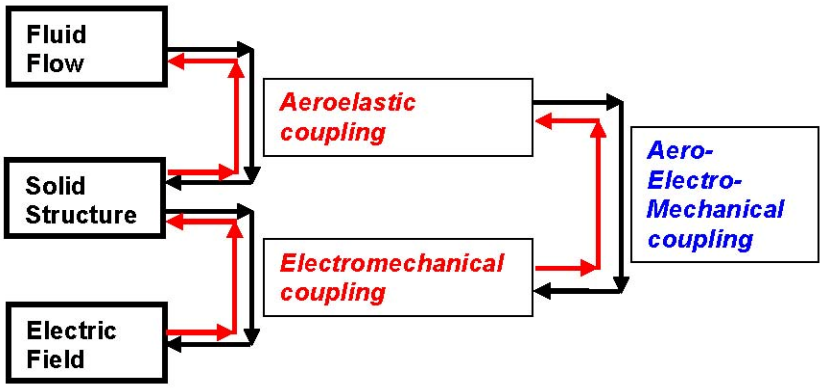

Figure 3: Schematic of three-way interaction between the flow, structure and electrical field.

If the structural response of a slender piezo-beam is modeled as a SDOF (single degree of freedom), the electromechanical response, i.e. equations (4) and (5), for a purely resistive load (R) is given by

$$m\ddot{y}_t + c\dot{y}_t + ky_t - \Theta v = F \tag{6}$$

with the initial conditions $y_t(t) = 0$ and $\dot{y}_t(t) = 0$ when $t = 0$ and

$$\Theta \dot{y}_t + C\dot{v} = -\frac{v}{R} = I \tag{7}$$

with the initial condition $v(t) = 0$ when $t = 0$. Here y_t is the tip deflection, v is the voltage, I is the current, F is the applied force, m is the mass, c the structural damping coefficient, k is the stiffness of the beam, C is the capacitance and Θ is the electromechanical coupling coefficient of the piezoelectric generator. The over-dot represents a derivative with respect to time. Note in Equation (6) that the viscous damping due to the ambient fluid (i.e. air) is neglected. Equations (6) and (7) are also known as the "actuator" and "sensor" equations, respectively.

In the case of open circuit analysis, we can set $R = \infty$ and obtain the following relation between the tip displacement and the open circuit voltage:

$$y_t = \frac{-C}{\Theta} v_{oc} \tag{8}$$

The open-circuit piezoelectric coupling can be added into the structural response simply in the form of added stiffness as

$$m\ddot{y}_t + c\dot{y}_t + \left(k + \frac{\Theta^2}{C}\right) y_t = F \tag{9}$$

In case of small deflections, the excitation force and the corresponding shape of the beam can be approximated by using a Rayleigh-Ritz weighted residual method (Elvin et al. 2006). If we consider only the first mode and neglect any contribution of the second and higher modes

$$F(t) = \int_{x=0}^{L} \bar{p}(x,t)\phi(x)\,dx \tag{10}$$

where L is the length of the beam, $\bar{p}(x,t)$ is the net pressure force acting on the surface of the beam per width and ϕ is the weighting function for the first-mode shape assumed to be

$$\phi(x) = \left[1 - \cos\left(\frac{\pi}{2}\frac{x}{L}\right)\right] \tag{11}$$

which relates the beam shape to the tip deflection as

$$y(x,t) = y_t(t)\phi(x) \tag{12}$$

The other terms in equations 6 and 7 (i.e. *m*, *c*, *k*, Θ and *C*) are also given as a function of ϕ (see for example Elvin at al., 2006).

The electrical energy generated in a time interval (t_0, t_1) is

$$E_{elec} = \frac{1}{R}\int_{t_0}^{t_1} v^2 dt \tag{13}$$

and the average power in the same interval would then be

$$P_{elec} = \frac{E}{t_1 - t_0} \tag{14}$$

In this paper, the two dimensional N-S equations (equation 2) were solved using the pressure-based model (which decouples the pressure and velocity fields) in FLUENT (Ansys, Inc. Canonsburg, PA. USA). The time step is set to 5×10^{-4} seconds, which gives approximately 40 solutions steps per vortex shedding cycle (i.e. approximately 50Hz). The SST (Shear Stress Transport) k-ω turbulence model is used for its good performance in predicting the lift and drag forces on the cylinder in the simulations when no beam is present. In the absence of the beam, the lift coefficient on the cylinder fluctuates about 0 and with peaks at $\pm$ 1.5 at a shedding frequency of 54 Hz; the drag coefficient fluctuated

about 1.44 with maximums of 1.54 and minimums of 1.35. These values compare well with those found in literature (Panton. 1996 and Dong et al., 2006). Figure 4 shows the computation domain, boundary conditions and the mesh. A total of 27057 cells are used in the whole domain. In the vicinity of the beam, triangular cells are used to facilitate simple dynamic remeshing at each time step. Quadrilateral cells are used otherwise. A high mesh density is required at the boundary layer for accurately modeling the viscous effects such as vorticity generation. Thus the cell heights near the walls are determined such that their dimensionless wall distances are always less than 1 ($y^{+}_{wall} < 1$) and as such there will be about 5 to 10 cells inside the viscous sublayer. Figure 5 show the detailed views of the mesh near the cylinder and the beam.

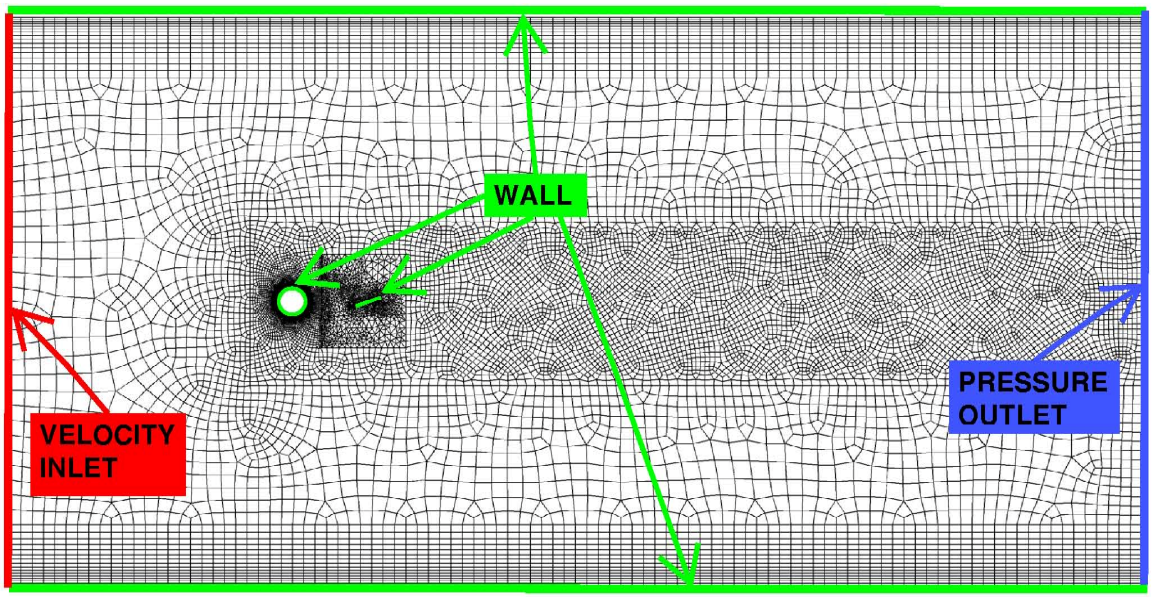

Figure 4: Computational domain, mesh and boundary conditions.

(a)

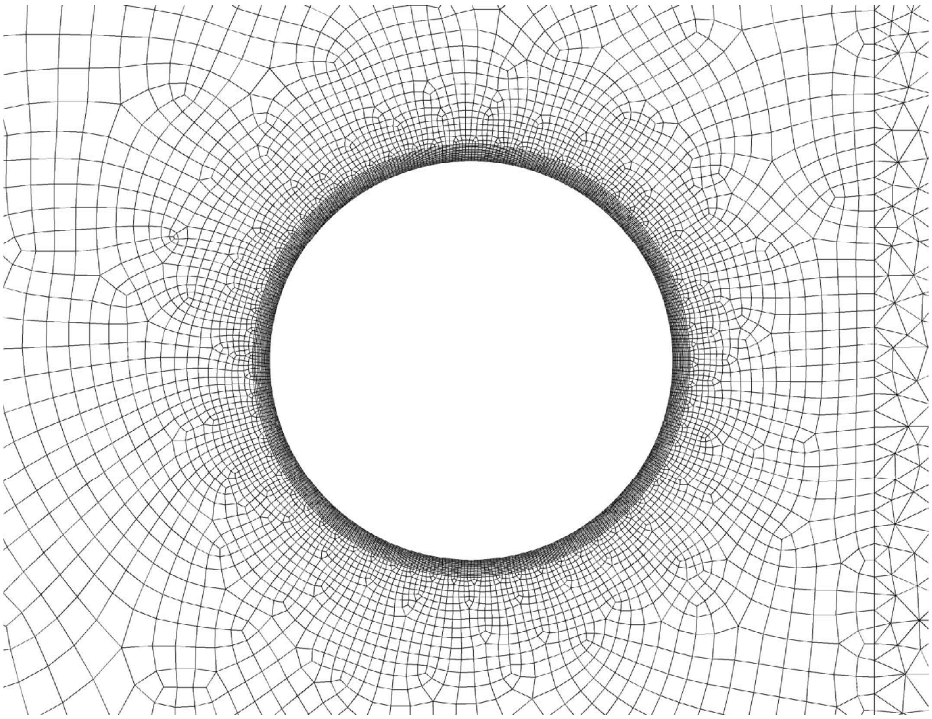

(b)

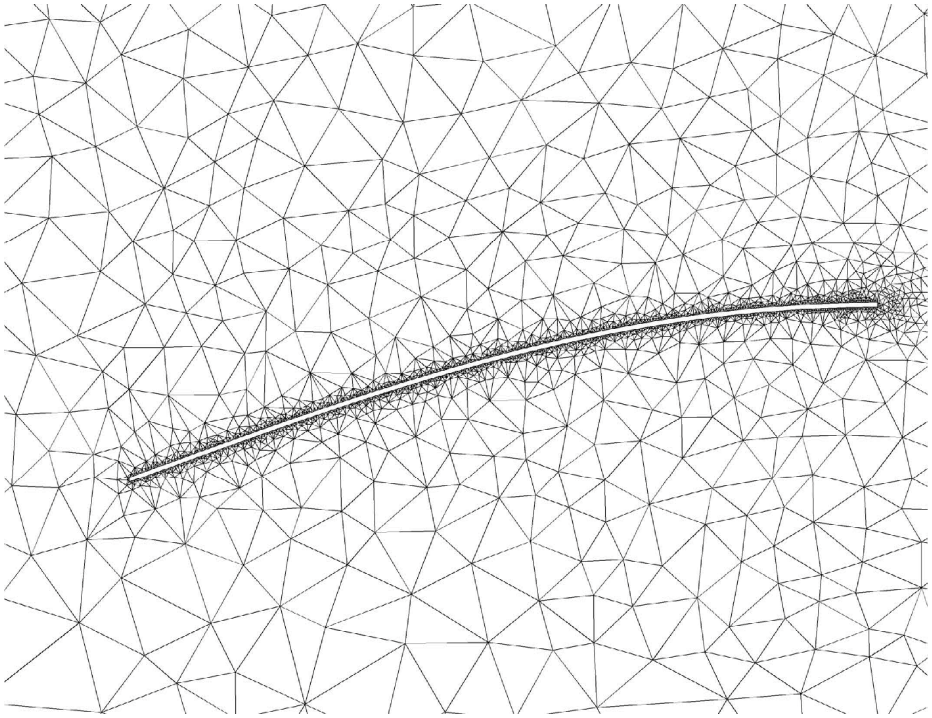

Figure 5: Detailed view of the mesh a) near the cylinder. b) near the beam.

In order to model the interactions between the flow, structure and the circuit, a sub-program, known as "user defined function" (UDF) within FLUENT, is developed to calculate the shape of the piezoelectric generator at each time step and to change the boundary conditions within the flow solver. While the flow solver handles the N-S equations (equation 2), the UDF handles solution of structural and electrical equations (equation 9 and 8, respectively, as shown in Elvin and Elvin (2009a)). The flow chart of this method is shown in Figure 6. The pressure distribution on the surface of the beam is found from a finite-volume solution of the N-S equations (Pane I). The UDF integrates this pressure distribution to find the force input in the actuator equation (equations 9) and calculates the tip deflection of the piezoelectric beam in the next time step using a SDOF lumped-parameter approach. The shape of the beam is approximated by a Rayleigh-Ritz method considering only the first mode. The sensor equation (equation 8) is also solved at this stage to find the piezoelectric voltage output (Pane II). The updated beam shape and flow field is then transferred back to the N-S solver as boundary and initial conditions of the next time step. The solid boundary and the flow domain are re-meshed and the pressure on the beam surface in its new shape is recalculated (Pane III). The simulation is stopped when the steady-state oscillation of the beam within the vortex street is reached. When solving the actuator equation (9), the force on the right hand side is assumed to stay constant within the given time interval and the available analytical solution (i.e. Duhamel's integral) is used for calculating the tip deflection at the next time step. Note that a global time step (Δt) is used for both for the N-S and structure equations, and the time increment required to capture the fluid dynamics was already

small enough as not to pose any stability or accuracy issues for the solution of structural response.

According to the classification of CAE (computational aeroelasticity) solvers presented by Kamakoti and Shyy (2005) the above approach falls into the "closely coupled" solutions category. Unlike "strongly coupled methods" in which the unified set of the governing equations for all the domains (fluid, structure and electrical) are solved simultaneously, the present approach solves each domain separately, but exchanges the necessary information between the domains periodically at small time-steps. This approach is widely used since it is computationally less expensive but still accurate even in complex non-linear problems (Kamakoti and Shyy, 2005).

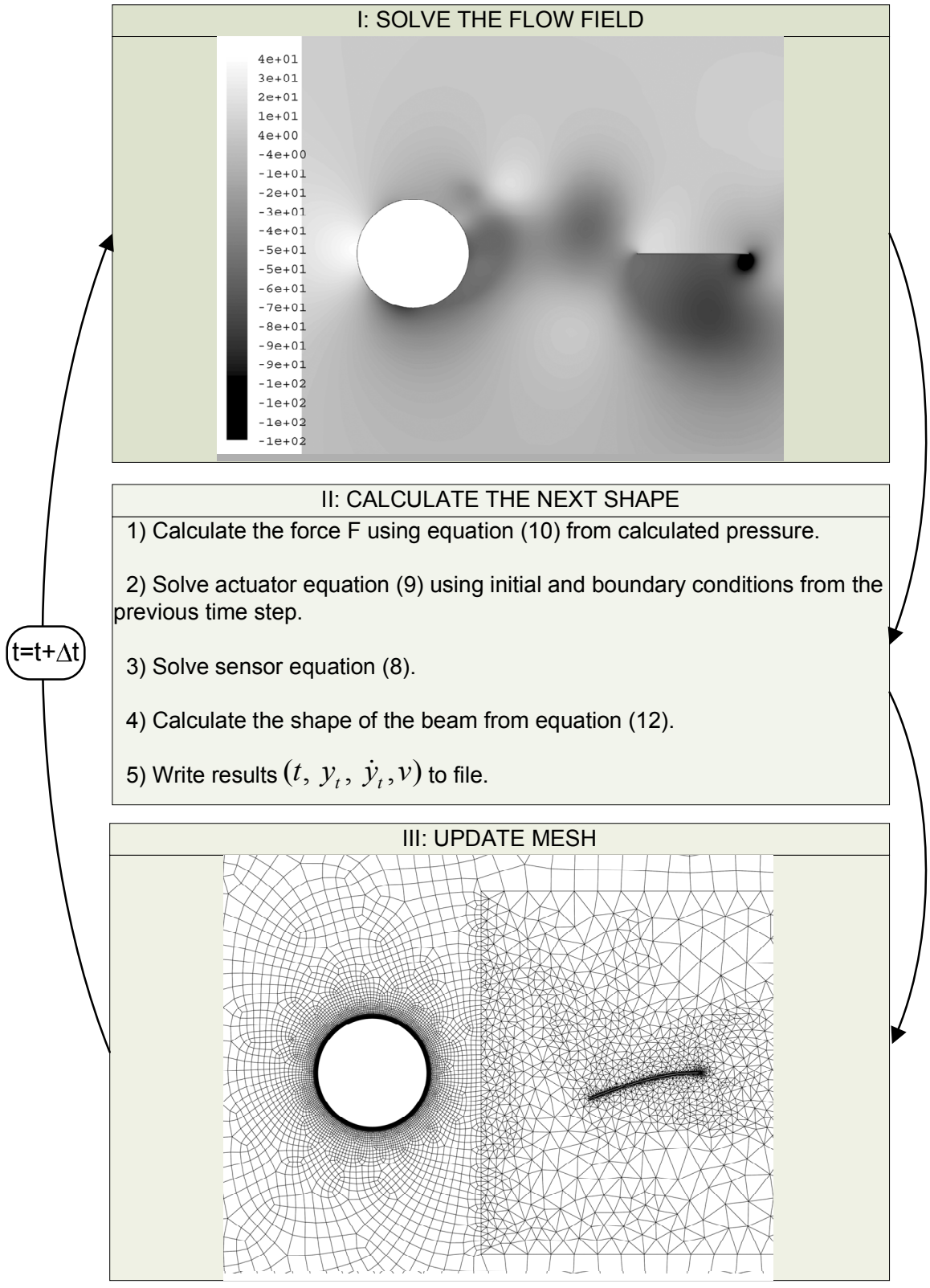

Figure 6: Procedure for numerical simulation of the aero-electro-mechanics of a piezo-beam using FLUENT and UDF programming.

3.2 Experimental Studies

3.2.1 The Experimental Setup and Instrumentation

The experiments in this research were conducted in the wind tunnel of The Mechanical Engineering Department at CCNY, which can produce flow speeds of up to 11 m/s in a rectangular cross section of $1.2\,\text{m}\times1.2\,\text{m}$. The piezoelectric beam used in the present investigation has dimensions of $30\,\text{mm}\times16\,\text{mm}\times0.2\,\text{mm}$ (Material Systems Inc., Littleton, MA. USA.), and is composed of a piezoelectric material PVDF and a Mylar backing material with thicknesses $t_p=28\mu\text{m}$ and $t_b=172\mu\text{m}$ respectively, as seen on Figure 1. The physical properties of this piezoelectric beam configuration have been previously calculated and are listed in Table 1 (Elvin, Lajnef, and Elvin, 2006). The electrical load has a resistance 100kΩ for the vortex-street experiment and 10MΩ for the turbulent boundary layer case. (The load resistance is greater in the turbulent boundary layer case since the tip deflections are small and require a larger resistance for adequate resolution of the voltage output). The output voltage was digitized by a 16 bit resolution analog-to-digital converter with a sampling frequency of 10,000 Hz. A digital oscilloscope was used to record voltages with amplitude greater than 10 volts at a rate of 1,000 samples/s for 2.5 s. Spectral analysis was carried out using MATLAB based FFT routines.

In the present configuration the beam was clamped at the tip of a long aluminum bar which was mounted on a manual traversing mechanism so that measurements of the output voltage at various locations inside the flow field could be obtained. An aluminum

cylinder of 30mm in diameter and 1.2 m in length was placed across the working section of the wind tunnel to generate a periodic vortex street wake.

Table 1: Properties of the PVDF-Mylar composite Beam

Symbol	Property	Value
m	Mass	$3.87\times10^{-5}\ kg$
k	Stiffness	$3.6\ N/m$
ξ	Damping ratio	3.85% (experimentally determined)
c	Damping coefficient	$9.089\times10^{-4}\ Nm/s$ ($c=2\xi\sqrt{km}$)
f_n	Natural frequency	$48.54\ Hz$ ($f=\frac{1}{2\pi}\sqrt{k/m}$)
Θ	Electromechanical coupling coefficient	$3.69\times10^{-6}\ C/m$
C	Capacitance	$1.38\ nF$

Erturk and Inman (2008b) have shown that for a cantilever piezoelectric generator with a single pair of electrodes, the maximum electrical power conversion occurs when the generator vibrates at its first natural frequency. Therefore it is desirable that the dominant frequency of the fluid-flow matches the first natural frequency of the generator and that the beam vibrates mainly in its first mode. As evidence of vibration of the generator in its first mode, digital images of the vibrating beam in the wake of the cylinder are shown in Figure 7. The images are taken by a high-speed camera (Imacon 200 from DRS Technologies) and each image has a 0.5 ms exposure time; the period between each of the frames is 2.5 ms. Processing of these images show that the first derivative of the beam shape is always non-zero except at the fixed end. Furthermore, the second derivative of the beam shape is zero very close to the tip indicating that the generator vibrates in its first mode.

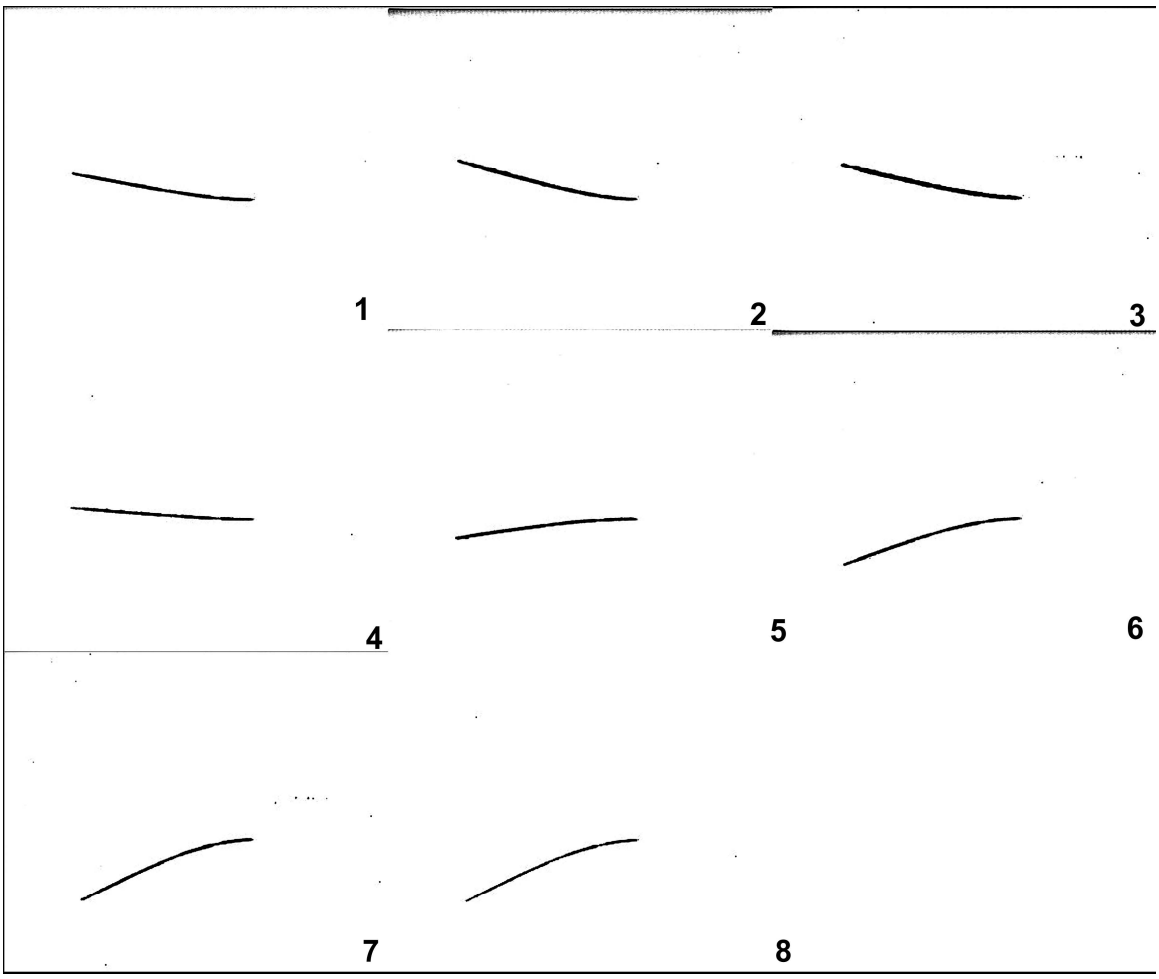

Figure 7: Eight consecutive photos of the vibrating beam in the wake. The flow is from left to right; the beam is fixed at its right end.

3.2.2. Vortex Street Experiments

In order to investigate the behavior of the piezoelectric generator in the large-scale fluctuations of a flow field, the piezoelectric beam was placed in the wake of a circular cylinder. The free stream velocity has been selected to provide a vortex shedding frequency close to the resonance frequency of the piezoelectric beam ($f_s = f_n$). The frequency of the vortex shedding from a bluff body can be calculated from the following equation (Panton, 1996):

$$f_s = \frac{StV_\infty}{D} \tag{15}$$

where St is the Strouhal number, V_∞ is the free stream velocity and D is the characteristic length of the bluff body (i.e. the diameter for a circular cylinder). For a large range of Reynolds number the Strouhal number has been shown to be 0.2 (Panton, 1996). Given the resonant frequency of the beam is approximately 48.5 Hz, a cylinder of diameter 0.03 m in a free stream velocity of 7.23 m/s would shed vortices in resonance with the natural oscillation of the beam. At this free stream speed and at room temperature, the Reynolds number is

$$\mathrm{Re} = \frac{V_\infty D}{\nu} = 14{,}843 \tag{16}$$

which indicates a fully turbulent wake behind the cylinder (Panton, 1996).

The location of the beam was moved within the wake to find the position of the highest voltage output. The beam was traversed across the wake by varying the distance *h* from the center line of the cylinder, and by varying the streamwise distance *d* from the tip of the beam to the center of the cylinder (Figure 2). Four of these locations roughly correspond to the points numbered 1 to 4 in Figure 2. It is anticipated that very close to the cylinder, the beam is in a relatively low-velocity recirculating zone where the vortices are not yet fully developed. While traveling downstream of the cylinder, the vortices first increase in strength as they become fully developed and then decay because of viscous dissipation. Hence there should be an optimum value of the distances *d* and *h* from the cylinder where the shedding vortices are at full strength and therefore the location where the voltage output is the maximum.

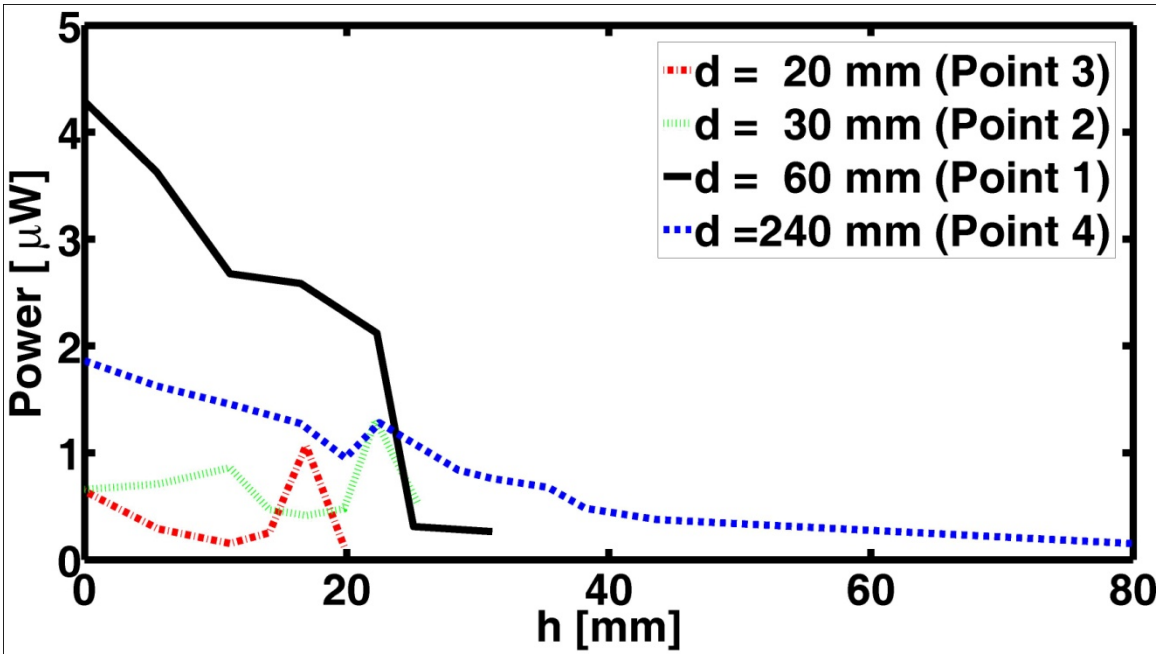

Figure 8: Variation of the mean electrical power of the PVDF beam depending on its location in the wake of the cylinder. The load resistance is $R = 100k\Omega$.

Figure 8 shows the variation of the average power output of the piezoelectric beam at different locations along (h) and across (d) the wake. The maximum electrical power is obtained along the centerline with h=0 and d=60 mm, i.e. at d=2D where the upstream tip of the beam is at Point 1 in Figure 2. Away from the centerline (as h increases) the electrical power decreases when $d = 60$ mm and $d = 255$ mm (Point 4). However, when the beam is very close to the cylinder ($d = 20$ mm and $d = 30$ mm) the local power maxima are somewhat off the center-line ($h = 17$ mm (Point 2) and $h = 22$ mm (Point 3), respectively). Of these three locations, Point 1 is the global, power maximum. Figure 9a shows the open circuit voltage signal when the tip of the beam is located at Point 1 and Figure 9b shows its frequency content. The voltage signal contains many harmonics, although some are relatively small, showing that the beam vibration in a turbulent vortex street is a multi-scale, mutual interaction of the flow and the structure.

It should be noted that the spectral analysis was carried out using a FFT of the entire signal (i.e. duration of 2.5 seconds). This long duration record contained several vortex shedding realizations which were slightly different from each other in frequency or amplitude mostly due the nature of turbulence, possible small disturbances in the incoming flow and the three-dimensional effects in the wake. As a result broadening of the spectral peak occurs with several dominant frequencies, each differing very little from the other in value; and combination of those leads to a modulated signal as seen on Figure 9a.

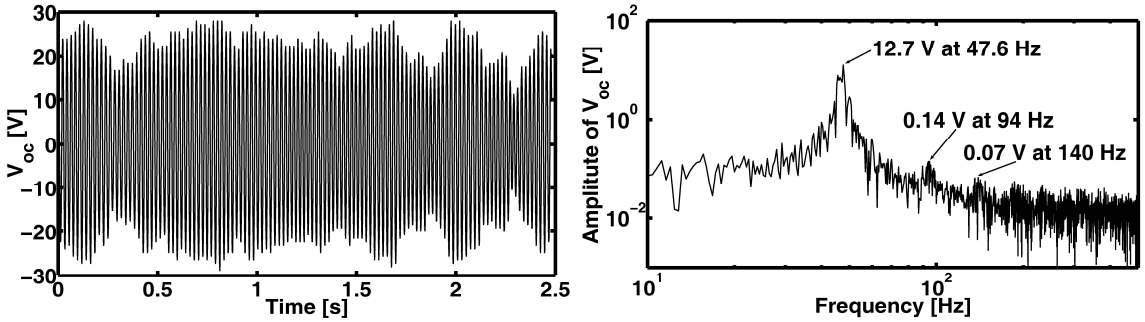

(a) (b)

Figure 9: a) The open circuit voltage output of the beam in the turbulent wake of the cylinder. b) The frequency content of that voltage signal. Frequency resolution is 0.4 Hz.

3.2.3. The Turbulent Boundary Layer Experiments

The piezoelectric beam was also placed into a turbulent boundary layer flow near the bottom wall of the wind tunnel as shown in Figure 10 at a distance of 5.12 m downstream of the start of the test section. The output voltage was recorded at various free stream velocities V_∞. The beam was traversed across the boundary layer and the output voltage was recorded at various distances from the wall, h. The maximum free stream speed was 11 m/s, giving a local Reynolds number based on momentum thickness (θ=11 mm) of Re_θ=7900 at the ambient conditions of the laboratory. Based on the

measurements of Andreopoulos and Honkan (2001) and Honkan and Andreopoulos (1997) in the same wind tunnel, the boundary layer thickness at this location and speed is estimated to be δ=115 mm.

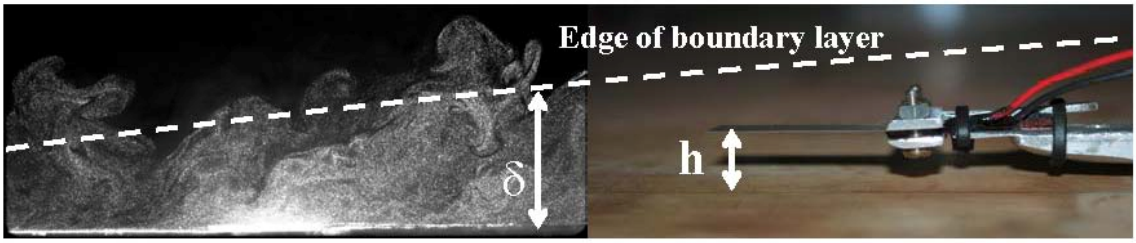

Figure 10: The concept of placing an elastic beam into turbulent boundary layer to induce vibration. Background image on left is flow visualization of a turbulent boundary layer with smoke.

The average electrical power output (through a 10MΩ load resistor) at various distances from the wall is shown in Figure 11 for $V_\infty = 11 m/s$. As seen on Figure 11a, the average generated power shows a maximum at h=40 mm from the wall. This position appears to be located in the lower part of the logarithmic law region and it is far from the maximum turbulent kinetic energy location which is at about 8 mm. Mean power drops at locations closer to the wall and at locations toward the outer layer. Interestingly enough it is not zero immediately beyond the edge of the boundary layer. A second local maximum can be observed at h=75 mm.

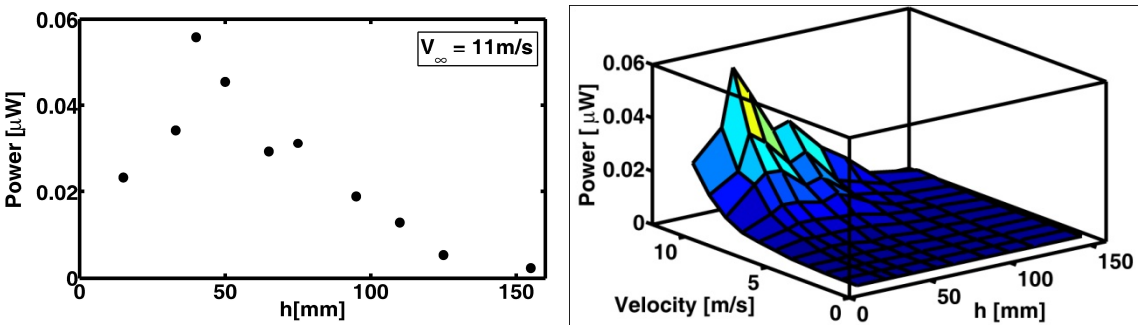

(a) (b)

Figure 11: The variation of time-averaged electrical power across a $R = 10M\Omega$ load resistor for various heights (h) within the turbulent boundary layer. a) at free stream velocity $V_\infty = 11m/s$. b) at various free stream velocities.

Figure 11b shows the variation of the average electrical power for various free stream velocities and wall distances. The electrical output monotonically increases with the free stream speed. It is interesting to observe that the global and local maxima of the generated power occur at 40 mm and 75 mm respectively and that these locations are independent of the free stream velocity. Further experimental work will try to validate such optimal points and their characteristics as well as comparing them with theoretical predictions and computer simulations.

Figure 12a shows a 5-second time history of the voltage output of the piezoelectric generator, 40mm within the boundary layer, (i.e. at the optimal power point). In Figure 12b one can observe that the dominant frequency of the voltage output is spread over three peaks centered around 46 Hz , which is close to the resonance frequency of the beam (48 Hz). The next group of peaks is centered around 317 Hz , which is comparable to the turbulence frequency calculated as $V_\infty / h = 275\ Hz$, where the free stream speed $V_\infty = 11m/s$ and $h = 40\,mm$ is the location within the boundary layer.

Although the amplitude of this second group of peaks is less than 3 % of that of the first one, it is still an evidence of higher frequency excitations due to turbulence.

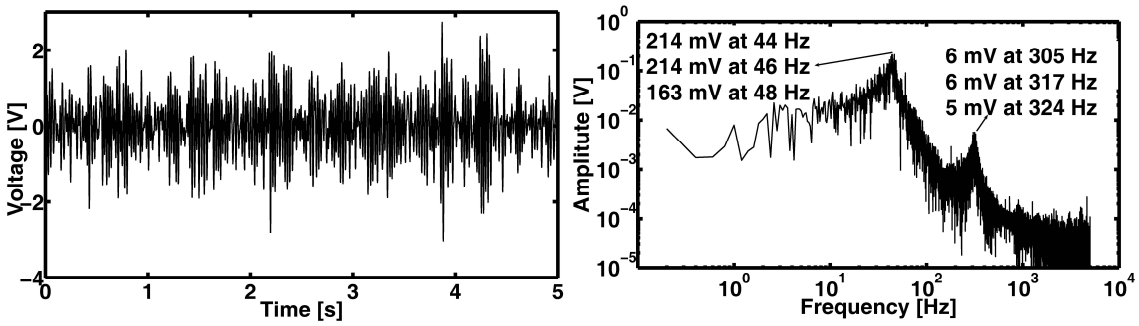

(a) (b)

Figure 12: a) The voltage history of the piezoelectric beam in turbulent boundary layer at the wall distance h=40 mm. b) The frequency content of the voltage signal.

3.4. Computational Results

The sequence of Figures 13 through 15 illustrates the interaction of passing vortices with the piezoelectric beam at two different instances. The flow pattern at the first instance shows the impact of the induced flow by the approaching vortex on the beam and the resulting stagnation region where dynamic pressure is converted to static which causes the beam to bend downwards. The flow at 4.6 ms later is characterized by the low pressure at the core area of the passing vortex which causes the beam to bend upwards. Figures 13 and 14 show the pathlines and vorticity contours at these two instances. The locations of the vortices are identified by circulatory zones where the vorticity is high. The stagnating flow region is clearly shown on the top of the beam in Figure 13a, while a vortex is approaching to the beam. The beam induces a stagnating flow region which opposes the forcing on the top surface of it. Figure 13b shows the vortex reaching at the top surface of the beam while the bottom is dominated by the impacting fluid of the induced vortex below. Thus the forcing of the beam is produced by

two mechanisms which act in phase and cause the beam to bend in the same direction: the passing of the low pressure vortex core on one side and the stagnating flow on the opposite side of the beam. It is remarkable to observe the similarities between the computational results displayed in Figure 13a and the flow visualization picture shown in Figure 2 which has been obtained by illuminating the flow with a thin laser sheet perpendicular to the axis of the cylinder. Both figures show an instant when the beam which is bent downwards under the impact of the vortex induced flow.

Additional information from the computational results provided in figures 14a and 14b indicates the existence of a shear layer emanating from the top and bottom sides of the cylinder Another shear layer which starts from the leading edge of the beam extends in the beam's lower side and defines the recirculating flow pattern there. The velocity field is shown in Figure 15 while the pressure contours are shown in Figure 16. It is clear from Figure 16 that the pressure difference between the either sides of the beam causes the deflection of the beam and the passage of the vortex core produces much stronger events than those produced by the stagnation pressure.

(a)

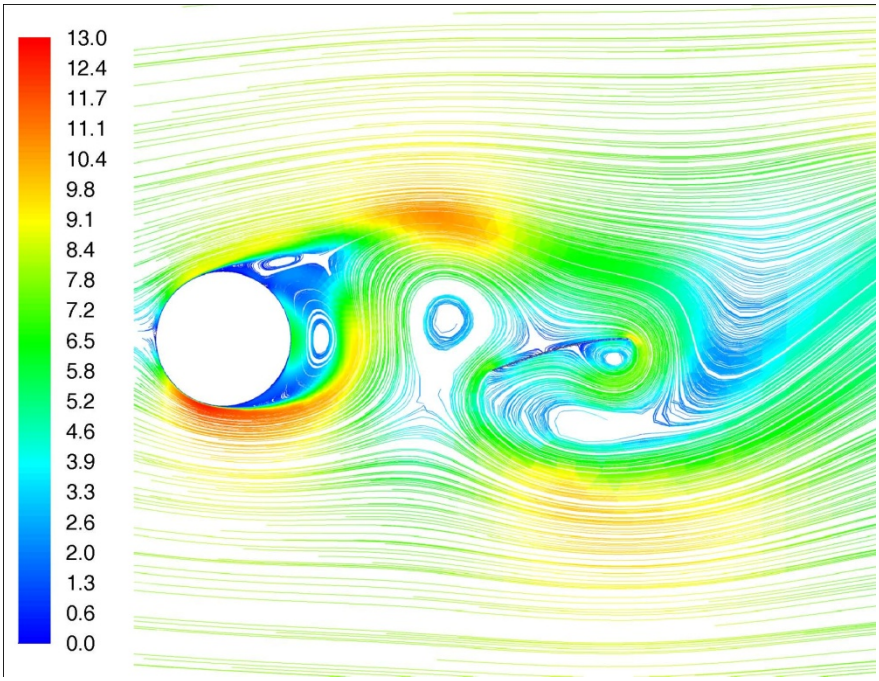

(b)

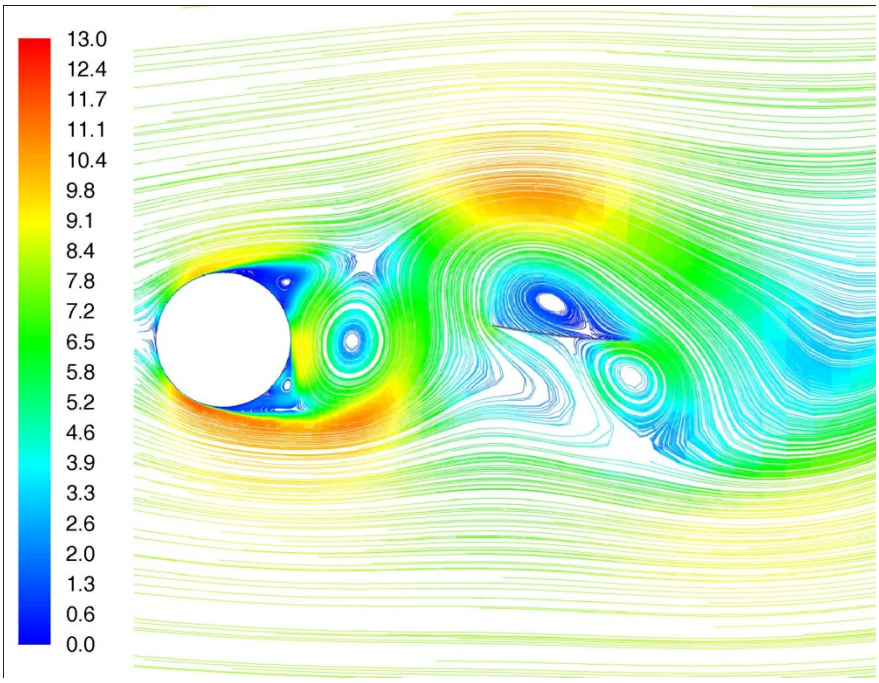

Figure 13: The pathlines for the flow around the cylinder with the flexible beam in its wake. a) At an instant when a vortex is approaching the beam b) At an instant 4.6 ms later, when the same vortex is located on the beam's upper surface. The pathlines are colored by the absolute value of the local instantaneous velocity.

(a)

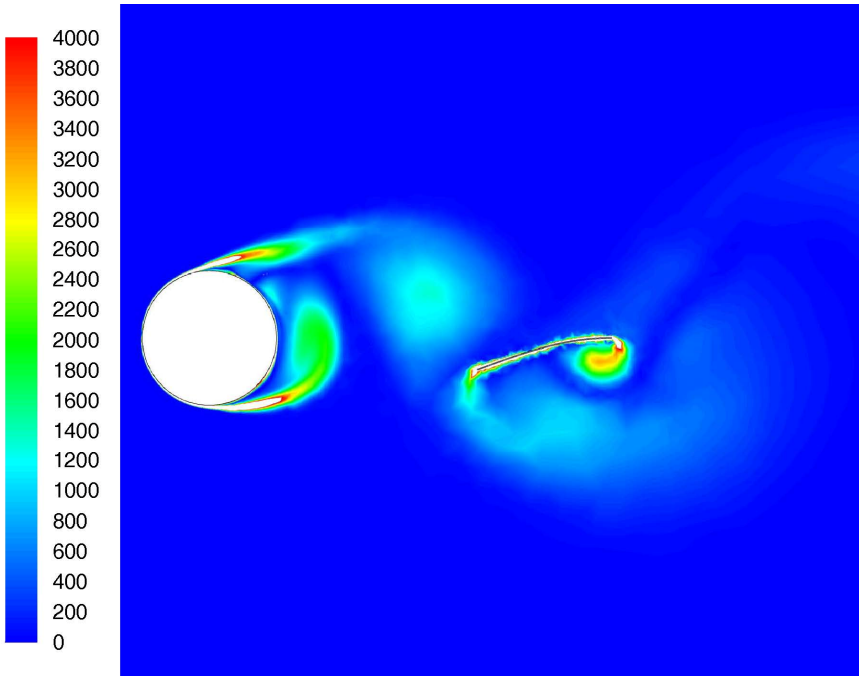

(b)

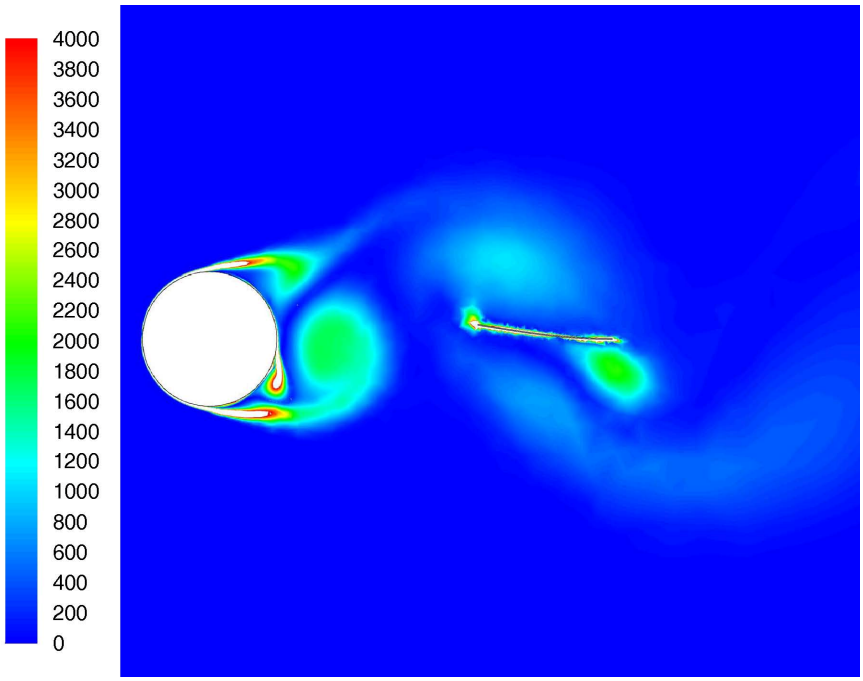

Figure 14: The vorticity contours for the flow around the cylinder with the flexible beam in its wake. a) At an instant when a vortex is approaching the beam b) At an instant 4.6 ms later, when the same vortex is located on the beam's upper surface. Note that upper limit of the vorticity is clipped at 4000 Hz in order to make the variations more visible.

(a)

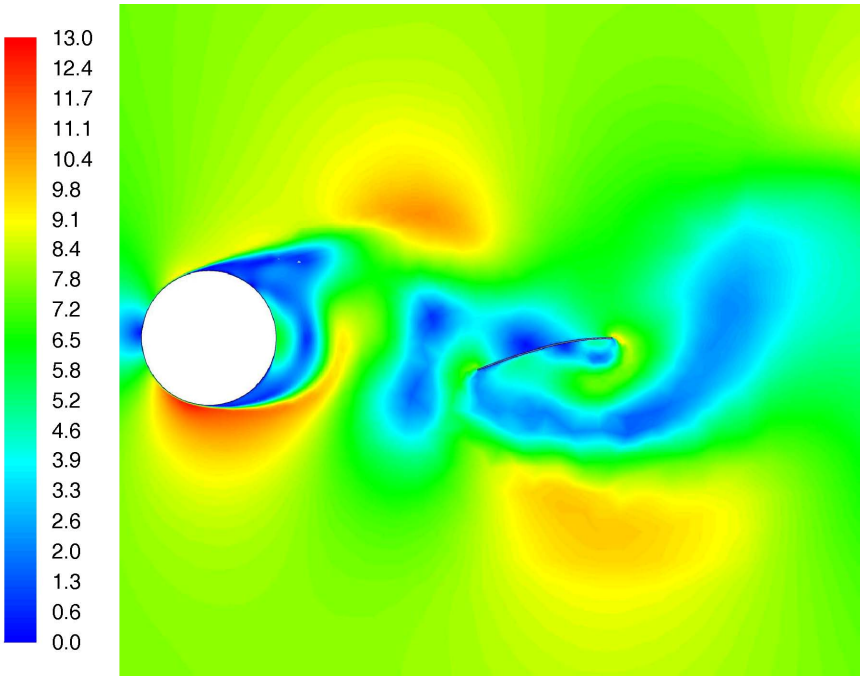

(b)

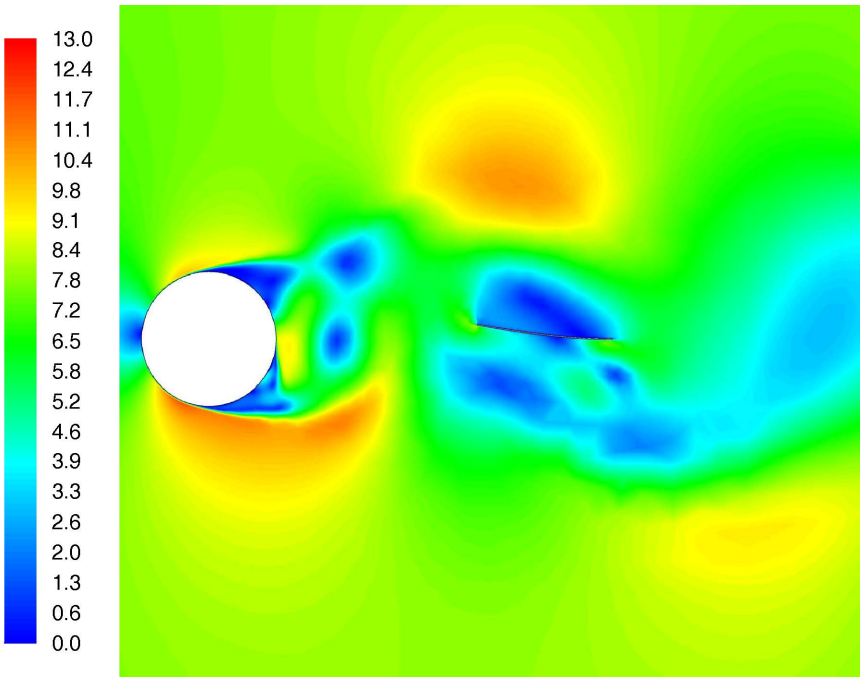

Figure 15: The velocity contours for the flow around the cylinder with the flexible beam in its wake. a) At an instant when a vortex is approaching the beam b) At an instant 4.6 ms later, when the same vortex is located on the beam's upper surface.

(a)

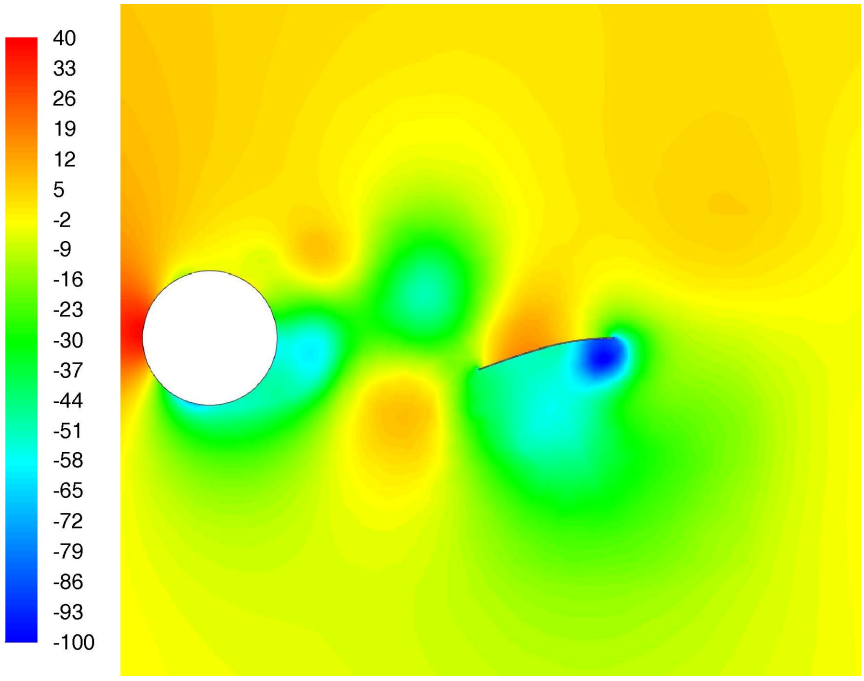

(b)

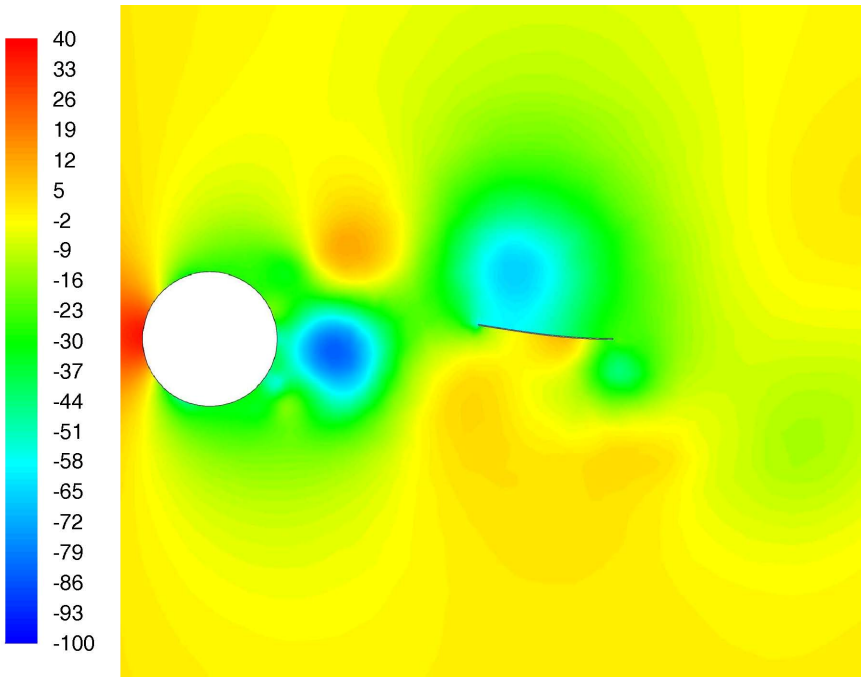

Figure 16: The pressure contours for the flow around the cylinder with the flexible beam in its wake. a) At an instant when a vortex is approaching the beam b) At an instant 4.6 ms later, when the same vortex is located on the beam's upper surface.

The calculated output voltages compared with the experimental results for various free stream velocities are shown in Figure 17. It can be seen from the experimental data that the voltage output is greatest at a freestream velocity of 7.125 m/s which produces a vortex shedding frequency close to the beam's resonant frequency. The voltage output decreases for freestream velocities lower or higher than this peak value. Similar behavior can be observed in the simulation data which capture the overall trend of the experimental data.

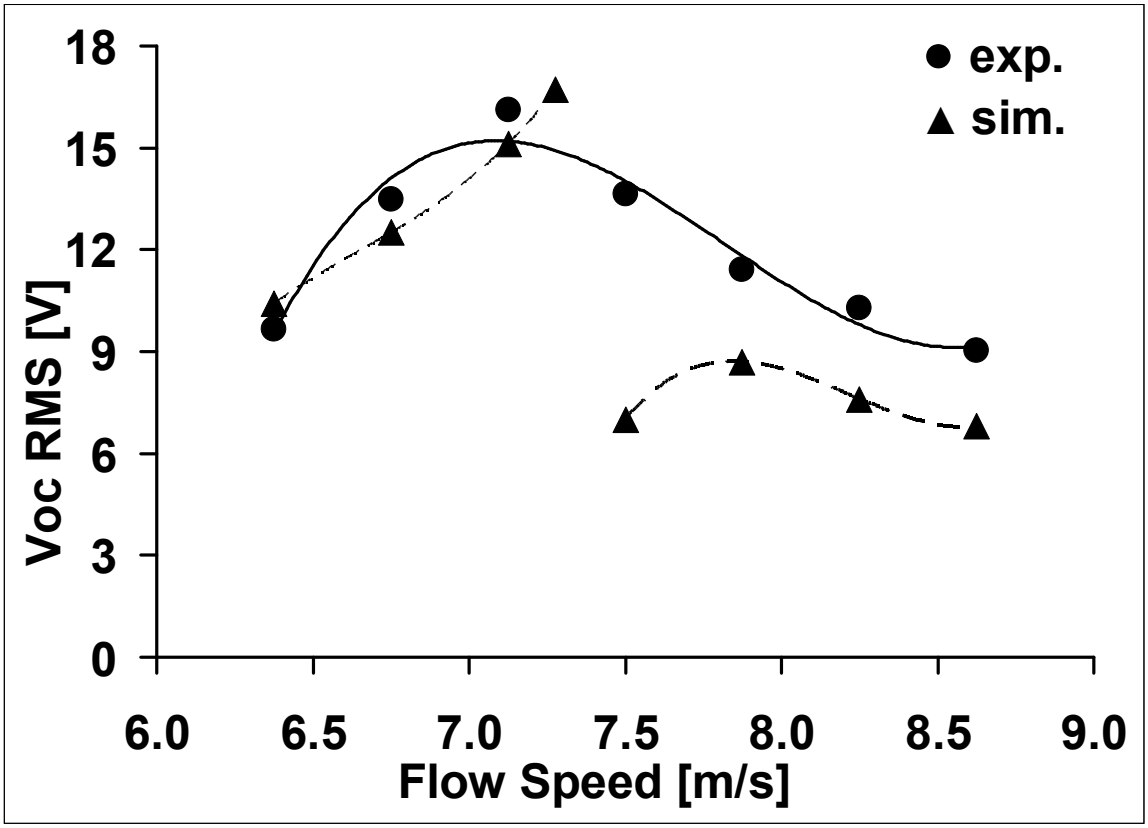

Figure 17: Comparison of open circuit voltage RMS for simulation (sim) and experiment (exp) of the piezoelectric beam in the wake of the cylinder for a range of free stream speeds.

One set of experimental and computational results of the voltage and tip displacement time-history, as well frequency content of the voltage at a fluid velocity of 7.125 m/s are shown in Figure 18. In these experiments, the open circuit voltage is

measured and is then used in Equation 8 to find the tip displacements. In the simulations, the tip displacement is calculated first and the corresponding voltage is obtained using Equation 8. The simulation and experimental voltage amplitudes in Figures 18a to 18e agree reasonably well, while the simulation indicates a lower dominant frequency. The reason for obtaining a lower dominant frequency in the simulations can be attributed to the 2D modeling of the problem. Note that in the experiments, the width of the piezo-beam is much smaller than the span of the cylinder. Thus the upstream effect of the beam on the flow in the experiment is relatively minor. However, in 2D simulations, the beam and the cylinder have identical unit depths, so the upstream effect of the piezo-beam is more pronounced than that in the real 3D case. It is known that the presence of splitter plates downstream of circular cylinders mitigate the vortex shedding from the cylinder (Blevins, 1977; Unal and Rockwell, 1988b; Shukla, 2009) which supports this observation. The lower frequency content of the 2D simulation is also visible through FFT analysis as shown in Figure 18c when compared with Figure18f. The upstream effect of the flexible beam generates a coupling between the vortex shedding and beam vibration that results in a lower resonant frequency (40 Hz vs 48.5) but increased tip deflection and voltage output. Therefore, even though the forcing frequency in the coupled system of the beam and vortex shedding is different from the natural frequency of the beam alone, the tip deflection and therefore the voltage output in case of the coupled system is higher than what would expected in case of an off-resonance forcing of the isolated beam.

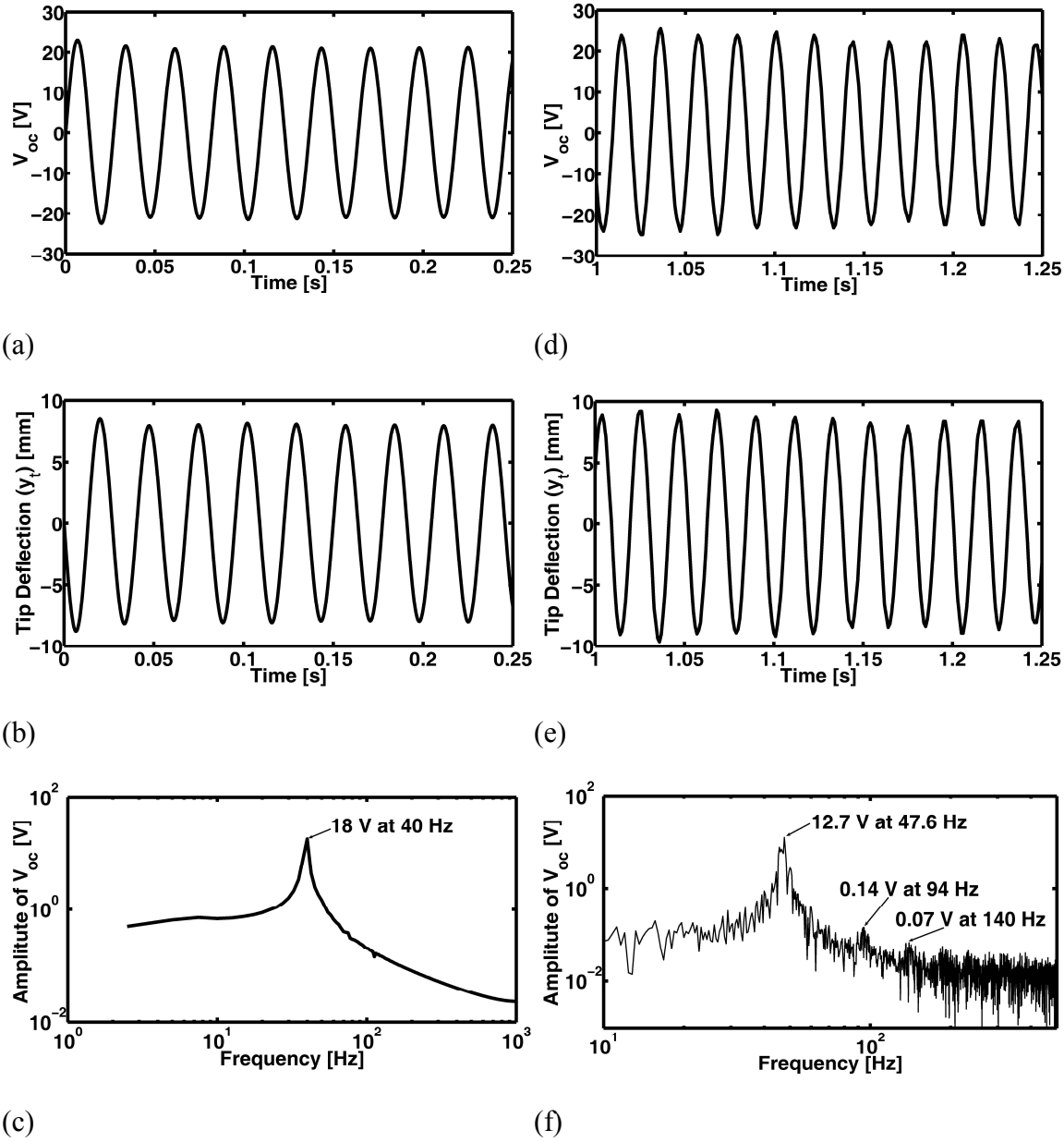

Figure 18: a) Simulated open-circuit voltage of the piezoelectric generator behind a 0.03 m diameter cylinder at a free air stream velocity of V_∞=7.125 m/s, b) corresponding tip displacement and c) frequency content of the voltage; d), e) and f) are the corresponding figures for the experiment at the same conditions. Frequency resolution for c) is 4Hz whereas that for f) is 0.4 Hz.

4. Discussion and Final Remarks

Energy harvesting is a diverse area of research and promises to provide a valuable alternate energy source that can be used for various applications in a number of

engineering and technological areas. Along with the structural mechanics and electronics, fluid mechanics is also involved when energy harvesting from fluid flows is considered. Unsteady fluid flow field can exert oscillatory forces to a piezoelectric structure immersed in it and thus can be used as an energy harvesting environment.

In this paper we investigated the energy harvesting capability of a piezoelectric beam in two types of unsteady air flows: 1) in the turbulent wake of a circular cylinder, and 2) in a turbulent boundary layer. We focused on turbulent, high Reynolds number flows (Re>10,000) with well defined coherent structures since the electrical output of a tuned piezoelectric harvester strongly depends on the forcing frequency. In the wake experiments, the driving mechanism was mainly due to the passage of the vortices over the beam and it was found that in order to obtain the maximum power output in the wake of a cylinder, the vortex shedding frequency should match the natural frequency of the piezo-beam. The effect on power output of the position of the generator within the wake was also investigated. The maximum non-rectified power from the piezoelectric generator with a load resistor of 100 $k\Omega$ in the wake of the cylinder subjected to a 7.23 m/s flow was $4\,\mu W$. In the second set of experiments, the driving mechanism was the turbulence contained in the boundary layer and we have found the position that maximizes the harvested energy for boundary layers of a wide range of Re. The non-rectified power obtained from the boundary layer was 0.06 μW over a 10 $M\Omega$ resistance.

An estimation of conversion efficiency of the piezoelectric beam has been attempted using the simulation data. The average mechanical power given to the beam is estimated by the following equation:

$$P_{mech} = \frac{1}{t_1 - t_0} \int_{t_0}^{t_1} F y_t \, dt \tag{17}$$

where F(t) is the equivalent time dependent tip force and $y_t(t)$ is the time dependent tip deflection. The mechanical conversion efficiency is then found by defining

$$\eta_{mech} = \frac{P_{elec}}{P_{mech}} \tag{18}$$

Based on the computed tip force and displacement histories of the simulation, the mechanical power input was estimated to be $P_{mech} = 60\mu W$ and the electrical power based on the AC voltage output over a 100kOhm resistor is about $P_{mech} = 7\mu W$ yielding a conversion efficiency of 11%.

A comparison of the presenter harvester configuration with wind turbines can also be made. The power available in a section of flow having a cross sectional area A and upstream velocity V_∞ is given by

$$P_{flow} = \frac{1}{2} \rho A V_\infty^3 \tag{19}$$

The maximum power that can be extracted from the flow with a turbine is

$$P_{max} = P_{flow} C_p \tag{20}$$

where C_p is the "coefficient of performance". The Betz limit mentioned earlier states that the maximum theoretical value of C_p is 0.593. While this limits the maximum attainable efficiency of wind turbines to 59.3%, the C_p values of micro wind turbines is typically 10% or less (Mitcheson et al., 2008) due to prevalent viscous and frictional losses. The cross sectional area of flow available for the piezoelectric harvester is

$$A = Db \tag{20}$$

where D is diameter of the cylinder and b is the width of the beam. Using the given dimensions and flow speed at resonance (V_∞=7.23 m/s) the available power from the entire harvester configuration (i.e. the cylinder and the piezoelectric beam downstream of it) is calculated to be

$$P_{flow} = 112\,mW \tag{21}$$

Given that the electrical power is $P_{elec} = 4\,\mu W$ at resonance, the efficiency of the harvester is:

$$\eta_{flow} = \frac{P_{elec}}{P_{flow}} = 0.36\% \tag{22}$$

Although this is more than an order of magnitude smaller than the efficiencies of comparable microturbines, the piezoelectric harvesters have their own design and operational benefits as mentioned earlier. Furthermore, piezoelectric energy harvesting from fluid flow is in its infancy; therefore, the efficiency of such harvesters should increase significantly in the future.

Energy harvesting from fluid flow is an "aero-electromechanical" problem and one needs to handle the mutual interactions between the fluid mechanics, the structural mechanics and the electronics of the problem simultaneously. We developed a computational framework that couples the structural and electrical equations into a fluid-flow solver in order to fully capture the interactions of a piezoelectric harvester in the turbulent wake of a cylinder. The open circuit voltages predicted by the simulation and the experimental measurements have shown good agreement.

Certain modifications can be attempted in order to increase the power output of such harvesters and improve the predictions of the simulations. Firstly, we present here the results of two relatively simple and well-defined flow configurations, i.e. a single piezoelectric beam in the wake of a cylinder and within a turbulent boundary layer. One relatively simple modification is to place several such beams (electrically connected in series or parallel) in the flow field to harvest larger amounts of energy. It may be even possible to eliminate the need of the upstream bluff body by carefully arranging many beams in a way that they can interact and excite each other even if the incoming stream does not fluctuate.

The computational framework can be improved by utilizing a strongly coupled method for the flow and structure interaction. 3D flow simulations would produce better results for the vortex shedding frequency, lift and drag forces and the effect of the flexible beam on the flow around the cylinder. However strong coupling and the 3D simulations will be significantly more computationally expensive.

The assumptions made in the present work in the modeling of the electromechanical behavior of the piezoelectric beam were adequate in providing physical information on the phenomena involved. The computational model can be improved by considering a distributed parameter analysis with many mode shapes rather than a SDOF lumped-parameter analysis. More sophisticated viscous damping can be included as suggested by Erturk and Inman (2008a, 2008b). Due to the relatively large deformations of the flexible beam, a nonlinear large-deformation solution (for example using a finite element approach) should provide a more accurate solution.

Note that the present work does not involve any circuit optimization to maximize the power output. Other studies have shown that improvements on the harvester circuit (Ottman et al. 2002; Lefeuvre et al. 2005; Robbins et al. (2006)) and the storage system (Sodano, Inman and Park, 2005) can significantly improve the performance of electrical energy harvesting systems. As the harvester circuit becomes more complicated, the analysis of the coupling between the piezoelectric beam and the circuit becomes more involved. Ignoring electromechanical back coupling between the harvesting circuit and the piezoelectric structure has been shown to often provide inaccurate power estimations (Erturk and Inman 2008b). Furthermore, there may not be an analytical solution for the more complicated harvesting circuits due to nonlinearities of the components and the circuit topology. In such cases, a numerical solution of the circuit equations is inevitable and attaching a circuit solver to the flow and structural solver is required. Extending the coupled structural-electrical approach for piezoelectric generator modeling previously developed by the Elvins (2009b) to the method detailed within this paper would allow for the nonlinear solution of the structural response of the piezoelectric generator using a finite element solver, the solution of the nonlinear harvesting circuit using a circuit simulator (such as SPICE), and the solution of the turbulent unsteady flow conditions using a Navier-Stokes solver.

Acknowledgement

The financial support provided by the Michael Pope Fund for energy research is greatly acknowledged.

References

Allen, J.J. and Smits, A. J. 2001. "Energy Harvesting Eel". *Journal of Fluids and Structures*, vol. 15 629-640

Andreopoulos Y., Honkan, A. 2001. "An Experimental Study of the Dissipative and Vortical Motion in Turbulent Boundary Layers". Journal of Fluid Mechanics, vol. 439, pp 131-163.

Anton, S. R., Sodano, H. A. 2007. "A review of Power Harvesting Using Piezoelectric Materials (2003–2006)," *Smart Materials and Structures*, 16 (2007) R1–R21. doi:10.1088/0964-1726/16/3/R01

Blevins, R.D. 1977. *Flow-induced Vibration*, Van Nostrand Reinhold Company, New York.

Discenzo, F.M., Chung, D., Loparo, K.A. 2006. "Pump Condition Monitoring Using Self-Powered Wireless Sensors," *Sound and Vibration,* 40 (5), pp. 12–15.

Dong S., Karniadakis G. E., Ekmekci, A. and Rockwell D. 2006. "A Combined DNS-PIV Study of the Turbulent Near Wake". *Journal of Fluid Mechanics*, vol. 569, pp. 185–207.

Douglas, J., Gasiorek, J. M., Swaffield, J. A., Jack, L. 2006., "Fluid Mechanics", *Pearson Prentice-Hall,* 5th ed, Harlow, U.K.

Elvin, N., Lajnef N, and Elvin A. 2006. "Feasibility of Structural Monitoring with Vibration Powered Sensors". *Smart Materials and Structures*, 15(4) pp. 977-986

Elvin, N. and Elvin, A. 2009a. "A General Equivalent Circuit Model for Piezoelectric Generators," *Journal of Intelligent Material Systems and Structures.* Vol. 20, pp. 3-9, January 2009.

Elvin, N. G., Elvin, A. A. 2009b. "A Coupled Finite Element-Circuit Simulation Model for analyzing Piezoelectric Energy Generators," *Journal of Intelligent Material Systems and Structures*, Vol. 20 pp. 587-595. March 2009 DOI: 10.1177/1045389X08101565

Erturk, A., Inman, D. J. 2008a. "Issues in Mathematical Modeling of Piezoelectric Energy Harvesters," *Smart Materials and Structures*, 17 (2008) 065016 (14pp). DOI:10.1088/0964-1726/17/6/065016

Erturk, A., Inman, D. J. 2008b. "On Mechanical Modeling of Cantilevered Piezoelectric Vibration Energy Harvesters" Journal of Intelligent Material Systems and Structures, Vol. 19, November 2008 DOI: 10.1177/1045389X07085639

Gilbert, J. M., Balouchi, F. 2008 "Comparison of Energy Harvesting Systems for Wireless Sensor Networks," *International Journal of Automation and Computing*, 05(4), October 2008, 334-347. DOI: 10.1007/s11633-008-0334-2

Ha, S., Chang, F.K. 2005. "Review of Energy Harvesting Methodologies for Potential SHM Applications," *Proc. of 2005 International Workshop on Structural Health Monitoring*, pp. 1451–1460.

Honkan, A. and Andreopoulos, J. 1997. "Vorticity, Strain-rate tensor and Dissipation in the Near Wall of Turbulent Boundary Layer," *J. Fluid Mech.*, 350, pp. 29-96.

Kamakoti, R., Shyy, W. 2005. "Fluid–structure Interaction for Aeroelastic Applications," *Progress in Aerospace Sciences*, 40 (2004) pp. 535–558.

Kimura, M. 1998. "Piezoelectric Generation Device," United States Patent Number 5,801,475.

Kymissis, J., Kendall, C., Paradiso, J., Gershenfeld, N. 1998. "Parasitic Power Harvesting in Shoes," *Second IEEE International Symposium on wearable Computers*. October 19-20th, Pittsburg, PA, pp. 132-139

Lajnef, N., Chakrabartty, S., Elvin, N., Elvin, A. 2006 "A Sub-microwatt Piezo-floating-Gate Sensor for Long-term Fatigue Monitoring in Biomechanical Implants," *Proceedings of the 28th IEEE EMBS Annual International Conference* New York City, USA, Aug 30-Sept 3, 2006, vol. 1 pp. 5936-5939.

Lefeuvre, E., Badel, A, Richard, C., Guyomar, **D**. 2005 "Piezoelectric Energy Harvesting Device Optimization by Synchronous Electric Charge Extraction," *Journal of Intelligent Material Systems and Structures*, Vol. 16, pp 865-876

Lienhard, J. H. 1966. "Synopsis of Lift, Drag and Vortex Frequency Data for Rigid Circular Cylinders", *Washington State University, College of Engineering, Research Division,* Bulletin 300*,* 1966.

Mitcheson, P.D, Yeatman, E. M., Rao, G. K, Holmes, A. S., Green, T.C. 2008. "Energy Harvesting from Human and Machine Motion for Wireless Electronic Devices," *Proceedings of the IEEE*. Vol. 96, No. 9, pp. 1457-1486, September 2008.

Myers, R. Vickers, M., Kim, H. 2007. "Small Scale Windmill," *Appl. Phys. Lett*., 2007 vol. 90, paper 054 106.

Ottman,G. K. Hofmann, H.F., Bhatt, A. C. Lesieutre, G.A. 2002. "Adaptive Piezoelectric Energy Harvesting Circuit for Wireless Remote Power Supply," *IEEE Transactions on Power Electronics*, Vol. 17, No. 5, September 2002 669-676

Panton, R. 1996 . "Incompressible Flow," *John Wiley & Sons, Inc*. 2nd Ed.

Paradiso, J.A., Starner, T., Energy Scavenging for Mobile and Wireless Electronics, *Pervasive Computing.* Volume 4, Issue 1, pp: 18 – 27, January-March 2005.

Pobering, S., Schwesinger, N. 2004. "A Novel Hydropower Harvesting Device". *Proceedings – 2004 International Conference on MEMS, NANO and Smart Systems*, ICMENS 2004, p 480-485.

Priya,S., Chen, C., Fye, D., Zahnd, J. 2005. "Piezoelectric Windmill: A Novel Solution to Remote Sensing" *Japanese Journal of Applied Physics*. 44 (2005) pp. L104-L107

Robbins, W. P., Marusic, I., Morris, D. Novak, T.O., 2006, "Wind-Generated Electrical Energy Using Flexible Piezoelectric Materials," *Proceedings of IMECE2006* 2006 ASME International Mechanical Engineering Congress and Exposition November 5-10, 2006, Chicago, Illinois

Roshko, A. 1953. "On the Development of Turbulent Wakes from Vortex Streets", *National Advisory Committee for Aeronautics Report* NACA-TN-2913

Roshko, A. 1961. "Experiments on the Flow Past a Cylinder at Very High Reynolds Number", *Journal of Fluid Mechanics* vol. 10, p. 345-356

Schmidt, V. H. 1992. "Piezoelectric Energy Conversion in Windmills," *Proceedings of IEEE Ultrasonics Symposium*, pp 897-904.

Shukla, S., Govardhan, R. N., Arakeri, J.H. 2009 "Flow Over a Cylinder With a Hinged-Splitter Plate," *Journal of Fluids and Structures*, In Press, Corrected Proof, Available online 5 March 2009, ISSN 0889-9746, DOI: 10.1016/j.jfluidstructs.2008.11.004.

Sodano, H. A., Inman, D. J., Park, G. 2005. "Generation and Storage of Electricity from Power Harvesting Devices," *Journal of Intelligent Material Systems and Structures.* Vol. 16, pp. 67-75 January 2005.

Sodano, H. A., Park, G. Inman, D. J. 2004. "A Review of Power Harvesting from Vibration Using Piezoelectric Materials," T*he Shock and Vibration Digest*, 36(3) 197–205, May 2004.

Taylor, G.W., Burns, J.R., Kammann, S.M., Powers, W. B., Welsh, T. R. 2001. "The energy Harvesting Eel: A Small Subsurface Ocean/River Power Generator". *IEEE Journal of Oceanic Engineering*. Vol 26, No 4, pp. 539-547.

Unal, M. F., Rockwell, D. 1988a. "On vortex formation from a cylinder. Part I: The initial instability," *Journal of Fluid Mechanics*, vol. 190, pp. 491-512

Unal, M. F., Rockwell, D. 1988b. "On vortex formation from a cylinder. Part II. Control by splitter-plate interference", *Journal of Fluid Mechanics*, vol. 190, pp. 513-529

Chapter 3

Wake of a cylinder: A paradigm for energy harvesting with piezoelectric materials

Hüseyin Doğuş Akaydın, Niell Elvin, Yiannis Andreopoulos

Published on 8 April 2010 in *Experiments in Fluids*, 49(1):291-304

Abstract

Short-length piezoelectric beams were placed in the wake of a circular cylinder at high Reynolds numbers to evaluate their performance as energy generators. The coherent vortical structures present in this flow generate a periodic forcing on the beam which, when tuned to its resonant frequency, produces maximum output voltage. There are two mechanisms that contribute to the driving forcing of the beam. The first mechanism is the impingement of induced flow by the passing vortices on one side of the beam, and the second is the low pressure core region of the vortices which is present at the opposite side of the beam. The sequence of these two mechanisms combined with the resonating conditions of the beam generated maximum energy output which was also found to vary with the location in the wake. The maximum power output was measured when the tip of the beam is about two diameters downstream of the cylinder. This power drops off the center line of the wake and decays with downstream distance as $(x/D)^{-3/2}$.

1. Introduction

The available power in a fluid flow is proportional to U_f^3 where U_f is a characteristic velocity which in the case of unsteady or turbulent flows, is proportional to a length scale L_f and a strain rate/frequency scale f_f. Thus, the available flow power is proportional to L_f^3 and f_f^3. This feature creates a unique opportunity to generate a substantial amount of energy by using piezoelectric material to convert fluid kinetic energy to electrical energy. Piezoelectric materials generate electricity when exposed to a mechanical strain and, conversely, change shape when exposed to an electric field. Since they are AC-coupled devices time-dependent forcing is required. The flow unsteadiness can produce mechanical strain energy in the piezoelectric material that in turn generates an electrical charge. This converted energy can readily be used for the continuous powering of a small electronic device, or it can be stored for intermittent use. Such a small electronic device can be a sensor to measure unsteady characteristics of the flow such as turbulence levels, vortex shedding frequency, etc., or it can be any small electronic system that is configured to work in the wake of a moving vehicle. Of particular importance is the design of energy harvesting devices to work in environments which are not easily accessible or are under conditions which do not facilitate the use of classical powering methods such as batteries.

These types of applications are now feasible through recent advances in piezoelectric materials research, which has enabled a greater conversion rate of ambient mechanical energy to electrical energy. Such developments now position these materials as viable alternative energy sources to obviate the need of batteries and wired power.

Piezoelectric energy harvesters are solid-state devices that do not require many moving components that are likely to need long-term maintenance. Piezoelectric materials also allow for microelectromechanical systems (MEMS) manufacturing methods that can greatly decrease the overall size of the device. Furthermore, their energy output typically produces relatively high voltages and low currents (when compared with traditional magnetic generators), which are more suitable for many sensor and low-power electronics applications.

Extensive research is being carried out on the use of piezoelectric materials as energy harvesters and as sensors and actuators. A detailed literature review on the use of piezoelectric energy harvesting from structural deformations and vibrations (Paradiso and Starner 2005; Mitcheson et al. 2008; Sodano et al. 2004; Anton and Soldano 2007) shows that the current research is focused mostly on the study of solid–solid interaction of the piezoelectric structures.

Two experiments have been carried out in the present investigation with two different forcing mechanisms. In the first one, which is the subject of the present paper, forcing was provided by a resonance mechanism between the passage of coherent structures in the form of Karman vortices shed off a circular cylinder and the vibration modes of the piezoelectric generator. In the second experiment, random forcing was provided by the interaction of the generator with turbulent eddies in a canonical two-dimensional boundary layer. The results of this investigation will be reported in the future.

The majority of past research on cylinder wakes has targeted the manipulation of vortex shedding with the aim of controlling the drag of bluff bodies. The reader is

referred to the classical review paper by Williamson (1996) for the basic characteristics of cylinder wakes. The onset of instability in the wake shear layer has been established in several investigations (Bloor 1964; Zdravkovich 1997; Prasad and Williamson 1996, 1997a, b; Brede 2004; Rajagopalan and Antonia 2005). The classical mixing layer develops through a convective instability mechanism (Monkewitz and Nguyen 1986) while a wake is a result of an absolute instability. Lin et al. (1995) suggested that since the initial shear layer zone of the wake exhibits a behavior similar to a mixing layer, the wake may undergo a transition from a convective instability to an absolute instability downstream.

The near wake of a circular cylinder at high Reynolds number is particularly complex. The recent work of Dong et al. (2006) has indicated that the flow patterns become significantly smaller and move toward the base of the cylinder as the Reynolds number increases from $4x10^3$ to $10x10^3$. These researchers also found that increased levels of turbulent stresses occur further upstream along the separating shear layer that suggests an earlier onset of transition. Figure 1 shows a visualization picture of flow past a cylinder at $Re=8x10^4$ configured in the CCNY wind tunnel. It can be observed that transition in the separating shear layer closest to the cylinder can take place within about ¼ cylinder diameters (D) from the point of separation. Shear layer vortices are formed as a result of a Kelvin–Helmholtz instability which grow in size and eventually are wrapped around the main large scale vortex at about x=2.5D from the center of the cylinder. The outer part of the shear layer with the higher velocity, i.e., the furthest smoke streak on the upper half of the flow, becomes unstable and subsequently turbulent at about x=5D.

Figure 1: Near wake of cylinder at $Re=8x10^4$.

As a result of Kelvin–Helmholtz instability, small scale vortices that grow continuously are superimposed on the large scale Karman vortices and the flow field now exhibits a rich variety of temporal and spatial scales with significant kinetic energy distributed over them. In the context of the present work, the term ‘‘coherent vortical structure’’ will be used to denote the turbulent Karman vortices in the present high Re case.

According to our current literature review, the published studies on the interaction of piezoelectric structures with fluid flow are limited to only a few papers, notably Schmidt (1992); Allen and Smits (2001); Taylor et al. (2001). The first application of piezoelectric materials to extract energy from fluid motion is described in the conference paper by Schmidt who proposed the concept of an oscillating blade generator and emphasized the importance of incorporating mechanical and electrical resonance in the design of the system.

Allen and Smits (2001) studied the behavior of long and very flexible piezoelectric beams made of PVDF (polyvinylidene fluoride) in the wake of a flat plate normal to a flow stream in a water tunnel. Albeit enlightening in terms of a PIV study of such a flow configuration, the paper does not present much detail about the electrical output and efficiency of the system, nor does it include a simulation of the electro-mechanical coupling present in this configuration. This concept has then been applied to harvest energy from ocean waves in Taylor et al. (2001). Aside from the flow tank testing and optimization study this work attempts to couple the flow and structure to simulate the interaction between the piezoelectric material and the surrounding flow. However, in Taylor et al. (2001) no comparison of the outcomes (power, voltage outputs and displacements) of the simulation and experiment is provided. A drawback related to this concept is the low operation frequency of the system which is in the order of 1 Hz. The power output of piezoelectric harvesters at resonance conditions increases quite rapidly with the forcing frequency; therefore, it can be stated that harvesting energy from unsteady flows of higher frequencies, such as turbulent wakes of bluff bodies, would be more effective. The study of Pobering and Schwesinger (2004) targeted kinetic energy extraction from flowing rivers. Flag-like membranes similar to those used in the water-based application of Taylor et al. (2001) were used by Robbins et al. (2006) to harvest energy from wind. These authors used bimorph PVDF sheets in the wake of a flat plate normal to the flow to generate 10 mW of DC power with a 250 kOhm load by using a novel semiresonant rectifier. The amount of power consumption of the electronic circuit is not given.

Studies show that improving the electrical coupling (Lesieutre et al. 2002; Sahele et al. 2005; Elvin and Elvin 2009a, b) and the storage system (Sodano et al. 2005) will drastically improve the performance of electrical energy harvesting systems.

The objective of the present research is to investigate the use of piezoelectric materials to harness energy from unsteady air flows. Full coupling of the flow scales with those of the vibrational modes of the piezoelectric generator is a challenging problem which involves not only the classical fluid structure interaction with moving boundaries but also the coupling of the electrical field of the piezoelectric materials. This three-way coupled interaction is the subject of the present research which includes an experimental as well as a computational component.

Although the density of air is about 800 times smaller than that of water, its velocity in usual environmental flows is much higher than that of water. Since the available energy is proportional to the density and the cube of the velocity and therefore proportional to L_f^3 and f_f^3, it is more feasible to attempt harvesting energy from air flows because of its higher frequency content. According to this scaling, for example, a wind velocity of 10 m/s can yield the same order of magnitude energy output as a 1 m/s ocean wave.

The present work complements and extends the work of Akaydin et al. (2010), hereafter mentioned as AEA, which describes the first published computational work involving a full three-way coupled interaction among the flowfield, mechanical structure and electrical field. Our experimental work involves an investigation into the wake of a circular cylinder where the flow field is scanned and mapped by the voltage output of the

piezoelectric cantilever beam. In this experiment the piezoelectric beam was oriented in a configuration parallel to the incoming flow and cantilevered at its downstream end.

2. Experimental set-up and instrumentation

The beam used in the present investigation consists of a layer of piezoelectric material PVDF (polyvinylidene fluoride) (from MSI-USA, Inc.) of thickness t_p = 28 μm deposited on a much thicker Mylar backing material of thickness t_b = 172 μm as seen on Fig. 2. The physical properties of this piezoelectric beam configuration have been previously calculated and agree well with experimental data found in Elvin et al. (2006). The beam had dimensions of 30 mm x 16 mm x 0.2 mm.

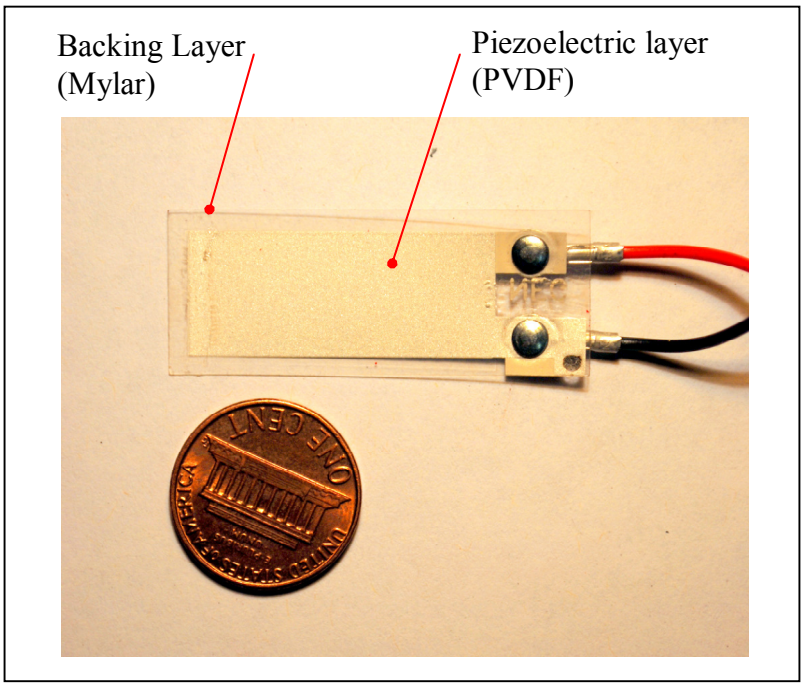

Figure 2: A photograph of the PVDF-Mylar beam.

The natural frequencies of the beam have been measured by using a shaker which could generate vibrations with variable frequency and amplitude. The first natural

frequency is measured to be 48.4 Hz whereas the second natural frequency was measured to be 310 Hz. The first natural frequency calculated from the mass and stiffness of the piezoelectric beam was estimated to be 48.5 Hz.

It is desirable that the beam vibrates in its first resonant mode because the appearance of a second mode with large amplitude will introduce an inflection point in the beam which will reduce its voltage output considerably due to charge cancelation (Elvin and Elvin 2009a; Erturk and Inman 2008). As will be seen later, the shedding frequency is determined to satisfy this requirement by matching it with the first natural frequency of the beam under investigation.

The experiments in this research have been carried out in the wind tunnel of The Mechanical Engineering Department at CCNY. The tunnel is an open-ended suction type tunnel powered by a 20 b.h.p electrical motor with fine speed control, providing up to 11 m/s stream speed in the test section. The test section has a 1.22 m x 1.22 m square cross section and it is 8.53 m long. The top and bottom of the tunnel are covered by plywood of 1-inch thickness, one side of the tunnel has hinged plywood doors for physical access, and the other side is covered by plexi-glass wall in order to have optical access into the test section. The turbulence level in the free stream is about 0.15% at 3 m/s and it goes down to 0.08% at the maximum speed of 11 m/s. (Andreopoulos and Agui 1996; Andreopoulos and Honkan 2001). The data acquisition system is a desktop PC equipped with a National Instruments PCI 6032E data acquisition card, which can retrieve data with 16 bit resolution at a rate of 100 kS/s.

A smooth cylinder made of aluminum with diameter D=0.03 m and 1.22 m length was placed across the working section of the wind tunnel without end plates at a distance

of 3.5 m from its entrance. Several experiments were carried out at different wind tunnel speeds U_∞ which resulted in a range of Reynolds number spanning from 10,000 to 21,000 with a value of Re=14,800 at the resonance frequency. It has been reported in the past that at Re>5,000 turbulent structures are less organized (Rajagopalan and Antonia 2005; Prasad and Williamson 1997b), and therefore some minor fluctuations in the forcing frequency are expected.

Flow visualization experiments were carried out by using a laser sheet generated by a pulsed YAG laser to illuminate the flow on a vertical plane perpendicular to the axis of the cylinder and parallel to the flow direction. Atomized olive oil was mixed into the flow upstream of the cylinder. Flow visualization images were obtained by a Nikon model D80 photographic camera with a Nikkor f1.8 85 mm prime lens at fully open diaphragm (f1.8). The image resolution is set to the maximum of 3,872 x 2,592 pixels. Images are captured in RAW format at an ISO sensitivity of 100 in order to minimize noise. The pulse duration of the laser was 0.01 ms, and time between each pulse was 100 ms. The shutter speed of the camera was set to 100 ms as well, so the entire length of only a single pulse is captured in one frame. Problems such as partial capture of the pulse duration and multiple or no exposures in a single frame are therefore avoided.

The Strouhal number defined as $Str = f_s D/U_\infty$ where f_s, the vortex shedding frequency, is reasonably constant with a value of 0.2 in this relative large range of Reynolds number where a fully turbulent wake is formed behind the circular cylinder. In the present experiments, as the velocity U_∞ was varied, the voltage output with a load resistance of 100 kOhm was recorded as a function of time and the shedding frequency f_s was determined through FFT calculations with a frequency window of 0.4 Hz.

Key flow parameters of interest characterizing the flow around the piezoelectric beam are the Reynolds number based on its length L_p defined as $\mathrm{Re}_p = U_f L_p/m$ where U_f is a typical velocity and the Stokes number, $\mathrm{St}=\omega L_p^2/\nu$ where ω is the angular velocity of the beam's motion. The Stokes number expresses the ratio of the unsteady boundary layer thickness on the beam, $\delta_a^2=\nu/\omega$, to its size L_p.

The Reynolds and Stokes numbers can be combined to form a Strouhal number of the vibrating beam based on its angular velocity ω_p at the tip rather than on its frequency: $\mathrm{Str}_p=\mathrm{St}/\mathrm{Re}_p=\omega_p L_p/U_f = U_t/U_f$ where U_t is the velocity at the tip of the beam which is equal to the time derivative of the tip displacement w_t. For ω_p corresponding to the natural frequency f_n, the Stokes number is St=18,000 suggesting that $\delta_a/L_p = \mathrm{St}^{-1/2} = 1/134$. According to Roshko (1954) $U_f \approx 0.6U_\infty$ at this flow regime and therefore Re_p = 12,600 and Str_p =1.42.

3. Results

It is very instructive to consider the analytical model describing the electromechanical processes of the beam. The model has been developed under the assumptions of the validity of a single degree of freedom dynamical system based on two governing equations that include the mechanical part (actuator equation) and the electrical part (sensor equation):

$$m\ddot{w}_t + c\dot{w}_t + kw_t - \Theta v = F \quad \text{(Actuator equation)} \tag{1}$$

$$\Theta\dot{w}_t + C\dot{v} = -\frac{v}{R} = I \quad \text{(Sensor equation)} \tag{2}$$

where w_t is the tip deflection in the coordinate system related to the beam (see Fig. 3), v is the voltage, I is the current, F_t is the equivalent tip force, m is the mass, c is the damping coefficient, and k is the stiffness of the lumped mass model of the piezoelectric beam. C is the piezoelectric capacitance and Θ is the electromechanical coupling coefficient of the piezoelectric beam.

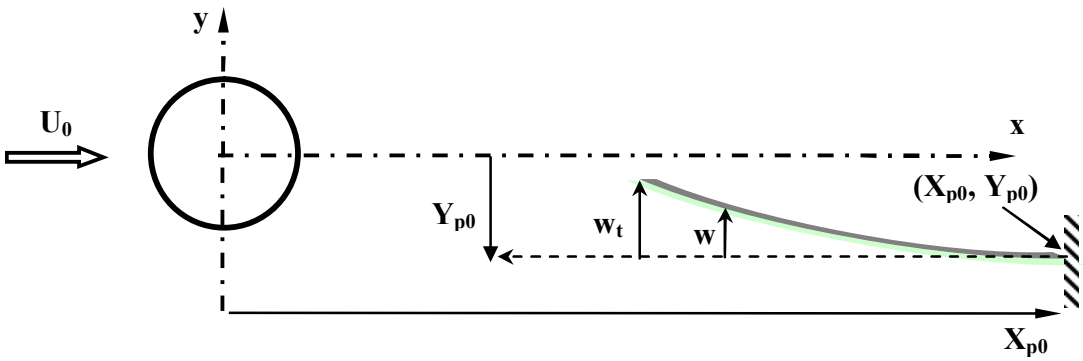

Figure 3: Coordinate systems of the flow and the beam.

The load circuit (for example a sensor) is assumed to be purely resistive with a resistance of R. The coefficients of Eq. 1 can be derived using a Rayleigh–Ritz approximation which is widely used in other similar piezoelectric research (Sahele et al.

2005; Sodano et al. 2005). In the present study, we consider only the first mode; however, it is possible to extend the analysis to include additional modes in the further stages of the research (Sahele et al. 2005; Elvin and Elvin 2009a). Furthermore, the effect of any electrical circuit (including non-linear components) and for any number of assumed vibration modes can be modeled using an equivalent circuit approach (Elvin and Elvin 2009b).

If the viscous force component in F_t is neglected and for large values of R, the tip displacement can be estimated from the voltage measurements assuming $R=\infty$ in the sensor equation and finding the linear relation between the tip displacement and the open circuit voltage below:

$$w_t = -\frac{C}{\Theta} v_{oc} \tag{3}$$

For power calculations, a load resistance of 100 kOhm was used, and the voltage across it was recorded digitally. In order for utilizing Eq. 3, however, measurement of open circuit voltage was required. This is done by measuring the output voltage directly by a digital oscilloscope using no load resistance. Since the impedance of the oscilloscope is high, it was safely assumed that $R=\infty$.

Figure 4a, b shows the results of a free vibration experiment in which the beam was put into motion with an initial displacement and the voltage across a resistance of 1 MOhm was acquired at a rate of 100 kS/s with a 16 bit resolution. The signal is typical for a piezoelectric beam undergoing damped, free vibration. The frequency spectrum shown in Fig. 4b demonstrates that the beam is predominantly vibrating at a single frequency which is very close to its natural frequency of 48.4 Hz. The power generated can be estimated from the instantaneous electrical power by $P = V^2/R$ and the average

electrical power is defined as The average electrical power defined as $\overline{P} = \frac{1}{t_1 - t_0}\int_{t_0}^{t_1} Pdt$. In this case, the free vibration of the beam generated an average power $\overline{P} = 0.148\,\mu W$.

a)

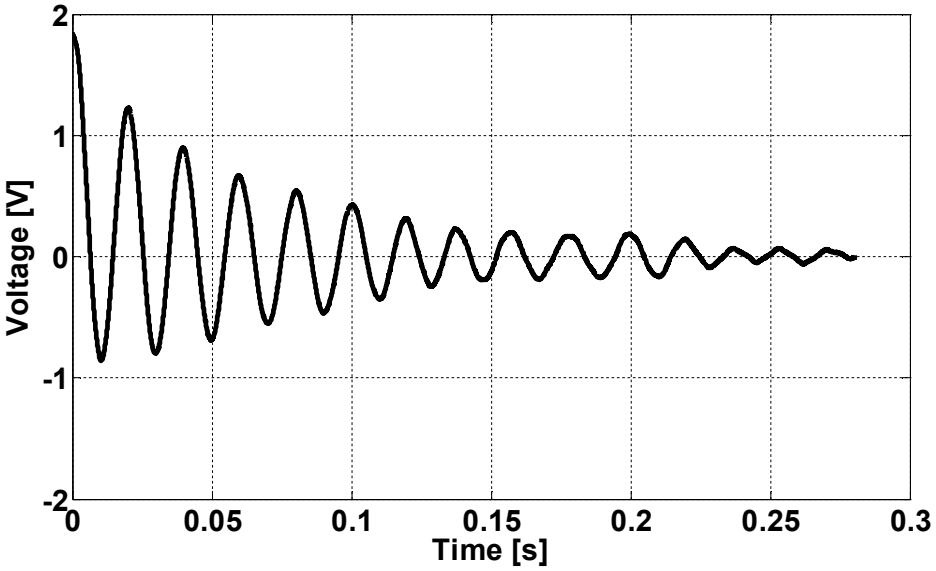

b)

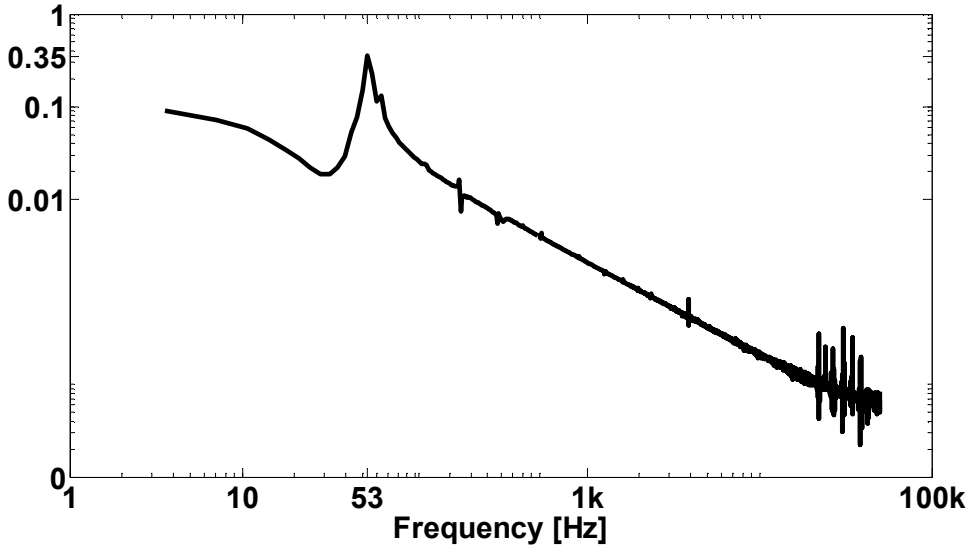

Figures 4: Measured free vibration output voltage with load resistance 1MOhm and its frequency content. a) Free vibration signal with average electrical power 0.148 μW. b) Voltage amplitude spectrum.

Figure 5a shows the recorded voltage when the tip of the beam is placed in the wake of circular cylinder at $x/d = 2$ with a shedding frequency of the vortices at about 48 Hz. This forced vibration pattern is characterized by variable maximum amplitude which is caused by the variable strength turbulent vortices shed off the cylinder at this Reynolds number. There is no DC component in the signal and the piezoelectric material seems to behave like a high-pass filter. The basic feature of these piezoelectric materials is that they do not produce charge under a mechanical load which does not alternate. Though the piezoelectric beam behaves mechanically as a band-pass filter, it behaves electrically as a high-pass filter. This is the basic reason for characterizing their behavior as high-pass filtering.

The amplitude spectrum of the signal shown in Fig. 5b exhibits a dominant frequency of 48.8 Hz and the presence of possible higher modes with significantly smaller amplitudes. The second highest peak at 93 Hz is about twice the Strouhal frequency f_s while the third peak at 140 Hz is close to $3f_s$. Of interest are also several peaks in low frequency range below the 48.8 Hz which appear to be associated with the slow variation of the signal's maximum amplitude. The output of the beam in this location is characterized as a narrow bandwidth signal with slowly fluctuating peak amplitude.

a)

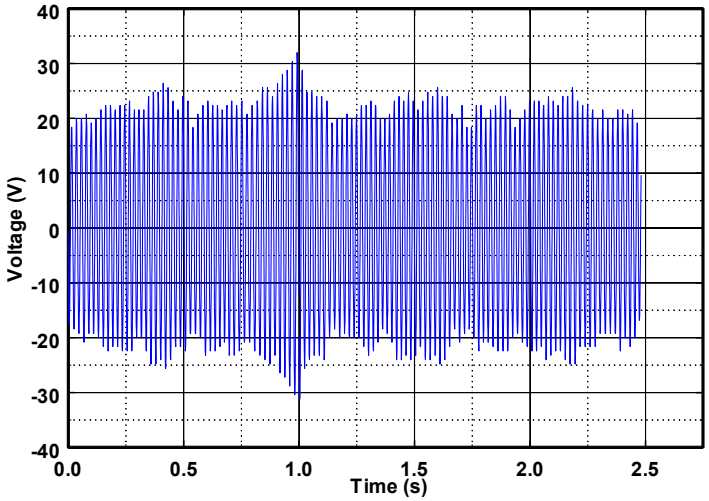

b)

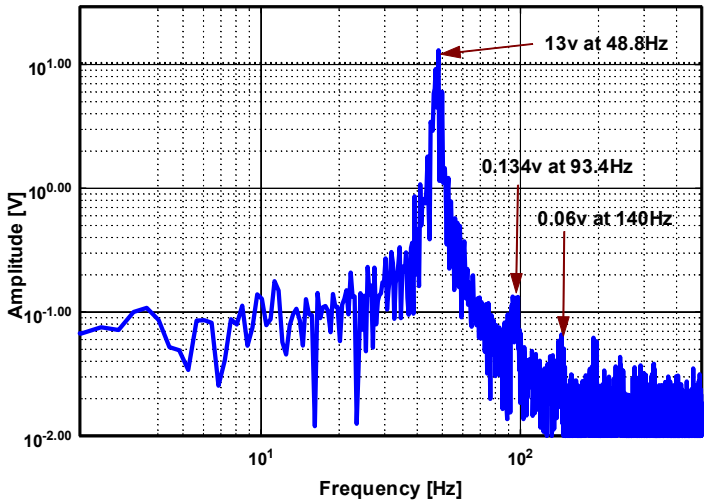

c)

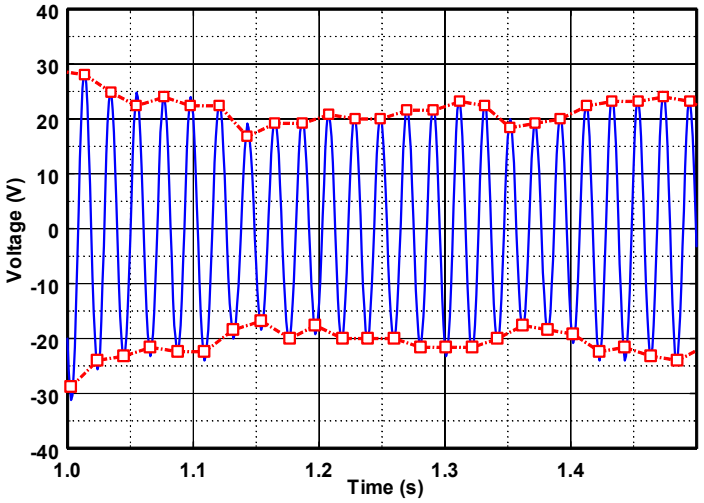

Figures 5a, b & c: a) Typical measured open circuit voltage of piezoelectric beam in the wake of a circular cylinder at x/D=2 Re=14,800 and b) its frequency content. c) Signal envelope.

Equation (3) indicates the relation between voltage, i.e., output power and tip deflection of the piezoelectric beam y_t for the case of an open circuit. Thus, by looking at some statistical properties of the local extremes of the open circuit voltage and tip deflection, one can characterize the interaction between the piezoelectric cantilever beam and the turbulent eddies in the wake of the cylinder. In fact, these points constitute the envelope of the signal. These local extremes were identified by thresholding the signal and its time derivative in a data processing code written in a MATLAB platform. In particular, the criteria used involved searching the change of sign of the product of the time derivatives of the signal $v_0 = dv/dt$ at two sequential time points of the time series of $v(t)$

$$I_v(t) = \dot{v}(t)\dot{v}(t+\Delta t) < 0 \tag{4}$$

In addition, a threshold criterion has been applied which required that the signal had to be greater or lower than a value th1

$$v(t)>\text{th1}$$

$$\text{for positive extremes or} \tag{5}$$

$$v(t)<\text{th2}$$

for negative ones. In the data presented here th1 and th2 are set to zero.

The results are shown in Fig. 5c, and they clearly demonstrate that the algorithm identified the local extremes correctly. Since the output signal depicted in Fig. 5a is characterized as the output of a narrow bandwidth filter, it can simply be represented

$$v(t)=A(t)\cos[2\pi\omega_c t+\Phi(t)] \tag{6}$$

where the envelope amplitude $A(t)$ and phase angle $\Phi(t)$ are slowly varying functions of time relatively to the oscillations at the center frequency f_c. Bendat and Piersol (2000)

show that the probability density function of A(t), pdf(A), governing the envelope $A(t)$ is the Rayleigh probability density function given as

$$\text{pdf}(A) = \frac{A}{\sigma_v^2} \exp\left(-\frac{A^2}{2\sigma_v^2}\right) \tag{7}$$

where σ_v^2 is the variance of the signal. Thus pdf(A) is independent of the frequency f_c. Figure 6a shows the pdf(A) of the positive values of the envelope of the output voltage shown in Fig. 5a. This distribution is characterized by a fast rise at small values of A followed by a slow decay with a long tail. The maximum of this pdf is reached when $A=\sigma_v$. The experimental data shown in Fig. 6a are compared with the pdf computed from the Eq. 7 by introducing the measured σ_v. As can be seen, the theoretical distribution agrees very well with the experimental data suggesting that the distribution of the tip deflections follows the Rayleigh pdf. The distribution of the negative values of the envelope is symmetrical to that of the positive values. The maxima of these two distributions occur at the same magnitude, which is equal to σ_v=20 volts, but opposite in sign locations of the signal. This variation in the maximum/minimum values can be attributed to change in the strength of the driving events which is not associated with any change in the frequency of appearance of these events.

a)

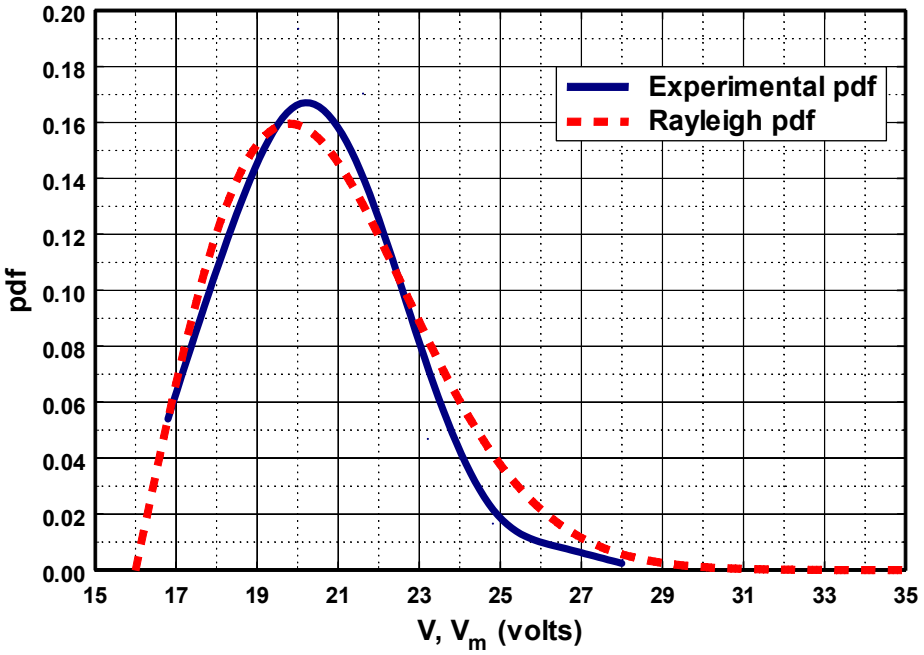

b)

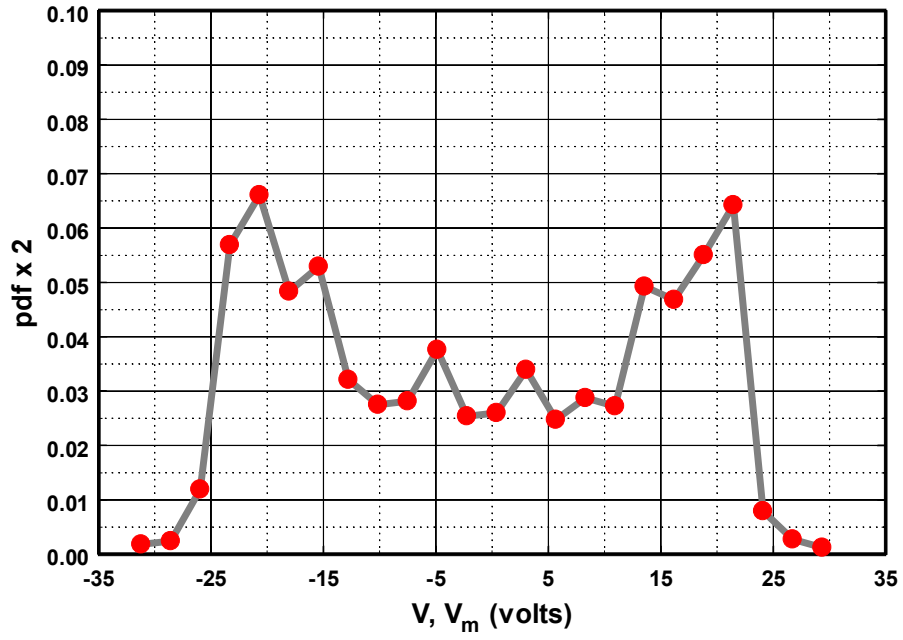

Figures 6: Probability density functions (pdf) in the wake of a cylinder at x/D=3 obtained from signals in figure 5a. a) pdf of signal maxima. b) pdf of total signal output.

For comparison, the pdf(v) of the continuous voltage signal v(t) is also plotted in Fig. 6b. The distribution of the voltage is bimodal, which is a typical characteristic of periodic signals that can be random if the phase angle θ(t) is considered as random variable with uniform distribution. The signal spends more time around its extreme values, and therefore the probability there is higher than during the fast rising or falling part of the signal.

The mutual interaction of the piezoelectric PVDF beam and the vortex dominated wake flow was explored by varying the free stream velocity U_∞ so that the shedding frequency could change under a practically constant Strouhal number, Str. The calculated rms values of the recorded voltages are plotted against the shedding frequency of the vortex street in Fig. 7. The data have been normalized by the maximum value of V_{rms} and the natural frequency of the beam f_{n}. The results in Fig. 7 demonstrate that maximum V_{rms} occurs when the forcing frequency of the vortex street f_{s} coincides with the natural frequency of the beam f_{n}. These data also show that the voltage drops significantly in non-resonance conditions. In particular, the data show that a 20% change in the forcing frequency results in a more than 40% drop in voltage rms. Of interest, however, are the cases where the forcing frequency f_{s} is greater than fn. The data in Fig. 7 clearly show that the output rms voltage does not drop to zero values; instead it seems to level off to a constant value of about 0.55 of the maximum level at resonance. This behavior suggests that in non-optimal operations, it is better to operate in frequencies higher than the natural one instead of generating forcing frequencies in the $f_{\text{s}}<f_{\text{n}}$ regime.

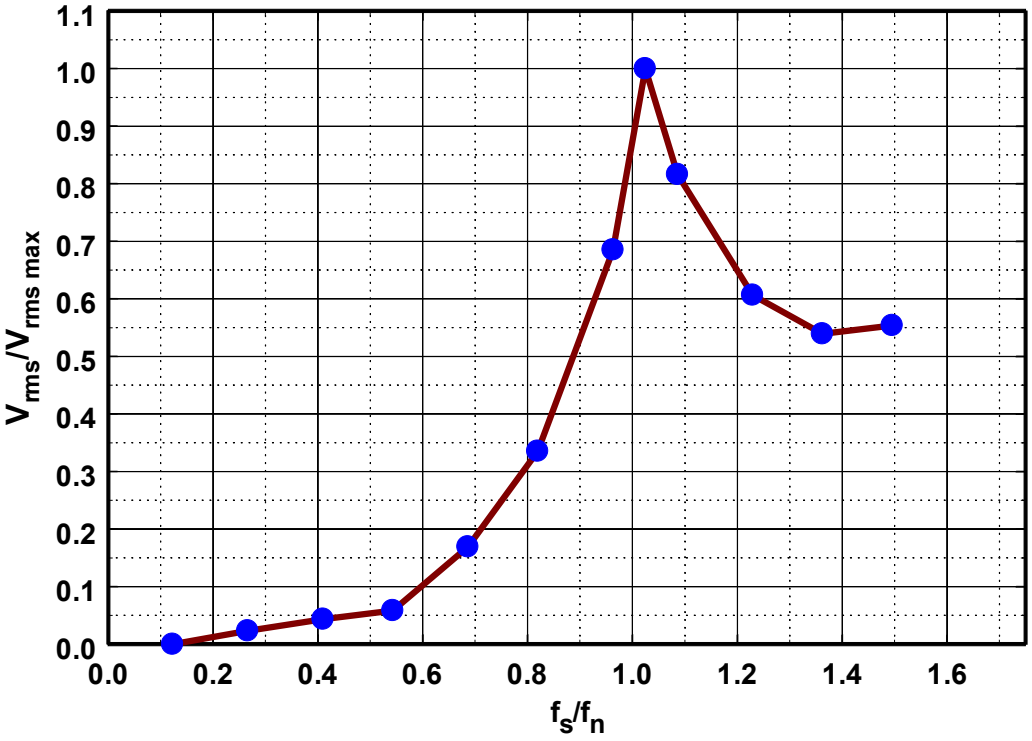

Figure 7: Rms voltage output dependence on forcing frequency of flow structures.

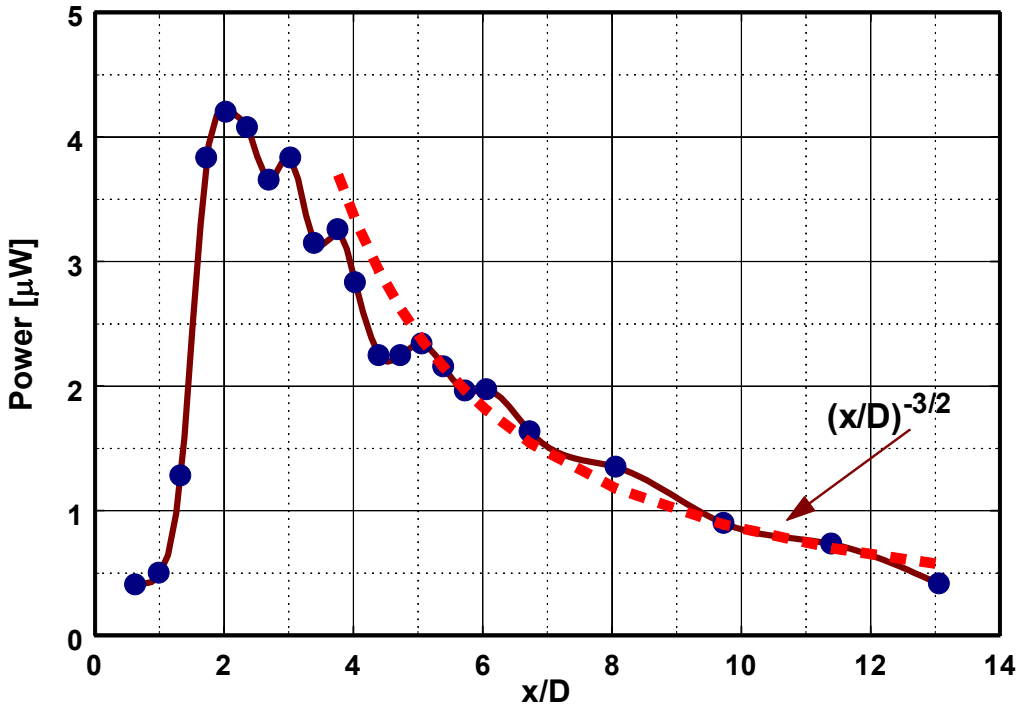

Figure 8: Mean power output along the central line of wake: Experimental data and decay relation.

The piezoelectric beam was placed first at several positions on the plane of symmetry of the wake of the cylinder at y=0 and the voltage was recorded which was then used to provide estimates of the average power. These data are plotted against the distance from the cylinder in Fig. 8. Very close to the cylinder, the average power is insignificant. However, power increases at further downstream locations, reaches a maximum at x/D=2 and subsequently decays slowly with x/D in a non-linear way. Dimensional analysis suggests that the force acting on the beam is proportional to the square of a velocity scale, and therefore the power is proportional to the cube of this velocity scale which for this particular case is the velocity deficit in the wake of the cylinder ΔU. Similarity arguments have shown that $\Delta U \sim (x/D)^{-1/2}$, and therefore the power is expected to be proportional to $(x/D)^{-3/2}$. Evidence of the validity of this argument is shown in Fig. 8 where this decay relation compares reasonably well with the experimental data. This decay is due to attenuation in vortex strength caused by viscous dissipation and scales growth with downstream distance.

The wake was also scanned to establish locations where the mean electrical power of the beam was the highest. The beam was positioned at different locations along the y=0 plane of symmetry and subsequently was traversed normal to the plane directions. Contours of this electrical power are plotted in Fig. 9 for the case of $f_s=f_n$. The data show that the electrical power is higher than 2 μW in the region bounded by $-1<y/D<1$ and $1<x/D\leq 8$ while higher power is generated along the center line when the beam is placed in the area defined by $-0.4<y/D<0.4$ and $1.5<x/D<3.5$. The peak value of the electrical power is about 4 μW which takes place at y/D=0 and x/D=2. One may consider that the region of maximum electrical output is associated with the high values of velocity

fluctuations which may cause the beam to vibrate at its maximum power. Although PIV measurements are yet to be performed, it is known from the work of Dong et al. (2006) that maximum velocity fluctuations occur off the plane of symmetry at $y/D \approx \pm 0.5$ at $x/D \approx 1.25$. However, when placed at $y/D=0$, the beam can make use of reciprocating pressure fluctuations of both shear layers at $y/D \approx +0.5$ and $y/D \approx -0.5$, which yields higher tip displacements and hence voltages. The computational work of AEA suggests that the generic cause of the beam's vibration is the passage of vortices above and below which are formed about 1.5D downstream of the cylinder by the shed off vorticity in the separated shear layers. This distance appears to be close to the formation length of the vortices described in Williamson (1996).

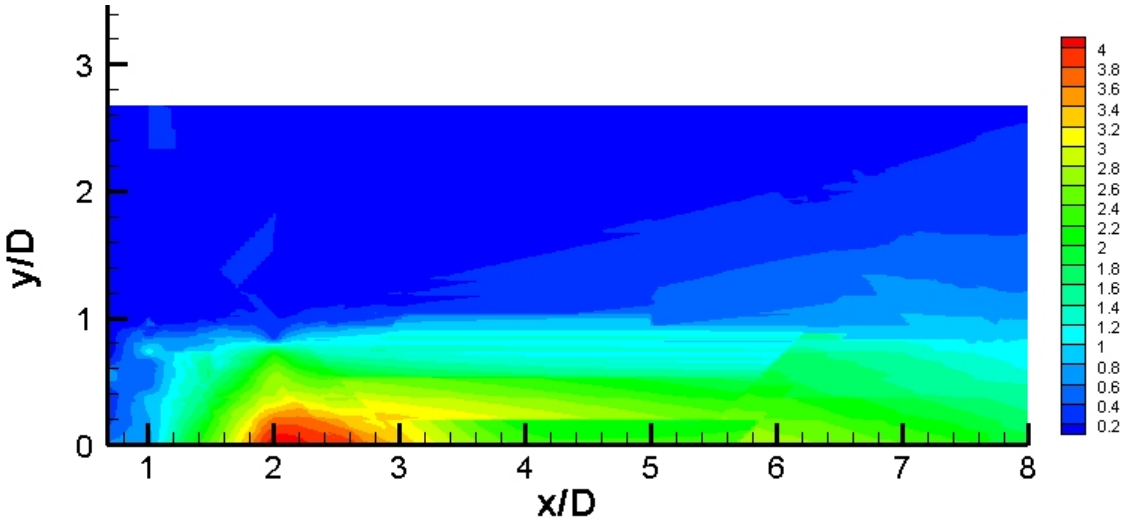

Figure 9: Contours of the mean electrical power of the PVDF beam in the wake of the cylinder with a load resistance of R=100kOhm at Re=14,800. Scale values in μW. x and y represent the coordinates of the un-flexed beam.

3.1 The far downstream region

At further downstream locations not only the output voltage is reduced significantly but its characteristics also change. Figure 10a shows a sample of the signal

obtained at x/D = 15.73 together with its envelope. The major difference from the signals in Fig. 5a, c is that the envelope appears to be shrinking occasionally, with amplitude less than half of the maximum values. Events with a bursting character can be identified, which are of a finite duration with the amplitude increasing toward a maximum and then decreasing to a small value. This cycle corresponds most probably to a beating mechanism with forcing and natural frequencies slightly apart which acts periodically. It has been reported in the past that turbulent structures are less organized at Re>5,000 (Rajagopalan and Antonia 2005; Prasad and Williamson 1997b), and therefore the forcing frequency fluctuates slightly with time. The range of these fluctuations is approximately 3 Hz about the nominal shedding frequency of 48.4 Hz. It is this small difference between the forcing and natural frequencies which is responsible for the beating phenomenon observed in Fig. 10a.

The spectral content of the signal shown in Fig. 10b indicates a major peak in the region between 48 and 52 Hz, which is associated with the first vibration mode of the beam followed by a peak at about 308 Hz, which is associated with the second vibration mode of the beam. The third peak at about 900 Hz most probably corresponds to the third natural frequency of the beam, which has not been measured, but estimated to be about 850 Hz.

Figure 10c shows the pdf(v) of the voltage signal with its bimodal distribution still evident at this location. However, the major difference from the near wake pdf(v) in Fig. 5c is that the part between the two peaks is filled more at this downstream position because the signal spends more time around zero values. The pdf of the envelope is shown in Fig. 10d for its positive values only. It follows very closely the Rayleigh

distribution except in the region around zero where the amplitudes are small and of broader bandwidth.

a)

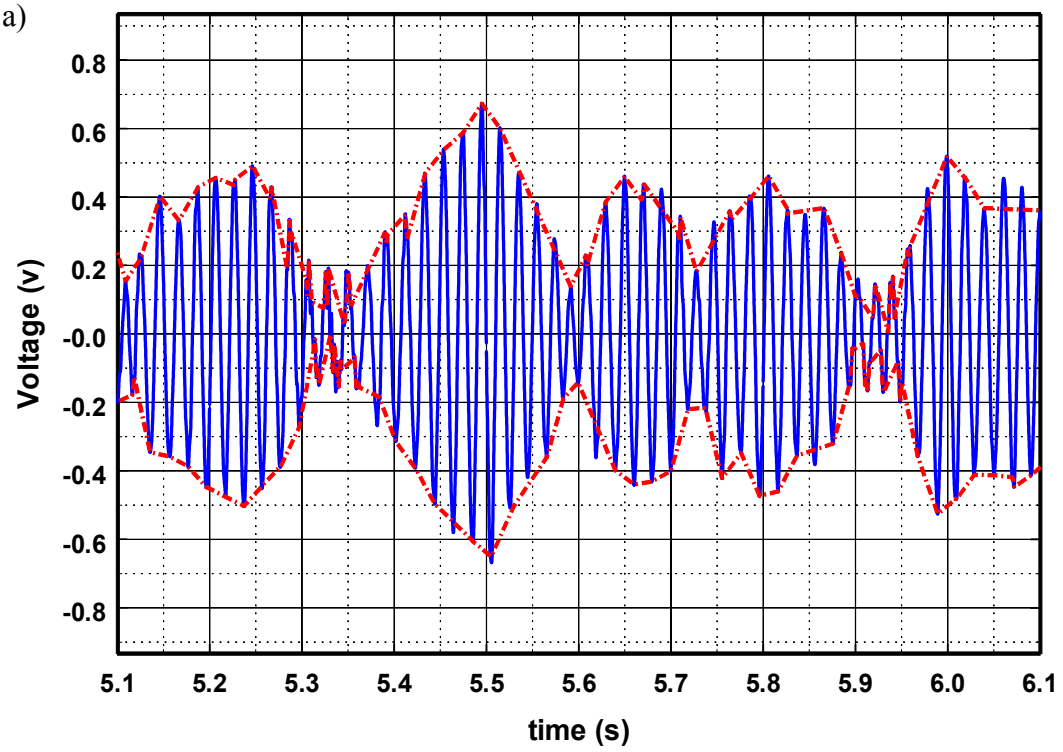

b)

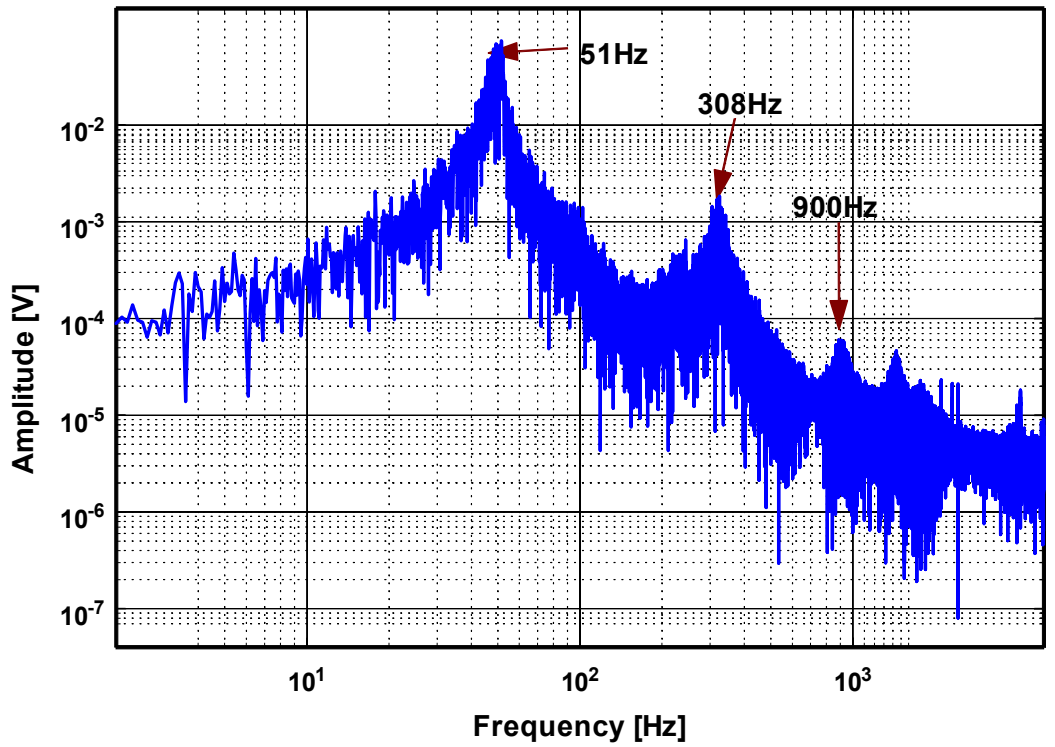

c)

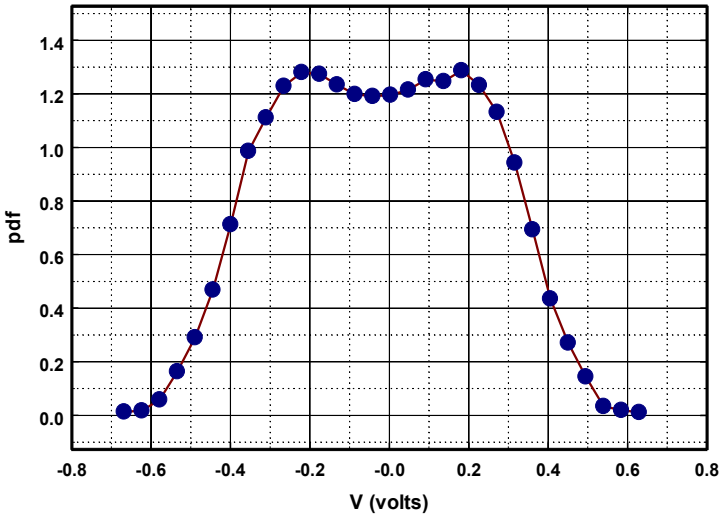

d)

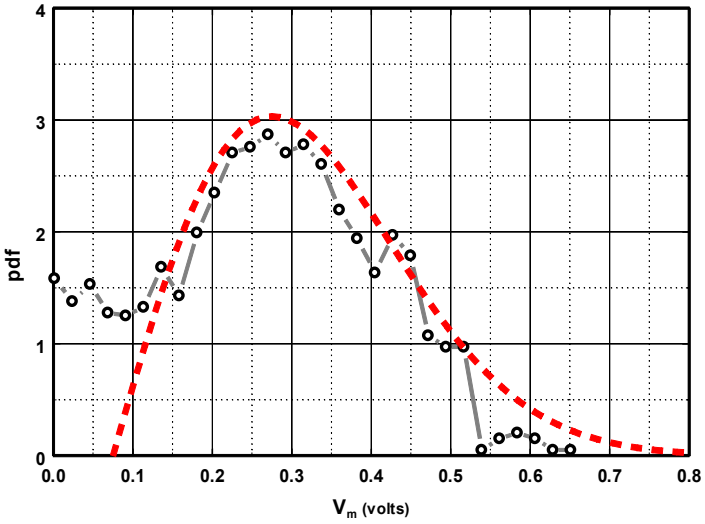

e)

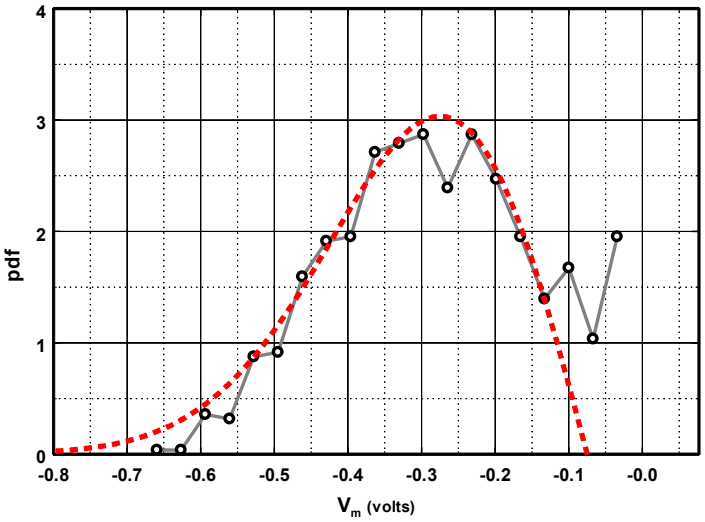

Figure 10: a) Output signal and its envelope measured at x/D=15.7. b) Corresponding amplitude spectrum. c) Probability density function. d) Probability density function of positive peaks. e) Probability density function of negative peaks.

3.2 The flow-structure interaction

As mentioned earlier the phenomena involved in the present application involve a three-way interaction between the flow field, the beam's structural field and the electric field. Several visualization experiments were conducted to explore details of the fluid structure interaction at Re=14,843. Figure 11 shows an image of the cylinder's wake interacting with the deflecting beam. As a result of the laser sheet illumination from the top of the wind tunnel, shadows below the cylinder and the piezoelectric beam are evident. Also evident in this picture are the deflecting piezoelectric beam and its electrical wires and support. The image was taken with the camera looking in the normal direction to the laser sheet plane.

In Fig. 11 small scale vortices are clearly shown in the shear layers emanating from the top and bottom of the cylinder that have been formed as a result of Kelvin–Helmholtz instabilities. These shear layers are wrapped around into larger scale vortices which start to interact with the piezoelectric beam. In this picture one clockwise vortex (CW) is depicted clearly on the top surface of the beam, while a counter-clockwise vortex (CCW) is vaguely visible in the lower side which is in the shadow of the beam. The passage of vortices above and below the piezoelectric beam causes the structure to deflect and induces its vibration.

Figure 12 depicts the beam deflected upward while the impinging flow induced by the CW vortex causes its downward motion. By the time, the beam is fully deflected downward this vortex finds itself on the top side of the beam. The low pressure core of the vortex then starts pulling the beam back upward.

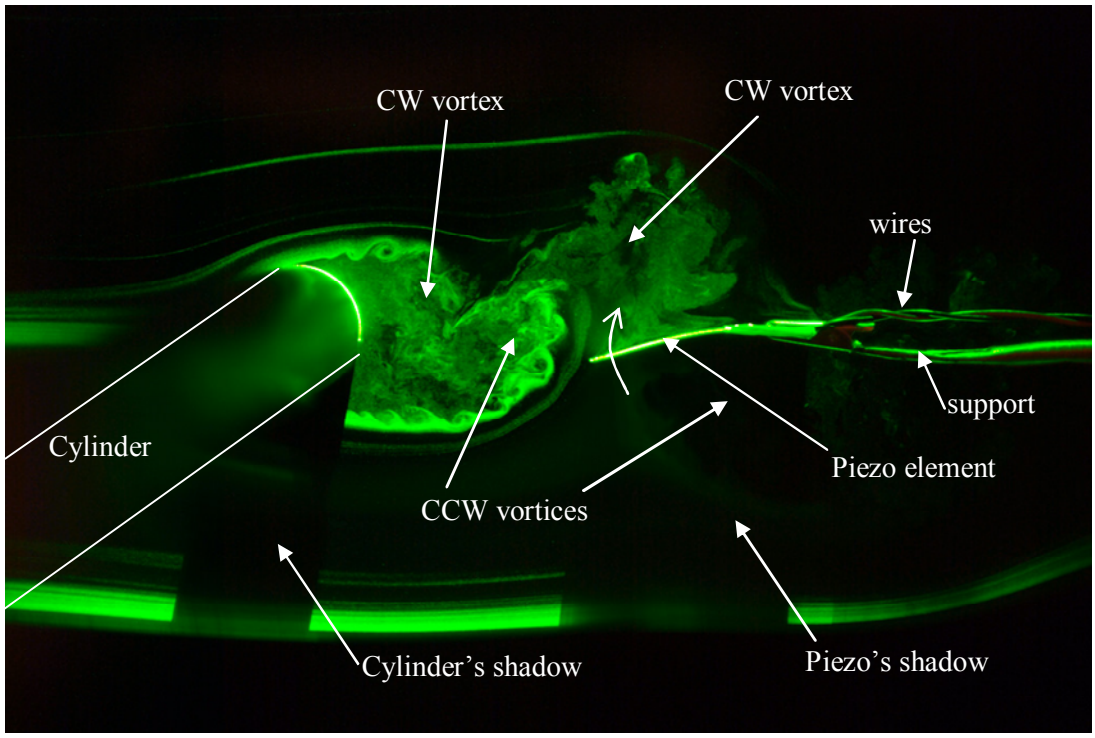

Figure 11: Visualization of fluid interaction with piezoelectric beam at Re=14,800. Flow from left to right. Piezoelectric beam deflected downward and moving upward.

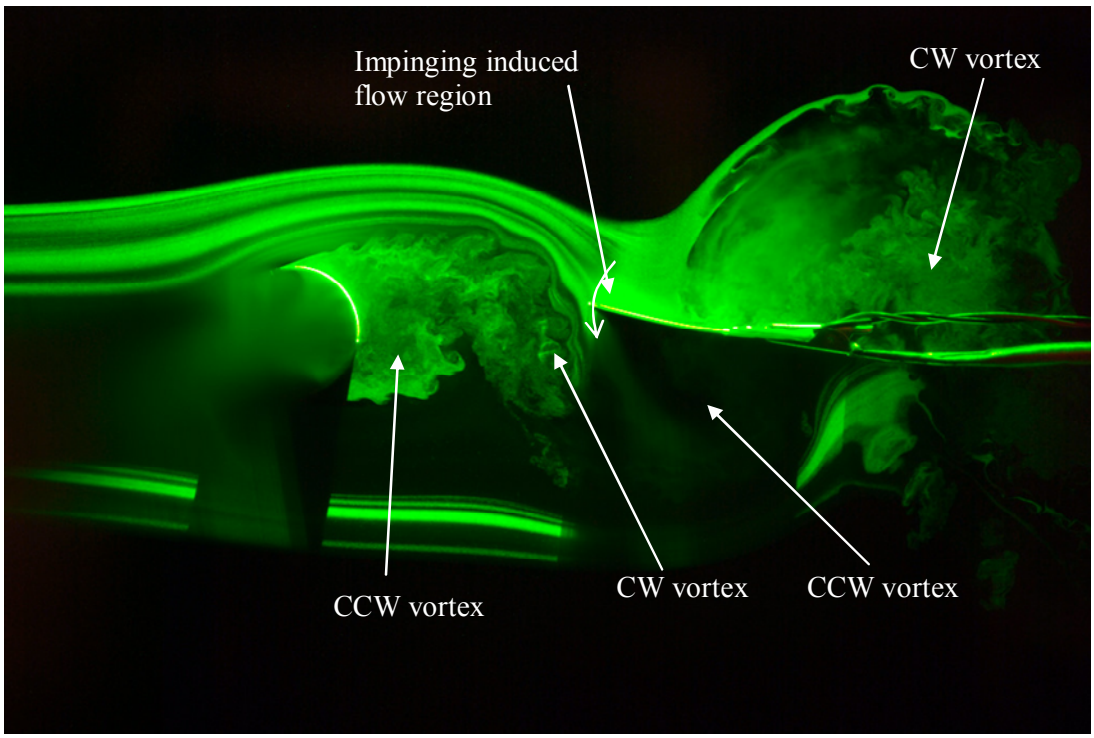

Figure 12: Visualization of fluid interaction with piezoelectric beam at Re=14,800. Flow from left to right. Piezoelectric beam deflected upward and moving downward.

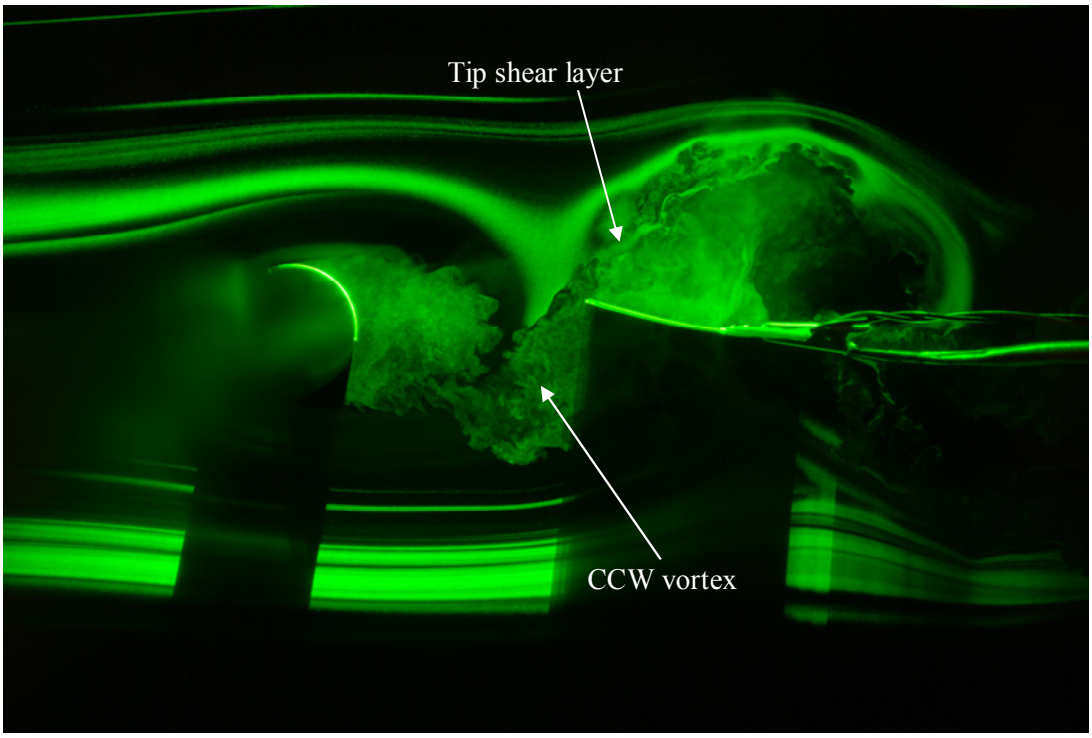

Figure 13: Mutual interaction and the formation of the tip shear layer.

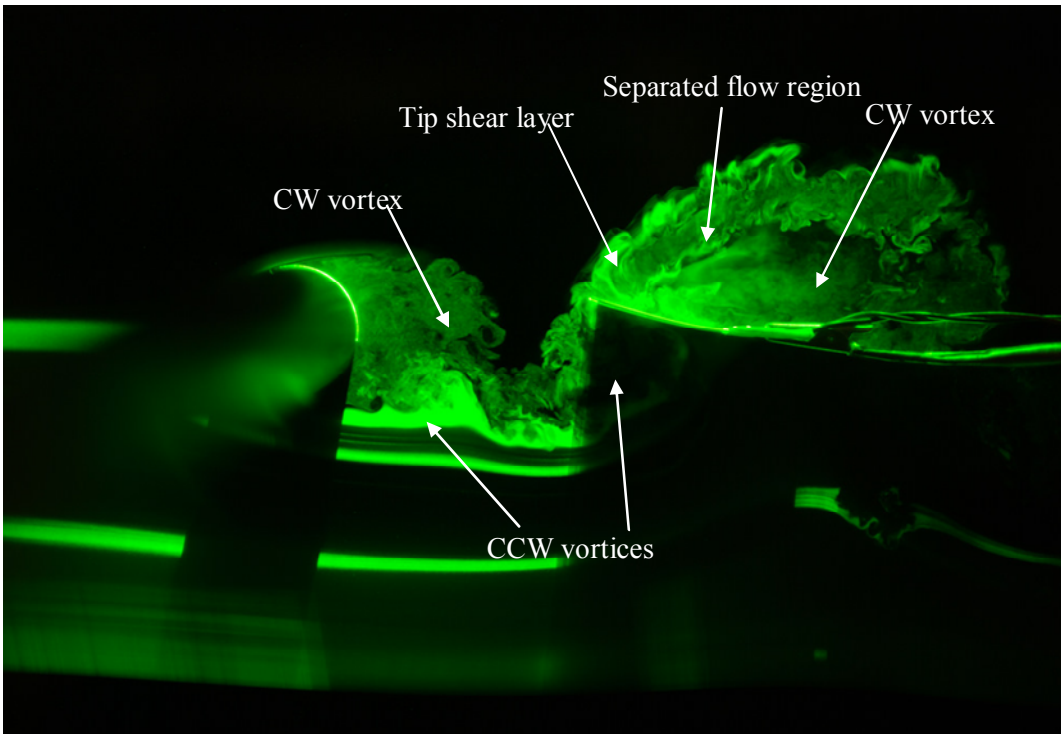

Figure 14: Mutual interaction with further viscous effects on the surfaces of the beam

The pressure on the beam is affected by two antagonist fluid flow mechanisms which are associated with (1) the induced flow ahead and behind the vortices and (2) the low pressure vortex core region. The induced flow ahead of the vortex impinges on the beam and its stagnation region creates an over-pressure which causes the beam to bend away from the vortex. Thus, when a vortex applies suction on one side, a region of positive pressure acts directly opposite on the other side so that the two effects work constructively to deflect the beam.

When the low pressure region of the vortex core is above the beam, the beam then starts to bend toward the vortex. The tail of the vortex brings fluid away from the beam's surface that is part of a recirculating pattern produced by the impinging flow on the other side of the beam.

Although the locations of clockwise and counterclockwise vortices on the top and bottom part of the vortex street are out of phase by 90°, the two mechanisms of pressure forces acting on the beam are always in phase, and therefore the beam is deflected under continuous alternating forcing. The sequence of these events combined with the resonating conditions of the beam itself results in maximum energy output. In a way the beam is slaloming in a train of alternating vortices in a similar way that fish or fish-like systems extract energy from large scale coherent motions to attain locomotion or propulsion (Beal et al. 2006; Eldredge and Piscani 2008).

So far, the role of the beam has been depicted as passive in the sense that its vibration is imposed by the passage of the large flow structures in the wake of the cylinder. It appears, however, that the interaction between the flow and the beam is mutual. The beam affects the local flow first by disrupting the streaklines between two

sequential alternating vortices and second by producing additional vorticity on its surface. Figure 13 shows the shear layer emanating from the tip of the beam toward the upper part of the flow above the beam. It is formed at the lower surface and carries CW vorticity, since it is produced by the impinging flow induced by the CCW vortex and the no-slip condition on this wall. The tip shear layer joins the outer structure of the large CW vortex that has passed the top side of the beam and it is also interacting with the boundary layer flow on the top surface of the beam formed by the recirculating flow pattern. Similar interactions taking place when the beam is deflected upward can be observed Fig. 14. A large separated shear layer is evident which emanates from the tip of the beam on the side of the top CW vortex. As explained above this tip shear layer of CW vorticity is formed on the lower side of the beam as a result of the no-slip condition at this wall. At the same time, the boundary layer formed over the top surface of the beam is separated from this wall to form a separated region which interacts with the tip shear layer and follows the large scale motion imposed by the CW vortex.

The piezoelectric beam in the wake of cylinder may be considered as a flexible splitter plate detached from the cylinder. The presence of splitter plates or other structures downstream of circular cylinders inhibits or alters the vortex shedding (Unal and Rockwell 1988; Mittal and Raghuvanshi 2001; Lau et al. 2004; Hwang and Yang 2007; Shukla et al. 2009). In the present experiments, however, the width of the piezoelectric beam (16 mm) is much smaller than the span of the cylinder (1.2 m); therefore, any upstream effect of the beam on quantities such as vortex shedding frequency is anticipated to be relatively minor.

In summary, the reverse interaction, i.e., the effects of the vibrating beam on the flow development is caused by the flow impingement between sequential alternating vortices on either surface of the beam and the no-slip conditions imposed on both sides of the beam. Thus, small-scale vortices with positive and negative vorticity are formed through this interaction within a larger vortical structure of a single sign circulation traveling downstream.

Some additional physical insights can be obtained if one considers the case of a stationary vortex in a uniform flow of U_∞ velocity above a stationary wall at distance h. Although this is a simple steady state potential flow solution and the pressure on the infinitely long wall and the velocity fields are easily obtained, it is important to revisit the effects of the vortex strength, its location from the wall h and the free stream velocity U_∞ on the pressure distribution along the wall. One parameter which is introduced here is the vortex induced velocity U_h at a distance $r=h$ and its relation to the free stream velocity expressed as the ratio U_h/U_∞. This ratio of velocity scales plays an important role in the distribution of the pressure coefficient C_p. In the case of a single vortex above the wall and in the absence of a cross flow, the pressure at the wall is negative, and therefore there is always a suction acting on the wall throughout its whole length. The presence of a cross flow, however, introduces and additional term in the pressure distribution which is always positive. Thus, the relation between these two terms in the equation controls the pressure distribution

$$C_p(x,0) = 4\frac{U_h}{U_\infty}\frac{h^2}{r^2}\left[1 - \frac{U_h}{U_\infty}\frac{h^2}{r^2}\right] \tag{8}$$

where $r^2=x^2+h^2$ with the origin of coordinate system at the foot print of the vortex. Therefore, the sign of C_p depends on whether the term in the bracket is positive or

negative. The ratio h_2/r_2 is always such that $\frac{h^2}{r^2} \leq 1$ and its value is further reduced with increasing distance r away from the origin. In order for the C_p to be negative, the velocity ratio should be $\frac{U_h}{U_\infty} > \frac{r^2}{h^2} \geq 1$. In the following, we will demonstrate the effects of varying h and U_h/U_∞ on C_p. In Fig. 15, the pressure distribution along the wall is plotted for the case of a vortex located at h=0.25 while the ratio U_h/U_∞ varies from 0.115 to 1.158. It is interesting to observe that C_p is positive far from the footprint of the vortex and it becomes negative at locations close to it. The points of sign change are determined by $\frac{r}{h} = \left[\frac{U_h}{U_\infty}\right]^{1/2}$ which is equivalent to $\frac{x}{h} = \pm\left[\frac{U_h}{U_\infty} - 1\right]^{1/2}$ which requires $\frac{U_h}{U_\infty} > 1$. Only the last two distributions with the highest velocity ratio U_h/U_∞ satisfy this condition.

The effect of increasing U_h/U_∞ is clearly to increase the magnitude of C_p. For h=0.1 m where the vortex is very close to the wall the ratio U_h/U_∞ reaches values between 0.288 and 2.895 and C_p is mostly negative in all but the three cases with the smallest U_h/U_∞. Far away from the origin, C_p is weakly positive but it becomes strongly negative in the region immediately below the vortex. The local extremes of C_p are at x=0 (r=h) and at $\frac{r}{h} = \left[2\frac{U_h}{U_\infty}\right]^{1/2}$ with the condition that $r>h$ which clearly suggests that only when $\frac{x}{h} = \left[2\frac{U_h}{U_\infty} - 1\right]^{1/2}$, i.e., when $\frac{U_h}{U_\infty} > 0.5$ there is a maximum or minimum off the x=0 location. Five of the ten distributions shown in Fig. 15 satisfy this requirement and have a

local maximum off the x=0 location. Nine out of the ten distributions in the case of h=0.25 have local maxima off the x=0 point at the positive C_p regions.

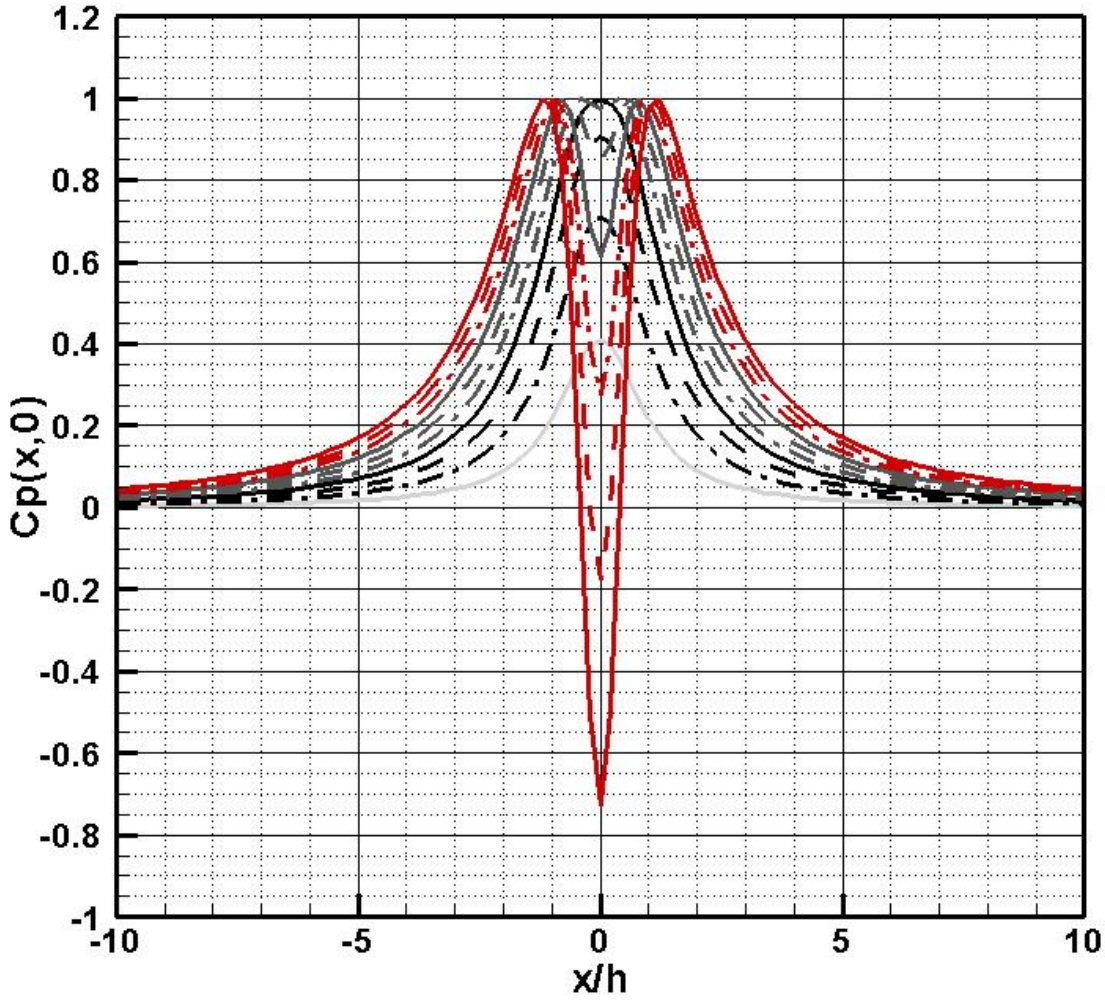

Figure 15: Case of vortex at h=0.25m with U_∞=11m/s. Effect of increasing circulation Γ from 2 to 20 m^2/s in steps of 2 m^2/s (corresponds to U_h/U_∞=0.115 through 1.158).

In order to understand further the cause of the pressure distribution in these flow cases, the streamline pattern has been computed. Figure 16 shows the streamline pattern in the case with the highest velocity ratio U_h/U_∞=2.88. There is a flow impingement on the wall in the aft of the vortex at x/h=2.2 which is associated to a positive C_p. In addition, the flow at x/h = -2.2 which bursts away from the wall is also associated with

positive C_p. In between these two stagnation points on the wall, the negative pressure induced by the vortex is enormous. As the velocity ratio decreases, these stagnation points approach each other toward the x/h = 0 location and at the end there is only one stagnation point inside the flow field below the vortex as Fig. 17 depicts. Thus, the two physical mechanisms identified in our experimental and CFD work (i.e., the dynamic interaction of a traveling vortex with a flexible finite wall) which cause the periodic forcing of the beam appear to be also present in this steady state case of a potential flow vortex interacting in an uncoupled way with a cross flow. The ratio U_h/U_∞ is the parameter which controls the pressure distribution. This also explains the drop in output voltage of the piezoelectric beam in location downstream and off the center line locations of the wake where the circulation is reduced or the distance h is increased. In both cases the ratio is reduced, and therefore the pressure is reduced.

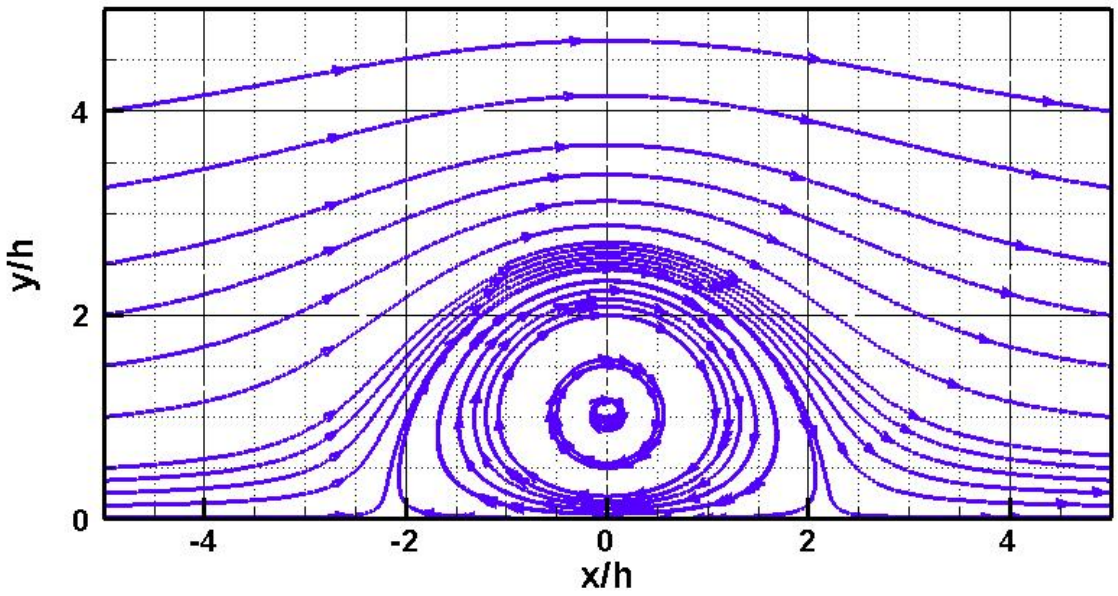

Figure 16: Streamlines pattern in case with U_h/U_∞=2.88.

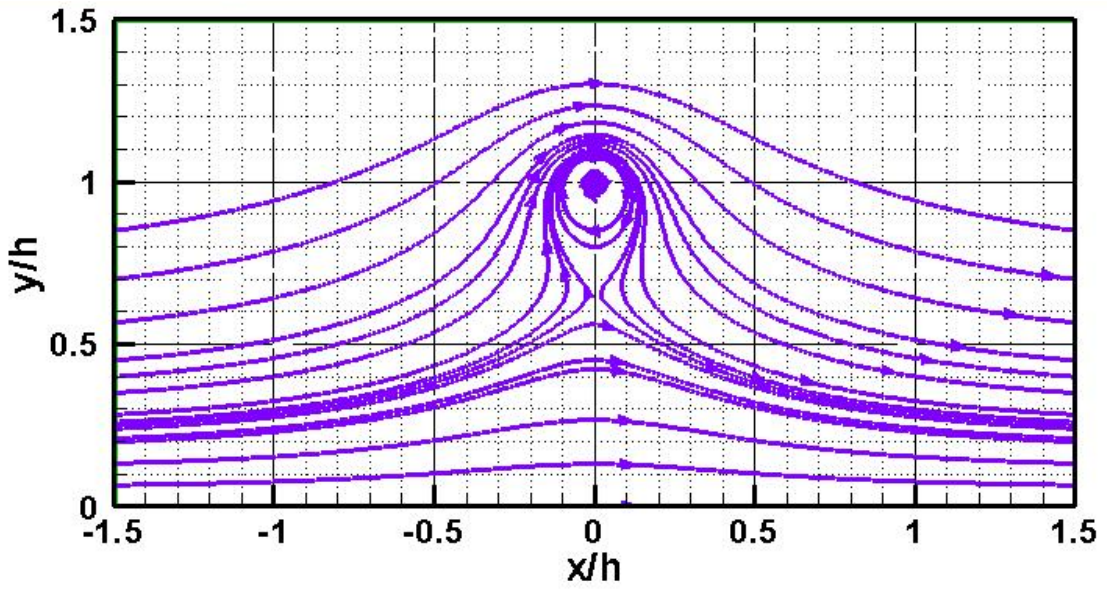

Figure 17: Streamlines pattern in case with U_h/U_∞=0.288.

3.3 Scaling considerations

Scaling laws describing the three-way interaction between the flow and the electromechanical fields have yet to be established. A starting point in this consideration is the available potential of fluid power which is proportional to the cube of the velocity $U(t)^3$. A control volume consideration inside the flow domain which involves the vibrating beam as a moving boundary shows that the two force components acting on the beam F_x and F_y in the case of a 2-dimensional flow can be expressed in terms of momentum exchanges through the introduction of coefficients C_{i1} and C_{i2} where A is the surface of the piezoelectric beam, t_b is its thickness

$$F_i = 1/2 C_{i1} A \rho U_i(t) U_i(t) + C_{i2} A t_b \rho \mathrm{d}U_i(t)/\mathrm{d}t \tag{9}$$

Thus, the work done by these forces will scale partly by $U_{ti}(t)U_i(t)^2$ and the surface of the beam A and by $U_{ti}(t)\mathrm{d}U_i(t)/\mathrm{d}t$ and the volume of the beam, where $U_{ti}(t)$ is the tip velocity of the beam. The case of the electromechanical field is more complicated.

If an equivalent harmonic excitation acting at the tip of the beam in the form $F_t = F_0 e^{j\omega t}$ causes a tip deflection in the form $w_t = w_0 e^{j\omega t}$ and if the loading circuit is purely resistive with a resistance R, then the transfer function of power per unit beam mass can be expressed in generic terms after extrapolating the work of Erturk and Inman (2008) as

$$P_{\mathrm{m}} = d_{31}^2 s_{11}^{-2} t^2 b^2 w_0^2 f(\lambda_{\mathrm{n}} / L, R, C, \omega_{\mathrm{s}} / \omega_{\mathrm{n}}) \tag{10}$$

In this notation 1 is the direction along the beam where the axial strain S_1 is applied and 3 is the direction of piezoelectric polarization. ω_{s} and ω_{n} are the operating and natural frequencies, respectively. It is assumed that the forcing frequency is close to first the natural frequency (i.e., $\omega_s/\omega_1 \approx 1$). $d_{31}=(\partial S_1/\partial E_3)^T$ is the piezoelectric constant, s_{11} is compliance which is the inverse of Young's modulus of elasticity, C is the capacitance of the piezoelectric element which contains the dielectric constant (permittivity) of the piezoelectric material. b is the width of the beam, w_0 is the amplitude of the tip vibration and k_1 is the dimensionless frequency number corresponding to the first natural frequency. $f(k_1/L, R, C, \omega_s/\omega_n)$ is a generic form of a function which includes the effects of the forcing mechanism and the loading and/or circuit model. It is this function that provides the shape of the experimentally determined frequency response shown in Fig. 8.

Thus, the specific power P_{m} is proportional to the material property d_{31}^2, its modulus of elasticity Y_{p}^2 and its cross-sectional area $(t_{\mathrm{p}}b)^2$. It is also proportional to the amplitude of vibration w_0 which in turn is inversely proportional to Y_{p} and the moment of inertia $I=t_{\mathrm{p}}^3 b/12$ and is proportional to L^3. Eventually $P_m = d_{31}^2 \frac{L^6}{t_p^4} f(\lambda_1 / L, R, C, \omega_{\mathrm{s}} / \omega_{\mathrm{n}})$. Surprisingly, this relation indicates that the specific output power P_{m} is independent of material's Young's modulus of elasticity and its width b in the mechanical part.

However, both parameters indirectly affect the function f since ω_n is proportional $Y_p^{1/2}$ and the capacitance of the material is proportional to b. The length and thickness of the piezoelectric beam seem to affect P_m more than d_{31} does. As was mentioned earlier the power is at maximum when the forcing mechanism matches in frequency with the natural frequency of the beam (i.e., $\omega_s/\omega_n=1$), a condition which is described in the function $f(k_1/L, R, C, \omega_s/\omega_n)$.

In the above considerations, the load circuit was simply resistive. In general, the output voltage depends on the load circuit which may also include capacitance and inductive components. Additional complications will be imposed by the fact that the load circuit should extract the maximum possible electrical power, which requires matching the electric impedances of the piezoelectric beam and the attached circuitry. For a purely resistive circuit formed by the load resistance R, this condition takes place at about $R=1/(C\omega)$.

4. Conclusions

In the present work, we have demonstrated the concept of energy harvesting from a turbulent flow exhibiting a large degree of coherence in its spatial and temporal scales by using piezoelectric generators. In particular, the turbulent wake flow of a cylinder at high Reynolds number (Re>10,000) provides a unique opportunity for energy harvesting because the coherent structures are still well-defined and are created at high frequencies. In the present study, this flow has been investigated experimentally by using thin flexible cantilevered beams consisted of a PVDF layer deposited on a Mylar substrate. Several orientations of the beam in reference to the flow have been explored but the most

promising appeared to be the case of the beam parallel to the upstream flow in a face-on configuration.

The piezoelectric beam was traversed in the wake of the cylinder and the generated voltage has been recorded as a function of time. The experiments were performed in a low speed wind tunnel with variable free stream velocity which allowed for variable frequency forcing of the piezoelectric beam. The experiments showed that it is critical to tune the predominant frequency of the flow with the natural frequency of the piezoelectric generator in order to maximize the piezoelectric output voltage. Minor mismatching between the two frequencies causes substantial reductions in the output power especially when $f_s < f_n$.

The driving mechanism is mainly due to the passage of vortices formed by the shear layers emanating from the cylinder over the piezoelectric beam. The pressure on the beam is affected by two different flow patterns which are associated with the induced flow ahead and behind the vortices and the low pressure vortex core region. The induced flow ahead of the vortex impinges on the beam and its stagnation region creates an over-pressure which causes the beam to bend toward the opposite side where the core of another vortex applies suction at the same time. The two effects work constructively to increase the forcing on the beam. The tail of the vortex brings fluid away from the beam surface and it is part of a recirculating pattern produced by the impinging flow on the other side of the beam. Since the two mechanisms of pressure forces acting on the beam are always in phase, the beam is deflected under continuously alternating force. The sequence of these events combined with the resonating conditions of the beam itself results in maximum energy output.

The near and far wakes were scanned to determine positions of the beam with maximum generated output power. The measurements have shown that the maximum electrical output power with the given PVDF beam was about 4 μW, and it occurred at y=0 and x/D=2. The maximum power generation does not occur very close to the cylinder since the large vortical structures are not fully formed at these locations. The power drops off the center line because of small values of the non-dimensional parameter U_h/U_∞. Along the center line, the electrical output decays as $(x/D)^{-3/2}$, because the vortical structures attenuate due to viscous dissipation and because they grow in size. It was demonstrated through analytical work that the distance of the beam from the vortices and their circulation affect the output power. In particular, it was shown that the induced velocity by one vortex at the beam's location and its relation to the flow velocity affects critically the forcing mechanism of the beam.

The amplitude of the output voltage was further investigated and its probability density function was found to obey a Rayleigh distribution, which is a feature that characterizes high-pass filters.

Finally, some scaling considerations are discussed which show that the output power consists of several contributions. The aerodynamic contribution which provides the force acting on the piezoelectric beam scales partly with its surface area and partly with its volume, while the electromechanical contribution scales with its volume. In addition, this power is more affected by the length and thickness of the beam rather than its electromechanical coupling coefficient.

Acknowledgment

The present work is sponsored by the Michael Pope Fund for Energy Research.

References

Akaydin HD, Elvin N, Andreopoulos Y (2010) Energy harvesting from highly unsteady fluid flows using piezoelectric materials. J Intell Mater Struct (accepted for publication)

Allen JJ, Smits AJ (2001) Energy harvesting Eel. J Fluids Struct 15:629–640

Andreopoulos J, Agui JH (1996) Wall-vorticity flux dynamics in a two-dimensional turbulent boundary layer. J Fluid Mech 209:45–84

Andreopoulos Y, Honkan A (2001) An experimental study of the dissipative and vortical motion in turbulent boundary layers. J Fluid Mech 439:131–163

Anton SR, Sodano HA (2007) A review of power harvesting using piezoelectric materials (2003–2006). Smart Mater Struct 16:R1–R21. doi:10.1088/0964-1726/16/3/R01

Beal DN, Hover FS, Triantafylou MS, Liao JC, Lader GV (2006) Passive propulsion in vortex wakes. J Fluid Mech 549:385–402

Bendat J, Piersol AG (2000) Random data, 3rd edn. Wiley, New York

Bloor MS (1964) The transition to turbulence in the wake of a circular cylinder. J Fluid Mech 19:290–304

Brede M (2004) Measurement of turbulence production in the cylinder separated shear layer using event triggered laser-Doppler anemometry. Exp Fluids 36:860–866

Dong S, Karniadakis GE, Ekmekci A, Rockwell D (2006) A combined DNS-PIV study of the turbulent near wake. J Fluid Mech 569:185–207

Eldredge JD, Piscani D (2008) Passive locomotion of a simple articulated fish-like system in the wake of an obstacle. J Fluid Mech 607:279–288

Elvin NG, Elvin AA (2009a) A general equivalent circuit model for piezoelectric generators. J Intell Mater Syst Struct 20:3–9

Elvin NG, Elvin AA (2009b) A coupled finite element-circuit simulation model for analyzing piezoelectric energy generators. J Intell Mater Syst Struct 20: 587–595. March 2009. doi: 10.1177/1045389X08101565

Elvin NG, Lajnef N, Elvin A (2006) Feasibility of structural monitoring with vibration powered sensors. Smart Mater Struct 15(4):977–986

Erturk A, Inman DJ (2008) A distributed parameter electromechanical model for cantilevered piezoelectric energy harvesters. J Vib. Acoust 130:041002

Hwang J-Y, Yang K-S (2007) Drag reduction on a circular cylinder using dual detached splitter plates. J Wind Eng Ind Aerodyn 95:551–564

Lau YL, So RMC, Leung RCK (2004) Flow-induced vibration of elastic slender structures in a cylinder wake. J Fluids Struct 19:1061–1083. DOI:10.1016/j.jfluidstructs.2004.06.007

Lin JC, Towfighi J, Rockwell D (1995) Instantaneous structure of the near wake of a circular cylinder: on the effect of Reynolds number. J Fluids Struct 9:409–418

Mitcheson PD, Yeatman EM, Rao GK, Holmes AS, Green TC (2008) Energy harvesting from human and machine motion for wireless electronic devices. Proc IEEE 96(9):1457–1486

Mittal S, Raghuvanshi A (2001) Control of vortex shedding behind circular cylinder for flows at low Reynolds numbers. Int J Numer Meth Fluids 35:421–447

Monkewitz P, Nguyen LN (1986) Absolute instability in the near wake of two-dimensional bluff bodies. J Fluids Struct 1:165–184

Paradiso JA, Starner T (2005) Energy scavenging for mobile and wireless electronics. Pervasive Comput 4(1):18–27

Pobering S, Schwesinger N (2004) A novel hydropower harvesting device. Proceedings—2004 International Conference on MEMS, NANO and Smart Systems, ICMENS 2004, pp 480–485

Prasad A, Williamson CHK (1996) The instability of the separated shear layer from a bluff body. Phys Fluids 8:1347–1349

Prasad A, Williamson CHK (1997a) The instability of a shear layer separating from a bluff body. J Fluid Mech 333:375–402

Prasad A, Williamson CHK (1997b) Three-dimensional effects in turbulent bluff body wakes at moderate Reynolds numbers. J Fluid Mech 343:235–265

Prasad A, Williamson CHK (1997c) Three-dimensional effects in turbulent bluff body wakes. Exp Therm Fluid Sci 14:9–16

Rajagopalan S, Antonia RB (2005) Flow around a circular cylinder—structure of the near wake shear layer. Exp Fluids 38:393–402

Robbins WP, Marusic I, Morris D, Novak TO (2006) Wind-generated electrical energy using flexible piezoelectric materials. Proceedings of IMECE2006 2006 ASME International Mechanical

Engineering Congress and Exposition, November 5–10, 2006, Chicago, Illinois

Roshko A (1954) On the development of turbulent wakes from vortex streets. NACA Report 1191

Sahele M, Liu Y, Hoffman H (2005) Piezoelectric energy harvesting using different approaches including control system. Annu Res J III:134–141

Schmidt VH (1992) Piezoelectric energy conversion in windmills. Proceedings of IEEE Ultrasonics Symposium, pp 897–904

Shukla S, Govardhan RN, Arakeri JH (2009) Flow over a cylinder with a hinged-splitter plate. J Fluids Struct. ISSN 0889-9746, doi: 10.1016/j.jfluidstructs.2008.11.004

Sodano HA, Park G, Inman DJ (2004) A review of power harvesting from vibration using piezoelectric materials. Shock Vib Digest 36(3):197–205

Sodano HA, Inman DJ, Park G (2005) Generation and storage of electricity from power harvesting devices. J Intell Mater Syst Struct 16:67–75

Taylor GW, Burns JR, Kammann SM, Powers WB, Welsh TR (2001) The energy harvesting eel: a small subsurface ocean/river power generator. IEEE J Ocean Eng 26(4):539–547

Unal MF, Rockwell D (1988) On vortex formation from a cylinder. Part II. Control by splitterplate interference. J Fluid Mech 190:513–529

Williamson CHK (1996) Vortex dynamics in the cylinder wake. Annu Rev Fluid Mech 28:477–539

Zdravkovich M (1997) Flow around circular cylinders, vol. 1. Oxford University Press, Oxford

Chapter 4

Experimental Study of a Self-Excited Piezoelectric Energy Harvester

Hüseyin Doğuş Akaydın, Niell Elvin, Yiannis Andreopoulos

Published on 28 September 2010 in

Proceedings of 3rd ASME Conference on Smart Materials, Adaptive Structures and Intelligent Systems, 28 Sep.-1 Oct. 2010, Philadelphia, PA. USA.

Article Number: SMASIS2010-3729

Abstract

In the present experimental work, we explore the possibility of using piezoelectric based fluid flow energy harvesters. These harvesters are self-excited and self-sustained in the sense that they can be used in steady uniform flows. The configuration consists of a piezoelectric cantilever beam with a cylindrical tip body which promotes sustainable, aero-elastic structural vibrations induced by vortex shedding and galloping. The structural and aerodynamic properties of the harvester alter the vibration amplitude and frequency of the piezoelectric beam and thus its electrical output. This paper presents results of energy-harvesting tests with one configuration of such a self-excited piezoelectric harvester using a PZT bimorph. In addition to the electrical voltage output, the strain on the surface of beam close to its clamped tip was also measured The measured strain and voltage output were perfectly correlated in the frequency range

containing the first natural mode of vibration of the system. It was observed that about 0.24 mW of electrical power can be attained with this harvester in a uniform flow of 28 m/s.

1. Introduction

In two recent papers by the authors [1 and 2], it has been demonstrated that fluid flow energy can be harvested by using piezoelectric generators to convert kinetic energy of the flow into electrical energy. These generators are AC-coupled elements and the produced energy can be used for continuously powering very small electronic devices or can be rectified and stored for intermittent use. The available power in a flowing fluid is proportional to the cube of its velocity, which typically for an air flow velocity of 10 m/s can be of the order of 500W per m^2 of flow cross section. In many cases this flow power is untapped and the energy is thus wasted. Hence, any power harvesting of this wasted energy is beneficial. Most of the previous research on piezoelectric energy harvesters has focused on applications involving only structural vibration [3 and 4] and very little work has been devoted to harvesters of ambient fluid energy with only a few contributions [5-9].

A steady and uniform fluid flow does not contain oscillating mechanical forces which are required for electromechanical energy conversion. In such circumstances, alternating forces need to be utilized to drive these energy harvesters. Such forces may be created by 1) Using a bluff body separate from and upstream of the harvester to create a vortex street which conveys a significant amount of velocity fluctuations. 2) Making use of flow-induced vibrations that can be generated and sustained by harvester body itself.

Piezoelectric energy harvesting using fluid flow involves the mutual interaction of three distinct dynamic systems, namely the fluid, the structure and the associated electrical circuit. Our recent experimental and analytical work has involved testing short length, flexible PVDF piezoelectric cantilever beams in a large scale wind tunnel under resonance and random excitation in a high Reynolds number wake of a cylinder and in a turbulent boundary layer flow, respectively. These tests have demonstrated that it is possible to generate relatively high voltage outputs from piezoelectric harvesters placed inside time-dependent flows with high or low degree of spatial and temporal coherence. Matching the flow's predominant frequency with the natural frequency of the piezoelectric beam appears to maximize the piezoelectric output voltage. This generated voltage depends on the location of the generator within the flow field. This work has also indicated that the conversion efficiency of fluid energy to vibration energy is of the order of 0.03% while the efficiency in converting this vibration into electrical energy is of the order of 11% per piezoelectric layer. This clearly suggests the need for further understanding of the issues limiting the efficiency in converting fluid energy into vibration energy which can lead to a substantial increase in generated electrical power.

Our previous work in piezoelectric fluid energy harvesting has been carried out in originally unsteady flows (i.e. in a turbulent boundary layer) as in [1] or originally steady flows where the oscillatory forces created using upstream bluff bodies (i.e. in a vortex street) as in [1 and 2]. In contrast, the present work explores the potential of harvesting wind energy with the use of piezoelectric devices located inside a *steady flow* where self-excited flow-induced vibrations will be generated and sustained by the harvester body itself. This configuration will extend the potential of using such energy harvesters in

flows beyond largely unsteady or turbulent cases. A self-excited configuration has potential advantages of having a smaller form factor, providing power over a broad frequency band and higher power output than before.

As a part of our efforts towards modeling self-excited piezoelectric harvesters, the present study shows some preliminary experimental results obtained by a cantilevered piezoelectric bimorph and a hollow circular cylinder as a tip body in a uniform, steady velocity field. The corresponding voltage output from the piezoelectric generator was recorded together with the strain measured by a strain gage attached on the surface of the beam close to its base as a function of the free stream velocity. Although use of other tip-mass geometries and beam configurations may result in higher power outputs, use of cylinder and a beam provides a configuration which can be analytically modeled and compared with the existing literature.

2. Present Approach

The operation of our harvesters is based on the vortex shedding phenomena associated with the flow field around circular cylinders in uniform flow of velocity V_∞. The non-dimensional frequency of this vortex shedding is characterized by the Strouhal number $St=Df_{shed}/V_\infty$ which dependents on the Reynolds number based on the diameter of the cylinder $Re=\rho DV_\infty/\mu$. St is around 0.2 for a fairly wide range of Reynolds number so that the shedding frequency

$$f_{shed} = \frac{V_\infty St}{D} \tag{1}$$

is proportional to velocity for a given diameter D.

The alternating shedding of vortices off the surface of the cylinder causes an asymmetry between the pressure distributions on the upper and lower halves of the cylinder's surface. This results in a time-dependent *lift force,* F_y, on the cylinder alternating in the $+y$ and $-y$ directions with zero mean and frequency f_{shed}. If the cylinder is attached to a beam as shown in Fig. 1 the aerodynamic lift creates an equivalent tip force and moment causing the beam to undergo transverse (y-axis) vibrations. It is this *flow-induced vibration* that is used for forcing the piezoelectric generator in transverse vibrations. In addition there is a time dependent *drag force,* F_x, which also acts on the cylinder in the direction of the fluid flow and has a non-zero mean value. In the present configuration, the drag force is ignored since it is much smaller than the buckling load of the beam. This configuration differs from the common cases of splitter plates in the wake of a cylinder used to control vortex shedding because the splitter plate in the present case is fixed at one end while its other end carries the cylinder and is free to vibrate. The flow-structure interaction aspect of this configuration i.e. its aero-elastic behavior has not been investigated before and the additional electromechanical characteristics and coupling of this energy harvester further complicates the understanding of its operation.

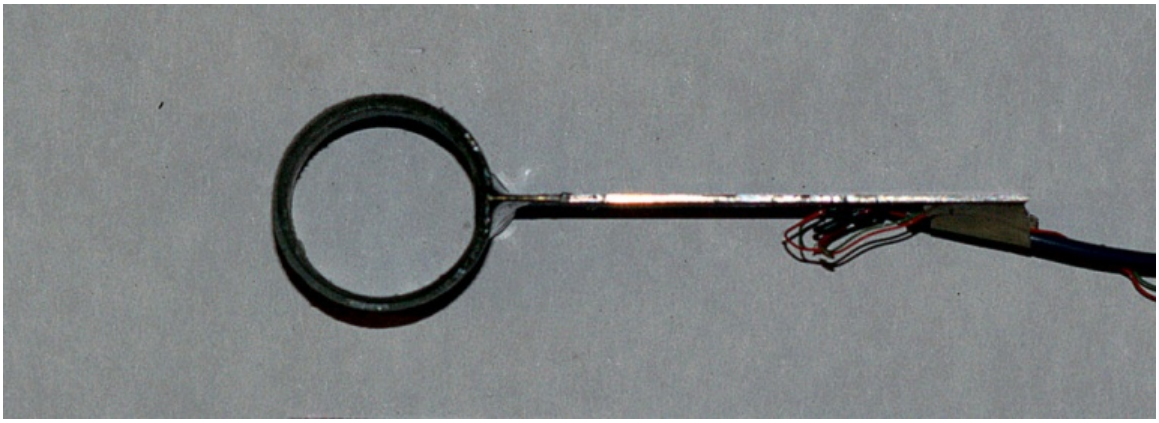

Figure 1: The piezoelectric beam with the cylinder attached to its tip.

In the present experiment, the generator is operated in at its first natural frequency. Our previous work has indicated the energy output is maximized when the frequency of forcing mechanisms coincides with the first natural frequency of the piezoelectric harvester.

3. Experimental Setup

A hollow cylinder with closed ends was attached to the free tip of the piezoelectric beam in order to induce self-excited vibrations on the harvester. The cylinder was light and rigid so that no deformation of the cylinder was expected under the applied aerodynamic loads.

The piezoelectric beam is a PZT bimorph from Piezo Systems, Inc. (model T226-A4-503X), which was also used in [10], operated in series mode. The beam is composed of a brass shim sandwiched between two layers of PZT-5A material. The geometric dimensions and material properties of the beam are listed in Table 1 where ε_0=8.854 pFm^{-1} is the permittivity of vacuum.

Table 1: Dimensions and properties of the PZT bimorph.

Dimensions and Properties	PZT layers	Shim
Total Length, L_t [mm]	63.5	63.5
Overhang (clamped) Length, L [mm]	50.8	50.8
Width, b [mm]	31.8	31.8
Thickness, h [mm]	0.26	0.14
Material	PZT-5A	Brass
Mass density, ρ [kg m-3]	7800	9000
Young's Modulus, Y [GPa]	66	105
Piezoelectric Constant d_{31} [pm V-1]	-190	-
Permittivity $\bar{\varepsilon}_{33}^{S}$ [F m-1]	$1500\varepsilon_0$	-

The beam with attached cylinder was clamped between two steel bars of dimensions 3.18 mm x 12.7 mm x 254 mm which formed a support structure. The volume occupied by the harvester in the channel is around 9x3.2x2.5=72 cm3. The support structure is mounted firmly on both ends in a small wind tunnel as shown in Fig. 2. Such a vertical arrangement is chosen in order to eliminate contribution of gravity from the transverse vibration of the beam.

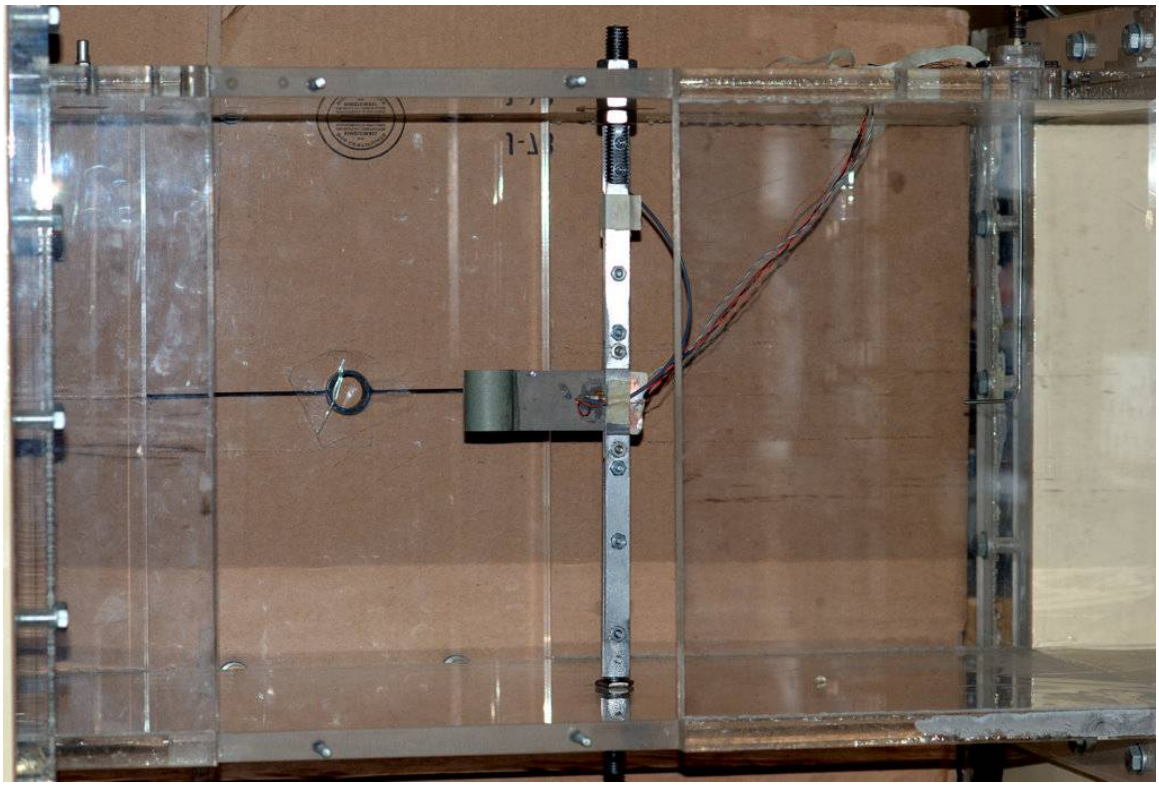

Figure 2: The harvester installed in the wind tunnel.

The beam in the wake of the cylinder acts as a "splitter plate" which is known to decrease the strength and frequency of the vortex shedding [11]. Therefore the *St* in presence of a splitter plate is expected to be less than 0.2 depending on the ratio *L*/*D*. With the given dimensions of the beam and the cylinder's length to diameter ratio *l*/*D*=2.5 gives St=0.15 [12]. If it is assumed that the maximum power would occur close

to the first resonant frequency ($f_{shed}=f_1$). Thus the speed for maximum output power is estimated to be approximately 5.8 m/s. At this speed *Re* is about 9300 with ρ =1.19 kgm^{-3} and μ =1.86 kgsm^{-1}.

It should be also noted that the vortex shedding may not be strong or present at all if the *l*/*D* ratio of the cylinder is small. This is because a greater part of the incoming flow passes over the ends of the cylinder rather than over its lateral surfaces. In fact, a test of this harvester with the walls of the wind tunnels at 152 mm above and below the ends of the cylinder as shown in Fig. 2 showed no significant voltage output. In order to obtain stronger vortex shedding, the cylinder was placed in a modified test section with a 36mm x300mm cross section, formed between two bounding walls inside the original wind tunnel section (Fig. 3). These walls, which act very similarly to the end wall used in many experiments with cylinders, were about 2 mm above and below either end of the cylinder. Although the flow was still somewhat three-dimensional due to boundary layer formation over the walls, the end effects due to the short length of the cylinder are reduced and visible oscillations of the cylinder were observed. The contraction of the intake of the wind tunnel was also modified to take as much flow into the narrowed-down test section as possible for increasing the maximum attainable flow speed within the wind tunnel.

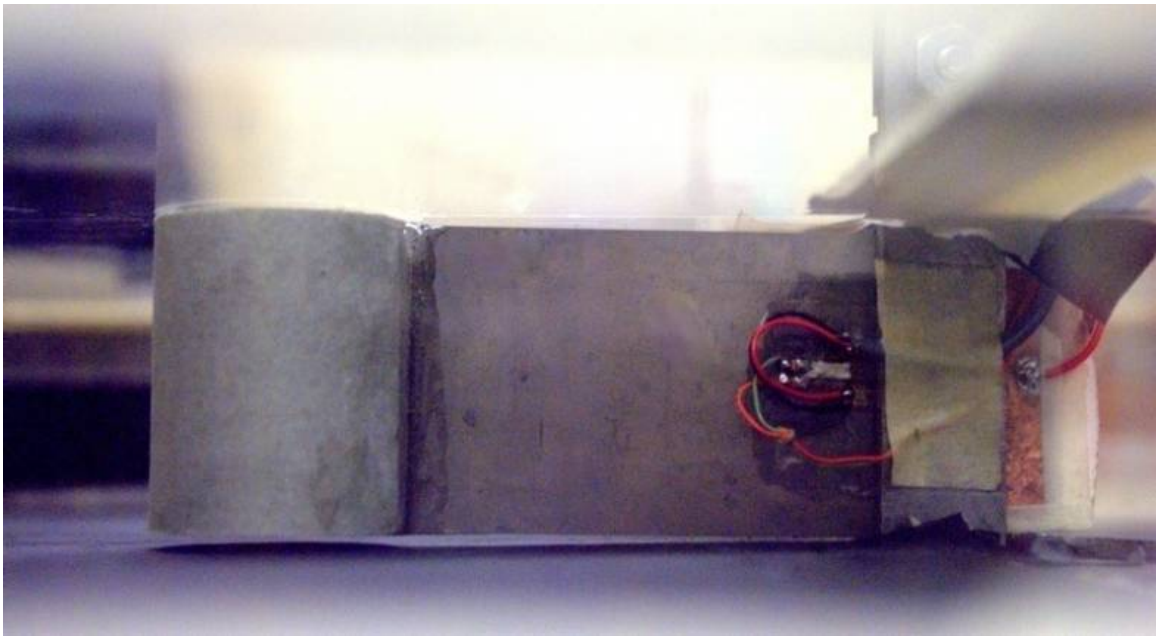

Figure 3: The harvester in the narrowed-down flow channel with 36 mm x 300 mm working section. The top wall is transparent. Note the gaps between the harvester and the bounding walls.

The charge generated by the piezoelectric beam was collected by two copper foils sandwiched between the end clamping elements and either surface of the beam. The time-dependent voltage v(t) on a load resistor R generated by the piezoelectric beam was measured using a digital oscilloscope. A strain gage was mounted on the surface of the beam about 3 mm from the clamp as shown in Fig. 5. Type-UHP5000-60 micro-strain gages fabricated by Kulite were used in this work. These gages have a size of 0.5 mm x 0.75 mm. They possess a frequency response of 10 kHz, high sensitivity (gage factor of 175) and high signal to noise ratio (15:1). While their miniature size allows for localized measurement of strain mounting and wiring these sub-miniature strain gages require special attention and skills. The voltage from the strain gage was amplified and recorded concurrently with *v(t)*. Data acquisition was carried out at a rate 500 S/s with 8 bits of resolution.

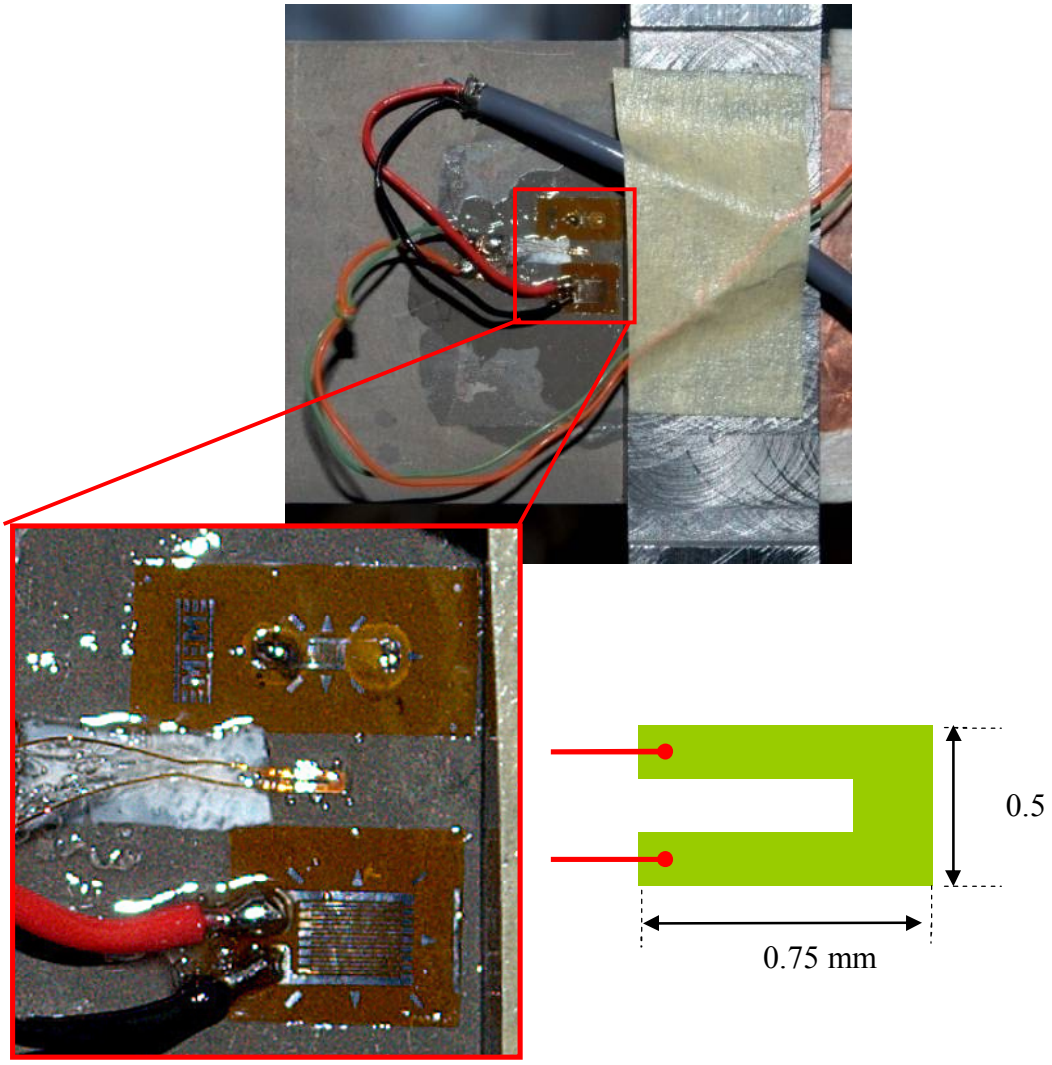

Figure 4: The strain gages attached on the piezoelectric beam. Only the central one was used while the other two were redundant (used for testing purposes).

4. Results and Discussion

A typical long-duration output voltage $v(t)$ measured at V_∞=28 m/s is shown in Fig. 5a; a portion of the same signal is shown in the inset Fig. 5b. The corresponding frequency spectrum is shown in Fig. 5c. The maximum amplitude of the signal is about 20 volts. Of interest is the modulated behavior of the signal which is due to multiple contributing components with frequencies close to each other. Apparently the vibration at

high flow speeds does not have a single harmonic component and it exhibits a beating pattern which is caused by slightly irregular shedding frequency according to our previous work [2]. The spectrum was computed by taking the FFT of the signal, using rectangular binning windows of 1000 data points with 50% overlap and resulted in a frequency resolution of 0.5 Hz. The highest peak in the spectrum at 45.5 Hz corresponds to the first natural frequency of the piezoelectric beam with the attached cylinder. A second peak can be also identified at 210Hz, while the second natural frequency is calculated to be around 290 Hz.

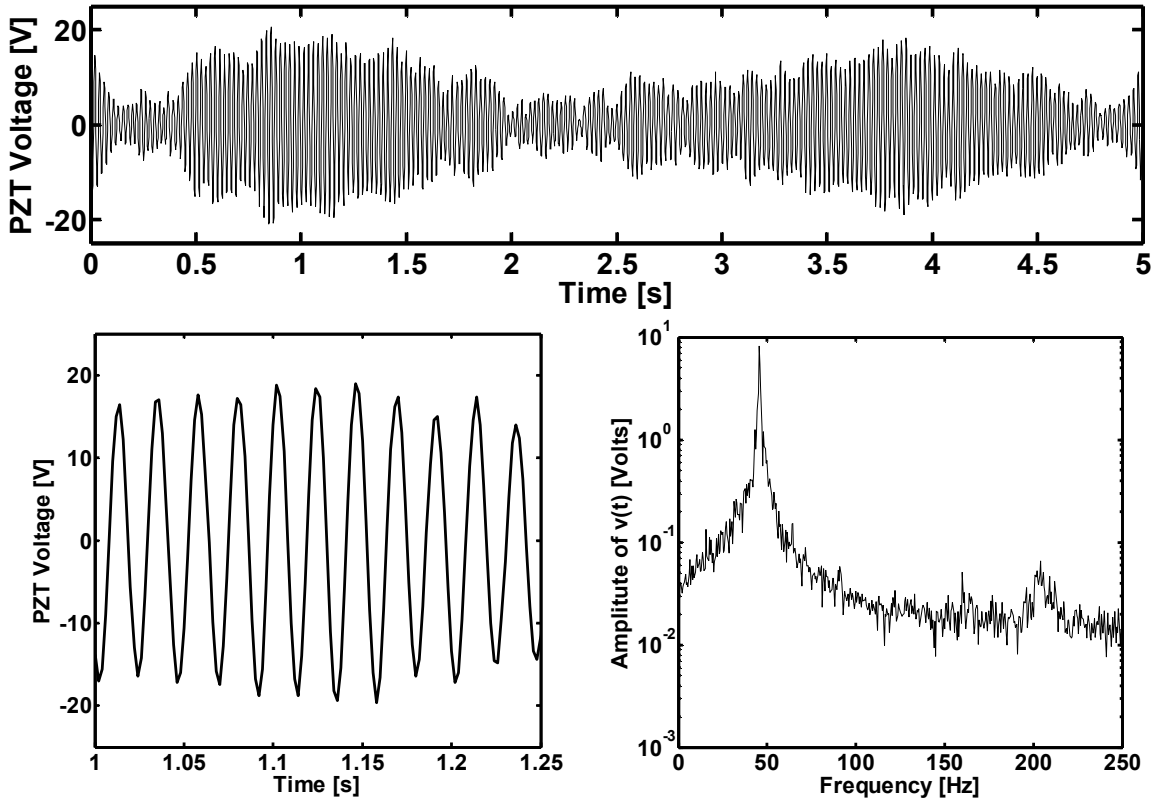

Figure 5: a) Long and b) short duration voltage signal at V_∞=28 m/s and c) its corresponding frequency spectrum

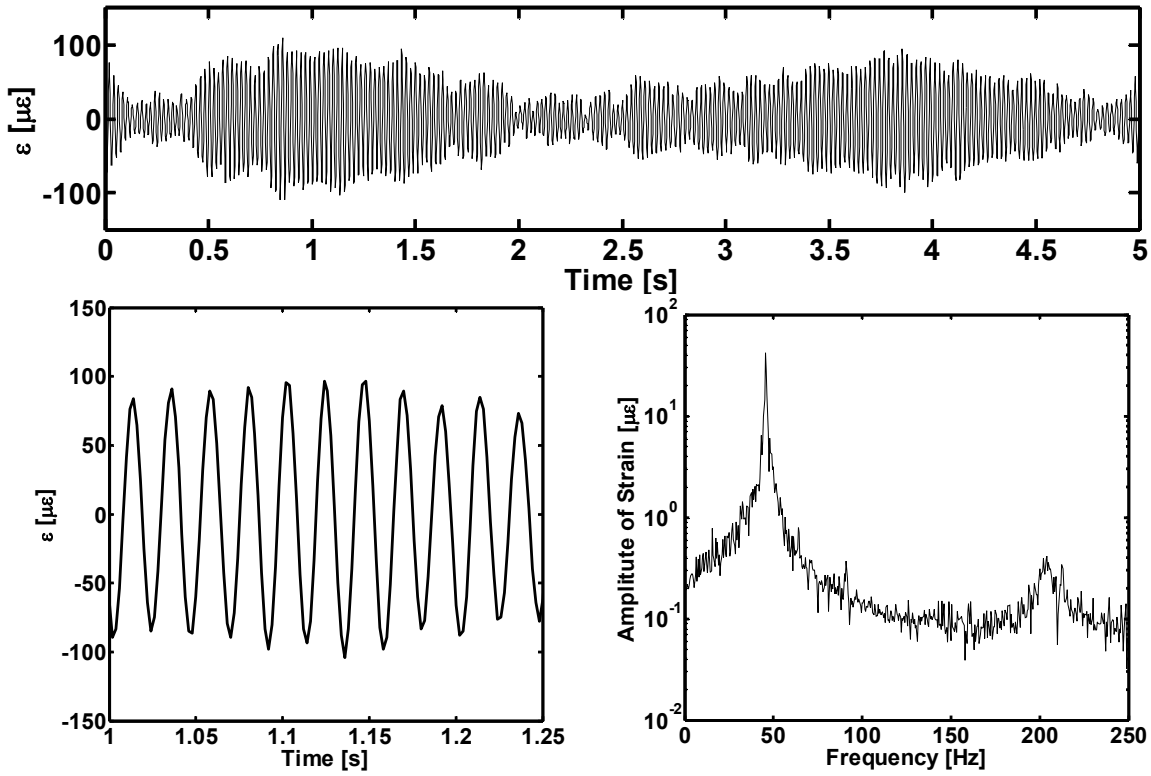

Figure 6: a) Long and b) short duration measured strain at V_∞=28 m/s and c) its corresponding frequency spectrum.

Figures 6a and 6b show long and short duration parts of the measured strain signal $\varepsilon(\tau)$ while its corresponding frequency spectrum calculated in the same way as that of $v(t)$ is shown in Fig. 6c. Note that the strain at the measured location barely exceeds 100με while the strain exactly at the clamping line is expected be somehow higher. The maximum allowable strain on the PZT beam which is likely to cause brittle fracture is approximately 500 με with a reasonable safety margin, so that much more bending is allowable and therefore more power can be extracted from this beam under higher excitation forces. Note that the output voltage and the strain signals are highly correlated while their frequency spectra are very similar with the amplitude peaks at the same frequencies. The output voltage of our generator is, in general, a result of multi mode vibration patterns present in the piezoelectric material which are best characterized by the

strain signal. The fact, however, that only one dominant mode, i.e. the first one, is present in the strain signal suggests that no charge cancellation has taken place in the present configuration with the current electrodes locations.

Further evidence of the high degree of correlation between the strain and the output voltage is shown in the coherence function defined as

$$Chr(f) = \frac{C_{XY}(f)}{[C_{XX}(f)C_{YY}(f)]^{1/2}} \tag{2}$$

where C_{XY} is the cross power spectral density between signals *X(t)* and *Y(t)* and *f* is the frequency. Figure 7 shows the coherence between the strain and the voltage output signals. The two signals are perfectly correlated with each other with *Chr* close to 1 throughout the frequency range from 0 to 65 Hz which contains the first mode of vibrations at 45.5 Hz. *Chr* subsequently drops to values less than 0.50 in the range of 100 Hz to 190 Hz. There is also a high correlation between the two signals around 210 Hz.

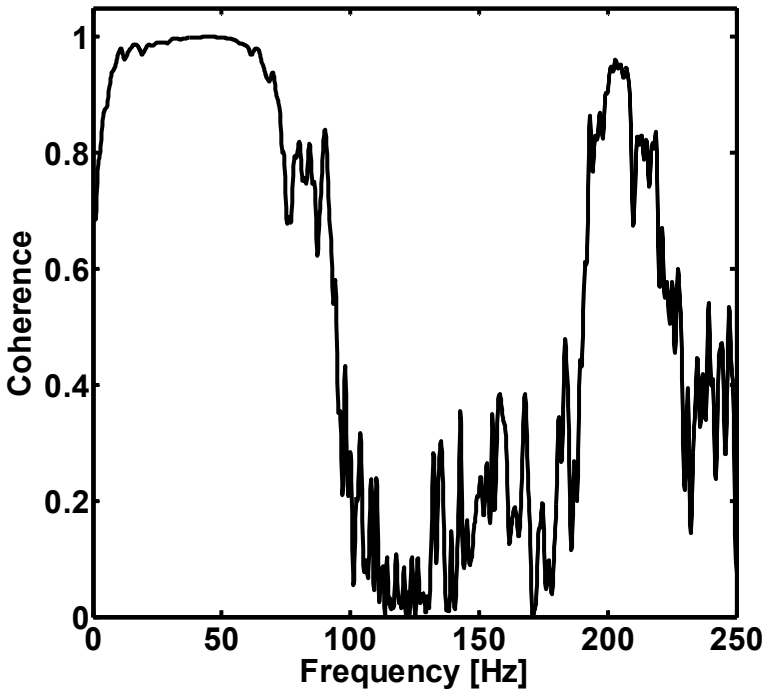

Figure 7: Coherence between strain and voltage output signals.

The average power over a length of time T was calculated by

$$P = \frac{1}{T}\frac{1}{R}\int_0^T v^2 dt \tag{3}$$

Figure 8 shows the variation of measured power with the flow velocity for three different values of load resistance R. The maximum power P=0.24mW was obtained at V_∞=28 m/s by using a load resistance of R=300kΩ. It appears that the power peaks around V_∞=26 m/s for R=33kΩ and R=3.3MΩ. The decrease in the slope of the power curve for R=300kΩ however, suggest that such a peak is likely to occur at velocities V_∞>28m/s, a value which was beyond the capability of the present wind tunnel setup. It should be noted that the maximum power occurs at a velocity nearly five times the estimated value of 5.8 m/s. There are several possible explanations for this disagreement. Firstly, the St may be actually much lower than the earlier estimation of 0.15. Secondly, although the piezoelectric generator is operated at off-resonance conditions, the power generated at a higher speed can be more than that generated at resonant speed due to increased magnitude of the aerodynamic lift forces. This sort of a response is quite different than other common sources of vibration where the magnitude of the vibration generally decreases as the frequency increases. Therefore such piezoelectric harvesters from fluid flow have an intriguing response that needs to be investigated further.

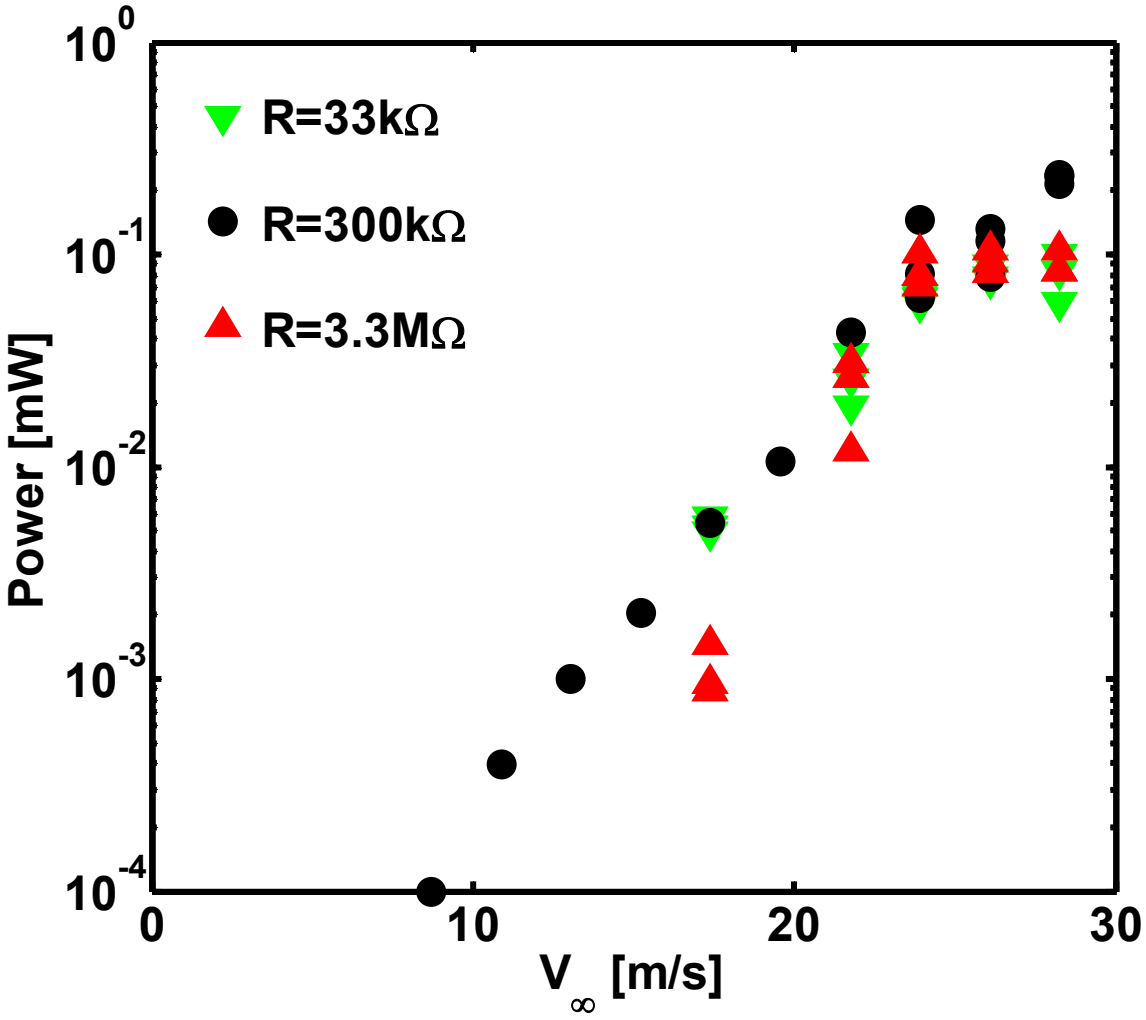

Figure 8: The variation of the average electrical power with the incoming flow velocity for various load resistances. Notice the scatter of the data at the high velocities.

5. Conclusions

A novel self excited piezoelectric energy harvester has been shown to work in steady, uniform flows. By attaching a circular cylinder to the upstream tip of a bimorph PZT cantilever beam, unsteady aerodynamic forces can be generated during the alternating vortex shedding from the surface of the cylinder. The new harvester has been tested in a narrow wind tunnel and the output voltage and strain on the surface of the beam have been measured. The maximum power generated by the harvester was

estimated to be around 0.24mW at maximum strain levels around $100\mu\varepsilon$. This level of straining is quite small compared to the PZT damage limit of $500\mu\varepsilon$ so it can be expected that the full power potential is not reached and can be increased to a level close 1 mW by a careful optimization of the dimensions, shapes and stiffness of the harvester elements. Power levels of 1mW would allow for the continuous operation of a wireless sensor node.

The present limited experimental results have shown that the new configuration holds some promises to work as a fully self-sustained and self-excited energy harvester. It will be further tested in a modified arrangement with the aim of studying the vortex shedding from the wake of the cylinder and the effect of the splitter plate and piezoelectric generator holder on suppressing this phenomenon. Additional challenges associated with the future work is to demonstrate self-excited energy generation in a true three dimensional configuration and to achieve optimal operation at flow velocities lower than 28 m/s.

Acknowledgement

The work is sponsored by the Michael Pope Fund for Energy Research.

References

[1] Akaydın H. D, Elvin N. and Andreopoulos Y., 2010, "Energy Harvesting from Highly Unsteady Fluid Flows Using Piezoelectric Materials" Journal of Intelligent Material Systems and Structures, doi:10.1177/1045389X10366317

[2] Akaydın H. D., Elvin N. and Andreopoulos Y., 2010, "Wake of a cylinder: A paradigm for energy harvesting with piezoelectric materials" Experiments in Fluids: Volume 49, Issue 1, Page 291-304.

[3] Anton S. R and Sodano H. A., 2007, "A review of power harvesting using piezoelectric materials (2003–2006)" Smart Materials and Structures, 16: R1-R21

[4] Sodano HA, Inman DJ and Park G, 2004, "A Review of Power Harvesting from Vibration using Piezoelectric Materials," The Shock and Vibration Digest, 136:197-205

[5] Allen, J.J. and Smits, A.J. 2001. ''Energy Harvesting Eel,'' Journal of Fluids and Structures, 15:629_640.

[6] Taylor, G.W., Burns, J.R., Kammann, S.M., Powers, W.B. and Welsh, T.R. 2001. ''The Energy Harvesting Eel: A Small Subsurface Ocean/River Power Generator,'' IEEE Journal of Oceanic Engineering, 26:539_547.

[7] Priya, S., Chen, C., Fye, D. and Zahnd, J. 2005. ''Piezoelectric Windmill: A Novel Solution to Remote Sensing,'' Japanese Journal of Applied Physics, 44:L104_L107

[8] Robbins, W.P., Marusic, I., Morris, D. and Novak, T.O. 2006.''Wind-generated Electrical Energy using Flexible Piezoelectric Materials,'' Proceedings of ASME International Mechanical Engineering Congress and Exposition, IMECE (2006) 5-10 November, Chicago, Illinois.

[9] Li, S., Xi'an, S. C., Lipson, H. "Vertical-Stalk Flapping-Leaf Generator for Wind Energy Harvesting," 2009, Proceedings of the ASME Conference on Smart Materials, Adaptive Structures and Intelligent Systems SMASIS2009-1276 September 20-24, Oxnard, California, USA

[10] Erturk, A., Inman, D. J. 2009, "An experimentally validated bimorph cantilever model for piezoelectric energy harvesting from base excitations," Smart Materials and Structures 18 (2009) 025009, doi:10.1088/0964-1726/18/2/025009

[11] Unal, M.F. and Rockwell, D. 1988b. ''On Vortex Formation from a Cylinder. Part II: Control by Splitter-Plate Interference,'' Journal of Fluid Mechanics, 190:513_529.

[12] Nakamura, Y., 1996, "Vortex Shedding From Bluff Bodies With Splitter Plates," Journal of Fluids and Structures 10, 147 – 158.

Chapter 5

Performance of a Self-Excited Fluidic Energy Harvester

Hüseyin Doğuş Akaydın, Niell Elvin, Yiannis Andreopoulos

Published on 24 January 2012 in

Journal of Smart Materials and Structures , 21(2):025007

Abstract

The available power in a flowing fluid is proportional to the cube of its velocity, and this feature has the potential of generating substantial electrical energy by exploiting the direct piezoelectric effect. The present work is an experimental investigation of a self-excited piezoelectric energy harvester subjected to a uniform and steady flow. The harvester consists of a cylinder attached to the free end of a cantilevered beam, which is partially covered by piezoelectric patches. Due to fluid-structure interaction phenomena, the cylinder is subjected to oscillatory forces, and the beam is deflected accordingly causing the piezoelectric elements to strain and thus develop electric charge. The harvester was tested in a wind tunnel and it produced approximately 0.1 mW of non-rectified electrical power at a flow speed of 1.192 m/s. The aeroelectromechanical efficiency at resonance was calculated to be 0.72%, while power per device volume was 23.6 mW/m^3 and power per piezoelectric volume was 233 W/m^3. Strain measurements

were obtained during the tests and were used to predict the voltage output by employing a distributed parameter model. The effect of non-rigid bonding on strain transfer was also investigated. While the rigid bonding assumption caused a significant (>60%) overestimation of measured power, a non-rigid bonding model gave a better agreement (<10% error).

Keywords: piezoelectric energy harvesting, fluid flow, strain transfer, non-rigid bonding effects, aeroelectromechanics, fluid-structure interaction, flow induced vibrations, vortex shedding

1. Introduction

Piezoelectric energy harvesting has been a prolific field of research over the past decade, with the major focus being on converting ambient structural vibrations into electric power [1 and 2]. The potential of fluid flow for piezoelectric energy harvesting has until recently received only limited attention. Interested readers are referred to a recent review on piezoelectric energy harvesting from fluid flow present in [3]. In our previous work, the potential of using fluctuations in the flow to induce time-dependent strains on unimorph piezoelectric beams for electrical energy generation was demonstrated [4-5]. In that configuration, the piezoelectric cantilever beam vibrates under resonant or random excitation already present in the upstream flow. The present study describes a new harvester configuration that can also operate in steady and uniform flows, i.e. flows which do not contain any temporal or spatial fluctuation upstream of the harvester.

The bulk mechanical power available in uniform and steady fluid flow is proportional to the cube of the flow speed [6]:

$$\overline{P}_{\mathrm{f}} = \frac{A_{\mathrm{f}}}{2}\rho U_{\infty}^{3} \tag{1}$$

where A_{f} is the frontal area of the harvester in operation, ρ is the density of the fluid and U_{∞} is the freestream speed (i.e. speed of the oncoming flow). For example, for an airflow of 1 m/s (typical for HVAC - Heat Ventilation and Air Conditioning systems) the available mechanical power is about 0.6 W/m^2, while airflow of 10 m/s speed (typical for wind power generation) carries about 600 W/m^2.

The direct piezoelectric effect is the generation of electric charge by a material under an applied strain. However the applied strain must be time-dependent to generate an electric current. The current generated is proportional to the rate of change of strain and the piezoelectric coupling coefficient. Two common engineering materials with strong piezoelectric properties are PZT (Lead Zirconate Titanate) and PVDF (Polyvinylidene Fluoride). While PVDF is more flexible than PZT, it has a smaller piezoelectric coupling coefficient.

Time dependent mechanical forces in a structure immersed in a flow can be generated either by: (a) velocity unsteadiness upstream in the flow, or (b) the mutual interaction of the structure and the fluid in an otherwise steady and uniform flow. As a result, time-dependent mechanical strains are developed on the body of the structure. Fluctuation of the strain can be converted in electrical power by means of the direct piezoelectric effect. The “aeroelectromechanical efficiency” of the harvester is defined as

$$\eta_{\text{aem}} = \frac{\bar{P}_{\text{e}}}{\bar{P}_{\text{f}}} \tag{2}$$

where $\bar{I}_{\text{e}}$ is the average electrical power harvested. Aeroelectromechanical efficiency can be expressed as multiplicative terms

$$\eta_{\text{ame}} = \eta_{\text{ae}}\eta_{\text{em}} \tag{3}$$

where η_{ae} is "aeroelastic efficiency" and η_{em} is "electromechanical efficiency". In this context, η_{ae} refers to conversion of the bulk flow power to mechanical vibration power ($\bar{P}_{\text{m}}$):

$$\eta_{\text{ae}} = \frac{\bar{P}_{\text{m}}}{P_{\text{f}}} \tag{4}$$

η_{em} refers to conversion of mechanical vibration power to electrical power, and is given by

$$\eta_{\text{em}} = \frac{\bar{P}_{\text{e}}}{\bar{P}_{\text{m}}} \tag{5}$$

The harvested electrical energy could be used for powering small electronic devices such as sensors and wireless transmitters to measure the flow rate, pressure, or temperature of the fluid. Such a self-charging capability makes it possible to develop untethered sensor nodes that do not require any wired connection or battery recharging/replacement. Such a technology could also significantly reduce the installation and maintenance costs of a metering network, which may include tens to hundreds of such sensor nodes in a typical HVAC system or process plant.

One of the methods to create the oscillatory forces needed to drive a piezoelectric harvester in a steady and uniform flow is to place bluff bodies upstream of the harvester.

At a certain flow speed, vortices start to form on the surfaces of a bluff body. As the vortices shed from the body, they travel downstream in the wake and form a so-called "Karman Vortex Street". The frequency of the vortex shedding, f_s, can be calculated from

$$f_s = St\frac{U_\infty}{d} \tag{6}$$

where d is a suitable characteristic length and St is the Strouhal number [6]. Strouhal number varies significantly depending on the Reynolds number defined as

$$Re = \frac{\rho U_\infty d}{\mu} \tag{7}$$

where μ is dynamic viscosity of the fluid and for a circular cylinder, d is the diameter [6].

A flexible, unimorph piezoelectric (PVDF) beam in the wake of a circular cylinder was investigated in our previous work [4-5]. In that configuration, the vortices shed from the cylinder created a pressure difference across the beam that results in a net force bending the beam in alternating directions. The maximum power was harvested when the vortex shedding frequency matched the first natural frequency of the beam. The aeroelectromechanical efficiency of the harvester was η_{aem}=0.0035%. The efficiency of the electromechanical conversion was estimated to be η_{em}=11% while the aeroelastic efficiency η_{ae} was only about 0.032%. It was thus concluded that the major portion of the losses took place in aeroelastic conversion, i.e. the creation of oscillatory motion of the beam from the uniform fluid flow.

Another method to induce oscillatory motion in the generator is by direct utilization of the forces created on the bluff body itself. Vortex shedding causes an asymmetry in pressure distribution on the surface of the bluff body, which results in time-dependent forces acting on the body. If the bluff-body is attached to the tip of an elastic

beam (for example, a cylinder attached to the tip of a cantilever), these vortex-induced forces will cause oscillatory deflection in the generator. A flow visualization photo obtained in our investigations using this configuration is shown in figure 1. The deflected beam, the cylinder attached to the tip of the beam and the vortex street in the wake are clearly depicted in this figure. Such a configuration can self-start and sustain the necessary oscillations under uniform and steady flow conditions. In addition to this advantage, such a harvester will potentially operate at a lower flow speed and have higher aeroelastic efficiency for the same value of $\bar{I}_c$, as indicated by equations (1) and (2) .

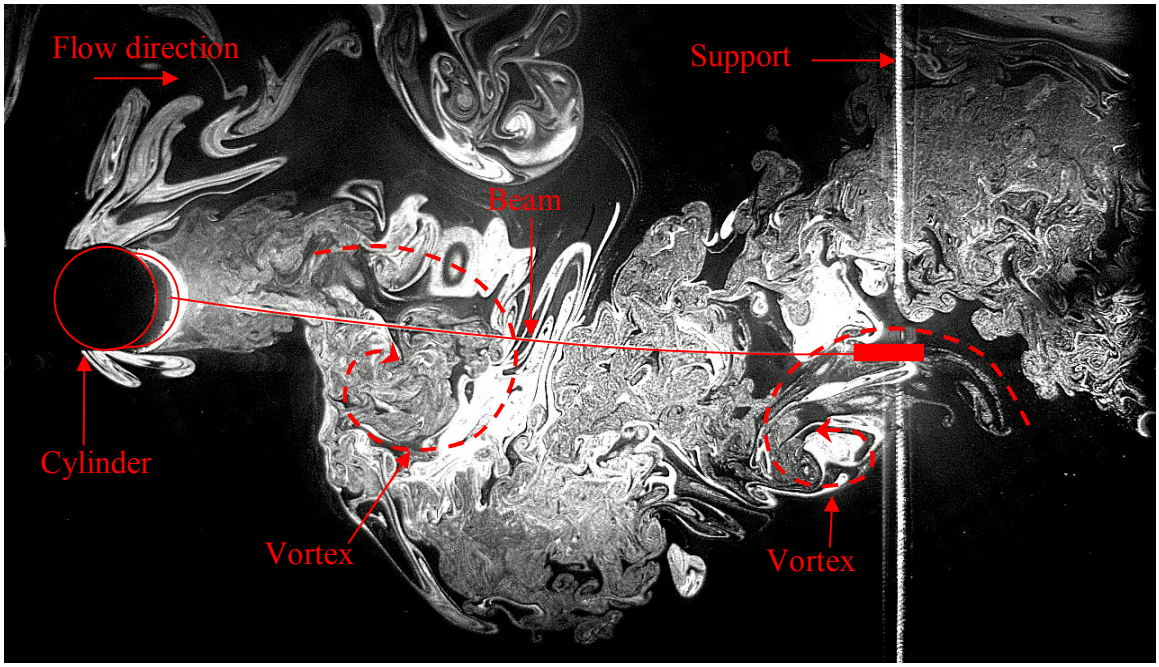

Figure 1. Flow visualization for the self-excited harvester. Illumination is provided by a laser sheet and the images were acquired by a high frame-rate digital camera.

A complete mathematical description of the behavior of a piezoelectric structure immersed in a fluid flow is quite challenging due to the three-way coupling between the fluid dynamics phenomena, its structural response and the generator's electrical behavior. Consideration of the mutual interaction between these three domains ideally requires an

"aeroelectromechanical" model of the system, i.e. a coupled solution of the system of the governing equations of the fluid flow, the structural dynamics, and the associated electrical field [4-5]. The goal of this paper is to introduce a novel flow energy harvester, predict its power through electromechanical modeling, and validate the results experimentally. The development of a fully-coupled model to predict the aeroelastic forces is left for a subsequent article.

2. The present configuration and the experimental setup

The present study explores a particular case where the bluff body is a finite hollow circular cylinder as shown in figure 2. The cylinder is attached to the free end of a cantilevered beam. The beam consists of an aluminum shim with piezoelectric patches bonded near the clamped end. The hollow cylinder has an outer radius r_o, inner radius r_i and width b_c. Both ends of the cylinder are covered. The beam has a length l_s, width b_s and thickness h_s. The flow direction is from the free end to the clamped end of the beam. The aerodynamic forces on the cylinder are resolved into time-dependent lift (L) and drag (D) components. The aerodynamic moment created on the cylinder is M_a. While the lift force varies around a mean value of zero, drag force varies around a positive value at twice the lift force frequency. Some test results obtained on a similar configuration with b_c/b_s=1.00 b_c/r_o=1.25 and l_s/r_o=2.5 were published earlier in [7], from which it was concluded that the ratios b_c/b_s and b_c/r_o have to be increased in order to reduce the adverse effects of splitter plate [8] and finite length on vortex shedding. In addition, the stiffness of the beam should be low enough to lock-in the flow-induced vibrations. This is

achieved by increasing l_s/r_o. By choosing a longer cylinder and a shim in the present study these ratios were increased to b_c/b_s=6.25, b_c/r_o=10.2 and l_s/r_o=13.3.

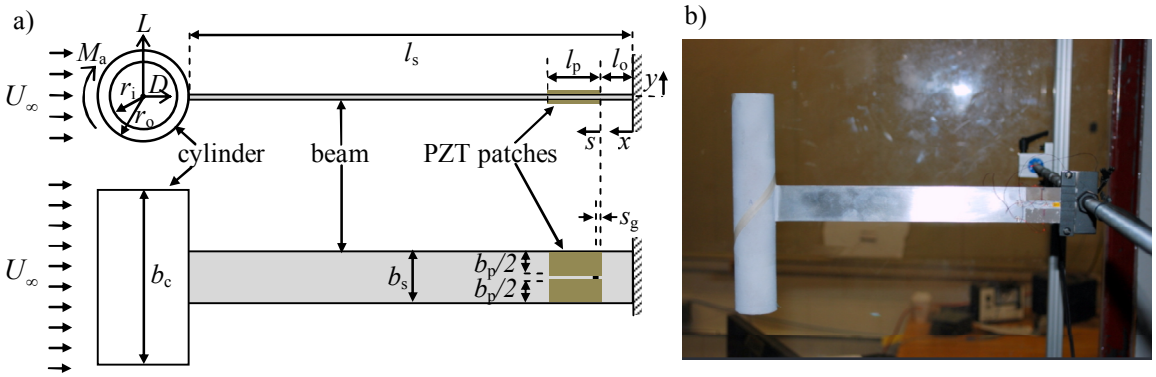

Figure 2. a) Top and side views of the self-excited harvester. b) Harvester installed in the wind tunnel.

In order to generate electrical charge, four PZT patches (Piezo Systems, Inc., model T110-A4E-602, two on each face) were bonded near the base of the shim forming a bimorph bender (figure 3). Each patch had a length l_p, thickness h_p and width $b_p/2$ where b_p is the combined width of two patches on one face. A small offset of l_o=0.5 mm between the piezoelectric elements and the clamp was provided to prevent the piezoelectric elements from touching the jaws of the clamp; s is the local coordinate along the patched section starting at $x=l_o$. Pertinent properties of the harvester components are given in table 1.

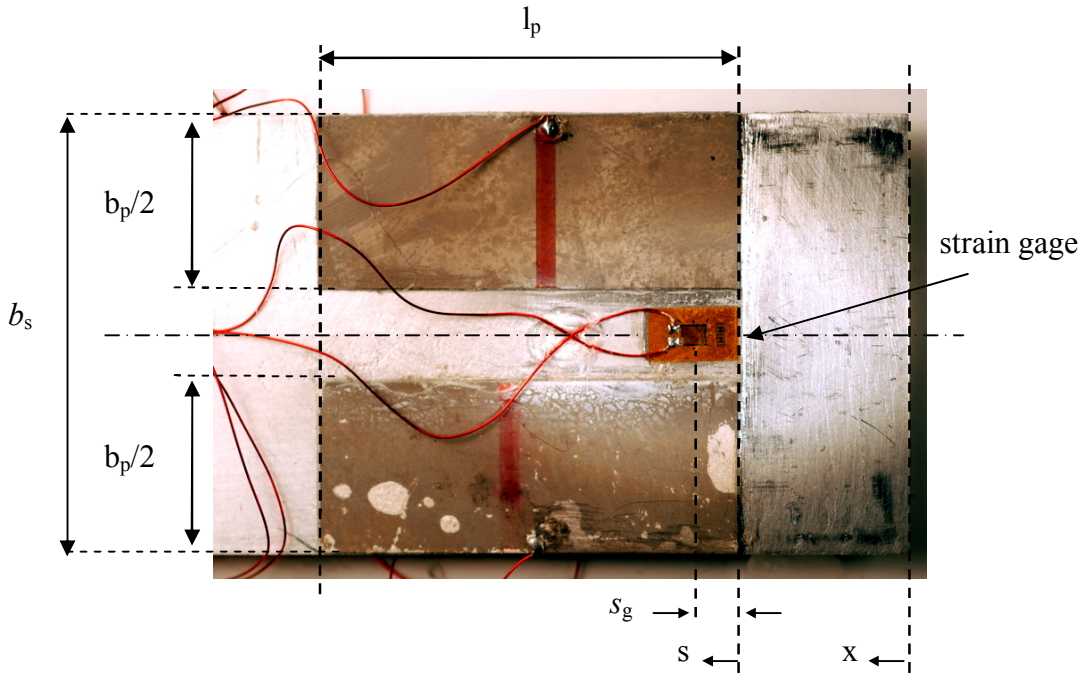

Figure 3. Close-up view of patches and the strain gage. The strain is sensed by the resistor grid visible in the center of the gage.

Table 1. Dimensions and properties of the harvester components.

Dimensions and Properties	PZT elements	Shim	Cylinder
Length, l_p, l_s [mm]	31.8	267	-
Width, $b_p/2$, b_s, b_c [mm]	12.7	32.5	203
Thickness, h_p, h_b [mm]	0.267	0.635	-
Radius, r_o, r_i [mm]	-	-	19.8, 19.2.
Material	PZT-5A	Aluminum (Alloy 2024)	Cardboard
Mass density, ρ [kg m^{-3}]	7800	2730	-
Mass, m_p, m_s, m_c [gr]	1.68	16	16
Young's Modulus, Y_p, Y_s [GPa]	66	73	-
Piezoelectric Constant d_{31} [pm V^{-1}]	-190	-	-
Permittivity at constant strain $\bar{\kappa}_{33}^{S}$ [nF m^{-1}]	13.28	-	-
Capacitance (calculated, measured) C_p [nF]	20.1, 20.3	-	-

The strains on the top and bottom surfaces of the shim near the clamped base were also measured using strain gages. The strain gages (model EA-06-062AP-120 from Vishay Micro-Measurements) were centered at s_g=3.92 mm along the midline (figure 3). To amplify the signal and to reduce thermal effects and bridge non-linearity, the strain gages were used as two active arms of a Wheatstone bridge. The gages were calibrated by applying a prescribed deflection to the tip of the beam and calculating the corresponding strain using Euler-Bernoulli beam theory. The gage factor found by this in-situ calibration method closely matched with that specified by the manufacturer. Therefore, the gage readings accurately indicate the strain on the shim through the tests.

Data acquisition was performed using a digital oscilloscope (Tektronix model DP2024) with high impedance (R_O=10MΩ) probes. The strain signal was amplified 1000 times using a low-noise preamplifier (Stanford Research Systems model SR560). Signals for the wind tunnel tests were sampled at a rate of 1.25kS/s for a duration of 100 seconds and band-pass filtered between 0.03 to 300 Hz before digitization. For free vibration tests sampling was done for 20 seconds at a rate of 6.25kS/s. Free vibration signals were further band-pass filtered between 0.3 to 30 Hz with a 4th order Butterworth filter during data processing. Software filtering was performed in the forward and reverse directions in time to eliminate any phase-shift caused by filtering.

3. Electromechanical Model

In the current configuration, the two piezoelectric elements on each face of the shim are bonded in the same poling direction and connected in parallel for collecting charges generated by bending strain (Figure 4a). The piezoelectric elements were

modeled as a current source in parallel with capacitors (figure 4b). Two elements on each face of the beam were treated as a single element with a total capacitance of

$$C_{\mathrm{p}} = \frac{\bar{\kappa}_{33}^{\mathrm{S}} b_{\mathrm{p}} l_{\mathrm{p}}}{h_{\mathrm{p}}} \tag{8}$$

where b_{p} is the combined width of the piezoelectric elements on one face of the shim, $\bar{\kappa}_{33}^{\mathrm{S}}$ is permittivity under constant strain with the assumption of plane-stress conditions. The equivalent capacitance of both faces is then $\bar{C}_{\mathrm{p}} = C_{\mathrm{p}}/2$. Thus the equivalent capacitance on one face is $\bar{C}_{\mathrm{p}}$ =20.1 nF, although the measured value of $\bar{C}_{\mathrm{p}}$ =20.3 nF is used throughout this analysis. Note that R_{L} is the load resistance in parallel with the oscilloscope impedance, R_{O}. Total resistance R is then

$$R = \left(\frac{1}{R_{\mathrm{O}}} + \frac{1}{R_{\mathrm{L}}} \right)^{-1} \tag{9}$$

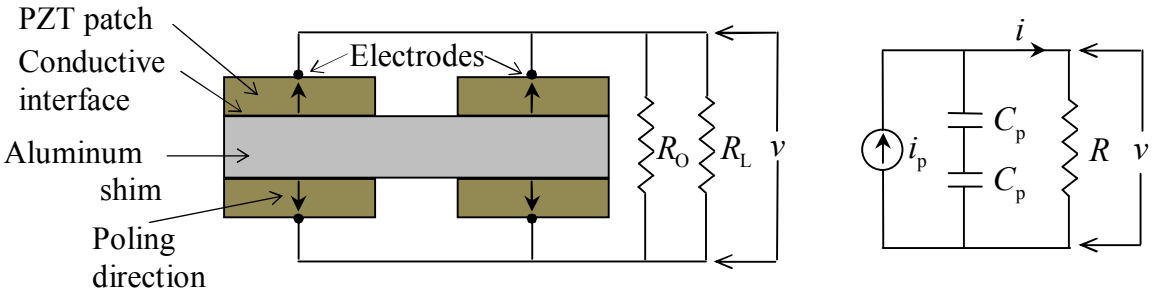

Figure 4. a) The electrode configuration for patches b) Corresponding circuit diagram.

The circuit equation is found by using Kirchhoff's Current Law

$$\bar{C}_{\mathrm{p}} \frac{\mathrm{d}v(t)}{\mathrm{d}t} + \frac{1}{R} v(t) = i_{\mathrm{p}}(t) \tag{10}$$

The piezoelectric current is related to deformation by

$$i_{\mathrm{p}}(t) = -d_{31} Y_{\mathrm{p}} b_{\mathrm{p}} \frac{\partial}{\partial t}\left(\int_{s=0}^{l_{\mathrm{p}}} \varepsilon_{\mathrm{pc}}(s,t)\,\mathrm{d}s \right) \tag{11}$$

where d_{31} is the piezoelectric coefficient, Y_{p} is the elastic modulus of the piezoelectric material and $\varepsilon_{\mathrm{pc}}(s, t)$ is the time-dependent strain distribution at $y=h_{\mathrm{pc}}$, i.e. the half-thickness of a piezoelectric element [9-10]. Determination of $\varepsilon_{\mathrm{pc}}(s, t)$ requires some elaboration of stress transfer from the structural substrate (i.e. the shim) to the piezoelectric elements and is presented in the next section.

For free vibration of the shim in the first mode, the measured strain $\varepsilon_{\mathrm{g}}(t)$ can be expressed as

$$\tilde{\varepsilon}_{\mathrm{g}}(t) = \varepsilon_{\mathrm{g,max}} \exp\left[-\omega_1 t \left(\zeta_1 - \sqrt{\zeta_1^2 - 1} \right) \right] \tag{12}$$

where $\varepsilon_{\mathrm{g,\,max}}=\varepsilon_{\mathrm{g}}(t=0)$, ω_1 is the undamped frequency for the first bending mode and ζ_1 is the corresponding damping ratio which can be determined from free vibration tests. This strain expression allows the ODE in equation (10) to be analytically solved. The solution of equation (10) with the initial condition $v(t=0)=0$ is

$$v(t) = \frac{i_{\mathrm{p}}(t)}{\frac{1}{R} - \bar{C}_{\mathrm{p}} \omega_1 \left(\zeta_1 - \sqrt{\zeta_1^2 - 1} \right)} \tag{13}$$

The ratio of the voltage to average strain in the piezoelectric element is

$$H_{\mathrm{v\text{-}\varepsilon}} = \frac{v(t)}{\bar{\varepsilon}_{\mathrm{pc}}(t)} = \frac{d_{31} Y_{\mathrm{p}} b_{\mathrm{p}} l_{\mathrm{p}}}{\frac{1}{R\omega_1 \left(\zeta_1 - \sqrt{\zeta_1^2 - 1} \right)} - \bar{C}_{\mathrm{p}}} \tag{14}$$

where

$$\bar{\varepsilon}_{\mathrm{pc}}(t) = \frac{1}{l_{\mathrm{p}}} \int_{x=0}^{l_{\mathrm{p}}} \varepsilon_{\mathrm{pc}}(s,t)\,ds \tag{15}$$

For a forced harmonic vibration of constant amplitude, the measured strain expression becomes

$$\tilde{\varepsilon}_{\mathrm{g}}(t) = \left|\varepsilon_{\mathrm{g}}\right| \exp\left(j\omega_{\mathrm{F}} t\right) \tag{16}$$

where ω_{F} is the forcing frequency and $j = \sqrt{-1}$. Accordingly the voltage and its ratio to average strain are found as

$$v(t) = \frac{i_{\mathrm{p}}(t)}{\frac{1}{R} + j\omega_{\mathrm{F}} \overline{C}_{\mathrm{p}}} \tag{17}$$

and

$$H_{\mathrm{v\text{-}\varepsilon}} = \frac{v(t)}{\overline{\varepsilon}_{\mathrm{pc}}(t)} = -j\omega_{\mathrm{F}} \frac{d_{31} Y_{\mathrm{p}} b_{\mathrm{p}} l_{\mathrm{p}}}{\frac{1}{R} + j\omega_{\mathrm{F}} \overline{C}_{\mathrm{p}}} \tag{18}$$

The voltage signal leads the strain by the phase angle

$$\Phi_{v\text{-}\varepsilon} = \mathrm{Arg}\left(H\right) \tag{19}$$

The current over the resistor is always in phase with the voltage and is given by Ohm's law:

$$i(t) = \frac{v(t)}{R} \tag{20}$$

The instantaneous electrical power dissipated on the resistor is then

$$P_{\mathrm{e}}(t) = v(t) i(t) = \frac{v(t)^2}{R} \tag{21}$$

The electrical energy dissipated during a time interval $[t_0, t_1]$ is

$$E_{\mathrm{e}} = \int_{t_0}^{t_1} P_{\mathrm{e}} \mathrm{d}t \tag{22}$$

while the average power over the same interval is

$$\overline{P}_{\mathrm{e}} = \frac{E_{\mathrm{e}}}{t_1 - t_0} \tag{23}$$

Note that $\tilde{\varepsilon}_g$, i_{p}, i, v and P_{e} are complex-valued functions.

4. Strain transfer through the bonding layer

In energy harvesting applications, the piezoelectric patches are often bonded to the host structure using an adhesive agent. The strain developed on the surfaces is then transferred through a thin layer of adhesive material. The amount of the strain transfer depends on the relative thickness and rigidity of the adhesive layer as compared to the host structure and the piezoelectric patch. The strain transfer problem for the case of a composite cross section undergoing bending was investigated earlier in [11-16] with the assumption of uniform strain distribution through the thickness of the bonded patch, which is valid if the patch is much thinner and more compliant than the host structure. A finite element formulation and solution for a three dimensional patch is presented in [17]. A closed form analytical solution considering the variation of strain along the thickness of plates bonded to concrete beams was later proposed in [18]. In this section, a strain transfer model for the case of a PZT patch bonded to an aluminum shim of comparable thickness and elastic modulus is presented.

The strain distribution through the beam at a cross section with local coordinate s consisting of the shim and piezoelectric patches is shown in figure 5. If the adhesive layer had zero thickness and infinite shear strength, then the bonding would be rigid. In this rigid bonding case, the strain induced on the two bonded surfaces would be identical and the strain distribution would be ε_{r}. In practice however, there is some loss of rigidity

depending on the shear modulus (G_a), thickness (h_a) and uniformity of the adhesive layer. Non-rigid bonding lessens the strain transferred between the piezoelectric elements and the structural shim resulting in a jump from ε_{si} on the shim surface to ε_{pi} on the surface of the piezoelectric patch through the bonding interface.

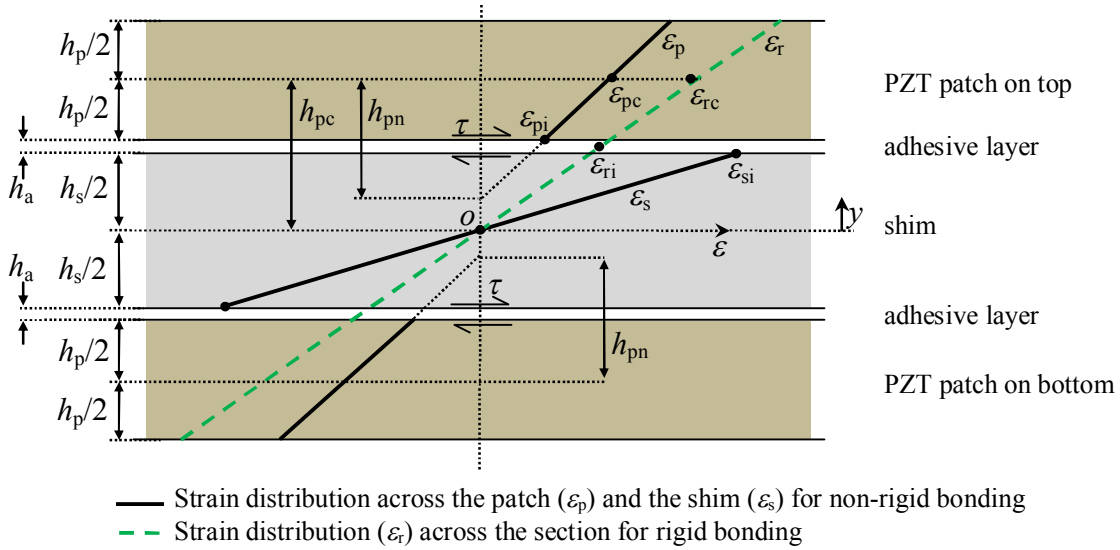

Figure 5. Strain transfer from shim to the piezoelectric patches. Subscript "s" is used for indicating "shim", "p" for piezoelectric patch, "a" for adhesive, "i" for "interface", "r" for "rigid" bonding assumption, "c" for "center" and "n" for neutral. Vertical axis y indicates the distance from the beam centerline while horizontal axis ε indicates the strain. Strains at particular points are indicated by solid dots.

In general, curvatures of the patches and the shim are not equal when bonding is non-rigid. In this case, the neutral axes (i.e. zero strain axes) of the patches do not coincide with that of the shim. The difference is more pronounced when the thicknesses of the patch and the shim are comparable. The distance from the centerline of a patch to its own neutral axis is denoted by h_{pn}. The distance from the center of a patch to the centerline of the cross section is denoted by h_{pc}. Due to symmetry, the neutral axis of the shim coincides with the centerline of the cross section. Also because of the symmetry, the top and bottom patches have the same h_{pn} and h_{pc} values. The strain distribution across

the cross section is thus symmetric around the origin "*o*" as shown in figure 5. Therefore, analysis of the strain transfer between the shim and one of the patches is sufficient. The strain distribution through the shim and the top patch are respectively

$$\varepsilon_{\mathrm{p}}(s,y)=\varepsilon_{\mathrm{pi}}(s)\left[1+\frac{y-h_{\mathrm{s}}/2}{h_{\mathrm{pn}}-h_{\mathrm{p}}/2}\right] \tag{24}$$

$$\varepsilon_{s}(s,y)=\varepsilon_{\mathrm{si}}(s)\frac{y}{h_{s}/2} \tag{25}$$

Note that since the shear modulus and thickness of the adhesive layer are usually very small compared to the sectional properties of the shim and piezoelectric elements, the rigidity of the adhesive layer and its effect on the bending strain distribution is ignored, i.e. $h_{\mathrm{a}}=0$ is used when finding the stiffness of and strain distribution through the cross section of the patch. The problem is thus to find $\varepsilon_{\mathrm{pi}}$, $\varepsilon_{\mathrm{si}}$ and h_{pn} under a given load on the shim with boundary conditions $\varepsilon_{\mathrm{p}}(0, y)=0$ and $\varepsilon_{\mathrm{p}}(l_{\mathrm{p}}, y)=0$.

For tip-forced vibrations around the first resonant mode, the dynamic mode shape of a shim with the cylinder and without patches is nearly the same as the static mode shape of the shim without the cylinder and patches. Therefore, it is assumed that a strain transfer analysis under static loading is applicable for the dynamic case and the added difficulty of modeling the dynamic behavior of a shim with non-rigidly bonded elements is thus avoided. The method presented in [13] was therefore extended to include the variation of strain along h_{p}.

The equilibrium of axial forces for the top patch and the adhesive layer result in two coupled ODEs: One for $\varepsilon_{\mathrm{pi}}$ and the other for the interfacial shear force, τ. For the shear force on the adhesive layer

$$\frac{\mathrm{d}\tau}{\mathrm{d}s} = \frac{G_\mathrm{a}}{h_\mathrm{a}}\left(\varepsilon_\mathrm{pi} - \varepsilon_\mathrm{si}\right) \tag{26}$$

where ε_si is strain on the surface of the shim. The horizontal balance of forces on a cross section of the patch requires

$$\tau = Y_\mathrm{p} \int_{y=\left(h_s/2\right)}^{y=\left(h_s/2+h_\mathrm{p}\right)} \frac{\partial \varepsilon_\mathrm{p}\left(s,y\right)}{\partial s}\mathrm{d}y \tag{27}$$

Assuming h_pn remains constant along the s-coordinate greatly simplifies the solution procedure while producing a reasonable strain distribution that satisfies the boundary conditions. This assumption gives

$$\frac{\mathrm{d}\varepsilon_\mathrm{pi}}{\mathrm{d}s} = \frac{\tau}{Y_\mathrm{p} h_\mathrm{pnp}} \tag{28}$$

where

$$h_\mathrm{pnp} = \frac{h_\mathrm{pn} h_\mathrm{p}}{h_\mathrm{pn} - h_\mathrm{p}/2} \tag{29}$$

It is now presumed that strains on the bonded surfaces develop quickly and bonding becomes rigid near the edges, i.e. towards the middle of the patch. In this case, the neutral axes of the patches and the shim are coincident for the bulk of the interface away from the edges, and assumption of h_pn=h_pc can reasonably be employed in equation (29). The local boundary conditions require $\varepsilon_\mathrm{pi}(0)$=0 and $\varepsilon_\mathrm{pi}(l_\mathrm{p})$=0. The solution of the system of equations (26) and (28) is then found to be

$$\varepsilon_\mathrm{pi} = \frac{\tau(0)}{Y_\mathrm{p}\gamma h_\mathrm{p}}\sinh\gamma s - \frac{G_\mathrm{a}}{Y_\mathrm{p}\gamma h_\mathrm{a} h_\mathrm{pnp}}\int_0^s \varepsilon_\mathrm{si}\sinh\gamma\left(s-\xi\right)\mathrm{d}\xi \tag{30}$$

$$\tau = \tau(0)\cosh\gamma s - \frac{G_\mathrm{a}}{h_\mathrm{a}}\int_0^s \varepsilon_\mathrm{si}\cosh\gamma\left(s-\xi\right)\mathrm{d}\xi \tag{31}$$

where

$$\gamma = \sqrt{\frac{G_a}{Y_p h_{pnp} h_a}} \tag{32}$$

and $\tau(0)$ is determined from the second boundary condition as

$$\tau(0) = \frac{G_a}{h_a \sinh \gamma l_p} \int_0^{l_p} \varepsilon_{si} \sinh \gamma \left(l_p - \xi\right) d\xi \tag{33}$$

Since ε_{pi} is not known *a priori*, a few iterations are required in order to obtain a converged solution. The calculation starts with an initial guess for the ε_{si} distribution which is used to calculate the ε_{pi} distribution (equations 30 to 33); ε_{si} is then corrected via the balance of bending moments. The total moment calculated at a cross section is

$$M_s(s) + 2M_p(s) = M_T(s) \tag{34}$$

where

$$M_s(s) = Y_s b_s \int_{-h_s/2}^{h_s/2} \varepsilon_s(s, y) y dy \tag{35}$$

$$M_p(s) = Y_p b_p \int_{h_s/2}^{h_s/2+h_p} \varepsilon_p(s, y) y dy \tag{36}$$

The moment at a cross section due to the loading conditions is given by

$$M_L(s) = M_a + L\left[r_o + l_s - l_o - s\right] \tag{37}$$

with the parameters defined in figure 2. If the total moment calculated at a cross section M_T is less (or more) than the moment load M_L carried at that section then ε_{si} is increased (or decreased) by

$$\varepsilon_{si,\,new} = \varepsilon_{si} \frac{M_T}{M_L} \tag{38}$$

The updated distribution of ε_{si} is iteratively used in the same procedure until M_T sufficiently converges to M_L. Each cross-section (i.e. shim without piezoelectric patches

and shim with piezoelectric patches) is divided in 1000 segments along their length. With the given geometric and material properties, the solution converges to a smooth strain distribution in less than 10 iterations.

For the present case, adhesive layer thickness is measured to be approximately h_a=25 μm. The value of G_a was then adjusted to obtain a consistent result with the strain measured by the gage, i.e. $\varepsilon_g=\varepsilon_{si}(s=s_g)$, in order find the unique solution for strain distribution. This condition is satisfied when G_a=86 MPa. Strain distributions at different values of G_a are shown in Figure 6. Note the reduction in strain transfer to the piezoelectric elements (ε_p) near the edges of the patch as G_a decreases.

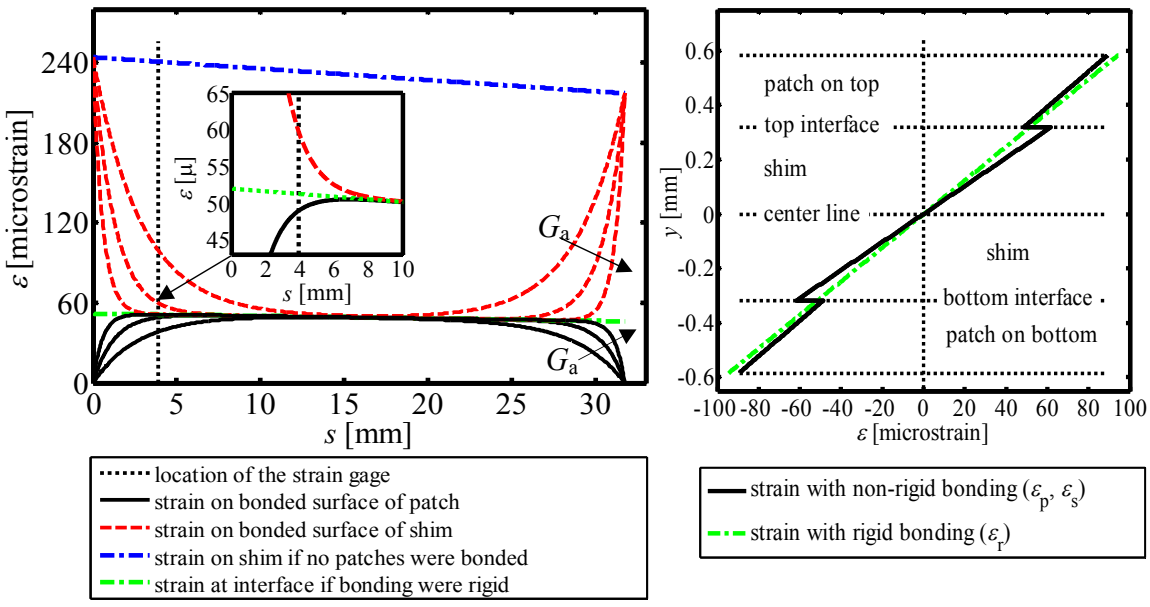

Figure 6. Strain distribution a) Along the length of the patched cross section for G_a=17 MPa, G_a=86 MPa and G_a=430 MPa and b) across the patched cross section at the gage location $s=s_g$.

The equivalent strain at the interface in the case of rigid bonding can be found from ε_g by

$$\varepsilon_{ri}(s_g)= \beta_{gage}\varepsilon_g \tag{39}$$

where β_{gage} is a transfer factor between the equivalent rigid bonding strain and the actual gage measurement. From the data in figure 6, β_{gage} is approximately 0.853. The rigid bonding strain along the patch is then linear and given by

$$\varepsilon_{ri}(s) = \varepsilon_{ri}(s_g)\left[\frac{\varepsilon_{ri}(l_p)}{\varepsilon_{ri}(s_g)} - \left(1 - \frac{\varepsilon_{ri}(l_p)}{\varepsilon_{ri}(s_g)}\right)\frac{l_p - s}{l_p - s_g}\right] \tag{40}$$

where the ratio $\varepsilon_{ri}(l_p)/\varepsilon_{ri}(s_g)$ is known from the loading conditions:

$$\frac{\varepsilon_{ri}(l_p)}{\varepsilon_{ri}(s_g)} = \frac{M_L(s = l_p)}{M_L(s = s_g)} \tag{41}$$

The ratio of the integrals of ε_{pi} and ε_{ri} over the length of the patch gives a correction factor to account for the strain distribution for non-rigid bonding:

$$\beta_{int} = \frac{\int_0^{l_p} \varepsilon_{pi}(s)\,ds}{\int_0^{l_p} \varepsilon_{ri}(s)\,ds} \tag{42}$$

From the data in figure 6a, this factor is found to be β_{int}=0.92. Since strain is distributed linearly across the thickness of the piezoelectric patches, the same correction factor applies for the integral of ε_{pc}. Thus the integral of time-dependent strain for rigid bonding can be corrected for non-rigid bonding as

$$\int_0^{l_p} \varepsilon_{pc}(s,t)\,ds = \beta_{int}\int_0^{l_p} \varepsilon_{rc}(s,t)\,ds \tag{43}$$

where

$$\varepsilon_{rc}(s,t) = \varepsilon_{ri}(s,t)\frac{h_{pn}}{h_{pn} - h_p/2} \tag{44}$$

The integral of ε_{pc} is then used in equation (11) to find i_p. Note that β_{gage} = 1 and β_{int} = 1 if bonding between the layers was assumed to be rigid.

It is worth mentioning that strain transfer effects on the measurements taken by properly attached strain gages are negligible. This is because strain gage foils ordinarily have much smaller length, width, thickness, and Young's modulus than those of the PZT patches and the shim. In addition, the actual sensing element (i.e. the resistor grid) on the gage foil is located in the middle of the gage foil, away from the edges. Therefore, the strain sensed by the gage is virtually the same as that develops on the attached surface. The fact that strain transfer to the strain gages can be ignored has been confirmed by applying the proposed strain transfer model and calculating the strain distribution on a patch having similar dimensions and compliance to the gage foil.

5. Free vibration tests

Free vibration ring-down tests were done to determine $\omega_1=2\pi f_1$ and ζ_1 in equation (12) by deflecting and releasing the tip of the beam. The same tip deflection was applied in each case; and the portion of the signal between the 20^{th} and 40^{th} cycles was used for all analyses. The first resonant frequency of the beam with the tip cylinder was calculated to be 2.93 Hz using modal analysis and not considering the patches. With the bonded piezoelectric patches, the resonant frequency increased to f_1=3.127 Hz. A range of resistance values were tested, from which it was found that R=2.46MΩ gave the maximum average electrical power output. For this value of load resistance, the measured strain ε_g and the fitted strain $\tilde{\varepsilon}_g$ are shown in figure 7a. The fitted strain expression is used in equation (11) to calculate the piezoelectric voltage given in equation (13). The calculated voltage signal is in very good agreement with the measured piezoelectric voltage signal as shown in figure 7b. In order to show the accuracy of the model, the

calculated and measured phase differences ($\Phi_{v\text{-}\varepsilon}$) are compared over the course of the 20 cycles. The measured strain, measured piezoelectric voltage and calculated piezoelectric voltage signals are scaled with their maximum values as $\varepsilon_g/\max(\varepsilon_g)$, $v_{meas}/\max(v_{meas})$ and $v_{calc}/\max(v_{calc})$, respectively. The scaled signals are then plotted together as shown in figure 8. The phase differences of calculated and measured voltages from the measured strain signal are in excellent agreement.

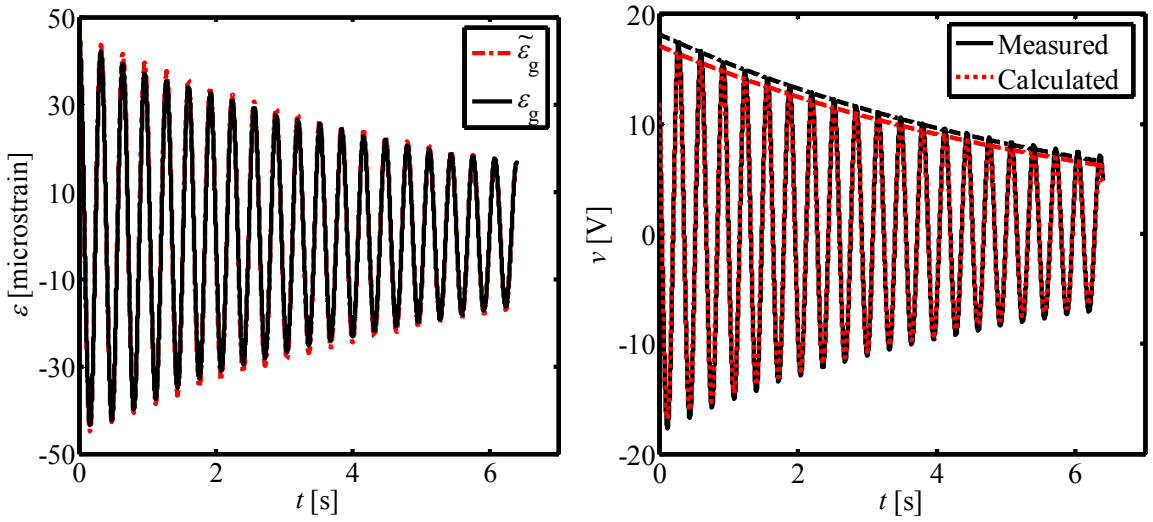

Figure 7. a) Comparison of measured strain (ε_g) and fitted strain ($\tilde{\varepsilon}_g$) using equation (12) with parameters ω_1 and ζ_1 determined from free-vibration tests. b) Comparison of measured piezoelectric voltage signal and calculated piezoelectric voltage signal using equation (13)

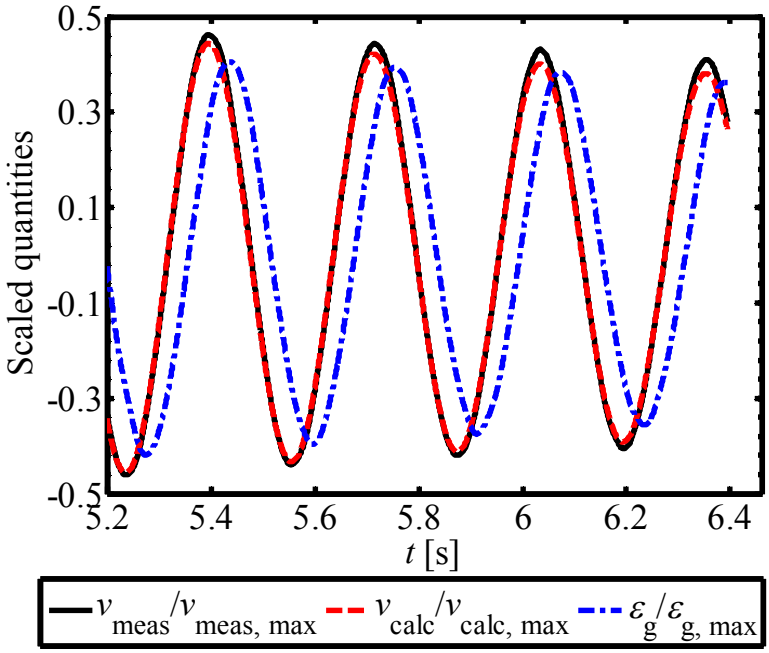

Figure 8. Comparison of the phase differences of the measured and calculated piezoelectric voltage signals from the measured strain signal.

Figure 9 shows the response of the harvester to different R_L values under free-vibration conditions. Note in figure 9a that the rigid bonding assumption results in more than 60% overestimation in power. When non-rigid bonding is considered, the power is underestimated by about 10%. Complimentary to figure 8, there is a very good agreement in measured and calculated phase differences for different resistances as shown in figure 9b. The first resonant frequency and damping ratio were found using the actual strain gage measurements, i.e. $\varepsilon_g(t)$. The first resonance frequency increases with resistance from short-circuit to open-circuit conditions as shown in figure 9c. This increase is relatively small (about 0.5% of the short-circuit value). The change in the damping ratio from short-circuit to open-circuit conditions is however more pronounced (about 24% of the short-circuit value) as shown in figure 9d. The deviations of the data points near $R\approx10^4$ and $R\approx10^5$ are within 0.2% uncertainty and probably due to experimental errors. It should also be mentioned that a ±5% change in s_g causes about ±10% difference in G_a

around 86MPa when matching the calculated strain versus the measured strain. With the adjustment made in G_a, the variation in $\overline{P}_e$ remained less than 0.5%. If s_g is changed by ±5% but G_a is left unchanged, then the variation in $\overline{P}_e$ is less than ±2.5%.

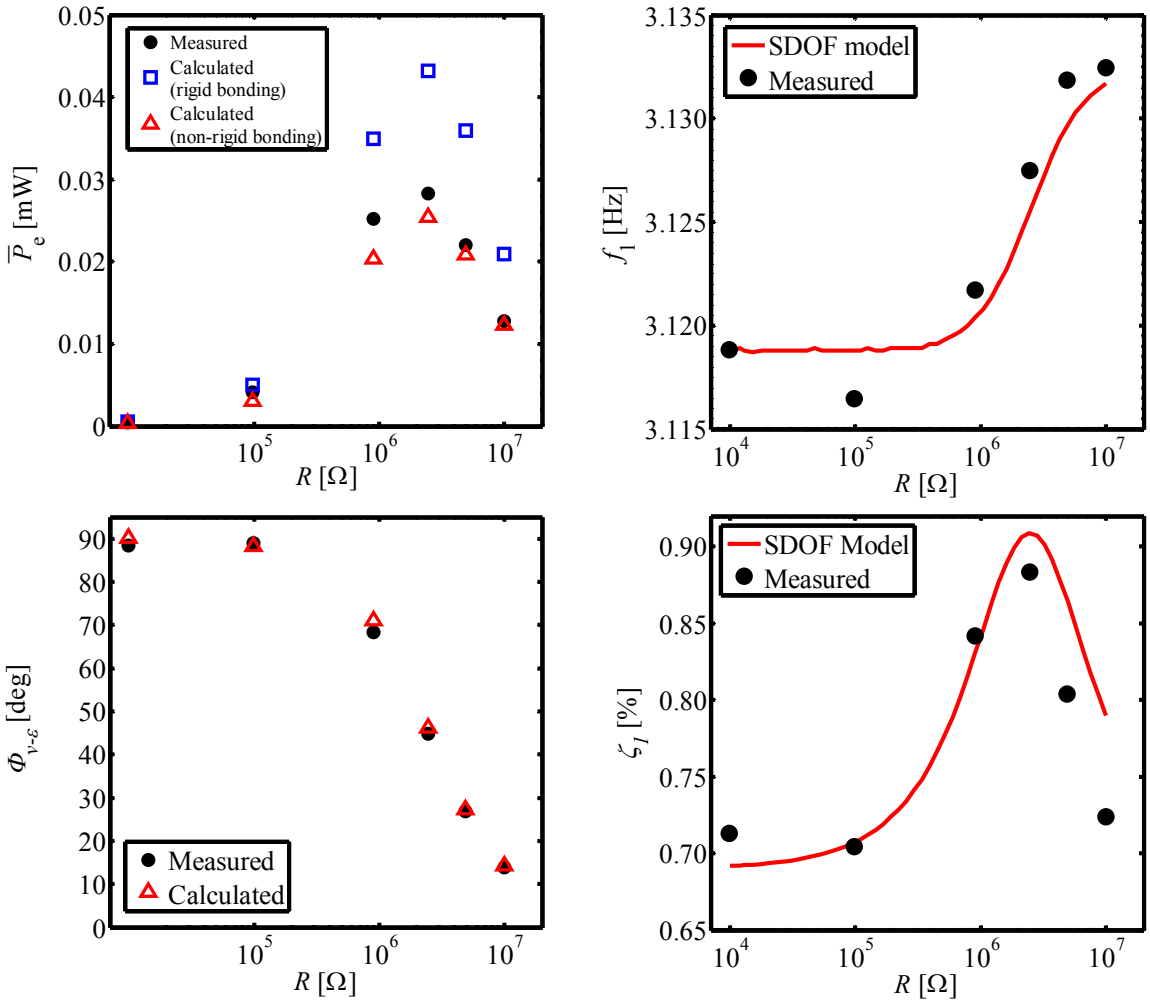

Figure 9. Effect of load resistance in free vibration tests on: a) average power b) first resonant frequency c) phase difference between voltage and strain d) damping ratio.

To estimate the effect of load resistance on resonant frequency and damping ratio, a single mechanical degree of freedom (SDOF), coupled piezoelectric generator model was developed. The model compares well with the distributed parameter model for

vibrations near the first resonance mode [19]. In the case of free vibration and a resistive electrical load, the model is given by

$$M\ddot{w}_{\text{tip}} + C\dot{w}_{\text{tip}} + Kw_{\text{tip}} - \vartheta v = 0 \tag{45}$$

$$\vartheta \dot{w}_{\text{tip}} + \bar{C}_{\text{p}}\dot{v} + v/R = 0 \tag{46}$$

where M, C, and K are the dynamic mass, damping and short-circuit stiffness of the piezoelectric beam, ϑ is the piezoelectric coupling coefficient, $\bar{C}_{\text{p}}$ is the capacitance, R is the total resistance, w_{tip} denotes the tip deflection and v is the piezoelectric voltage. A dot above the variable represents a derivative with respect to time. K is taken as the measured static stiffness, which is reasonably close to the dynamic value. M is then calculated using f_{sc}=3.119 Hz measured close to short circuit conditions (R=$10^4\Omega$). The piezoelectric coupling coefficient is found to be $\vartheta = 4.32\times10^{-5}$ N/V from

$$\vartheta = \sqrt{K\bar{C}_{\text{p}}\left[\left(\frac{f_{\text{oc}}}{f_{\text{sc}}}\right)^2 - 1\right]} \tag{47}$$

where f_{oc}=3.132 Hz measured close to open circuit conditions (R=$10^7\Omega$). The coupled ordinary differential equations (45) and (46) were solved using an explicit Runge-Kutta method (MATLAB®) over a 20-seconds simulation time for various load resistances. The resonant frequencies and equivalent damping ratios were then calculated between the 20^{th} and 40^{th} cycle as in the experiments. The computational results compare relatively well with the experimental results for both frequency and damping over a range of load resistance from R=$10^4\Omega$ to R=$10^7\Omega$ as shown in figures 9c and 9d.

The measured strain signal may be used as a method to estimate the voltage output of a harvester without actually using any piezoelectric elements. If the

piezoelectric patches are replaced with mechanically equivalent non-piezoelectric patches then the measured strain can be related to the short circuit performance of the harvester. If the electromechanical coupling is weak, the effect of the harvested electrical energy on the dynamics of the harvester can be ignored. In this weak electromechanical coupling case, the performance of the harvester with finite resistance values may be predicted using a simple RC circuit model.

6. Wind tunnel tests

The harvester was mounted in a wind tunnel (1.2 m×1.2 m cross section) which provided a steady and controllable airflow up to U_∞=11 m/s. One sidewall and the bottom wall of the tunnel are transparent for optical access. The voltage of the harvester over R=2.46 MΩ was recorded at different flow speeds. In order to eliminate any dynamic effect remaining from a previous velocity setting, recordings were taken no earlier than a minute after the flow velocity was set. The electrical power was calculated using strain measurements and compared against the measured power. Figure 10 shows that a maximum power of $\overline{P}$ =0.1 mW is obtained at U_∞=1.192 m/s. The measured average power calculated from the strain gages and measured from the piezoelectric elements were in good agreement up to three times the resonance speed. At higher speeds, excitation in higher modes becomes more pronounced and assumption of first-mode vibration causes overestimation of the average power.

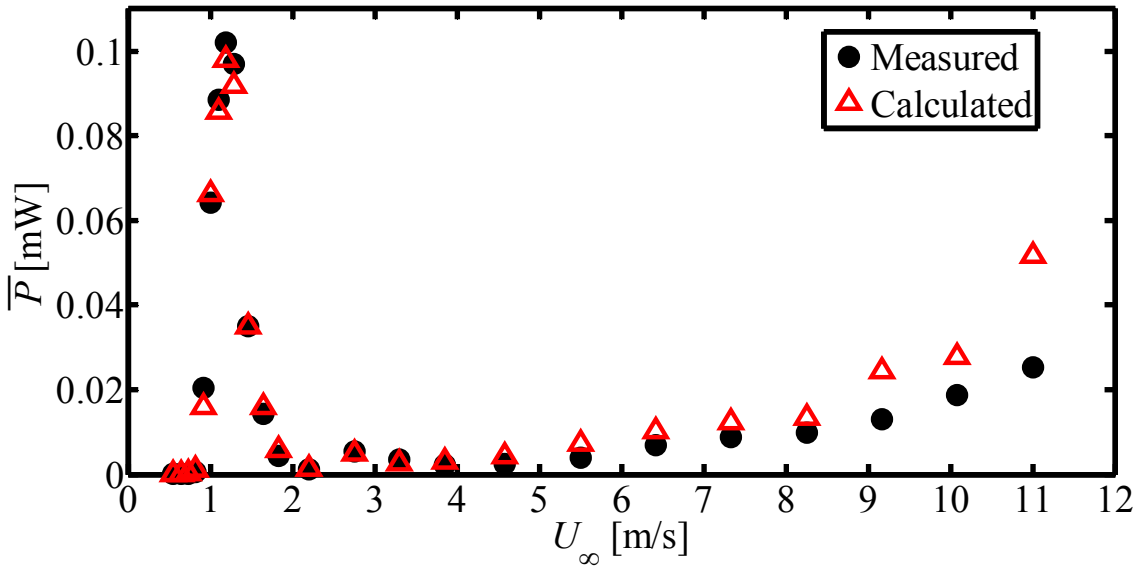

Figure 10. Electrical power output at various flow speed.

The piezoelectric voltage signal and its frequency content at resonance are shown in figures 11a and b. Data of the spectrum reveals that the forcing frequency at resonance is f_F=3.140±0.005 Hz. The corresponding Strouhal number at resonance and U_∞=1.192 m/s is found to be 0.105 from equation (6). Reynolds number at this speed is 3078 using ρ_{air}=1.194 kg/m^3 and μ_{air}=1.85×10^{-5} kg/ms in equation (7). Near Re=3000, the Strouhal number is approximately 0.21 for a long, stationary circular cylinder clear of any obstruction in its wake [20]. This would require the forcing frequency to be f_F=6.28 Hz at U_∞=1.192 m/s. Such decrease in the forcing frequency for cylinders oscillating due to flow-induced vibrations has been previously observed [21-22].

Pure structural resonance would occur at f_F=f_1=3.127 Hz when flow speed is U_∞=1.187 m/s for St=0.105. However peak power occurs at a slightly higher speed and frequency (U_∞=1.192 and f_F=3.140 Hz). This shift is most likely because the aerodynamic forces increase with U_∞ and translate the power peak to a speed higher than structural resonance.

The change in the aerodynamic forcing frequency (from 6.28 Hz to 3.140 Hz) depending on the motion and dimensions of the structure; and the deviation of the peak power frequency from the first resonant frequency of the structure (from 3.127 Hz to 3.140 Hz) are clear evidences of an aeroelastic coupling between the flowfield and the structure. Therefore, in the present case, there is an interaction between the electrical circuit and aerodynamic forces via the structure albeit relatively weak.

The tip force and displacement of the beam can be calculated from the strain measurement. At resonance speed, the strain at gage location was periodic with a 60-microstrain amplitude. Considering non-rigid bonding, the tip deflection necessary to produce this strain is found to be $|w_{tip}|$=14 mm. The corresponding dynamic tip force, $|F_{tip,d}|$, can then be found by using the measured M, C, K and ϑ values in the SDOF model equations (45) and (46). This is done by using $F_{tip,d}=|F_{tip,d}|\sin(2\pi f_F t)$ as a forcing term on the right hand side of equation (45) and adjusting $|F_{tip,d}|$ to result in $|w_{tip}|$=14 mm in the solution. The dynamic tip force is found to be $|F_{tip,d}|$=3.05 mN using f_F=3.140 Hz from figure 11b. An approximate comparison of this force to available aerodynamic data can be done by ignoring the contributions of drag force (D) for small deflections and the aerodynamic moment (M_a)* as well as the distributed aerodynamic loads on the beam. This leaves the lift force on the cylinder as the only load acting on the beam, i.e. $|F_{tip,d}|=|L|$. The amplitude of the lift coefficient is then calculated as

$$C_L = \frac{|L|}{\frac{1}{2}\rho_{air}U_\infty^2(2r_c b_c)} = \pm 0.44 \tag{48}$$

* Pressure forces on a circular cylinder do not contribute to M_a as their lines of action pass through the center of the cylinder. M_a is then only caused by the shear forces and is negligible at this Reynolds number as compared to other loads.

This value is in the upper range of lift coefficients for oscillating cylinders shown in [21]. Consideration of the neglected aerodynamic loads would bring the estimated C_L value down and lead to a better agreement with previously published results. Note that for stationary cylinders of finite length, C_L values ranging from ±0.03 to ±0.07 have been experimentally measured at Reynolds numbers near 3000 [23]. This indicates that when the cylinder is free to move in the cross-flow direction, there is a significant increase in the associated lift force.

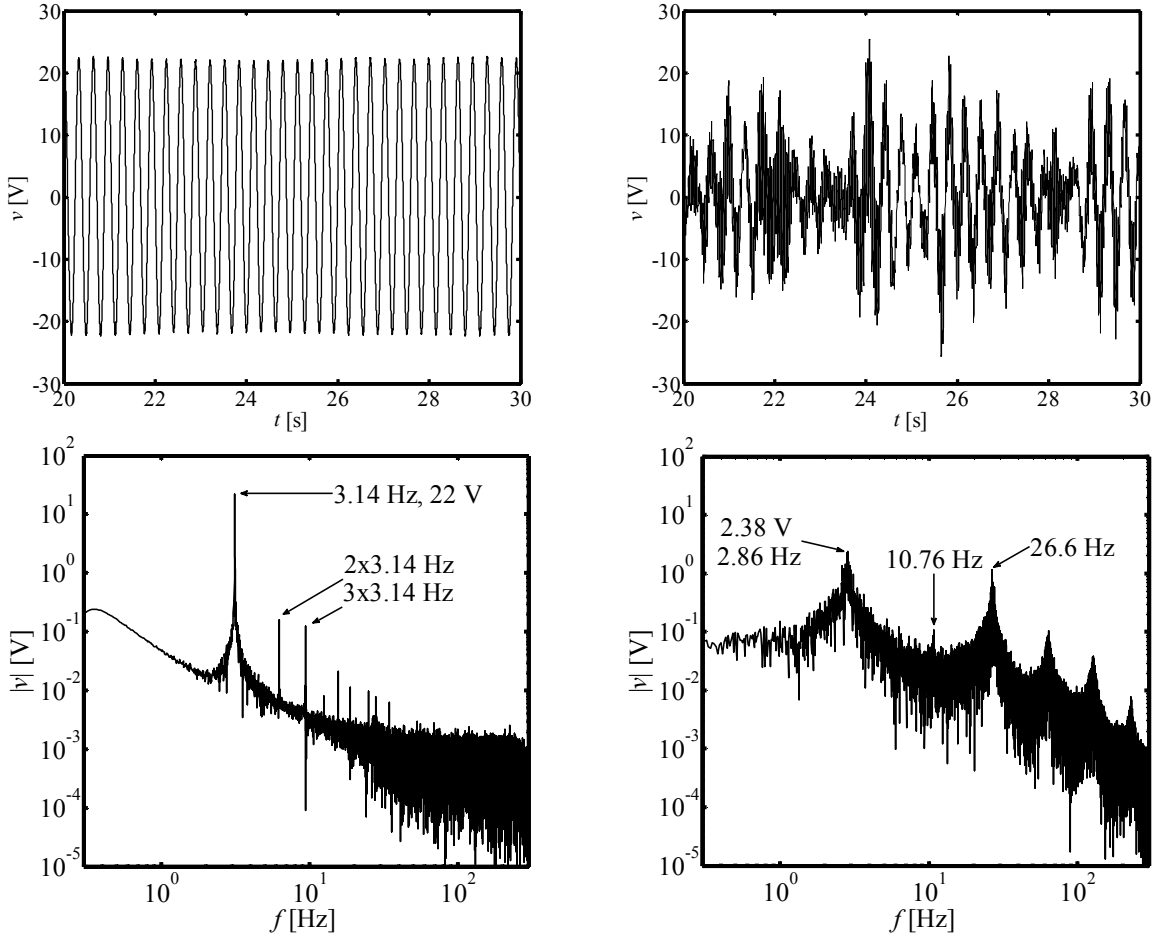

Figure 11. a) Voltage signal and (b) spectrum at resonance the first bending mode (U_∞=1.192 m/s). c) Voltage signal and (d) spectrum for U_∞=10.41 m/s showing the first torsional (10.76Hz) and second bending (26.6Hz) modes.

Two form factors, power per operational device volume and power per piezoelectric element volume are now calculated. Operational device volume and piezoelectric element volumes are respectively

$$\forall_{\text{device}} = A_{\text{f}} \left(l_{\text{s}} + 2r_{\text{c}} \right) \tag{49}$$

$$\forall_{\text{piezo}} = 2 l_{\text{p}} b_{\text{p}} h_{\text{p}} \tag{50}$$

At resonance, power per operational device volume is $\bar{P} / \forall_{\text{device}} = 23.6$ mW/m^3 while the power per piezoelectric element volume is $\bar{P} / \forall_{\text{piezo}} = 233$ W/m^3. The corresponding numbers for our previous design [4-5] were approximately $\bar{P} / \forall_{\text{device}} = 408$ mW/m^3 and $\bar{P} / \forall_{\text{piezo}} = 298$ W/m^3. Note that the $\bar{P} / \forall_{\text{device}}$ value calculated for our previous design does not include the volume of the bluff body upstream of the generator. Had the volume of the bluff body been included, the power per operational device volume (i.e. 408 mW/m^3) would be significantly smaller.

The efficiency of the present harvester can now be calculated using equations (1) and (2). The frontal area when the harvester is in operation is given by

$$A_{\text{f}} = 2 \left(r + w_{\text{tip}} \right) b_{\text{c}} \tag{51}$$

At resonance with $w_{\text{tip}}=\pm 14$ mm and the frontal area is $A_{\text{f}}=1.38\times10^{-2}$ m^2. Available power in flow is then found to be $P_{\text{f}}=13.9$ mW using equation (1). Since the electrical power output at resonance is 0.1 mW the aeroelectromechanical efficiency is $\eta_{\text{aem}}=0.72\%$, which is a large improvement on previous designs. To estimate the electromechanical efficiency, the instantaneous mechanical power is calculated by

$$P_{\text{m}} = F_{\text{tip,d}} \dot{w}_{\text{tip}} \tag{52}$$

The mechanical energy generated during the time interval $[t_0, t_1]$ is then given by

$$E_{\mathrm{m}} = \int_{t_0}^{t_1} P_{\mathrm{m}} \mathrm{d}t \tag{53}$$

while the average power over the same interval is found to be $\overline{P}_{\mathrm{m}}$=0.38mW by

$$\overline{P}_{\mathrm{m}} = \frac{E_{\mathrm{m}}}{t_1 - t_0} \tag{54}$$

Using the pertinent values calculated before, the electromechanical efficiency given by equation (5) is found to be η_{em}=26%. The following expression is suggested to predict the electromechanical efficiency of a piezoelectric system for the case of small electromechanical coupling coefficient after full-wave diode bridge rectification [24]:

$$\eta_{\mathrm{em,\,rect}} = \frac{1}{1 + \dfrac{C}{2R\vartheta^2}\left(RC_{\mathrm{p}}\omega_{\mathrm{F}} + \dfrac{\pi}{2}\right)^2} \tag{55}$$

Substituting the measured values in equation (55) $\eta_{\mathrm{em,rect}}$ is found to be 16%. This translates to non-rectified electromechanical efficiency of η_{em}=20% if the rectification process is assumed to be ideal with 81% efficiency. It should be noted that $\eta_{\mathrm{em,rect}}$ is highly sensitive to f_{sc} used for calculation of ϑ for very small values of ϑ. For example, a 0.1% decrease in f_{sc} value results in η_{em}=23% which is about 15% larger than the originally calculated value of η_{em}=20%. Therefore, a very precise measurement of f_{sc} is necessary for a better agreement between the calculated and predicted electromechanical efficiencies.

The aeroelastic efficiency is then calculated to be η_{ae}=2.8% using equation (3) with η_{em}=20% and η_{aem}=0.72% found earlier. Comparing the efficiency values and form factor of our present design and earlier designs [4-5], it is noted that:

(i) There is nearly a two order of magnitude increase in □ae with the present design (2.8% compared with 0.032%). This clearly shows the improvement due to the attachment of the cylinder on the tip of the harvester beam.

(ii) The increase in η_{em} is nearly three-fold with the present, tip-cylinder design (26% compared with 11%). However, this increase is not only due to change of harvester configuration but also due to the higher piezoelectric coupling coefficient of PZT as compared to PVDF (d31= 190 pm/V for PZT and d31= 23 pm/V for PVDF).

(iii) Power per piezoelectric material volume is comparable in both designs although PVDF has a smaller piezoelectric coefficient. This is because the PVDF beam in earlier designs experienced much larger strains. Note in figure 6b that the maximum strain on the outer surface of the present beam is about 90 microstrain, which is far less than damage limit of 500 microstrain for PZT. The piezoelectric patches in the present design can thus allow for higher applied strains and this would increase the voltage and power output.

(iv) Although the previous design was less efficient, it has a much smaller form factor as indicated by power per device volume values.

7. Resonance in other modes of vibration

As the flow speed increases past the first bending mode resonance, the generator is excited in the first torsional mode and then the second bending mode. If the torsion moment of inertia of the beam, the presence of patches and coupling between the torsion

and bending modes are ignored then the first torsional mode frequency of the harvester is calculated by

$$g_1 = \frac{1}{2\pi}\sqrt{\frac{G_s J_s}{l_s I_{yy,c}}} \tag{56}$$

where G_s is the shear modulus of shim material, J_s is torsion constant of the shim's cross section given by [25]

$$J_s = \frac{b_s h_s^3}{3}\left\{1 - \frac{192 h_s}{b_s \pi^5}\sum_{i=1}^{\infty}\frac{1}{(2i-1)^5}\tanh\left[(2i-1)\frac{\pi b_s}{2h_s}\right]\right\} \tag{57}$$

and $I_{yy,c}$ is the mass moment of inertia of the cylinder along y-axis given by

$$I_{yy,c} = m_c \frac{1}{12}\left[3\left(r_o^2 + r_i^2\right) + b_c^2\right] \tag{58}$$

Using G_s = 28 GPa for aluminum and the relevant dimensions of the shim and the cylinder, the first torsional mode frequency is found to be g_1=11.20 Hz. The second bending mode frequency is calculated to be f_2=27.43 Hz with modal analysis also without considering the piezoelectric patches. Figures 11c and 11d show the piezoelectric voltage signal and its frequency content at U_∞=10.41 m/s. Note that all three modes of vibration are excited to some extend as seen on the spectrum. It should be noted that in the current configuration of electrodes, the torsion mode did not produce any significant piezoelectric voltage. It is possible, however, to harvest energy in torsional mode with a special arrangement of electrodes as shown in [26]. Furthermore, contribution of the second bending mode to the harvested energy can be increased by placing piezoelectric patches near the middle of the beam where the maximum strains due to second bending mode occur.

8. Conclusions

Fluid flow is a significant energy source for piezoelectric energy harvesting. The focus of the present fluidic energy harvester is the conversion of energy of a uniform and steady flow into periodic motion of the solid structure with the aim of obtaining high efficiency, small form factor, and having a capability to self-start and sustain the periodic motions. In this study, a self-excited piezoelectric energy harvester which can operate in steady, uniform flows is presented. The harvester is comprised of a cantilevered aluminum shim carrying a circular cylinder on its tip and partially covered by piezoelectric material near its base. Due to structural vibrations induced by the fluid flow, periodic strains are generated in the piezoelectric material, which converts the strain energy into electrical charge.

In order to characterize the harvester, both free vibration and wind tunnel tests were performed. The strain developed near the base on the shim was measured to predict the piezoelectric voltage output using a distributed parameter model. It was observed that rigid bonding assumptions between the piezoelectric elements and the support structure may significantly overestimate the strain transferred from the structure to the piezoelectric elements. In order to consider non-rigid bonding effects, a strain-transfer model was incorporated into the distributed parameter model. This led to significant improvement in voltage and power predictions. Variation of the first-mode resonant frequency and damping coefficient over a large range of resistances were modeled using a single mechanical degree of freedom system. Furthermore, in the case of weak electromechanical coupling, strain measurements alone can be used for predicting the voltage of a harvester without using piezoelectric materials.

The wind tunnel tests at various flow speeds showed that a maximum of 0.1 mW non-rectified electrical power was attained at a flow speed of about 1.192 m/s. At this speed, the vibration frequency and amplitude were 3.14 Hz and ±14 mm. The magnitude and frequency of the lift force was significantly different from what would be anticipated using a stationary cylinder assumption. Furthermore, the forcing frequency at this speed was slightly higher than the structural resonance frequency. It can thus be concluded that aeroelastic interactions play a significant role in fluidic energy harvesters and that this coupling is critical in future modeling efforts. Attachment of a vibration-inducing body to the tip of the harvester beam resulted in a tremendous increase in the aeroelastic efficiency of the harvester. The flow velocity required for maximum power is also greatly reduced which is desirable for sensing in low velocity flows such as those in HVAC systems.

The change of resonant frequency and structural damping due to electrical resistance for the present case is relatively weak but measurable. Had the piezoelectric patches covered a larger area of the shim, the electromechanical coupling would be stronger and variation of the damping with electrical resistance would be more pronounced. In that case, changes in load resistance would significantly alter the motion of the beam and ultimately the flowfield around the harvester. Such a system is an "aeroelectromechanical" one. A complete description of the behavior of such a system then requires an interdisciplinary consideration of all three constituting domains, i.e. the aerodynamic, structural, and electrical domains. Therefore, future work should focus on fully coupled aeroelectromechanical modeling of the system which considers both the

coupled response of the harvester due to electromechanical and the aeroelastic interactions.

Acknowledgement

The financial support provided by National Science Foundation under CBET grant # 1033117 is greatly appreciated.

References

[1] Anton S R and Sodano H A 2007 A review of power harvesting using piezoelectric materials (2003–2006) Journal of *Smart Materials and Structures*, **16** R1-21

[2] Sodano H A, Inman D J and Park G 2004 A review of power harvesting from vibration using piezoelectric materials *The Shock and Vibration Digest*, **136** 197-205

[3] Erturk A, Inman D J 2011 *Piezoelectric Energy Harvesting* John Wiley & Sons

[4] Akaydın H D, Elvin N, Andreopoulos Y 2010 Wake of a cylinder: A paradigm for energy harvesting with piezoelectric materials *Experiments in Fluids*, **49** (1) 291-304

[5] Akaydın H D, Elvin N, Andreopoulos Y 2010 Energy harvesting from highly unsteady fluid flows using piezoelectric materials *Journal of Intelligent Material Systems and Structures*, **21** (13) 1263-78

[6] Panton R L 1993 *Incompressible Flow* John Wiley & Sons

[7] Akaydın, H D, Elvin N, Andreopoulos Y 2010 Experimental study of a self-excited piezoelectric energy harvester, *Proceedings of 3rd ASME Conference on Smart Materials, Adaptive Structures and Intelligent Systems* SMASIS2010-3729 September 28 - October 1 2010, Philadelphia, PA. USA.

[8] Unal M F and Rockwell D 1988 On vortex formation from a cylinder. Part II: Control by splitter-plate interference *Journal of Fluid Mechanics*, **190** 513-29

[9] Erturk A and Inman D J 2008 A distributed parameter electromechanical model for cantilevered piezoelectric energy harvesters *Journal of Vibration and Acoustics* **130** 041002-1

[10] Erturk A, Inman D J 2009 An experimentally validated bimorph cantilever model for piezoelectric energy harvesting from base excitations *Journal of Smart Materials and Structures* **18** 025009

[11] Crawley E, Anderson H, 1990, Detailed Models of Piezoceramic Actuation of Beams *Journal of Intelligent Material Systems and Structures* **1** (1) 4-25

[12] Pietrzakowski M 2001 Active damping of beams by piezoelectric system: effects of bonding layer properties *International Journal of Solids and Structures* **38** (44-45) 7885-97

[13] Ye J Q 2001 Interfacial shear transfer of RC beams strengthened by bonded composite plates *Cement & Concrete Composites*, **23** 411-7

[14] Han L, Wang X D, Zuo M 2009 The dynamic behavior of a surface-bonded piezoelectric actuator with a bonding layer *Acta Mechanica* **206** (3-4) 193-205

[15] Guenaneche B, Krour B, Tounsi A, Fekrar A, Benyoucef S, Bedia A, 2010, Elastic analysis of interfacial stresses for the design of a strengthened FRP plate bonded to an RC beam *International Journal of Adhesion and Adhesives*, **30** 636-42

[16] Jin C, Wang X 2011 The effect of adhesive layers on the dynamic behavior of surface-bonded piezoelectric sensors with debonding *Journal of Intelligent Material Systems and Structures* **22** (7) 655-67

[17] De Faria A R 2003 The impact of finite-stiffness bonding on the sensing effectiveness of piezoelectric patches Journal of Smart Materials and Structures **12** (4) N5-8

[18] Yang J, Ye J 2010 An improved closed-form solution to interfacial stresses in plated beams using two-stage approach *International Journal of Mechanical Sciences* **52** (1) 13-30

[19] Elvin N, Elvin A, 2009 A general equivalent circuit model for piezoelectric generators *Journal of Intelligent Material Systems and Structures*. **20** (1) 3-9

[20] Lienhard, J H 1966 Synopsis of lift, drag, and vortex frequency data for rigid circular cylinders *College of Engineering, Research Division, Bulletin 300, Technical Extension Service* Washington State University Pullman, Washington. USA

[21] Blevins R D 1977 *Flow-induced Vibration*, Van Nostrand Reinhold Company

[22] Dong S, Karniadakis G E 2005 DNS of flow past a stationary and oscillating cylinder at Re=10000 *Journal of Fluids and Structures* **20** 519-31

[23] Norberg C 2002 Fluctuating lift on a circular cylinder: Review and new measurements, *Journal of Fluids and Structures* **17** 57-96

[24] Shu Y C, Lien I C 2006 Efficiency of energy conversion for a piezoelectric power harvesting system *Journal of Micromechanics and Microengineering* **16** (11) 2429-38

[25] Rao S S 2007 *Vibration of Continuous Systems* John Wiley & Sons

[26] De Marqui C, Erturk A, Inman D 2010 Piezoaeroelastic Modeling and Analysis of a Generator Wing with Continuous and Segmented Electrodes *Journal of Intelligent Material Systems and Structures* **21** (10) 983-93

Chapter 6

Further Work

This chapter presents some of done but not included in the manuscripts published earlier.

1. Effect of tip-body shape

It was shown in the previous chapter that self-excited vibrations of significant amplitudes can be created by adding a circular cylinder to the free end of the cantilever beam. Investigating the behavior of a circular cylinder is advantageous for comparative research purposes since the flow around circular cylinders has been extensively studied as a benchmark case; thus a large quantity of both experimental and computational data is available. However, tip-body shapes other than a circular cylinder may result in more power as compared to a circular cylinder shape. In this section, we present the performances of harvesters carrying half cylinder (D-section) tip-body and a flat plate (I-section) tip-body (Figure 1). The performance of these tip bodies are compared with the that of the circular cylinder (O-section) tip-body case investigated in the previous chapter.

a)

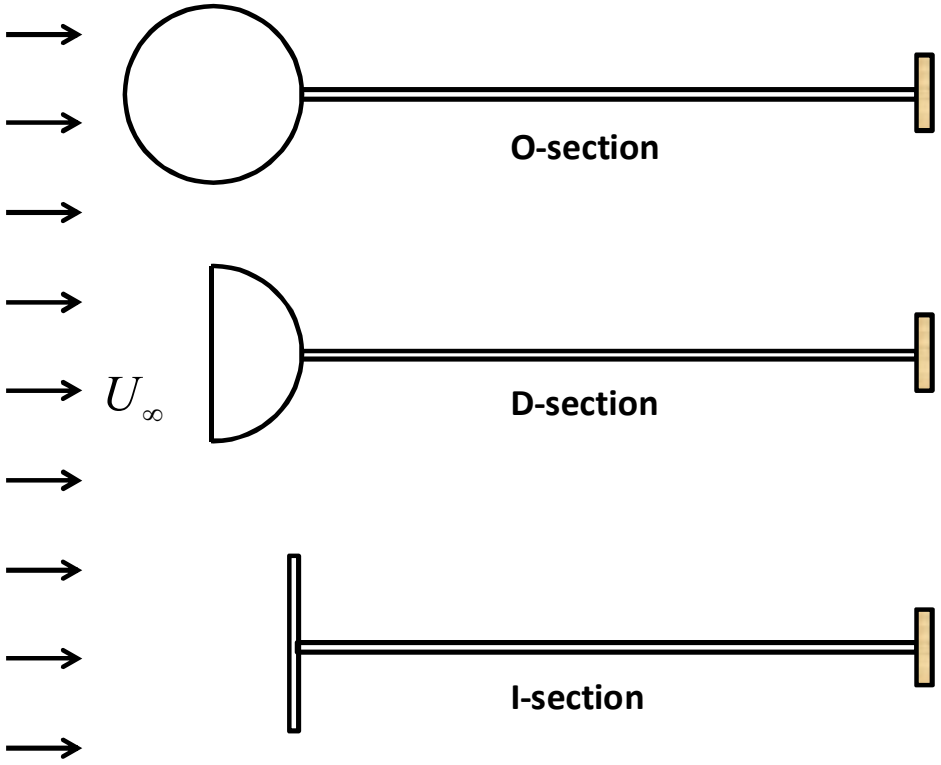

b)

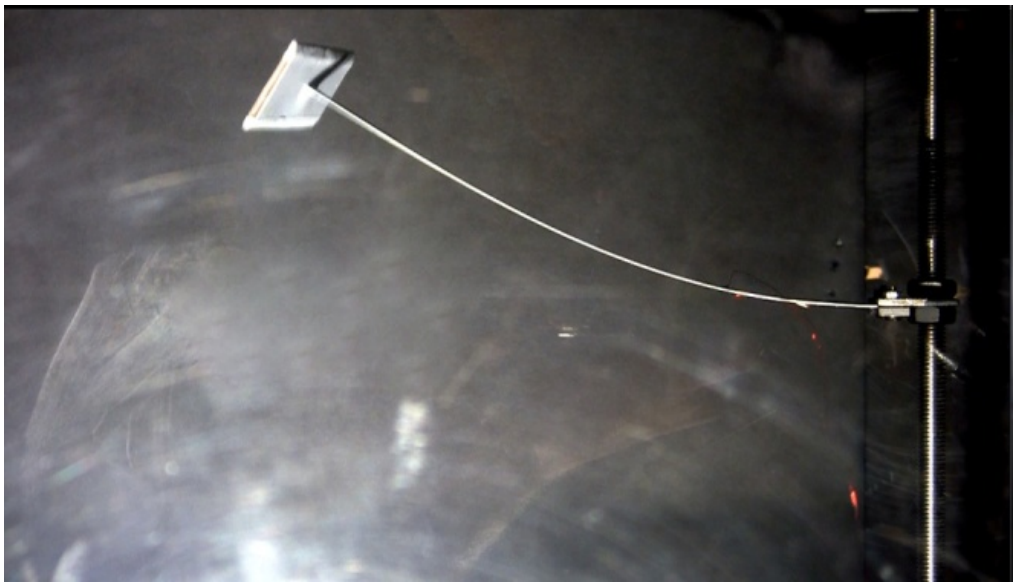

Figure 1: a) The tested tip body shapes. Both the "O-section" and "D-section" cylinder were 40 mm in diameter with masses of 16 g and 21 g, respectively. Two "I-section" cylinders were tested: "I-section 1" had a width of 32.5mm and mass of 16 g; " I-section 2" had a width of 40 mm and a mass of 24 g. All cylinders had a length of b_c=203 mm. b) A photograph of the I-section harvester exhibiting large tip deflections.

Wind tunnel tests showed that both the D-section and I-section harvesters significantly increased the harvested power (Figure 2). The D-section and O-section harvesters exhibited similar resonant power output responses below U_∞<1.47 m/s. Above this speed however, the response of the D-section harvester was very different from that of the O-section one investigated in the previous section. After passing through the first bending resonance, the O-section harvester resonated in the first torsional mode (at about 11.2 Hz) and then the second bending mode (at about 27.4 Hz)* with little tip deflection. In contrast, the D-section harvester's tip deflection grew larger with increasing flow speed, while its vibration frequency remained fixed at 3.2 Hz. This matching of the vortex shedding frequency to the resonant frequency of the structure with increasing flow velocity is known as "lock-in" [1] and is observed commonly in galloping instability of cylinders of non-circular cross sections. [2, 3]. The I-section harvester did not exhibit a pronounced resonance as its vibration amplitude increased steadily throughout the velocity range. The increase in amplitude of oscillations for the D-section harvester was so rapid that the test had to be stopped before reaching U_∞=3 m/s to prevent damage to the piezoelectric patches. The voltage amplitudes obtained at the last data points for the D-section, I-section 1 and I-section 2 in Figure 2b were approximately ±107V, ±93V and ±82V, respectively with vibration frequencies near 3.18 Hz, 3.16 Hz and 3.83 Hz.

* Due to the construction and electrical connection of the harvester, the voltage output of the modes higher than the first bending mode were small and cannot be seen in Figure 2. However, visual observation of the harvester and FFT analysis of the strain signal showed resonances in the first torsional mode and the second bending mode as detailed in the previous section.

At the highest flow speeds, the oscillation amplitudes of the D- and I-section harvesters exceeded 100 mm, which was more than 35% of the beam's length (Figure 2b). When the tip deflections are large, the contributions of the drag force and the aerodynamic moment to the deflection of the beam cannot be neglected. In addition, the geometric (and possibly material) nonlinearities in the structure of the beam become significant. Thus simplified models of the harvester behavior need to be used with caution, since these models generally assume that (a) the beam undergoes small deflections, and (b) only lift forces act on the beam.

From a practical point of view, the D-section harvester outperformed the other tested shapes. At 1.19 m/s, the D-section harvester's total efficiency is approximately η_t=0.80%, which is slightly larger than that of the O-section harvester (η_t=0.75%) at the same speed. However, once past the resonant regime, the power output of the D-section harvester rapidly increases to 2 mW at a flow speed of 2.75 m/s. The total efficiency of the D-section harvester decreases to η_t=0.31% at this speed since large tip deflections increase the operational frontal area. However, it should be noted that the efficiency of O-section harvester at 2.75 m/s is negligible since its electrical power is nearly zero at this speed. Since strain data is not available for the D-section and I-section harvesters, the electromechanical efficiencies of these models are not currently known; and a full breakdown of their efficiency components cannot be performed.

a)

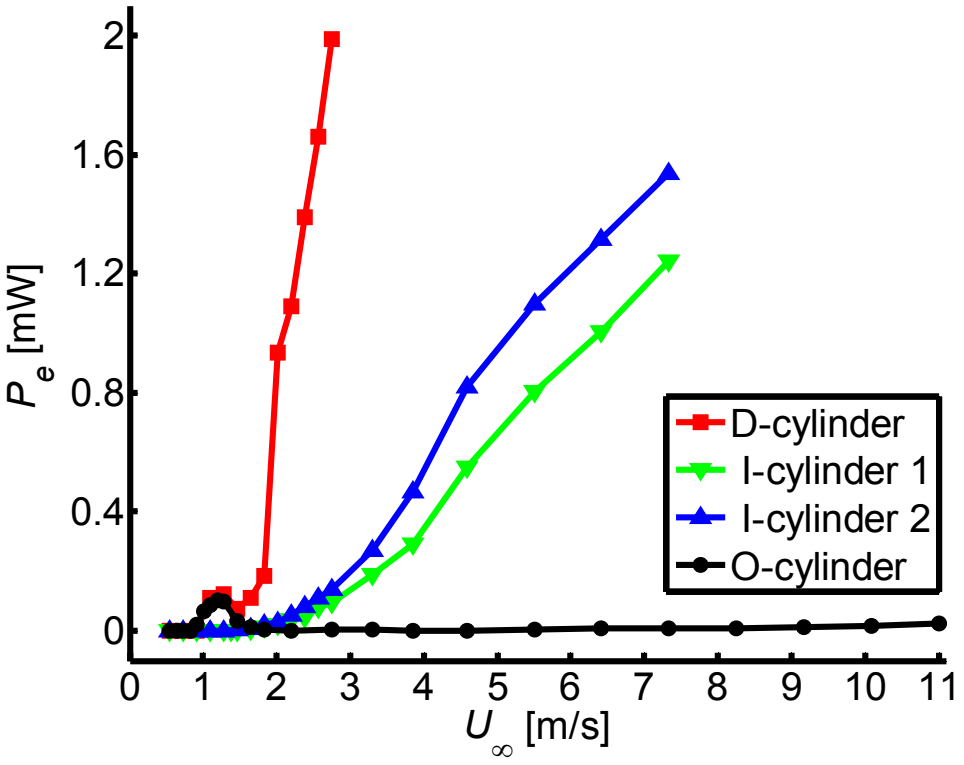

b)

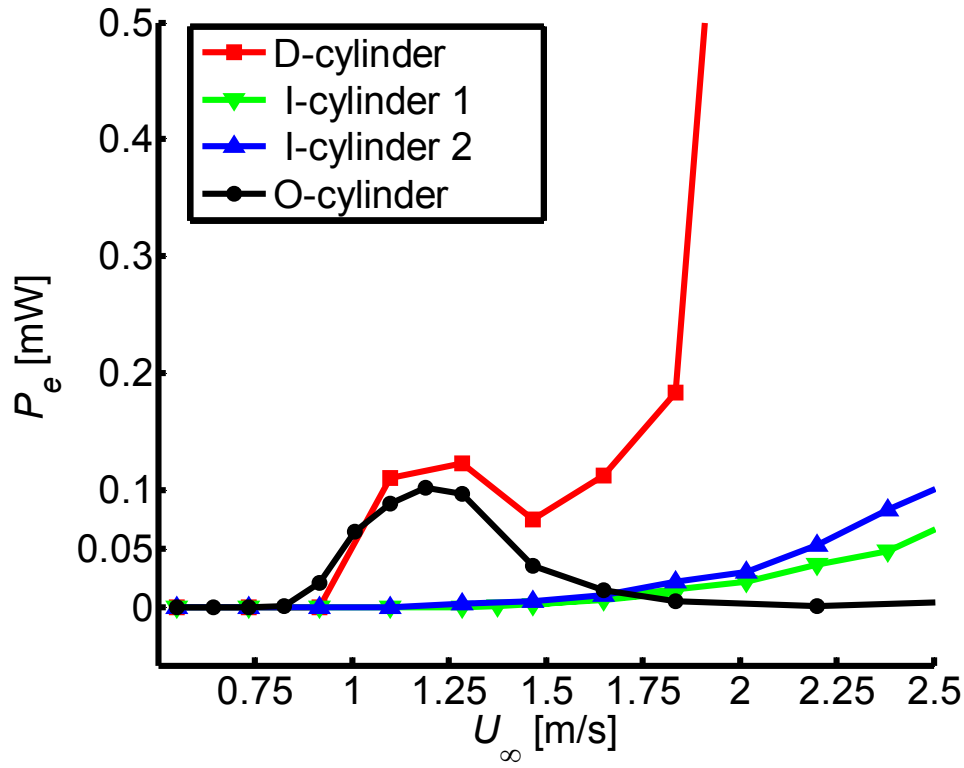

Figure 2: Electrical power output using different tip body shapes.

2. Turbulent boundary layer tests

A set of experiments with a PVDF unimorph beam of dimensions 30 mm x 16 mm x 0.2 mm ("long beam") in turbulent boundary layer was presented earlier in Chapter 1. In order to investigate the effect of the length of the beam, additional experiments were done with a shorter PVDF unimorph beam of dimensions 15 mm x 13 mm x 0.2 mm ("short-beam"). The first bending mode frequencies (f_1) of the long and short beams measured using shaker as 48.5 Hz and 198 Hz, respectively. An extra set of data with the long beam was also taken during these experiments for a better comparison between the long and short beam cases and for checking the repeatability of the long beam tests. The measurements were taken at the same location as before, i.e. 5.12 m downstream of the beginning of the test section. The beam is held at zero degree of angle of attack by a rod connected to a traverse protruding from a hole on the bottom wall of the tunnel. As before, a load resistance of 10 MOhm was used. Signals were recorded using a data acquisition card on a PC at a sampling rate of 1kHz for long beam and of 10kHz for short beam.

The boundary layer developing over the bottom wall of this wind tunnel has been extensively characterized in [4, 5]. The thickness of the boundary layer (δ) at the position of be measurements is found from

$$\delta = c\frac{x_{\mathrm{BL}}}{\mathrm{Re}_{x_{\mathrm{BL}}}^{1/5}} \tag{1}$$

where the parameter c=0.353 is obtained from the experimental data present in [4, 5] and Re_x is the local Reynolds number given by

$$\mathrm{Re}_{x_{\mathrm{BL}}} = \frac{\rho U_\infty x_{\mathrm{BL}}}{\mu} \tag{2}$$

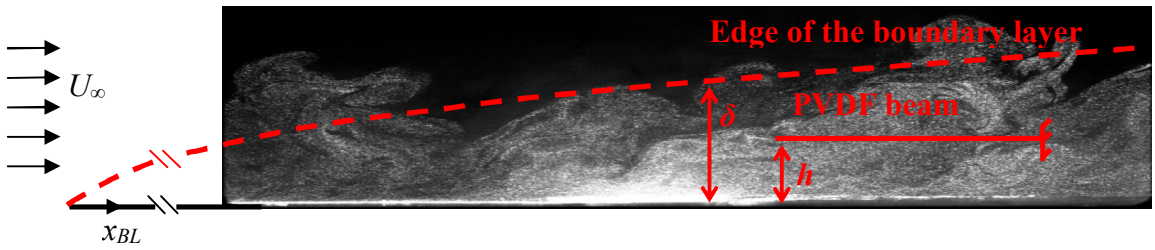

Figure 3: A flow visualization image of the turbulent boundary layer.

The voltage signals obtained at U_∞=11 m/s for long beam placed at h=34 mm and for short beam placed at h=22 mm are shown in Figure 3. The intermittent form of the responses to turbulent fluctuations for both cases is evident.

a)

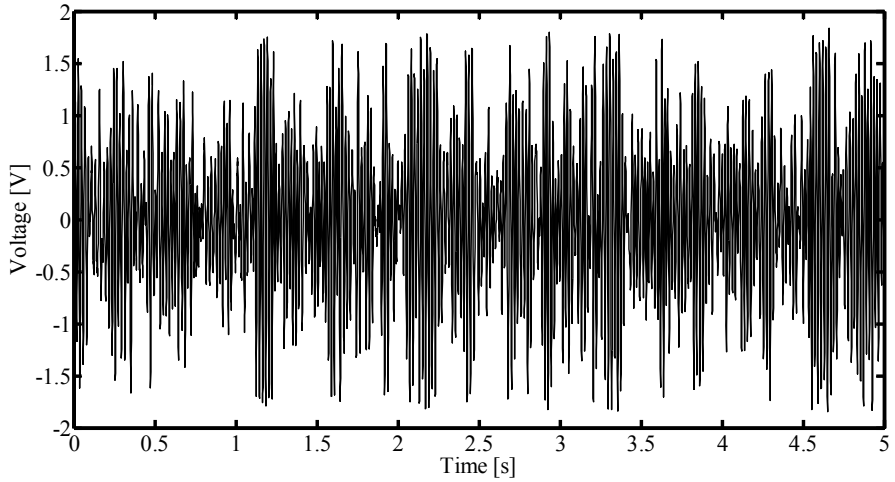

b)

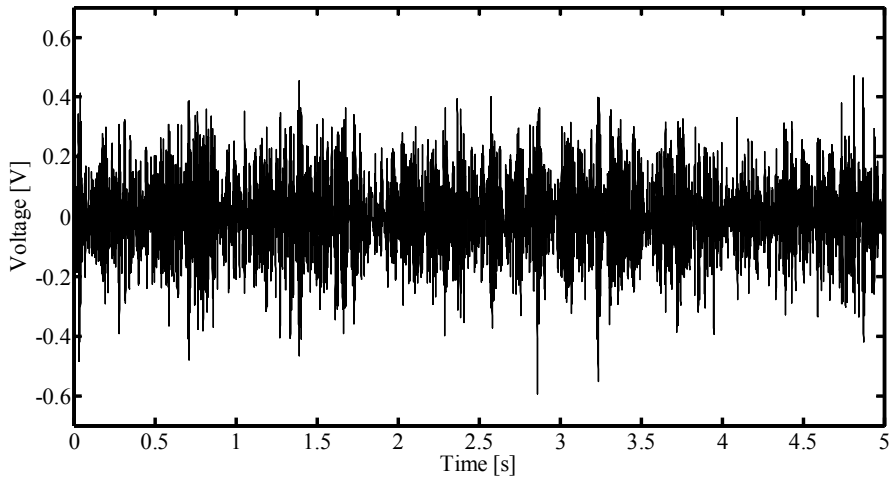

Figure 4: Voltage signals at U_∞=11 m/s for a) long beam placed at h=34 and b) short beam placed at h=22 mm.

The "power landscape" of turbulent boundary layer is measured by taking measurements at different wall distances and free stream speeds. The variation of harvested power with respect to these variables is shown in Figure 5. It should be noted in this figure that the wall distance is normalized by the boundary layer thickness whereas the free stream velocity is reduced to a non-dimensional frequency $f^* = U_\infty/(\delta f_1)$. The maximum electrical power harvested over a load resistance of 10 MΩ was 60 nW for the long beam and 1.6nW for the short beam. Within the range of flow speeds tested (i.e. 0 to 11 m/s), the harvester power from both beams increased monotonically and reached maximal levels at U_∞=11 m/s for which δ=95 mm. However, the wall distance for the maximum power was in a range of 25 to 50 mm for the long beam whereas this range was 15 to 60 mm for the short beam. Maximum power is harvested inside a region where h/δ is approximately 0.4 for both the long and the short beams. However, the use of a shorter beam expands the region of maximal energy harvesting while decreasing the peak power magnitude. Contrary to our initial anticipation, the normalized frequency $U_\infty/\delta f_1$ was not close to unity at the maximum values of power harvested since the harvested power increased monotonically with freestream speed. While this may mean that the response of the beam to turbulent fluctuations is of "lock-in" type rather than a resonant type, it invites one to look for expressions other than $f^* = U_\infty/(\delta f_1)$ for reducing the freestream speed to make further assessments.

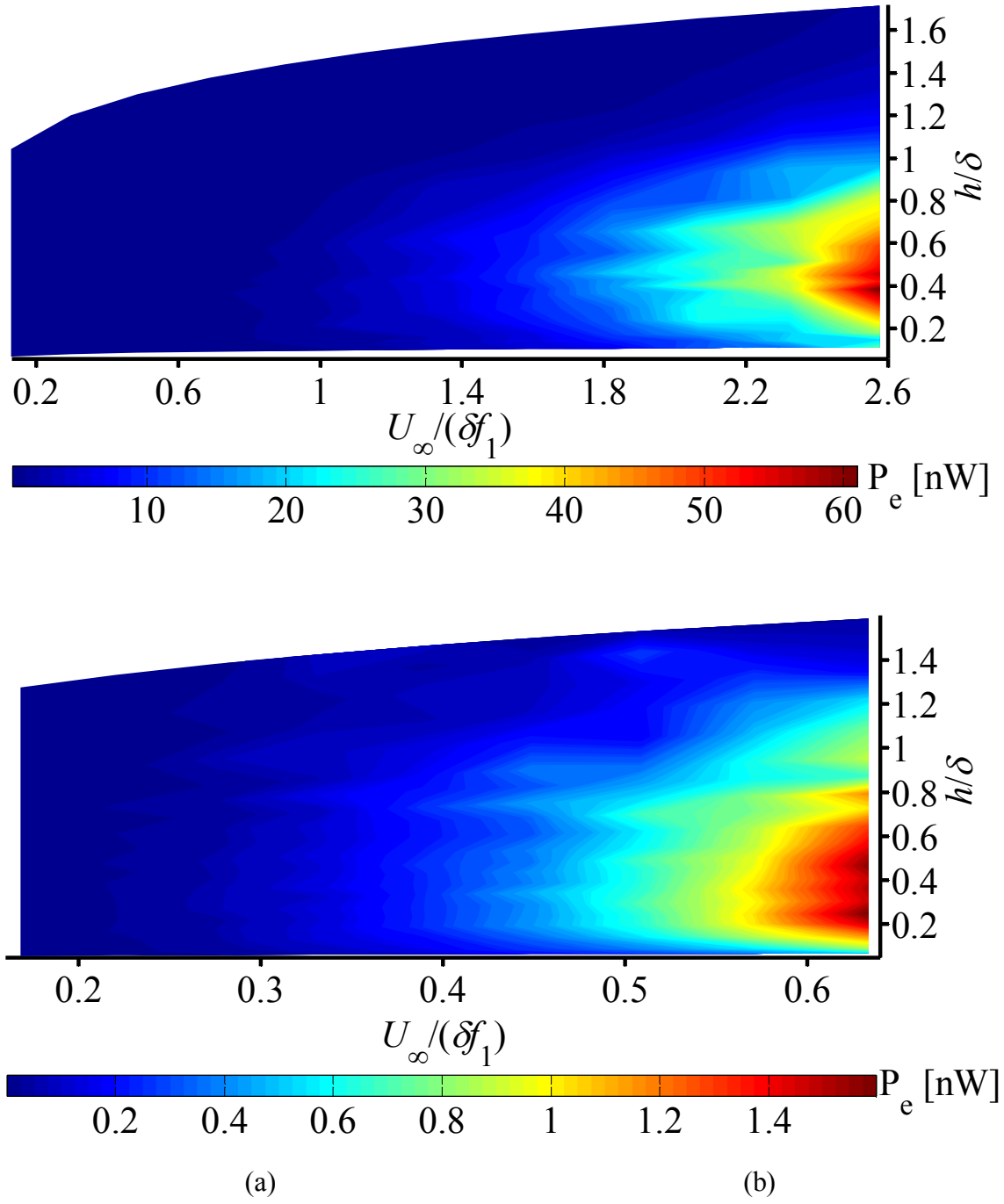

Figure 5: The contour plots of the electrical power harvested in a turbulent boundary layer, a) for the long beam and b) for the short beam.

3. Interaction of a flexible piezoelectric beam with a vortex ring

In Chapter 3, the mechanism by which the vortices deform a flexible beam in the wake of a circular cylinder was explained. It was stated that the induced velocity of a vortex approaching the beam first creates a positive pressure load over a surface of the beam. Therefore, the vortex first pushes away the cantilevered beam while approaching. Once the vortex comes on top of the beam, however, the vortex pulls back the beam due to the low pressure in its core. This mechanism occurs repeatedly on either side of the beam due to counter-rotating vortices being shed off alternate (top and bottom) sides of the cylinder. There is a 180-degree phase difference between the events on either side of the beam: While the beam is pulled by a vortex is on one side, the next vortex approaching pushes the beam further away from the other side. The reciprocal action of the counter rotating vortices traveling opposite sides of the beam, if in resonance with the natural frequency of the beam, results in large deflections.

In this section, an experiment to further study the effect of a vortex on a flexible beam will be presented. The behavior of an elastic beam subject to the impact of a vortex ring was investigated recently [6, 7]. The experiment present here, however, investigates the behavior of a flexible beam as vortex ring travels nearby. The vortex ring was created using a "vortex cannon", which is a plastic bucket covered with a silicone membrane and has a 10-cm circular opening on its bottom (Figure 6). Tension and sudden release of the membrane creates a shear layer around the periphery of the opening and this shear layer rolls up and forms a vortex tube in the form of a hollow ring. This vortex ring travels away from the cannon opening with a speed U_{ring}. The vortex rings can be made visible

by filling the cannon with theatrical smoke prior to the release. With this setup, it is possible to repeatedly create vortex rings with core diameters of about d_{ring}=15 cm after some practice.

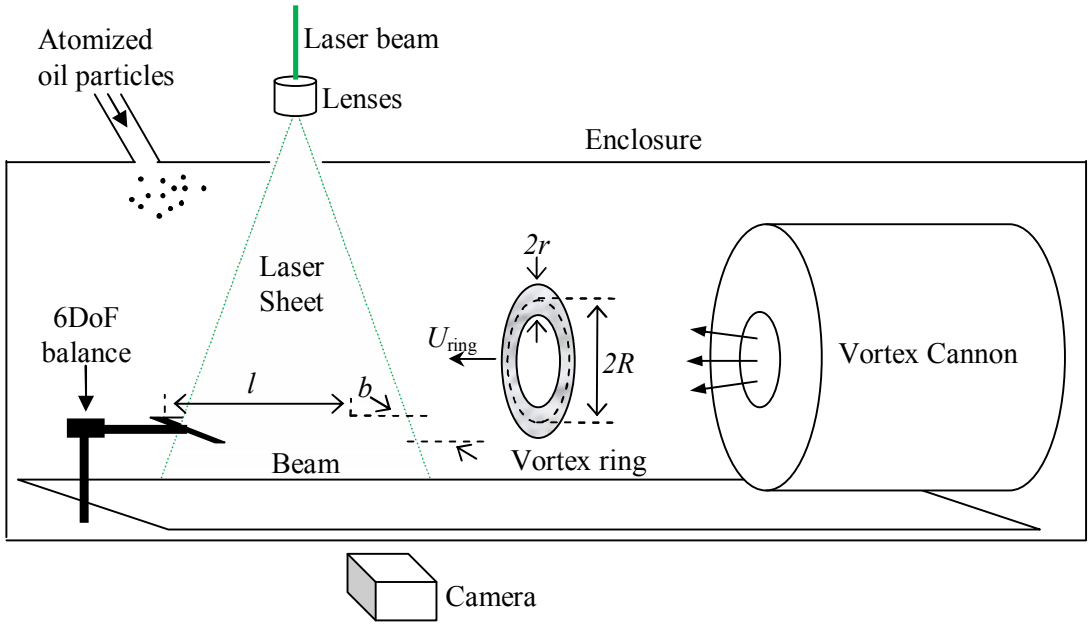

Figure 6: The configuration of the vortex cannon and the flexible piezoelectric beam.

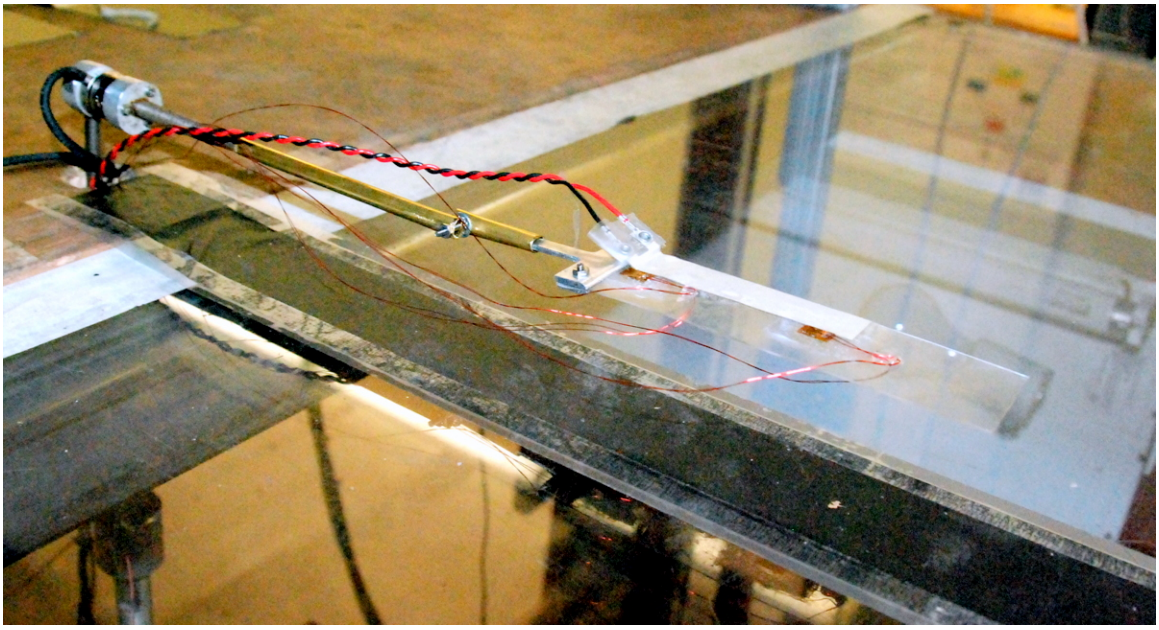

Figure 7: The flexible and transparent Mylar beam carried by a 6DoF force and moment balance system. The beam is partially covered with PVDF on top and furnished with two strain gages and a partially coated by a PVDF layer.

During the experiments, the cannon was placed on the bottom wall inside the wind tunnel so that the vortices are sent along the length of the tunnel horizontally. A flexible and transparent Mylar beam was hold parallel to the wall at a distance of about 8 cm by a rod connected to traverse protruding from an opening on the wall (Figure 7). The rod and the tip of the traverse were connected to each other with a 6DoF (six degree of freedom) force and moment sensor (ATI Industrial Automation, model Nano 17). The Mylar beam was furnished near its first and second mode peak strain locations with two couples of strain gages in half-bridge configuration. The beam was partially covered on top with a 28μm-thin PVDF layer (Measurement Specialties, Inc) to generate some piezoelectric voltage.

For time-resolved PIV (particle image velocimetry) measurements, a continuous wave (CW) diode laser (Newport Corporation, Spectra Physics Lasers, model Millennia VS110) was used to produce green laser beam of 532 nm wavelength and 5.5W power. A thin sheet of laser light was created by directing the laser beam to a cylindrical lens followed by a spherical lens. The laser was pointed directly on the lenses without using any mirrors to keep laser power losses to a minimum. The laser sheet is then aligned perpendicularly on top of the Mylar beam, halving the width of the beam along the length. Since the Mylar beam is transparent and only partially covered with PVDF, the laser sheet was able to illuminate through the beam. The shadows in PIV field underneath the beam were thus greatly eliminated. A high-speed camera (Vision Research, Inc., model Phantom v710) was used to capture images for PIV as well as for tracking the motion of the beam. The images had a resolution of 1280x800 pixels and they were taken at a rate of 5000 frames per second with 50μs exposure using a 50mm Zeiss lens at f1.4

aperture. At these settings of resolution and rate, the camera was able to store a video of about 4.5-seconds long in its memory. An extensive description of this time-resolved PIV system, explanation of its theoretical background and its applications to flapping wings inside turbulent boundary layer flows is presented in [8].

With the configuration described above, a cross section of the vortex ring can be visualized as the ring travels over the top of the flexible beam. The ring can easily be made visible by filling the cannon with smoke prior to release of the vortex ring. The vortex ring then coherently carries a part of the smoke, which makes the ring distinguishable from the rest of the quiescent fluid. However, for PIV images to give vector data in the entire field, the seed particles must preexist everywhere in the flowfield before and after the vortex ring passes. This problem was solved by building an enclosure around the whole setup inside the tunnel and by injecting in this enclosure atomized olive oil particles. The reason for using atomized olive oil was its crisp light scattering properties and reasonable settling time. The vortex cannon is then used to send a vortex ring in this particle-filled volume and the motion of the vortex is traced primarily by motion of particles in PIV images rather than following visually the displacement of a bulk of tracer elements.

The data acquisition system for the strain gages, the piezoelectric voltage and the force and moment sensor was set to a sampling rate of 5000 S/s for 4.5 seconds in concert with the video acquisition rate. The data acquisition system and the camera shared a push-button trigger to start their recordings at the same instant. For a typical test, the laser was first set to full power, particles in enclosure was replenished, the system was triggered and a few vortex rings were released during a period of about 4.5 seconds. In a

successful capture, a vortex ring would travel horizontally with its lower side 10-20 mm above the beam. The signals from the strain gages, the piezoelectric voltage and the force and moment sensor are all recorded synchronously with the video images. Figure 8 shows a sequence of images taken by using smoke for flow visualization purposes, along with the corresponding strain gage, piezoelectric voltage and force sensor data acquired.

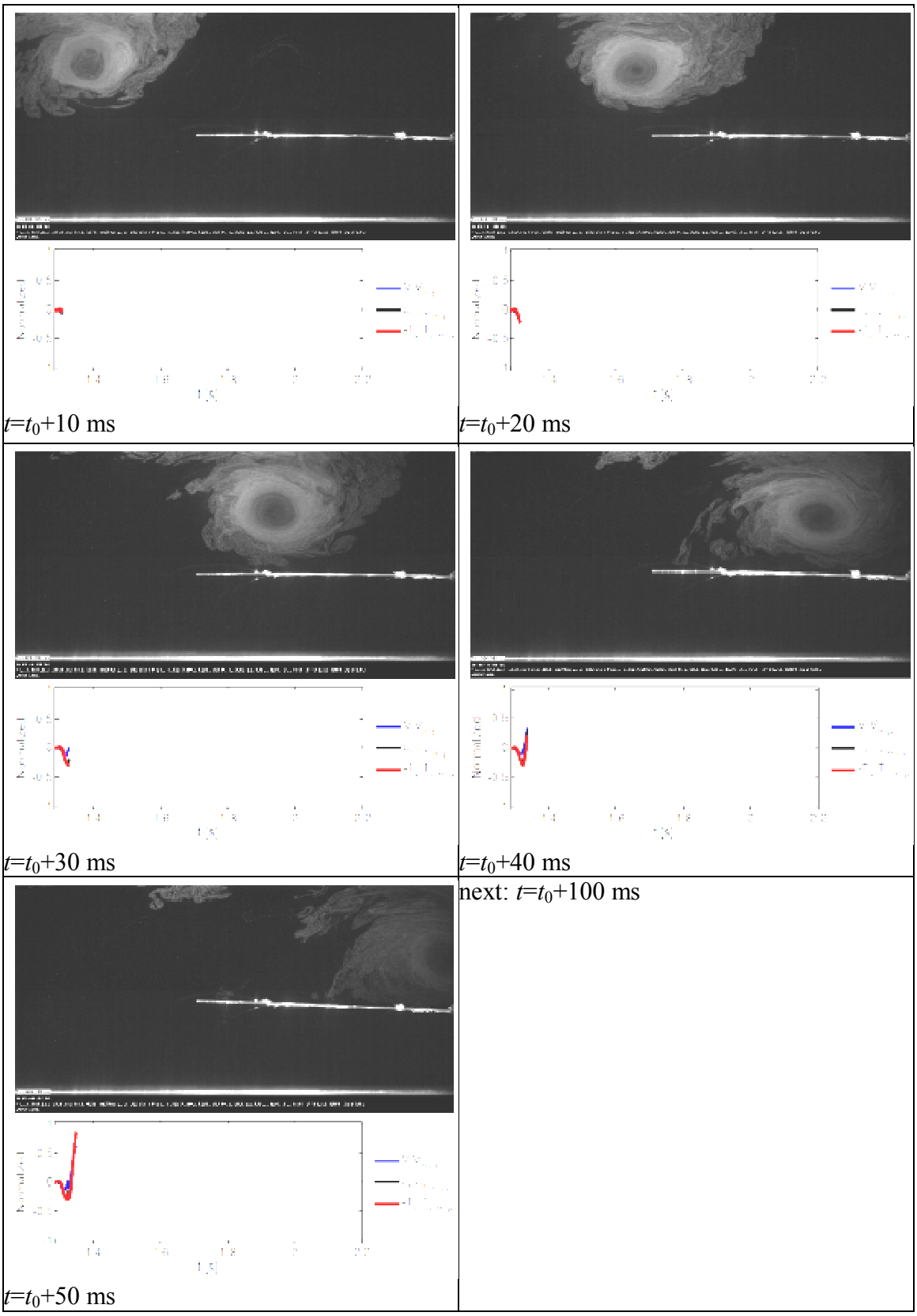

Figure 8: See next page for the caption.

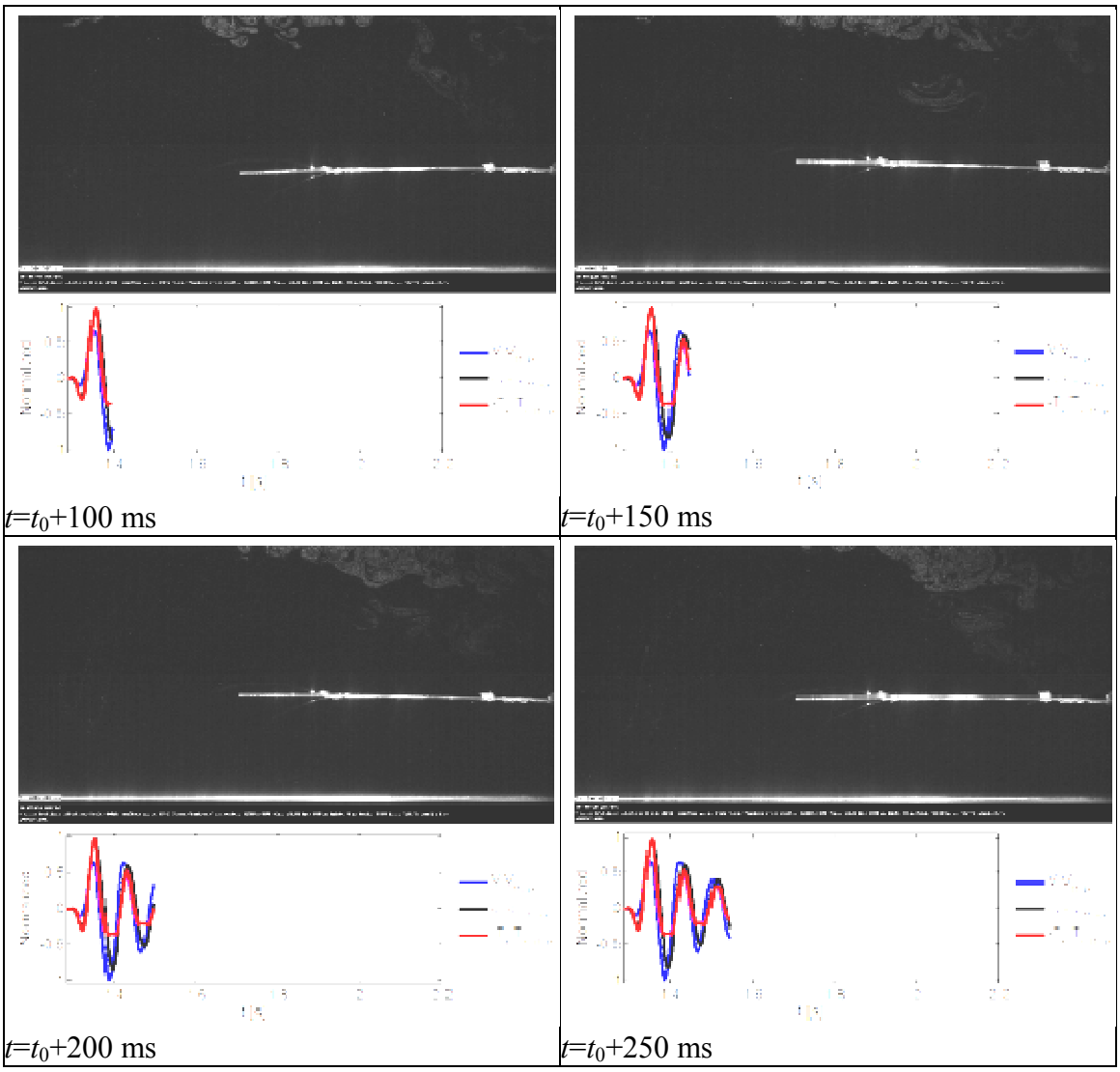

Figure 8 continued: Flow visualization images taken by using theatrical smoke. Time-variation of normalized strain, piezoelectric voltage and bending moment signals recorded simultaneously with the high-speed video. Advancement of pictures is from left to right to next row.

Figure 9 shows a sample PIV image taken by using atomized olive oil and the corresponding velocity contours obtained by using Insight 3G software (TSI, Inc.). Note that the travel speed U_{ring} of the vortex is subtracted from the entire velocity field in order to bring contrast to the variations in the contour plots. A closer view of the velocity contours is shown in Figure 10, along with the superimposed vector field indicating a counter-clockwise rotation near the location of the vortex. Figure 11 shows the contour

plots of horizontal and vertical components of velocity field. The core radius of the vortex is approximately r_{vtx}=10 mm while the center of the vortex is about h=10 mm away from the surface of the beam.

The strength of the vortex is found to be around Γ=0.324 m^2/s by taking the contour integral of velocity field over the path C shown in Figure 9b.

$$\Gamma = \oint_C \mathbf{U} \cdot \mathbf{ds} \tag{3}$$

The travel speed of the velocity is measured to be around $U_{ring.}$=−1.8 m/s (from right to left) using the video images. Note that a formula given below for the speed of vortex rings in viscous fluids [9, 10] produces $U_{ring.}$=−1.21 m/s based on the measured values of Γ, d_{ring} and r_{vtx}.

$$U_{ring} = \frac{\Gamma}{4\pi r_{vtx}} \left[\ln\left(\frac{16R}{d_{ring}} \right) - 0.558 \right] \tag{4}$$

While this discrepancy can be due to determination of r_{vtx} and d_{ring} values based on imprecise observations, it may also suggest that the actual circulation of the vortex ring could be higher than the Γ value found by contour integration.

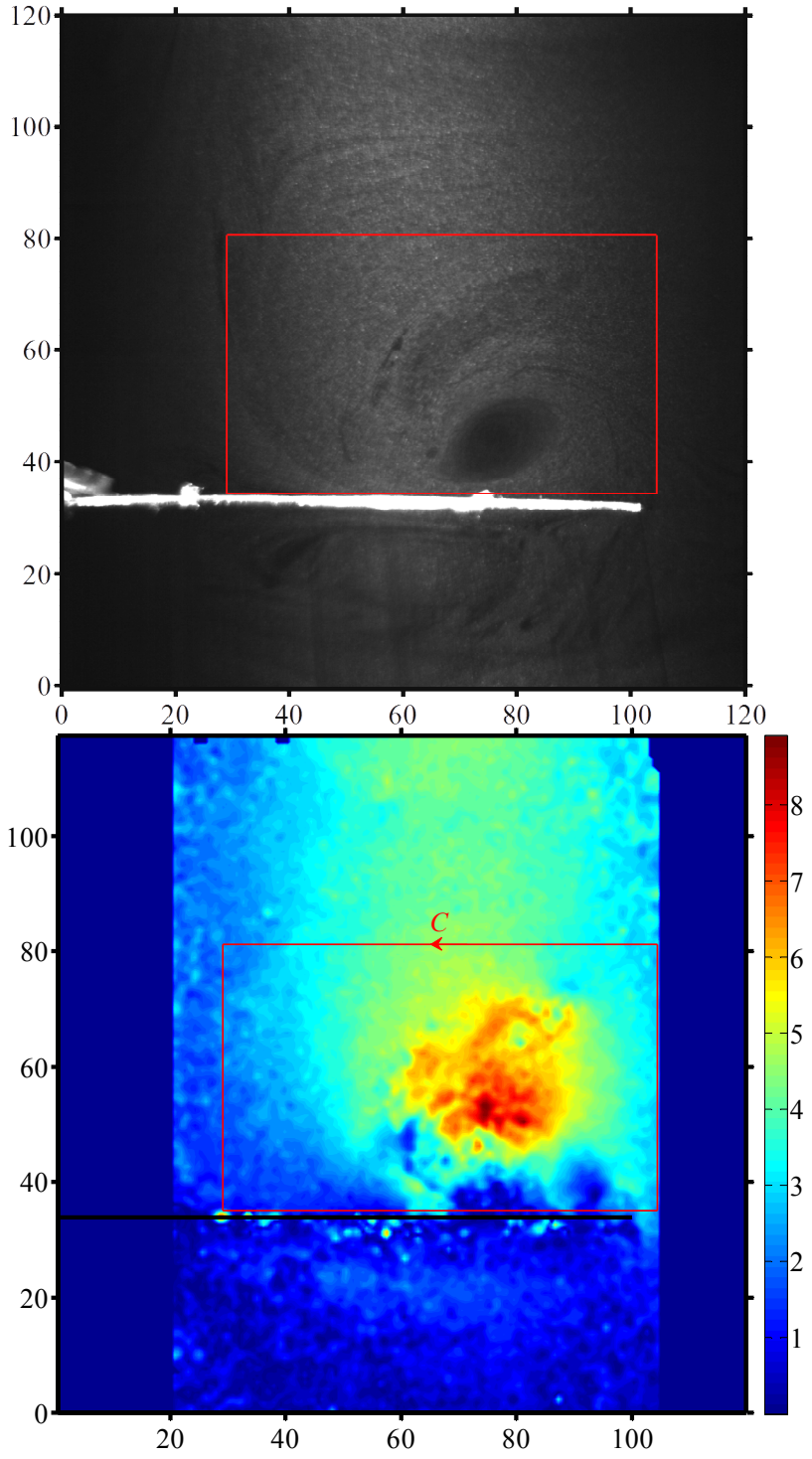

Figure 9: a) A PIV image taken by using atomized olive oil particles for seeding. The beam is fixed on the left end, vortex moves from the right to the left while rotating counter-clockwise. b) The velocity contours obtained from the image after subtracting the travel speed of vortex U_{ring}=-1.8 m/s from the entire field. Circulation of the vortex is found by taking contour integral of velocity field along the red rectangle counter-clockwise direction. Units of axes are in mm, velocity contours are in m/s.

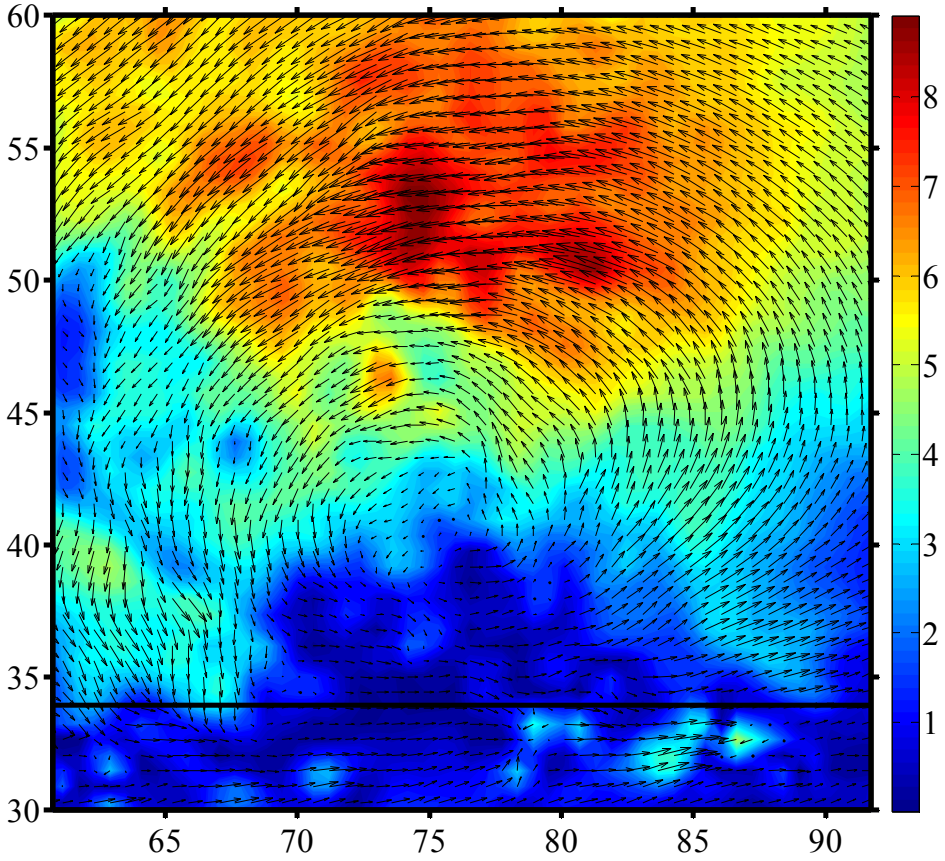

Figure 10: A closer view of the velocity magnitude contours shown in Figure 9b near the center of the vortex. The velocity vectors are also superimposed. Units of axes are in mm, velocity contours are in m/s.

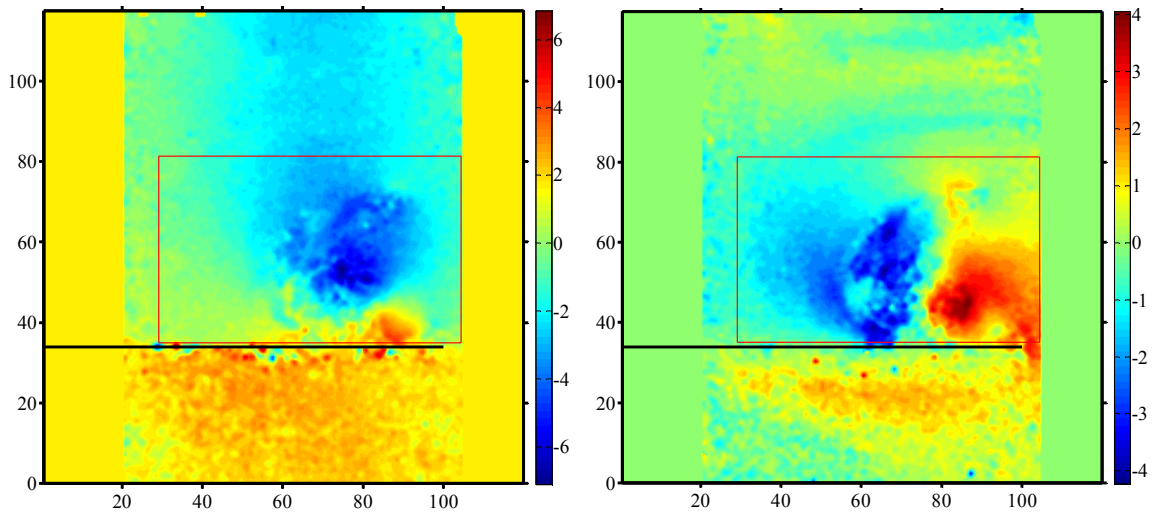

(a) (b)

Figure 11: Contours of a) u-velocity b) v-velocity. Units of axes are in mm, velocity contours are in m/s.

In an attempt to estimate the pressure load on the beam due to the vortex, potential flow theory was used. A study of a potential vortex near an infinitely long beam was presented earlier in Chapter 3. In this section, we take it a step further and investigate the case involving a beam of finite length (Figure 12). The pressure distribution over the beam in this case is expected to be quite different, especially when the vortex is close to one of the ends of the beam. Of particular interest is the pressure distribution near the free tip if the beam is cantilevered. The pressure distribution around the free end is expected to play a big role on the overall response of the beam due to its long moment arm.

The complex potential for a vortex standing near a straight wall of finite length with equal distances from the ends beam (i.e. $\mathrm{Re}\{z_o=0\}$) can be found by conformal mapping and invoking Milne-Thomson's circle theorem [11, 12]. The mapping function used is

$$z = 0.5\left(\zeta + 1/\zeta\right) \tag{5}$$

which maps the entire flow field from the physical plane (z-plane) to a solution plane (ζ-plane) while converting the finite wall of length $2a$ in (z-plane) to a circular cylinder of radius a in ζ-plane. The original configuration is thus converted to another configuration where a vortex stands near a circular cylinder of radius a, which encloses within two images of the vortex outside. In this study, the method is extended for the case of a vortex located at an arbitrary point z_o in the physical plane as seen on Figure 12.

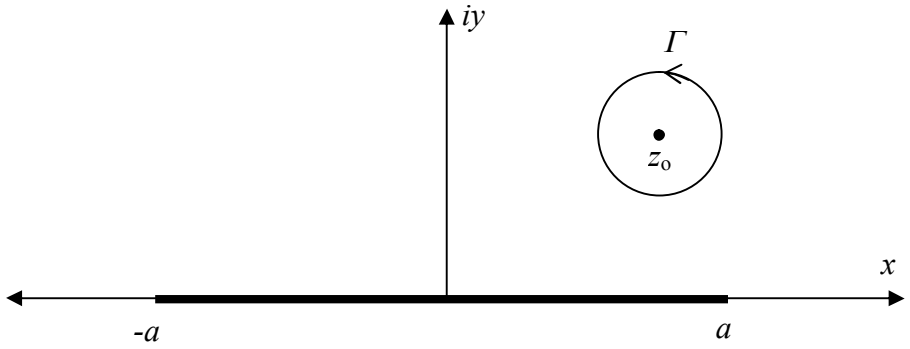

Figure 12: The physical plane (z-plane) for vortex near a finite rigid wall.

The complex potential for the flow of a vortex near a finite wall in quiescent fluid is found by Milne-Thomson's circle theorem as

$$\Phi = \frac{i\Gamma}{2\pi}\ln\left(\zeta - z_o\right) - \frac{i\Gamma}{2\pi}\ln\left(\zeta - \frac{a^2}{z_o^*}\right) - \frac{i\gamma}{2\pi}\ln\zeta \tag{6}$$

when mapped onto the ζ-plane. Here a is the half-length of the beam ($a=l/2$) and γ is the circulation around the beam given by

$$\gamma = \frac{\left|z_o\right|^2 - a^2}{\left(a - z_o\right)\left(a - z_o^*\right)} \tag{7}$$

after enforcing Kutta condition only at the free end (i.e. z=a)[*]. The velocity components in the physical plane are then found by

$$u(z) = \mathrm{Re}\left\{\frac{\mathrm{d}\Phi}{\mathrm{d}\zeta}\Big/\frac{\mathrm{dz}}{\mathrm{d}\zeta}\right\} \qquad \text{and} \qquad v(z) = -\mathrm{Im}\left\{\frac{\mathrm{d}\Phi}{\mathrm{d}\zeta}\Big/\frac{\mathrm{dz}}{\mathrm{d}\zeta}\right\} \tag{8}$$

The circle theorem ensures that $v(z=z_w)=0$ where z_w is the coordinates of the points on the solid wall describing the beam, i.e. $\mathrm{Im}(z_w)=0$ and $-a \leq \mathrm{Re}(z_w) \leq a$. Since there is no flow across the beam, the beam can be treated as a streamline of the flow field. The

[*] Enforcement of Kutta condition at both ends is only possible when the vortex is exactly in the middle of the beam (i.e. $\mathrm{Re}\{z_o=0\}$).

pressure load on the beam is then found via Bernoulli's equation written along this streamline representing the beam:

$$p_{\text{net}} = p_{\infty} - p = \frac{1}{2}\rho\left(U_{\infty}^2 - u_w^2\right) \tag{9}$$

where $u_w=u(z_w)$ and $U_{\infty}=0$ in quiescent fluid. The distributed load on the beam at a given instant is then found as $f=bp_{\text{net}}$ where b is the width of the beam. We now assume that the vortex is initially at a distant point $z_o=2a+ih$ and it approaches the beam horizontally with a speed $U_{\text{ring}}<0$. Then the time-dependent coordinate of the center of the vortex is given by:

$$z_o = 2a + U_{\text{ring}}t + ih \tag{10}$$

The motion of the vortex thus creates a travelling load on the beam. In this study, we estimated this load by first calculating the coordinate z_o using the measured travel speed U_{ring} in Equation (10), and then finding the instantaneous pressure load using Equations (6) to (9). We assume that a quasi-steady approximation on dynamics of vortex motion is reasonable for a preliminary investigation. Based on the particular PIV video, in addition, we observed that the vortex broke down and disappeared near the middle of the beam. Therefore we set a time limit $t_{\max}=(2a+a)/U_{\text{ring}}$ so that calculations stop when the vortex reaches to the middle of the beam.

While application of Kutta condition at z=+a yields a reasonable pressure distribution near the tip, the lack of it at the clamped end results in unbounded velocities and pressures at z=−a. Therefore, the downstream part of the distribution after the net pressure decreases to zero was disregarded. The rationale of this workaround was that the error introduced by doing so would be smaller than those due to the rest of the approximations. The distribution of pressure load on the beam at various time steps is

shown in Figure 13. It should be mentioned that the pressure distribution when the vortex is in the center of the beam is almost identical to that in case of an infinitely long wall. Once the time-dependent pressure distribution is obtained, it is used as a travelling load Euler Bernoulli beam equation to calculate the resulting tip deflection.

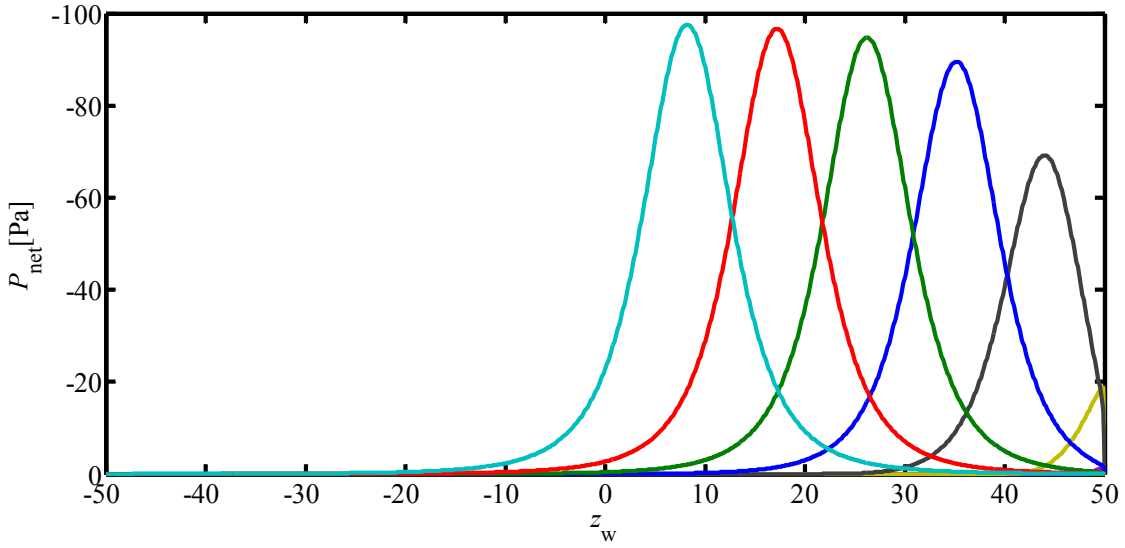

Figure 13: Pressure distribution over the beam as a potential vortex travels with U_{ring}=1.8 m/s from right to left with at 10 mm distance from the wall. Time difference between each curve is 10 ms.

The actual tip deflection in the tests is determined using the stain gage data taken. In order to do this, the stain gage voltage is first calibrated using the tip deflection value measured on a video image at a given instant (Figure 14). The measured deflection value is then used in static bending shape to find the strain at the location of the gage. This calibration yielded a gage factor of 2.07 which is close to the gage factor specified by the manufacturer of the strain gages. The deflection at any other instant can then be found using this gage factor to convert the voltage signal from the gages to strain values at any other instant. A comparison of the tip deflection measured this way, and calculated using the PIV data in conjunction with potential flow theory and Euler-Bernoulli beam equation

is shown in Figure 15. The results agree unexpectedly well despite several factors that would significantly affect the accuracy of the obtained results. These factors are: 2D inviscid quasi-steady flow assumption for a 3D viscous unsteady flow, the improper boundary condition at the clamped end, flow separation at the free end, ignored deformation of the beam and the vortex, imprecise determination of center, radius and travel speed of the vortex, and of Γ value. It may be argued that some cancellation of counter effects of these simplifications might have resulted in a seemingly good prediction of tip deflection.

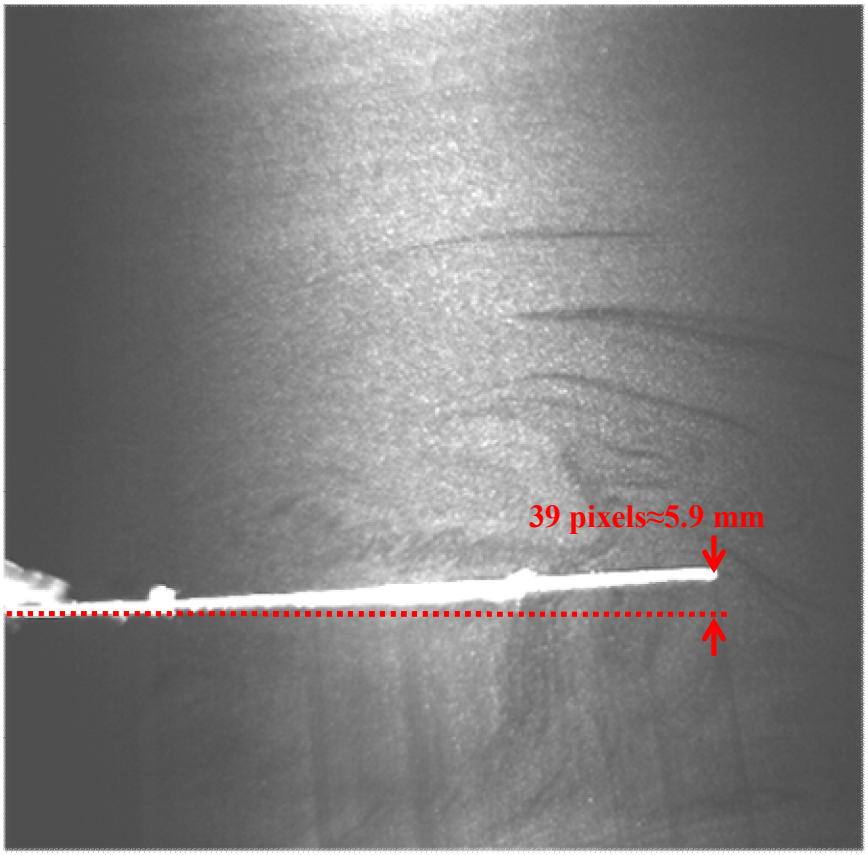

Figure 14: The image taken at t=0.0578 seconds (the first large peak in the strain gage signal on Figure 15) is used for calibration of the strain gage signal.

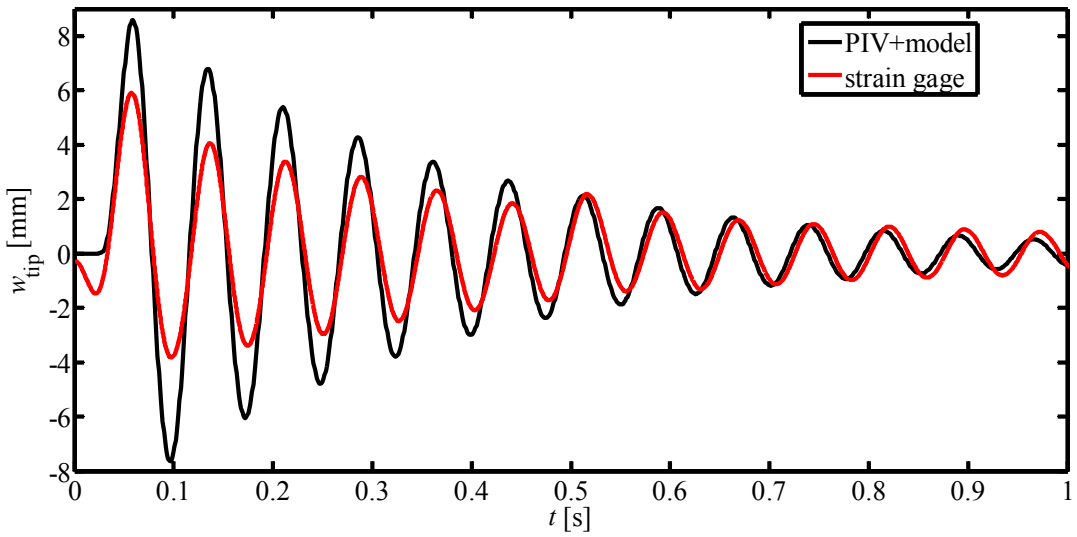

Figure 15: Tip deflection of the beam of the beam found by using PIV data in potential flow theory for Euler-Bernoulli beam model (piv+model) vs using strain gage data calibrated by deflections seen on video images.

An estimation of the aeroelastic efficiency is also performed by calculating the kinetic energy supplied by the vortex and the strain energy transferred to the beam. The kinetic energy of the vortex at the earliest visible time step was estimated based on corresponding PIV data using two methods. In the first method, the kinetic energy density of the flow field in the PIV image was found from

$$e = \frac{1}{2}\rho\left(u^2 + v^2\right) \tag{10}$$

Assuming the flow field is axis-symmetric around the centerline of the vortex ring, the 3D flow field can be reconstructed by revolving the PIV plane around this centerline (Figure 16). The kinetic energy of the entire vortex ring is then calculated from

$$E_v = 2\pi \int_{x=0}^{0.120} \int_{y=0}^{y_c} e\left(y_c - y\right) dydx \tag{11}$$

where y_c=0.103 m is approximately the vertical coordinate of the centerline of the vortex ring and x=0.120 m is the horizontal extend of the PIV frame (Figure 16).

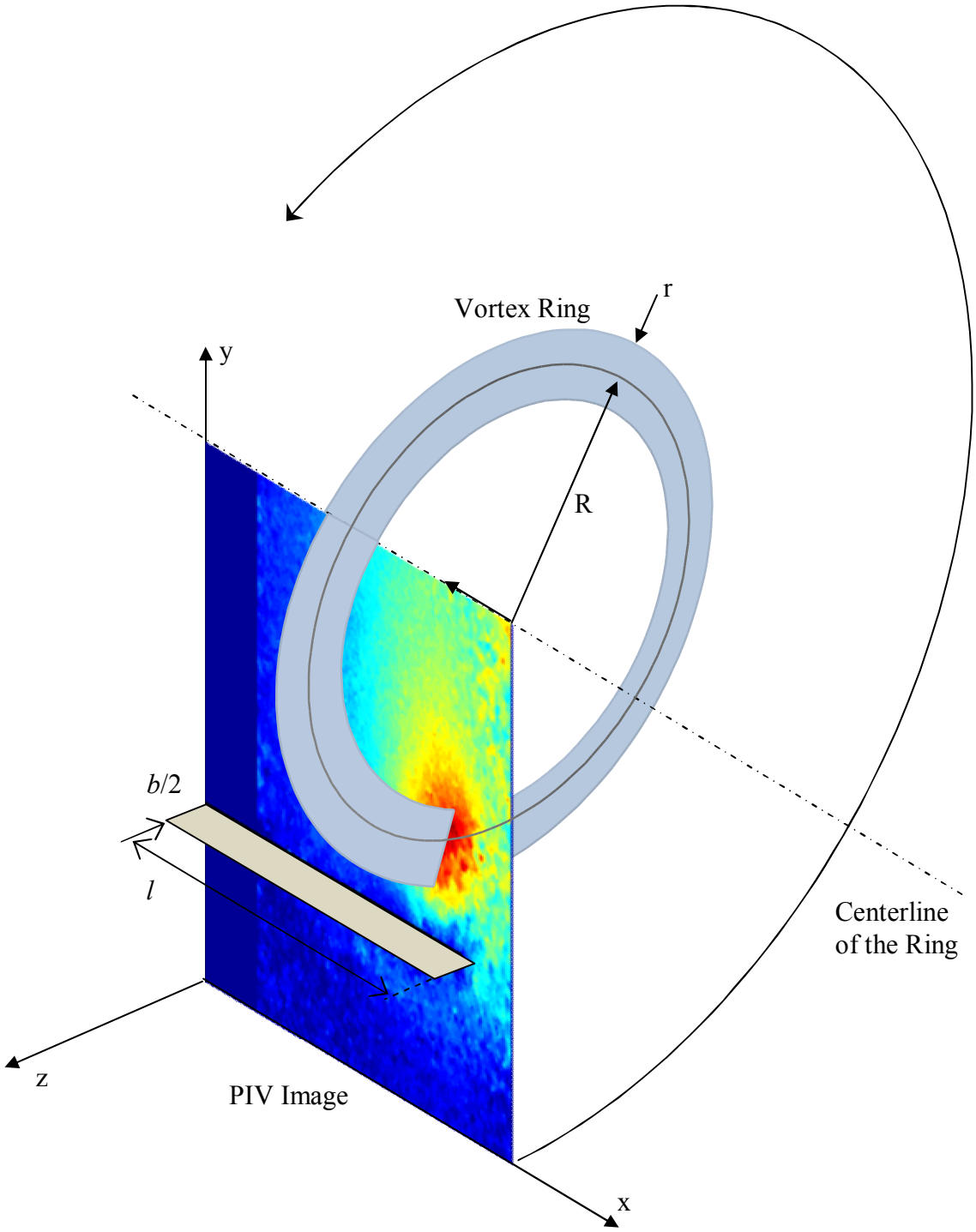

Figure 16: The revolution of planar PIV data around the centerline of the vortex ring.

In the second method, the vortex energy is calculated based on Fraenkel's second order formula [9, 13]:

$$E_{\mathrm{v}} = \frac{1}{2}\rho R\Gamma^2\left[\ln\frac{8R}{r} - \frac{7}{4} + \frac{3}{16}\left(\frac{r}{R}\right)^2 \ln\frac{8R}{r}\right] \tag{12}$$

The kinetic energies found by Equations (11) and (12) are about 13 mJ and 9 mJ respectively. The difference between the two results is attributed mainly to the rather crude determination of parameters r, R and Γ from the PIV images. The elastic mechanical energy transferred to the beam is found from

$$E_{\mathrm{b}} = \frac{1}{2}kw_{\mathrm{tip}}^2 \tag{13}$$

where k=3.92 N/m is the stiffness of the beam and w_{t} = 5.9 mm is the measured tip deflection at t=50 ms. The mechanical energy transferred to the beam is then found to be E_{b}=0.068 mJ. Note that this energy dissipates in approximately 2 seconds due to structural and viscous damping. Based on the kinetic energy found from Equation (11), the aeroelastic efficiency of the vortex-beam interaction is calculated as

$$\eta_{\mathrm{ae}} = \frac{E_{\mathrm{b}}}{E_{\mathrm{v}}} = 0.52\% \tag{14}$$

References

1. Blevins R D 1977 *Flow Induced Vibration* Litton Educational Publishing, Inc

2. Alonso G Valero E Meseguer J 2009 An analysis on the dependence on cross section geometry of galloping stability of two-dimensional bodies having either biconvex or rhomboidal cross sections *European Journal of Mechanics - B/Fluids* 28(**2**): 328-34

3. Alonso G Meseguer J Perez-Grande I 2005 Galloping instabilities of two dimensional triangular cross-section bodies *Experiments in Fluids* 38:789-95

4. Andreopoulos J Agui J 1996 Wall Vorticity Flux Dynamics in a Two-dimensional Turbulent Boundary Layer *Journal of Fluid Mechanics* 309: 45-84

5. Andreopoulos Y Honkan A 2001 An experimental study of the dissipative and vortical motions in turbulent boundary layers *Journal of Fluid Mechanics* 439:131-63

6. Peterson S D Porfiri M 2012 Energy exchange between a vortex ring and an ionic polymer metal composite *Applied Physics Letters* 100(**11**): 114102

7. Peterson S D Porfiri M 2012 Interaction of a vortex pair with a flexible plate in an ideal quiescent fluid *Journal of Intelligent Material Systems and Structures*

8. Elzawawy A 2012 Time Resolved Particle Image Velocimetry Techniques with Continuous Wave Laser and Their Application to Transient Flows. Doctoral Dissertation. ID 3499230. The City University of New York Graduate School and University Center, New York, United States

9. Sullivan I S Niemela J J Hershberger R E Bolster D Donnelly R J 2008 Dynamics of thin vortex rings *Journal of Fluid Mechanics* 609: 319-47

10. Saffman P G 1970 The velocity of viscous vortex rings *Studies in Applied Mathematics* 49: 371–80

11. Saffman P G 1993 *Vortex Dynamics* Cambridge University Press

12. Batchelor G K 2002 *An Introduction to Fluid Dynamics*, Cambridge University Press

13. Fraenkel L E 1972 Examples of steady vortex rings of small cross-section in an ideal fluid *Journal of Fluid Mechanics* 51: 119–35

Chapter 7

Summary

The major tasks of this doctoral research were stated earlier in Preface section as follows:

(i) Experimentally investigate the behavior of flexible piezoelectric structures subject to various flow conditions

(ii) Develop and verify a computational framework to predict the electrical output of a piezoelectric structure subject to a certain flow configuration

In this chapter, a summary of the dissertation will be given based on the work done for each of these tasks and their outcomes.

1. Experimental Investigations

1.1 Piezoelectric beam in the wake of a circular cylinder

A series of wind tunnel experiments were conducted to investigate the behavior of several piezoelectric structures subject to various flow configurations. In the first series of tests, a PVDF unimorph of dimensions 30 mm x 16 mm x 0.2 mm was placed in the wake of a circular cylinder. The length of the beam was equal to the diameter of the beam while its width was much smaller than the span of the cylinder. It was found out that the maximum power is generated at a resonant speed, i.e. when the vortex shedding frequency, adjusted by the wind speed, matches the first bending mode frequency of the

beam. It was also found out that, the harvested power is maximum if the beam is placed along the centerline of the wake and if the tip of the beam is located around two diameters downstream of the center of the cylinder. The extracted power decays gradually as the beam is moved downstream or cross stream. The maximum non-rectified power obtained with this PVDF unimorph was about 4uW over a 100-kOhms resistor at an airflow speed of 7.2 m/s. At these conditions, the power density based on the volume of piezoelectric material is found to be 298 mW/m^3 of PVDF. The power density based on operational device volume, including the section of the upstream cylinder was found to be $78mW/m^3$. If the volume of the cylinder section is excluded (i.e. only the operational volume of the vibrating beam is considered), then the power density based on operational device volume becomes 408 mW/m^3. The total efficiency of the configuration was found to be 0.0035% based on the fluid's kinetic energy input through the frontal area of the configuration facing uniform flow upstream. A breakdown of efficiency revealed that the electromechanical efficiency was around 11% whereas the aeroelastic efficiency was about 0.032%. It was concluded from these efficiency figures that the major losses take place during the creation of flow-induced vibrations from uniform flow.

1.2 Self-excited piezoelectric energy harvester

After the key role of aeroelastic interactions were understood, other harvester configurations were designed and tested in another series of experiments. This configuration consisted of a cantilevered piezoelectric beam carrying a circular cylinder on its free end. Such a configuration takes advantage of the aerodynamic forces acting on the cylinder to create and maintain flow-induced vibrations even if the oncoming flow is a uniform and steady. The initial designs, which did not perform well, showed that the

selection of dimensions and material properties of the components are not straightforward. It was understood that the change of a single design variable affects more than one leg of the "aeroelectromechanical" tripod introduced in Chapter 2. For example, a change in the length of the cylinder not only alters the aerodynamic forces, but also changes the structural response parameters such as bending and torsion mode frequencies of the beam. The width of the beam not only changes the structural response of the beam but also affects vortex shedding through splitter-plate effect. This argument can be extended for the case of high electromechanical coupling where the aerodynamic forces could be affected by changes in the electric circuit through the altered structural response of the piezoelectric beam.

A configuration that gave a significant electric output was found after few design iterations. This design yielded about 100μW of electrical power over 2.46 MOhm load resistance at an airflow speed of about 1.19 m/s. The geometric dimensions of this design were such that the end-effects and splitter-plate effect hindering vortex shedding are significantly reduced. In addition, reduced stiffness of the piezoelectric beam allowed the harvester to create flow-induced vibrations at speeds much lower than needed by previous designs. The low-speed operation increased the efficiency of the harvested a great deal since the input power is proportional to the cube of the incoming flow velocity. At the maximum power conditions, the power density of the self-excited configuration based on piezoelectric material volume was 233 mW/m^3 of PZT 5A while its power density based on operational device volume was 23.6 mW/m^3. The electromechanical efficiency of this configuration was about 30% which is comparable to that of the beam-in-wake design investigated in chapters 2 and 3. However, its aeroelastic efficiency is

about 2.4% which is two orders of magnitude larger than before. As a result, the self-excited design has a total efficiency of about 0.75%.

The lift force acting on the cylinder was estimated based on strain gage measurements. It was found out that the cross-flow motion of the cylinder caused significantly larger lift forces than what would be created by a stationary cylinder. Furthermore, low damping ratio of the structure resulted in a dynamic amplification factor of nearly 60 around resonance. The combined of the increased lift due to cylinder's motion and the high dynamic amplification due to low damping resulted in large tip deflections and piezoelectric strain, and thus yielded a higher electric output.

1.3 Self-excited harvesters with non-circular tip mass shapes

Due to availability of data in literature, the initial self-excited harvester designs had tip masses of circular cylinders. In order to seek for a possible increase in the power output, tip mass shapes other than a circular cylinder were also explored in Chapter 5. Two shapes that gave an outstanding performance were flat plate and half-circular cylinder (flat side facing upstream). For the most part of the velocity range tested, the tip deflection and harvested power were much larger than what was obtained by a circular cylinder. The harvested power increased with the free stream speed for both of the cases, but the half-circular cylinder shape demonstrated a much rapid increase whereas the power of the harvester with flat-plate tip mass was more gradual. The harvester using half-circular cylinder tip mass produced nearly 2mW of non-rectified electrical power at about 2.75 m/s.

1.4 Strain measurements to predict power output of a harvester

When an experimental design exploration is to be conducted to find an optimal harvester, it may be necessary to test several different harvester models. Use of PZT while building the models can be costly and laborious. In the study present at Chapter 5, it was demonstrated that there is no need to use piezoelectric materials to predict the electrical output of a harvester if the electromechanical coupling is negligibly small. While building the harvesters to be tested, the PZT parts can be replaced by mechanically-equivalent substitutes made of dummy materials (e.g. aluminum). The voltage output can then be predicted by measuring strain on appropriate locations on the dummy model and then using this strain data in a distributed-parameter model to predict the piezoelectric voltage output.

If the strain measurements are taken somewhere on the shim, it should be noted that the strain developed on the shim will not be transferred completely to the piezoelectric (or dummy) elements through the bonding layer. In the study present at Chapter 5, a strain transfer model was developed for finding the value of strain inside the piezoelectric elements based on the strain measurements taken on the shim. It was found out that rigid bonding assumption overestimated the electrical power of the harvester by more than 60% for that particular harvester. However, consideration of the strain transfer through non-rigid bonding layer yielded the electrical power about 10% less than the measured electrical power.

1.5 Interaction of a flexible beam with a vortex ring

The deformation mechanism of a flexible beam due to passing-by vortices was explained earlier with the flow visualization photos in beam-in-wake experiments

(Chapter 3). This interaction was investigated quantitatively with a separate experiment present in Section 3 of Chapter 6. In that experiment, base force, strain and piezoelectric voltage measurements on a flexible piezoelectric beam were taken simultaneously with PIV videos as the beam interacts with a vortex ring passing by. The time-resolved PIV videos provided data on strength, position, and travel speed of the vortex ring. These data were used in a potential flow solution to estimate the pressure load over the beam. Using the pressure load estimated, the corresponding deflection on the tip of the beam was calculated. The tip deflection calculated based on PIV data results are found to be comparable with the actual tip deflection measured by strain age data. The energy of the vortex has also been reasonably estimated using PIV data. Aeroelastic efficiency of the beam and vortex interaction was calculated based on these estimations.

1.6 Piezoelectric beam in turbulent flow

Another set of experiments were conducted to investigate the potential of turbulent boundary layers for energy harvesting (Chapter 2 and Chapter 6). Flexible cantilevered beams were positioned parallel to the wall of the wind tunnel at various distances. Two PVDF unimorph beams of dimensions 30 mm x 16 mm x 0.2 mm ("long beam") and 15 mm x 13 mm x 0.2 mm ("short beam") were found to generate a maximum of around 60 nW and 1.6nW of electrical power, respectively, over a load resistance of 10 MOhm. Normalization of the beam's distance from the wall with local boundary layer thickness revealed that maximum power is harvested when the beam is within the neighborhood of 35% boundary layer thickness, and that this neighborhood is larger for the shorter beam. Turbulent fluctuation length scale with 1st natural bending

frequency of the beam indicated that electrical response of the beam is not of a resonant type since the harvested power monotonically grew larger with freestream speed.

2. Computational Framework

An experimental design exploration to find an optimal harvester configuration may not always be possible due to various practical reasons. A computational framework is desirable to predict the performance of a given harvester configuration. Such a framework should capture the aeroelectromechanical aspects of the problem, i.e. it should take into account the interactions between the fluid flow, structure and the electric field in a coupled manner.

In this study, a commercial CFD (computational fluid dynamics) program was integrated through external scripting with an electrical circuit simulation program for modeling aeroelectromechanical interactions in a "loosely coupled" manner. This computational framework was used to predict the electric output of a flexible piezoelectric beam in the turbulent wake of a cylinder. The pressure load on the beam due to fluid flow was calculated by the CFD program. The corresponding electromechanical response of the beam was found by an electric circuit simulator that solves the circuit equivalent of SDOF (single degree of freedom) vibration equations of a piezoelectric beam connected to a resistor. The results of the simulation were comparable to the experimental results. It was concluded that a better agreement could be obtained at the computational expense of performing three dimensional flow simulations with meshes fine enough to use more advanced turbulence models. It was also stated that it is possible to add other vibration modes and more complex electrical circuits to the existing

framework if needed. It should be noted that, to the best of our knowledge, this simulation was the first in the literature in that it considered the interaction between the fluid flow, structural dynamics, and the response of the electric circuit at run time.

Bibliography

References for Chapter 1

1. Piezo Systems, Inc. www.piezo.com

2. Measurement Specialties, Inc. www.meas-spec.com

3. Mitcheson P D Yeatman E M Rao G K Holmes A S Green T C 2008 Energy Harvesting from Human and Machine Motion for Wireless Electronic Devices *Proceedings of the IEEE* 96(9): 1457-86

4. Panton R 1996 *Incompressible Flow* John Wiley & Sons, Inc. 2nd Ed.

5. Erturk A, Inman D J 2011 *Piezoelectric Energy Harvesting* John Wiley & Sons, Inc.

References for Chapter 2

Allen, J.J. and Smits, A. J. 2001. "Energy Harvesting Eel". *Journal of Fluids and Structures*, vol. 15 629-640

Andreopoulos Y., Honkan, A. 2001. "An Experimental Study of the Dissipative and Vortical Motion in Turbulent Boundary Layers". Journal of Fluid Mechanics, vol. 439, pp 131-163.

Anton, S. R., Sodano, H. A. 2007. "A review of Power Harvesting Using Piezoelectric Materials (2003–2006)," *Smart Materials and Structures*, 16 (2007) R1–R21. doi:10.1088/0964-1726/16/3/R01

Blevins, R.D. 1977. *Flow-induced Vibration*, Van Nostrand Reinhold Company, New York.

Discenzo, F.M., Chung, D., Loparo, K.A. 2006. "Pump Condition Monitoring Using Self-Powered Wireless Sensors," *Sound and Vibration,* 40 (5), pp. 12–15.

Dong S., Karniadakis G. E., Ekmekci, A. and Rockwell D. 2006. "A Combined DNS-PIV Study of the Turbulent Near Wake". *Journal of Fluid Mechanics*, vol. 569, pp. 185–207.

Douglas, J., Gasiorek, J. M., Swaffield, J. A., Jack, L. 2006., "Fluid Mechanics", *Pearson Prentice-Hall,* 5th ed, Harlow, U.K.

Elvin, N., Lajnef N, and Elvin A. 2006. "Feasibility of Structural Monitoring with Vibration Powered Sensors". *Smart Materials and Structures*, 15(4) pp. 977-986

Elvin, N. and Elvin, A. 2009a. "A General Equivalent Circuit Model for Piezoelectric Generators," *Journal of Intelligent Material Systems and Structures.* Vol. 20, pp. 3-9, January 2009.

Elvin, N. G., Elvin, A. A. 2009b. "A Coupled Finite Element-Circuit Simulation Model for analyzing Piezoelectric Energy Generators," *Journal of Intelligent Material Systems and Structures*, Vol. 20 pp. 587-595. March 2009 DOI: 10.1177/1045389X08101565

Erturk, A., Inman, D. J. 2008a. "Issues in Mathematical Modeling of Piezoelectric Energy Harvesters," *Smart Materials and Structures*, 17 (2008) 065016 (14pp). DOI:10.1088/0964-1726/17/6/065016

Erturk, A., Inman, D. J. 2008b. "On Mechanical Modeling of Cantilevered Piezoelectric Vibration Energy Harvesters" Journal of Intelligent Material Systems and Structures, Vol. 19, November 2008 DOI: 10.1177/1045389X07085639

Gilbert, J. M., Balouchi, F. 2008 "Comparison of Energy Harvesting Systems for Wireless Sensor Networks," *International Journal of Automation and Computing*, 05(4), October 2008, 334-347. DOI: 10.1007/s11633-008-0334-2

Ha, S., Chang, F.K. 2005. "Review of Energy Harvesting Methodologies for Potential SHM Applications," *Proc. of 2005 International Workshop on Structural Health Monitoring*, pp. 1451–1460.

Honkan, A. and Andreopoulos, J. 1997. "Vorticity, Strain-rate tensor and Dissipation in the Near Wall of Turbulent Boundary Layer," *J. Fluid Mech.*, 350, pp. 29-96.

Kamakoti, R., Shyy, W. 2005. "Fluid–structure Interaction for Aeroelastic Applications," *Progress in Aerospace Sciences*, 40 (2004) pp. 535–558.

Kimura, M. 1998. "Piezoelectric Generation Device," United States Patent Number 5,801,475.

Kymissis, J., Kendall, C., Paradiso, J., Gershenfeld, N. 1998. "Parasitic Power Harvesting in Shoes," *Second IEEE International Symposium on wearable Computers*. October 19-20th, Pittsburg, PA, pp. 132-139

Lajnef, N., Chakrabartty, S., Elvin, N., Elvin, A. 2006 "A Sub-microwatt Piezo-floating-Gate Sensor for Long-term Fatigue Monitoring in Biomechanical Implants," *Proceedings of the 28th IEEE EMBS Annual International Conference* New York City, USA, Aug 30-Sept 3, 2006, vol. 1 pp. 5936-5939.

Lefeuvre, E., Badel, A, Richard, C., Guyomar, **D**. 2005 "Piezoelectric Energy Harvesting Device Optimization by Synchronous Electric Charge Extraction," *Journal of Intelligent Material Systems and Structures*, Vol. 16, pp 865-876

Lienhard, J. H. 1966. "Synopsis of Lift, Drag and Vortex Frequency Data for Rigid Circular Cylinders", *Washington State University, College of Engineering, Research Division,* Bulletin 300*,* 1966.

Mitcheson, P.D, Yeatman, E. M., Rao, G. K, Holmes, A. S., Green, T.C. 2008. "Energy Harvesting from Human and Machine Motion for Wireless Electronic Devices," *Proceedings of the IEEE*. Vol. 96, No. 9, pp. 1457-1486, September 2008.

Myers, R. Vickers, M., Kim, H. 2007. "Small Scale Windmill," *Appl. Phys. Lett*., 2007 vol. 90, paper 054 106.

Ottman,G. K. Hofmann, H.F., Bhatt, A. C. Lesieutre, G.A. 2002. "Adaptive Piezoelectric Energy Harvesting Circuit for Wireless Remote Power Supply," *IEEE Transactions on Power Electronics*, Vol. 17, No. 5, September 2002 669-676

Panton, R. 1996 . "Incompressible Flow," *John Wiley & Sons, Inc*. 2nd Ed.

Paradiso, J.A., Starner, T., Energy Scavenging for Mobile and Wireless Electronics, *Pervasive Computing.* Volume 4, Issue 1, pp: 18 – 27, January-March 2005.

Pobering, S., Schwesinger, N. 2004. "A Novel Hydropower Harvesting Device". *Proceedings – 2004 International Conference on MEMS, NANO and Smart Systems*, ICMENS 2004, p 480-485.

Priya,S., Chen, C., Fye, D., Zahnd, J. 2005. "Piezoelectric Windmill: A Novel Solution to Remote Sensing" *Japanese Journal of Applied Physics*. 44 (2005) pp. L104-L107

Robbins, W. P., Marusic, I., Morris, D. Novak, T.O., 2006, "Wind-Generated Electrical Energy Using Flexible Piezoelectric Materials," *Proceedings of IMECE2006* 2006 ASME International Mechanical Engineering Congress and Exposition November 5-10, 2006, Chicago, Illinois

Roshko, A. 1953. "On the Development of Turbulent Wakes from Vortex Streets", *National Advisory Committee for Aeronautics Report* NACA-TN-2913

Roshko, A. 1961. "Experiments on the Flow Past a Cylinder at Very High Reynolds Number", *Journal of Fluid Mechanics* vol. 10, p. 345-356

Schmidt, V. H. 1992. "Piezoelectric Energy Conversion in Windmills," *Proceedings of IEEE Ultrasonics Symposium*, pp 897-904.

Shukla, S., Govardhan, R. N., Arakeri, J.H. 2009 "Flow Over a Cylinder With a Hinged-Splitter Plate," *Journal of Fluids and Structures*, In Press, Corrected Proof, Available online 5 March 2009, ISSN 0889-9746, DOI: 10.1016/j.jfluidstructs.2008.11.004.

Sodano, H. A., Inman, D. J., Park, G. 2005. "Generation and Storage of Electricity from Power Harvesting Devices," *Journal of Intelligent Material Systems and Structures.* Vol. 16, pp. 67-75 January 2005.

Sodano, H. A., Park, G. Inman, D. J. 2004. "A Review of Power Harvesting from Vibration Using Piezoelectric Materials," T*he Shock and Vibration Digest*, 36(3) 197–205, May 2004.

Taylor, G.W., Burns, J.R., Kammann, S.M., Powers, W. B., Welsh, T. R. 2001. "The energy Harvesting Eel: A Small Subsurface Ocean/River Power Generator". *IEEE Journal of Oceanic Engineering*. Vol 26, No 4, pp. 539-547.

Unal, M. F., Rockwell, D. 1988a. "On vortex formation from a cylinder. Part I: The initial instability," *Journal of Fluid Mechanics*, vol. 190, pp. 491-512

Unal, M. F., Rockwell, D. 1988b. "On vortex formation from a cylinder. Part II. Control by splitter-plate interference", *Journal of Fluid Mechanics*, vol. 190, pp. 513-529

References for Chapter 3

Akaydin HD, Elvin N, Andreopoulos Y (2010) Energy harvesting from highly unsteady fluid flows using piezoelectric materials. J Intell Mater Struct (accepted for publication)

Allen JJ, Smits AJ (2001) Energy harvesting Eel. J Fluids Struct 15:629–640

Andreopoulos J, Agui JH (1996) Wall-vorticity flux dynamics in a two-dimensional turbulent boundary layer. J Fluid Mech 209:45–84

Andreopoulos Y, Honkan A (2001) An experimental study of the dissipative and vortical motion in turbulent boundary layers. J Fluid Mech 439:131–163

Anton SR, Sodano HA (2007) A review of power harvesting using piezoelectric materials (2003–2006). Smart Mater Struct 16:R1–R21. doi:10.1088/0964-1726/16/3/R01

Beal DN, Hover FS, Triantafylou MS, Liao JC, Lader GV (2006) Passive propulsion in vortex wakes. J Fluid Mech 549:385–402

Bendat J, Piersol AG (2000) Random data, 3rd edn. Wiley, New York

Bloor MS (1964) The transition to turbulence in the wake of a circular cylinder. J Fluid Mech 19:290–304

Brede M (2004) Measurement of turbulence production in the cylinder separated shear layer using event triggered laser-Doppler anemometry. Exp Fluids 36:860–866

Dong S, Karniadakis GE, Ekmekci A, Rockwell D (2006) A combined DNS-PIV study of the turbulent near wake. J Fluid Mech 569:185–207

Eldredge JD, Piscani D (2008) Passive locomotion of a simple articulated fish-like system in the wake of an obstacle. J Fluid Mech 607:279–288

Elvin NG, Elvin AA (2009a) A general equivalent circuit model for piezoelectric generators. J Intell Mater Syst Struct 20:3–9

Elvin NG, Elvin AA (2009b) A coupled finite element-circuit simulation model for analyzing piezoelectric energy generators. J Intell Mater Syst Struct 20: 587–595. March 2009. doi: 10.1177/1045389X08101565

Elvin NG, Lajnef N, Elvin A (2006) Feasibility of structural monitoring with vibration powered sensors. Smart Mater Struct 15(4):977–986

Erturk A, Inman DJ (2008) A distributed parameter electromechanical model for cantilevered piezoelectric energy harvesters. J Vib. Acoust 130:041002

Hwang J-Y, Yang K-S (2007) Drag reduction on a circular cylinder using dual detached splitter plates. J Wind Eng Ind Aerodyn 95:551–564

Lau YL, So RMC, Leung RCK (2004) Flow-induced vibration of elastic slender structures in a cylinder wake. J Fluids Struct 19:1061–1083. DOI:10.1016/j.jfluidstructs.2004.06.007

Lin JC, Towfighi J, Rockwell D (1995) Instantaneous structure of the near wake of a circular cylinder: on the effect of Reynolds number. J Fluids Struct 9:409–418

Mitcheson PD, Yeatman EM, Rao GK, Holmes AS, Green TC (2008) Energy harvesting from human and machine motion for wireless electronic devices. Proc IEEE 96(9):1457–1486

Mittal S, Raghuvanshi A (2001) Control of vortex shedding behind circular cylinder for flows at low Reynolds numbers. Int J Numer Meth Fluids 35:421–447

Monkewitz P, Nguyen LN (1986) Absolute instability in the near wake of two-dimensional bluff bodies. J Fluids Struct 1:165–184

Paradiso JA, Starner T (2005) Energy scavenging for mobile and wireless electronics. Pervasive Comput 4(1):18–27

Pobering S, Schwesinger N (2004) A novel hydropower harvesting device. Proceedings—2004 International Conference on MEMS, NANO and Smart Systems, ICMENS 2004, pp 480–485

Prasad A, Williamson CHK (1996) The instability of the separated shear layer from a bluff body. Phys Fluids 8:1347–1349

Prasad A, Williamson CHK (1997a) The instability of a shear layer separating from a bluff body. J Fluid Mech 333:375–402

Prasad A, Williamson CHK (1997b) Three-dimensional effects in turbulent bluff body wakes at moderate Reynolds numbers. J Fluid Mech 343:235–265

Prasad A, Williamson CHK (1997c) Three-dimensional effects in turbulent bluff body wakes. Exp Therm Fluid Sci 14:9–16

Rajagopalan S, Antonia RB (2005) Flow around a circular cylinder—structure of the near wake shear layer. Exp Fluids 38:393–402

Robbins WP, Marusic I, Morris D, Novak TO (2006) Wind-generated electrical energy using flexible piezoelectric materials. Proceedings of IMECE2006 2006 ASME International Mechanical

Engineering Congress and Exposition, November 5–10, 2006, Chicago, Illinois

Roshko A (1954) On the development of turbulent wakes from vortex streets. NACA Report 1191

Sahele M, Liu Y, Hoffman H (2005) Piezoelectric energy harvesting using different approaches including control system. Annu Res J III:134–141

Schmidt VH (1992) Piezoelectric energy conversion in windmills. Proceedings of IEEE Ultrasonics Symposium, pp 897–904

Shukla S, Govardhan RN, Arakeri JH (2009) Flow over a cylinder with a hinged-splitter plate. J Fluids Struct. ISSN 0889-9746, doi: 10.1016/j.jfluidstructs.2008.11.004

Sodano HA, Park G, Inman DJ (2004) A review of power harvesting from vibration using piezoelectric materials. Shock Vib Digest 36(3):197–205

Sodano HA, Inman DJ, Park G (2005) Generation and storage of electricity from power harvesting devices. J Intell Mater Syst Struct 16:67–75

Taylor GW, Burns JR, Kammann SM, Powers WB, Welsh TR (2001) The energy harvesting eel: a small subsurface ocean/river power generator. IEEE J Ocean Eng 26(4):539–547

Unal MF, Rockwell D (1988) On vortex formation from a cylinder. Part II. Control by splitterplate interference. J Fluid Mech 190:513–529

Williamson CHK (1996) Vortex dynamics in the cylinder wake. Annu Rev Fluid Mech 28:477–539

Zdravkovich M (1997) Flow around circular cylinders, vol. 1. Oxford University Press, Oxford

References for Chapter 4

[1] Akaydın H. D, Elvin N. and Andreopoulos Y., 2010, "Energy Harvesting from Highly Unsteady Fluid Flows Using Piezoelectric Materials" Journal of Intelligent Material Systems and Structures, doi:10.1177/1045389X10366317

[2] Akaydın H. D., Elvin N. and Andreopoulos Y., 2010, "Wake of a cylinder: A paradigm for energy harvesting with piezoelectric materials" Experiments in Fluids: Volume 49, Issue 1, Page 291-304.

[3] Anton S. R and Sodano H. A., 2007, "A review of power harvesting using piezoelectric materials (2003–2006)" Smart Materials and Structures, 16: R1-R21

[4] Sodano HA, Inman DJ and Park G, 2004, "A Review of Power Harvesting from Vibration using Piezoelectric Materials," The Shock and Vibration Digest, 136:197-205

[5] Allen, J.J. and Smits, A.J. 2001. ''Energy Harvesting Eel,'' Journal of Fluids and Structures, 15:629_640.

[6] Taylor, G.W., Burns, J.R., Kammann, S.M., Powers, W.B. and Welsh, T.R. 2001. ''The Energy Harvesting Eel: A Small Subsurface Ocean/River Power Generator,'' IEEE Journal of Oceanic Engineering, 26:539_547.

[7] Priya, S., Chen, C., Fye, D. and Zahnd, J. 2005. ''Piezoelectric Windmill: A Novel Solution to Remote Sensing,'' Japanese Journal of Applied Physics, 44:L104_L107

[8] Robbins, W.P., Marusic, I., Morris, D. and Novak, T.O. 2006.''Wind-generated Electrical Energy using Flexible Piezoelectric Materials,'' Proceedings of ASME International Mechanical Engineering Congress and Exposition, IMECE (2006) 5-10 November, Chicago, Illinois.

[9] Li, S., Xi'an, S. C., Lipson, H. "Vertical-Stalk Flapping-Leaf Generator for Wind Energy Harvesting," 2009, Proceedings of the ASME Conference on Smart Materials, Adaptive Structures and Intelligent Systems SMASIS2009-1276 September 20-24, Oxnard, California, USA

[10] Erturk, A., Inman, D. J. 2009, "An experimentally validated bimorph cantilever model for piezoelectric energy harvesting from base excitations," Smart Materials and Structures 18 (2009) 025009, doi:10.1088/0964-1726/18/2/025009

[11] Unal, M.F. and Rockwell, D. 1988b. ''On Vortex Formation from a Cylinder. Part II: Control by Splitter-Plate Interference,'' Journal of Fluid Mechanics, 190:513_529.

[12] Nakamura, Y., 1996, "Vortex Shedding From Bluff Bodies With Splitter Plates," Journal of Fluids and Structures 10, 147 – 158.

References for Chapter 5

[1] Anton S R and Sodano H A 2007 A review of power harvesting using piezoelectric materials (2003–2006) Journal of *Smart Materials and Structures*, **16** R1-21

[2] Sodano H A, Inman D J and Park G 2004 A review of power harvesting from vibration using piezoelectric materials *The Shock and Vibration Digest*, **136** 197-205

[3] Erturk A, Inman D J 2011 *Piezoelectric Energy Harvesting* John Wiley & Sons

[4] Akaydın H D, Elvin N, Andreopoulos Y 2010 Wake of a cylinder: A paradigm for energy harvesting with piezoelectric materials *Experiments in Fluids*, **49** (1) 291-304

[5] Akaydın H D, Elvin N, Andreopoulos Y 2010 Energy harvesting from highly unsteady fluid flows using piezoelectric materials *Journal of Intelligent Material Systems and Structures*, **21** (13) 1263-78

[6] Panton R L 1993 *Incompressible Flow* John Wiley & Sons

[7] Akaydın, H D, Elvin N, Andreopoulos Y 2010 Experimental study of a self-excited piezoelectric energy harvester, *Proceedings of 3rd ASME Conference on Smart Materials, Adaptive Structures and Intelligent Systems* SMASIS2010-3729 September 28 - October 1 2010, Philadelphia, PA. USA.

[8] Unal M F and Rockwell D 1988 On vortex formation from a cylinder. Part II: Control by splitter-plate interference *Journal of Fluid Mechanics*, **190** 513-29

[9] Erturk A and Inman D J 2008 A distributed parameter electromechanical model for cantilevered piezoelectric energy harvesters *Journal of Vibration and Acoustics* **130** 041002-1

[10] Erturk A, Inman D J 2009 An experimentally validated bimorph cantilever model for piezoelectric energy harvesting from base excitations *Journal of Smart Materials and Structures* **18** 025009

[11] Crawley E, Anderson H, 1990, Detailed Models of Piezoceramic Actuation of Beams *Journal of Intelligent Material Systems and Structures* **1** (1) 4-25

[12] Pietrzakowski M 2001 Active damping of beams by piezoelectric system: effects of bonding layer properties *International Journal of Solids and Structures* **38** (44-45) 7885-97

[13] Ye J Q 2001 Interfacial shear transfer of RC beams strengthened by bonded composite plates *Cement & Concrete Composites*, **23** 411-7

[14] Han L, Wang X D, Zuo M 2009 The dynamic behavior of a surface-bonded piezoelectric actuator with a bonding layer *Acta Mechanica* **206** (3-4) 193-205

[15] Guenaneche B, Krour B, Tounsi A, Fekrar A, Benyoucef S, Bedia A, 2010, Elastic analysis of interfacial stresses for the design of a strengthened FRP plate bonded to an RC beam *International Journal of Adhesion and Adhesives*, **30** 636-42

[16] Jin C, Wang X 2011 The effect of adhesive layers on the dynamic behavior of surface-bonded piezoelectric sensors with debonding *Journal of Intelligent Material Systems and Structures* **22** (7) 655-67

[17] De Faria A R 2003 The impact of finite-stiffness bonding on the sensing effectiveness of piezoelectric patches Journal of Smart Materials and Structures **12** (4) N5-8

[18] Yang J, Ye J 2010 An improved closed-form solution to interfacial stresses in plated beams using two-stage approach *International Journal of Mechanical Sciences* **52** (1) 13-30

[19] Elvin N, Elvin A, 2009 A general equivalent circuit model for piezoelectric generators *Journal of Intelligent Material Systems and Structures*. **20** (1) 3-9

[20] Lienhard, J H 1966 Synopsis of lift, drag, and vortex frequency data for rigid circular cylinders *College of Engineering, Research Division, Bulletin 300, Technical Extension Service* Washington State University Pullman, Washington. USA

[21] Blevins R D 1977 *Flow-induced Vibration*, Van Nostrand Reinhold Company

[22] Dong S, Karniadakis G E 2005 DNS of flow past a stationary and oscillating cylinder at Re=10000 *Journal of Fluids and Structures* **20** 519-31

[23] Norberg C 2002 Fluctuating lift on a circular cylinder: Review and new measurements, *Journal of Fluids and Structures* **17** 57-96

[24] Shu Y C, Lien I C 2006 Efficiency of energy conversion for a piezoelectric power harvesting system *Journal of Micromechanics and Microengineering* **16** (11) 2429-38

[25] Rao S S 2007 *Vibration of Continuous Systems* John Wiley & Sons

[26] De Marqui C, Erturk A, Inman D 2010 Piezoaeroelastic Modeling and Analysis of a Generator Wing with Continuous and Segmented Electrodes *Journal of Intelligent Material Systems and Structures* **21** (10) 983-93

References for Chapter 6

1. Blevins R D 1977 *Flow Induced Vibration* Litton Educational Publishing, Inc

2. Alonso G Valero E Meseguer J 2009 An analysis on the dependence on cross section geometry of galloping stability of two-dimensional bodies having either biconvex or rhomboidal cross sections *European Journal of Mechanics - B/Fluids* 28(**2**): 328-34

3. Alonso G Meseguer J Perez-Grande I 2005 Galloping instabilities of two dimensional triangular cross-section bodies *Experiments in Fluids* 38:789-95

4. Andreopoulos J Agui J 1996 Wall Vorticity Flux Dynamics in a Two-dimensional Turbulent Boundary Layer *Journal of Fluid Mechanics* 309: 45-84

5. Andreopoulos Y Honkan A 2001 An experimental study of the dissipative and vortical motions in turbulent boundary layers *Journal of Fluid Mechanics* 439:131-63

6. Peterson S D Porfiri M 2012 Energy exchange between a vortex ring and an ionic polymer metal composite *Applied Physics Letters* 100(**11**): 114102

7. Peterson S D Porfiri M 2012 Interaction of a vortex pair with a flexible plate in an ideal quiescent fluid *Journal of Intelligent Material Systems and Structures*

8. Elzawawy A 2012 Time Resolved Particle Image Velocimetry Techniques with Continuous Wave Laser and Their Application to Transient Flows. Doctoral Dissertation. ID 3499230. The City University of New York Graduate School and University Center, New York, United States

9. Sullivan I S Niemela J J Hershberger R E Bolster D Donnelly R J 2008 Dynamics of thin vortex rings *Journal of Fluid Mechanics* 609: 319-47

10. Saffman P G 1970 The velocity of viscous vortex rings *Studies in Applied Mathematics* 49: 371–80

11. Saffman P G 1993 *Vortex Dynamics* Cambridge University Press

12. Batchelor G K 2002 *An Introduction to Fluid Dynamics*, Cambridge University Press

13. Fraenkel L E 1972 Examples of steady vortex rings of small cross-section in an ideal fluid *Journal of Fluid Mechanics* 51: 119–35